

PERFORMANCE EVALUATION OF RECYCLED PLASTIC PINS IN TWO LAYERS
TO STABILIZE DEEP SLOPE FAILURES

By

SACHINI MADANAYAKE

Presented to the Faculty of Graduate School of
The University of Texas at Arlington in Partial Fulfillment
of the Requirements
for the Degree of

DOCTOR OF PHILOSOPHY IN CIVIL ENGINEERING

THE UNIVERSITY OF TEXAS AT ARLINGTON

December 2022

Copyright © by Sachini Madanayake 2022

All Rights Reserved



ACKNOWLEDGEMENTS

I would like to express my sincere and utmost gratitude to my supervising professor, Dr. Sahadat Hossain, for his motivation and continuous support during my graduate studies. He created an environment to nourish research and improve my capabilities beyond expectations. I am grateful for his confidence and belief in me. I am greatly thankful for the opportunity to complete my PhD under his guidance.

I would like to acknowledge Dr. Xinbao Yu, Dr. Laureano Hoyos and Dr. Muhammad N. Huda, my dissertation committee, for providing assistance with constructive comments and guidance. I would also like to thank the Texas Department of Transportation (TxDOT) for funding this project.

My heartfelt gratitude goes to the SWIS family for their immeasurable support during my research period. I am especially grateful for all the SWIS members who worked with me during my time and were present through thick and thin. Thank you for making me feel at home. I am forever grateful to Muhasina Manjur Dola and Prabesh Bhandari for their immense help during field work, research, and for a lifetime of memories.

Finally, I would like to thank my parents, my aunt, uncle, cousin, and fiancé for their endless support, encouragement, and love. I would not be here without them. Thank you for believing in me. I am grateful to each and every person who helped me throughout this journey.

October 15, 2022

ABSTRACT

PERFORMANCE EVALUATION OF RECYCLED PLASTIC PINS TO STABILIZE DEEP SLOPE FAILURES

Sachini Madanayake

The University of Texas at Arlington, 2022

Supervising Professor: Dr. MD Sahadat Hossain

Slope failures are a common occurrence in highway embankments throughout Texas due to the presence of high plastic clays with expansive behavior. Although shallow slope failures are prevalent, slope failures extending deeper into the slope occur due to the development of micro and macro cracks. The cracks facilitate the infiltration of rainwater deeper into the slope over time. Slope failures incur thousands of dollars' worth of repairs every year for transportation departments across the country.

Recycled Plastic Pins (RPP) have been identified as an effective, cost efficient, and sustainable solution to stabilize shallow failures. The resistance of RPP is mobilized when the slip surface intersects the reinforcing member. When slip surfaces extend beyond the length of RPP, little to no resistance is mobilized against failure. Hence, a two layered design is proposed in this study to extend reinforcement deeper into the slope as a solution for deeper failures while maintaining the cost and ingenuity of the solution.

The main objective of this study is to investigate the effectiveness of the use of RPP in a two layered design to stabilize deep slope failures. Two sites in Texas were selected to conduct a field study. The sites were reinforced with 10 feet RPP with the first layer

installed at the surface of the slope after failure and second layer flush to the ground after backfilling. The reinforcement extended a total of 15-16 feet into the slope. The spacing between the layers was varied in the two sites.

The performance monitoring indicated up to 40% reduction in lateral deformation due the use of the novice design compared to the control section. Vertical deformation results showed that the use of closer spacing between the layers reduced the occurrence of increased surface erosion and creation of rills. Numerical analysis conducted showed up to 15% reduction of deformation at the crest of the slope and up to 45% reduction of deformation at the slip surface due the overlap design compared to conventional design. The study also showed that the factor of safety increased, and the deformation decreased, when the slip surface intersects both layers of reinforcement for failure depths less than 8 feet. However, the anchorage depth takes precedence when the failure planes extend deeper into the slope. Three limiting failure criteria were considered to determine the resistance provided by the reinforcement: Limit soil resistance, limit displacement, and limit flexure. Design charts and prediction models were developed using a modified equation and modeling results. Based on the performance monitoring results and further analysis, it can be concluded that the incorporation of a two layered design is effectively aiding against deep slope failures.

Table of Contents

ACKNOWLEDGEMENTS.....	ii
ABSTRACT.....	iv
List of Figures.....	xi
List of Tables.....	xx
Chapter 1 INTRODUCTION.....	1
1.1 Background.....	1
1.2 Problem Statement.....	4
1.3 Research Objective.....	5
1.4 Dissertation Organization.....	6
Chapter 2 LITERATURE REVIEW.....	8
2.1 Slope Failures.....	8
2.1.1 Expansive Soils.....	8
2.2 Shallow Slope Failures.....	10
2.2.1 Methods of Repair for Shallow Slope Failures.....	11
2.3 Deep Slope Failures.....	15
2.3.1 Methods of Repair for Deep Slope Failures.....	16
2.4 Recycled Plastic Pins (RPP).....	24
2.4.1 Manufacturing Process of Recycled Plastic Pins.....	24
2.4.2 Engineering Properties of Recycled Plastic Pins.....	25
2.5 Design for stabilizing slopes with Recycled Plastic Pins.....	27
2.5.1 General Approach.....	27
2.5.2 The Effect of Pile Characteristics on the Resisting Force.....	29
2.6 Field Studies.....	34
2.6.1 Emma I-70.....	34

2.6.2	I-435 & Wornall Road.....	36
2.6.3	U.S 54 - Fulton.....	37
2.6.4	U.S 287 - Midlothian.....	38
2.7	Limitations of Previous Studies.....	40
Chapter 3	SITE INVESTIGATION AND SLOPE STABILIZATION PLAN.....	41
3.1	Background.....	41
3.2	Site 1: IH-820 & Rosedale Street.....	42
3.2.1	Site Investigation.....	42
3.2.2	Geotechnical Investigation.....	43
3.2.3	Analyses of Site Investigation Results.....	50
3.2.4	Slope Stability Analysis.....	51
3.3	Site 2: U.S 67 – Alvarado.....	54
3.3.1	Site Investigation.....	54
3.3.2	Geotechnical Investigation.....	56
3.3.3	Analyses of Site Investigation Results.....	60
3.3.4	Slope Stability Analysis.....	61
Chapter 4	SLOPE STABILIZATION USING RECYCLED PLASTIC PINS.....	64
4.1	Mechanism of Slope Stabilization.....	64
4.2	Selection of Materials.....	65
4.3	Design of Slope Stabilization Scheme: IH-820 & Rosedale Street.....	67
4.4	Installation of RPP: IH-820 & Rosedale Street.....	70
4.5	Design of Slope Stabilization Scheme: U.S 67- Alvarado.....	75
4.6	Installation of RPP: U.S 67- Alvarado.....	78
4.7	Cost Analysis.....	82

Chapter 5	INSTRUMENTATION AND PERFORMANCE MONITORING	83
5.1	Instrumentation in IH-820 & Rosedale Street	83
5.1.1	Inclinometer.....	85
5.1.2	Topographic Survey.....	86
5.2	Performance Monitoring Results: IH-820 & Rosedale Street.....	87
5.2.1	Inclinometer Monitoring.....	87
5.2.2	Topographic Survey Monitoring.....	93
5.3	Instrumentation in U.S 67: Alvarado	96
5.3.1	Inclinometer.....	96
5.3.2	Topographic Survey.....	97
5.3.3	Piezometer.....	98
5.4	Performance Monitoring Results: U.S 67: Alvarado	99
5.4.1	Inclinometer Monitoring.....	99
5.4.2	Topographic Survey Monitoring.....	102
5.4.3	Piezometer Monitoring.....	104
5.5	Summary.....	107
Chapter 6	NUMERICAL STUDY.....	109
6.1	Introduction.....	109
6.2	IH-820 & Rosedale Street.....	109
6.2.1	Model Calibration	109
6.2.2	Performance Evaluation of Reinforced Section	112
6.3	U.S 67- Alvarado.....	119
6.3.1	Model Calibration	119
6.3.2	Performance Evaluation of Reinforced Section	121

6.4	Parametric Study	126
6.4.1	Effect of Construction Sequence on Factor of Safety	126
6.4.2	Effect of Location of Reinforcement on Factor of Safety.....	129
6.4.3	Effect of the Number of Deep Layers on Factor of Safety	132
6.4.4	Effect of Spacing between Layers on Factor of Safety.....	133
6.4.5	Effect of Overlap Depth on Factor of Safety and Lateral Deformation.....	135
6.5	Summary.....	142
Chapter 7	DEVELOPMENT OF DESIGN CHARTS.....	144
7.1	Introduction.....	144
7.2	Limit Soil Resistance	147
7.2.1	Limit Soil Resistance for Two Layered Layout.....	152
7.3	Limit Lateral Displacement and Limit Maximum Flexure.....	163
7.4	Statistical Analysis	170
7.4.1	Limit Resistance with Failure modes	171
7.4.2	Maximum Lateral Displacement.....	186
7.4.3	Maximum Flexure.....	200
7.5	Calculation of Factor of Safety.....	213
7.5.1	Conventional Method of Slices.....	213
7.6	Limitations of the Design Model	222
Chapter 8	CONCLUSIONS AND RECOMMENDATIONS.....	223
8.1	Summary and Conclusion	223
8.2	Recommendations for Future Studies.....	227
APPENDIX A	229
APPENDIX B	266

REFERENCES	271
BIOGRAPHY	281

List of Figures

Figure 1.1 Slope Reinforced with RPP(a) Shallow Slope Failure.; (b) Deep Slope Failure.	5
Figure 2.1 Soil Map of Texas (www.tellafirmafoundaions.com).	9
Figure 2.2 Shallow Slope Failure (Rauss, 2019).....	10
Figure 2.3 Geogrid Repair (Day, 1996).....	12
Figure 2.4 Geotextile Slope Repair (Rowe & Soderman, 1985).....	13
Figure 2.5 Pipe Pile and Wood Lagging (Day, 1996).....	14
Figure 2.6 Soil- Cement Repair (Day, 1996)	15
Figure 2.7 Stone Column Reinforced Embankment (Abusharar & Han, 2011).	17
Figure 2.8 Variation of Spacing, Cohesion and Height with FOS (Abusharar & Han, 2011).	17
Figure 2.9 Failure Plane for Route 23A, NY (Jutkofsky et al., 1999).....	18
Figure 2.10 Geofam Repair (Jutkofsky et al.,1999).....	19
Figure 2.11 Inclinator Results (Jutkofsky et al.,1999).....	19
Figure 2.12 Installation of Micropiles and Results (Sun et al., 2013).....	20
Figure 2.13 Construction of Drilled Shafts.....	21
Figure 2.14 Installation Procedure (Fox & Cowell, 1998).....	22
Figure 2.15 Mitigation of Cracks Due to Reinforcement (Wu & Helwany, 2001).....	23
Figure 2.16 Stack of Recycled Plastic Pins (RPP).....	25
Figure 2.17 Deflection Versus Time Response for RPP loaded with 222 N at free end (Chen et al., 2007).....	26
Figure 2.18 Method of Slices (Loehr et al.,2014)	27
Figure 2.19 Addition of Resisting Forces into the Method of Slices (Loehr et al.,2014). 28	28
Figure 2.20 Composite Limit Resistance Curves for RPP (Loehr et al., 2014).	29
Figure 2.21 Variation of Resistance Developed by Piles with Pile Spacing and Pile Length (Poulos, 2011).....	30
Figure 2.22 Variation of FOS With Angle of Soil Nail Inclination and Length of Soil Nails (Altalhe and Abdalftah, 2019).	30

Figure 2.23 Variation of FOS with Location of the Pin and the Spacing (Altalhe and Abdalftah, 2019).	31
Figure 2.24 Variation of FOS with Location of Pile and Spacing (Idiculla & Dasaka).	31
Figure 2.25 Variation of FOS with Location of the Pile and Diameter (Idiculla & Dasaka).	32
Figure 2.26 Effect of Pile Location on FOS.	33
Figure 2.27 Variation of FOS and Maximum Horizontal Displacement with RPP Spacing (Khan et al., 2014).	33
Figure 2.28 Location of Slide Areas in I-70 (Parra et al., 2003).	34
Figure 2.29 Inclinomater results for site Emma, I-70 (Parra et al., 2003).	35
Figure 2.30 Stabilization Scheme for I-70 Emma- Section 3 (Loehr & Bowders, 2007)..	35
Figure 2.31 Cumulative Displacement Plot of Inclinomater I-2 at I-435 Site (Parra et al., 2003).	36
Figure 2.32 Inclinomater readings for Section C of U.S 54-Fulton Site (Loehr & Bowders, 2007).	37
Figure 2.33 Layout of RPP for US287 (Khan et al., 2015).	38
Figure 2.34: Topographic Survey Results (Khan et al., 2015).	39
Figure 2.35 Inclinomater Results (Khan, Hossain, & Kibria, 2015).	39
Figure 2.36 Slope failures observed in Northbound Control Slope (Khan, 2017)	40
Figure 3.1 Location of Project Sites.....	41
Figure 3.2 Site Location: IH-820 & Rosedale Street Site.	42
Figure 3.3 Slope Failure at IH-820 & Rosedale Street (a) Soil Debris Bulging at the Bottom of the Slope (b) Head Scrap at the Crest of the Slope.....	42
Figure 3.4 Schematic of 2D Electrical Resistivity Imaging Location	43
Figure 3.5 Collection of Samples.....	44
Figure 3.6 Shelby Tube Samples (a) Depth 5 ft; (b) Depth 10 ft.....	44
Figure 3.7 Grain Size Distribution Curve	45
Figure 3.8 Plasticity Chart for Collected Soil Samples.....	46
Figure 3.9 Direct Shear Testing.....	47

Figure 3.10 (a)Variation of Moisture Content (b) Variation of TCP-N Blow Count with Depth	48
Figure 3.11 Location of Resistivity Imaging	49
Figure 3.12 Result of Resistivity Imaging	50
Figure 3.13 IH-820 & Rosedale St. (a) Slope Failure; (b) Head Scarp	51
Figure 3.14: Soil Profile	52
Figure 3.15 (a) Deformed Mesh Showing Crest Fall and Bulging, (b) Slip Circle: FS=1.00.	52
Figure 3.16 Site Location: U.S 67 Alvarado.	54
Figure 3.17 U.S 67 Alvarado (a) Slope Failure (b) Saturated Soil.	55
Figure 3.18 Location of Boreholes and ERI Lines.	55
Figure 3.19 Plasticity Chart for Collected Soil Samples.	57
Figure 3.20 (a)Variation of Moisture Content (b) Variation of TCP Blow Count with Depth	58
Figure 3.21 Location of ERI Lines.	59
Figure 3.22 Result of Resistivity Imaging; (a) Crest (b) Middle (c) Toe	60
Figure 3.23 Cross Section of the Slope Embankment	61
Figure 3.24 Soil Profile.	62
Figure 3.25 (a) Deformed Mesh Showing Crest Fall and Bulging, (b) Slip Circle: FS=1.00.	63
Figure 4.1 Schematic of Mechanism of Slope Failure	64
Figure 4.2 Relationship between Cost and Length of RPP.	65
Figure 4.3 Relationship between L/D ratio and Length of RPP.	66
Figure 4.4 Cross-sectional view of the Slope and Possible Failure Plane.	67
Figure 4.5 Schematic of (a) Benched and Compacted Slope, (b) First Layer of Reinforcement (Deep Layer)	68
Figure 4.6 Cross-section Design Layout	69
Figure 4.7 Proposed RPP Layout at IH-820 & Rosedale Street.	69
Figure 4.8 Slope Stability Analysis using RPP: Slip Circle: FS = 1.61	70

Figure 4.9 RPP Installation Equipment; Excavator Equipped with Hydraulic Hammer, (b) Hydraulic Hammer	71
Figure 4.10 Benching and Compaction of the Crest of the Slope.	72
Figure 4.11 Installation of Deeper Pins.	72
Figure 4.12 (a) Backfilling of the Slope; (b) Installation of Shallow Pins (at grade).....	73
Figure 4.13 Fully Reinforced Section.	73
Figure 4.14 As-built Design.....	73
Figure 4.15 Cross-sectional Slope Profile.	75
Figure 4.16 Schematic of (a) Benched and Compacted Slope, (b) First Layer of Reinforcement (Deep Layer)	76
Figure 4.17 (a) Cross-sectional Design Layout; (b) Design Layout	77
Figure 4.18 Slope Stability Analysis using RPP: Slip Circle: FS = 1.67.....	78
Figure 4.19 (a) Benching and Compaction (b) Installation of the First Layer of RPP.....	78
Figure 4.20 (a) Backfilling of Slope and (b) Installation of Second Layer of RPP.....	79
Figure 4.21 As-built drawing of RPP Installation.....	80
Figure 4.22 (a) Geotechnical Drill Rig delivery truck stuck, (b) Excavator stuck at the toe of the slope, (c) Visible perched water in the middle of the slope and (d) Installation equipment stuck due to the extremely soft soil.	81
Figure 4.23 Cost Comparison for Slope Stabilization Methods (Redrawn using data from Kioussis et al., 2010, Sabatini et al., 1997 cited in Lazarte et al., 2003).....	82
Figure 5.1 Vertical Probe Inclinometer (Jeng, 2017)	84
Figure 5.2 Total Station	84
Figure 5.3 Inclinometer Location	85
Figure 5.4 Inclinometer Casings Installation: a) Drilling and Placing Inclinometer Casing, b) Inclinometer Casing After Installation.	86
Figure 5.5 Schematic of Topographic Survey Lines.....	87
Figure 5.6 Lateral Movement in the Control Section.	88
Figure 5.7 Surface Erosion (a) Unrepaired Shoulder Cracks, (b) Surface Erosion, (c) Rill Erosion in the Reinforced Section.	89
Figure 5.8 Lateral Movement in the Reinforced Section.....	89

Figure 5.9 Comparison of Lateral Displacement of the Crest in the Reinforced Section and the Control Section.	90
Figure 5.10 Comparison of Incremental Lateral Displacement of the Crest in the Reinforced and Control Section.	91
Figure 5.11 Cumulative Lateral Displacement with Depth for Reinforced and Control Sections.	92
Figure 5.12 Percentage Reduction of Lateral displacement due to the Layered Design.	92
Figure 5.13 Vertical Displacement on the Crest of the Slope.	93
Figure 5.14 Vertical Displacement in the Middle of the Slope.	93
Figure 5.15 Surface Erosion in December 2021 exposing the RPP at the Crest.	94
Figure 5.16 Grass Cover in the Reinforced Section and Control Section in November 2021.	94
Figure 5.17 Backfill of Slope.	95
Figure 5.18 Biodegradable erosion control.	95
Figure 5.19 Inclinometer Location.	96
Figure 5.20 Inclinometer Installation at U.S 67- Alvarado (a) Connected Inclinometer casings (b) Inserting the casing into the borehole (c) Fixing the top with bentonite.	97
Figure 5.21 Survey Line Location.	98
Figure 5.22 (a) Piezometer Location, (b) Cross sectional view of piezometer location.	98
Figure 5.23 (a) Standard Piezometer (Model 4500) (b) Installation of Piezometer and Data Logger.	99
Figure 5.24 Variation of Lateral Displacement with Rainfall in the Reinforced Section.	100
Figure 5.25 Variation of Lateral Displacement with Rainfall in the Control Section.	101
Figure 5.26 Cumulative Lateral Displacement with Depth for Reinforced and Control Sections.	102
Figure 5.27 Variation in Vertical Displacement at the (a) Crest & (b) Middle of the Slope.	103
Figure 5.28 Variation of Average Pore Water Pressure with Rainfall.	104
Figure 5.29 Variation of Average Ground and Atmospheric Temperature.	105

Figure 5.30 Variation of Pore Water Pressure with Ground Temperature.....	106
Figure 6.1 Soil Profile.....	111
Figure 6.2 (a) Deformed Mesh Showing Crest Fall and Bulging, (b) Slip Circle: FS=1.00	111
Figure 6.3 : Deformation Analysis in Reinforced Section; (a) Maximum Lateral Deformation = 2.40 inches, (b) Maximum Vertical Deformation = 3.11 inches.	112
Figure 6.4 Comparison of Lateral Deformation between the Field and Model.	113
Figure 6.5 : Variation of Lateral Deformation of RPP with Depth; (a) Layered Layout, (b) Normal Layout.....	114
Figure 6.6 (a) Lateral Deformation in Two Layer Layout (b) Lateral Deformation in Normal Layout.....	115
Figure 6.7 Lateral Deformation Reduction due to Two Layers with Depth.....	116
Figure 6.8 Bending Moment	117
Figure 6.9 Variation of Moment Transfer with Depth of RPP.....	118
Figure 6.10 Soil Profile	120
Figure 6.11 (a) Deformed Mesh Showing Crest Fall and Bulging, (b) Slip Circle: FS=1.00	120
Figure 6.12 : Deformation Analysis in Reinforced Section; (a) Maximum Lateral Deformation = 2.01 inches, (b) Maximum Vertical Deformation = 1.60 inches.	121
Figure 6.13 Comparison of Lateral Deformation between the Field and Model.	122
Figure 6.14 Variation of Lateral Deformation of RPP with Depth; (a) Layered Layout, (b) Normal Layout.....	123
Figure 6.15 (a) Lateral Deformation in Two Layer Layout (b) Lateral Deformation in Normal Layout.....	124
Figure 6.16 Lateral Deformation Reduction due to Two Layers with Depth.....	125
Figure 6.17 : (a) Slip circle for Cut Phase; FS: 1.21, (b) Vertical Displacement.	127
Figure 6.18 : (a) Slip circle for Deep Pin Phase; FS: 1.19, (b) Vertical Displacement. ..	127
Figure 6.19 : (a) Slip circle for Fill Phase; FS: 1.17, (b) Vertical Displacement.....	128
Figure 6.20 : (a) Slip circle for All Pin Phase; FS: 1.61, (b) Vertical Displacement.	128
Figure 6.21 Variation of Factor of Safety with Construction Phases.	129

Figure 6.22 Variation of Factor of Safety by Row with Fraction of Slope Reinforced. ...	130
Figure 6.23 Variation of Factor of Safety with Different Reinforced Sections.	130
Figure 6.24 Comparison of Factor of Safety with U.S-54 Fulton Site (Loehr & Bowders, 2007)	131
Figure 6.25 Comparison of Factor of Safety with I-435 Wornall Site (Loehr & Bowders, 2007)	131
Figure 6.26 Variation of factor of safety with the number of deep layers	132
Figure 6.27 Spacing between Reinforcement.....	134
Figure 6.28 Variation of Factor of Safety with the Spacing Between Layers.	135
Figure 6.29 Schematic of 5 feet Overlap	136
Figure 6.30 Variation of Factor of Safety with Sliding Depth of Failure for Different Overlap Depths.....	138
Figure 6.31 Variation of Lateral Deformation with Overlap Depth for Sliding Depth of; (a) 5 ft Failure (b) 8 ft Failure	139
Figure 6.32 Variation of Lateral Deformation with Sliding Depth of 12 ft Failure for Different Overlap Depths.....	140
Figure 7.1 Static Equilibrium of Individual Slice in the Method of Slices (a) Unreinforced Slope (b) Reinforced Slope (Loehr and Bowders, 2007)	145
Figure 7.2 Combined Limit Resistance Curve (Loehr and Bowders, 2007)	146
Figure 7.3 Schematic of plastic deformation for theory by Ito and Matsui (1975)	148
Figure 7.4 Limit Soil Pressure	150
Figure 7.5 Failure Modes (a)Failure Mode I (b) Failure Mode II.....	151
Figure 7.6 Re-plotted to represent the Composite Resistance for Failure modes I and II based on Loehr and Bowders, 2007.	151
Figure 7.7 Schematic of Two-Layered Layout.....	152
Figure 7.8 Limit Soil Pressure for Two-Layered Layout.....	157
Figure 7.9 (a) Limit Resistance for Two-Layered Layout of Failure modes 1 and 2. (b) Composite Limit Resistance Curve for Overlap Depth of 4 feet.	158
Figure 7.10 Comparison of Limit Soil Resistance for the Two Layouts.....	159
Figure 7.11 Limit Resistance Matrix	160

Figure 7.12 Variation of Limit Resistance with Overlap Depth.	161
Figure 7.13 Effect of Cohesion (a) 4 ft OD; (b) 1 ft OD.....	162
Figure 7.14 Effect of Friction Angle (a) 4 ft OD; (b) 1 ft OD.....	162
Figure 7.15 Effect of Spacing for Sliding Depths (a) 4 ft OD; (b) 1 ft OD.	163
Figure 7.16 Determination of Maximum Bending Moment and Maximum Lateral Displacement	165
Figure 7.17 Numerical Model Matrix	166
Figure 7.18 Variation of Maximum Lateral Displacement with Limit Resistance for varying Overlap Depths (Slip Surface Depth = 8 ft).....	167
Figure 7.19 Variation of Maximum Flexure with Limit Resistance for varying Overlap Depths (Slip Surface Depth = 8 ft).....	168
Figure 7.20 Effect of Cohesion on Maximum Lateral Displacement (a) 4 ft OD; (b) 1 ft OD.	168
Figure 7.21 Effect of Friction on Maximum Lateral Displacement (a) 4 ft OD; (b) 1 ft OD.	169
Figure 7.22 Effect of Cohesion on Maximum Flexure (a) 4 ft OD; (b) 1 ft OD.....	169
Figure 7.23 Effect of Friction Angle on Maximum Flexure (a) 4 ft OD; (b) 1 ft OD.....	169
Figure 7.24 Steps of Statistical Model Development	171
Figure 7.25 Residuals vs. Fitted Values for the Preliminary Model.....	177
Figure 7.26 Normality Probability Plots and Density Plots for Preliminary Model.	179
Figure 7.27 Cook's Distance plot for Preliminary Model (5 ft OD).....	180
Figure 7.28 Box-Cox Plot for Transformation of Response Variable (5 ft OD) ($\lambda = 0.0606$)	181
Figure 7.29 Residual vs. Fitted Values Plot for Final Model.....	183
Figure 7.30 The Normal Plot for Final Model.	184
Figure 7.31 Validation of the Final Model.	186
Figure 7.32 Variation of Limit Soil Resistance and Slip Surface Depth ($c=60$ psf, $\phi=12^\circ$)	186
Figure 7.33 Residuals vs. Fitted Values for the Preliminary Model.....	191
Figure 7.34 Normality Probability Plot for Preliminary Model.....	192

Figure 7.35 Density Plot for Preliminary Model.	193
Figure 7.36 Cook’s Distance plot for Preliminary Model.	194
Figure 7.37 Box-Cox Plot for Transformation of Response Variable ($\lambda = 0.3030$).....	195
Figure 7.38 Residual vs. Fitted Values Plot for Final Model.....	197
Figure 7.39 The Normal Plot for Final Model	198
Figure 7.40 Density Plot for Final Model.....	198
Figure 7.41 Validation of the Final Model	200
Figure 7.42 Residuals vs. Fitted Values for the Preliminary Model.....	205
Figure 7.43 Normality Probability Plot for Preliminary Model.....	206
Figure 7.44 Density Plot for Preliminary Model.	206
Figure 7.45 Residual vs. Fitted Values Plot for Final Model.....	209
Figure 7.46 The Normal Plot for Final Model	209
Figure 7.47 Density Plot for Final Model.....	210
Figure 7.48 Validation of the Final Model.	212
Figure 7.49 Schematic of the Calculation of the Ordinary Method of Slices (Sapkota, 2019).	214
Figure 7.50 Schematic of the Calculation of the Ordinary Method of Slices with Reinforcement (Sapkota, 2019).	217
Figure 7.51 Decision Matrix	218
Figure 7.52 Limit Soil Resistance.....	219
Figure 7.53 Limit Lateral Displacement	220
Figure 7.54 Limit Flexure.....	220

List of Tables

Table 3.1 Summary of Grain Size distribution.	45
Table 3.2 Shear Strength Test Results.	47
Table 3.3 TCP Results for I-820 & Rosedale St.	48
Table 3.4 Parameters for FE Analysis.	53
Table 3.5 Shear Strength Test Results.	57
Table 3.6 TCP Results for U.S 67 & Alvarado.....	58
Table 3.7 Parameters for FE Analysis	63
Table 4.1 Summary of RPP Driving Time	74
Table 4.2 Cost Analysis	82
Table 6.1 Parameters for FE Analysis	111
Table 6.2 RPP Properties used in Numerical Model.....	112
Table 6.3 Parameters for FE Analysis	120
Table 6.4 RPP Properties used in Numerical Model.....	120
Table 6.5 Details of Overlap.....	136
Table 6.6 Numerical Model Matrix for Overlap Depth Analysis.....	137
Table 6.7 Optimum Overlap Depth.....	141
Table 7.1 Soil and RPP Parameters for Conventional Layout	149
Table 7.2 Failure Modes	150
Table 7.3 Limit Soil Resistance Equations and Conditions.	155
Table 7.4 RPP and Soil Parameters for Two Layered layout.....	156
Table 7.5 Correlation between Predictors and Outcome Variables.	173
Table 7.6 Parameter Estimates of Preliminary Model for Varying Overlap Depths.....	174
Table 7.7 ANOVA Summary of Preliminary Model for Varying Overlap Depth.	175
Table 7.8 Parameter Estimates of the Final Model.....	182
Table 7.9 ANOVA Summary of the Final Model.	182
Table 7.10 Correlation between Predictor Variables	188
Table 7.11 Correlation Limit Resistance and Predictor Variables.....	188
Table 7.12 Parameter Estimates of Preliminary Model.....	190

Table 7.13 ANOVA Summary of Preliminary Model	190
Table 7.14 Parameter Estimates of the Final Model.....	196
Table 7.15 ANOVA Summary of the Final Model.	196
Table 7.16 Summary of Best Subset Selection Method.....	199
Table 7.17 Correlation between Predictor Variables	202
Table 7.18 Correlation Limit Resistance and Predictor Variables.....	202
Table 7.19 Parameter Estimates of Preliminary Model.....	204
Table 7.20 ANOVA Summary of Preliminary Model	204
Table 7.21 Parameter Estimates of the Final Model.....	208
Table 7.22 ANOVA Summary of the Final Model.	208
Table 7.23 Best Subset Selection.....	211
Table 7.24 Ordinary Method of Slices Calculation.....	216
Table 7.25 Calculation of Limit Resistance.....	221

CHAPTER 1

INTRODUCTION

1.1 Background

Slope failures are defined as the collapse of the compacted and stable soil body due to the decrease of the shear strength of soil particles. Strength of soil particles decrease due to the increase of moisture from rainwater intrusion, cyclic wet-dry conditions, and expansive behavior of the soil. According to Abusharar and Han, there are mainly three types of failures: Surficial failure (Shallow slope failure), General slope failure, and Deep-seated failures (Abusharar & Han, 2011). These types of failures have been observed in highway embankments in the state of Texas.

Texas is classified as a subtropical climate zone where it experiences long periods of dry weather paired with periods of average rainfall and thunderstorms. The soil in the north Texas region is mostly composed of high plasticity clays with expansive behavior. The three most common types of clay mineral are Kaolinite, Illite, and Montmorillonite. Among them, Montmorillonite has a high surface area that increases the potential for water absorption (Khan et al., 2017). The soil particles expand with the absorption of water and shrink with the evaporation of water. The occurrence of this behavior due to the wet and dry cyclic weather patterns, decreases the shear strength of the soil particles over time; ultimately leading to slope failures.

Slope failures in highway embankments cause damages to highway infrastructure and can cause loss of life in the case of a catastrophic failure. Maintenance and repair costs

for Departments of Transportation across U.S. were recently estimated to exceed \$100 million annually (Loehr et al., 2002).

Most highway embankments are observed to have surficial failure (shallow slope failure) while deep seated failures are not common but probable. The moisture intrusion on the top 4 ft. of the slope facilitates the occurrence of shallow slope failures while the micro and macro cracks due to swell and shrinkage behavior over time progressively makes way to deeper failures.

Shallow slope failures are often repaired by rebuilding the failure area. This method is easy and economical but observed to be quite ineffective due to the swelling in the wet season leading to the loss of the effect of compaction (Day, 1996). Other methods like geogrid repair, soil-cement repair, use of pipe pile and wood lagging are used. Geogrid repair involves the use of high-density polyethylene resins (HDPE) textile to increase the shear strength of the soil. The geogrid is placed on cut benches on the slope after the removal of the failed soil and rebuilt using layers of geogrid and compacted fill. Soil cement repair is similar to geogrid repair; cement mixed with granular fill is used instead of geogrid reinforcement. Pipe piles and wood lagging method rebuilds the slope with hollow galvanized steel pipe piles which are either driven or placed into predrilled holes filled with concrete. Major concerns using these methods are uncemented zones and low flexural strength in the steel pipes which ultimately leads to the failure of the slope. These methods involve intensive groundwork and are time sensitive and cost prohibitive.

Deep slope failures are more than 6 ft. in depth. Most deep slope failures are repaired using stone columns, geofoam, micropiles, deep mixed columns and drilled shafts.

According to Abusharar and Han (2011), stone columns add strength to the ground and the effectiveness of this method increases with the thickness of the column. Geofam repair involves rebuilding the slope packed with expanded polystyrene (EPS) geofam blocks. Micropiles are small diameter, drilled and grouted non-displacement piles. According to Sun et al. (2013), micropiles range from 50 ft to 60 ft and can easily be installed without disturbing the equilibrium of the slope. Although micropiles are an effective solution for deep seated failure, buckling in soft soil has been found to be a major issue (Bjerrum, 1957). Drilled Shafts are cylindrical shafts drilled into the soil filled with concrete. Each of these methods have significant limitations in terms of stabilizing slope embankments with regards to strength, time, and cost.

Recycled Plastic Pins (RPP) have been used as a cost effective, sustainable and practical solution for stabilizing shallow slope failures in the last decade (Khan et al., 2015). RPPs are made from recycled plastic and other waste materials (polymers, sawdust and fly ash) (Chen et al., 2007). Composition of RPP is of High-Density Polyethylene (HDPE; 55-70%), Low Density Polyethylene (LDPE; 5-10%), Polystyrene (PS; 2-10%), Polypropylene (PP; 2-7%), Polyethylene-terephthalate (PET; 1-5%) and varying amounts of additives (sawdust, flyash; 0-5%) (Lampo & Nosker, 1997). Due to this composition of RPP, they are less susceptible to chemical and biological degradation. Research done on RPP showed that there was negligible strength reduction after being exposed to UV lighting, freeze-thaw conditions, wet-dry cycles and acidic or hydrocarbon environments but was prone to creep (Chen et al., 2007).

Recycled Plastic Pins were first installed in Missouri to stabilize a section with shallow slope failure with 8 ft. RPP. Results showed minimal movement and the movement observed were believed to be movements required to mobilize the resistance in the reinforcing member (Parra et al., 2003). Another field study was conducted in Texas by Khan in 2011 where 10 feet RPP were used to reinforce a slope with shallow slope failure. The research showed decreased vertical and lateral movement in the reinforced section compared to the unreinforced section (Khan, 2014). There have been no studies on the use of RPP for stabilization of deep slope failures.

1.2 Problem Statement

Recycled plastic pins (RPP) have been successfully used to stabilize shallow slope failures (Khan, 2014; Khan et al., 2015). RPPs are installed perpendicular to the slip surface and flush to the ground to prevent shallow slope failures. But rainwater intrusion from cracks in the shoulder of the pavement also makes highway embankments susceptible to failures in deeper slip surfaces. Figure 1.1 shows a schematic of a slope reinforced with RPP using the current installation layout. While a 10 ft. RPP is provides sufficient anchorage in the case of shallow slope failure, the RPP is not intersecting deeper failure planes leaving the slope susceptible for deep slope failures. The slope will fail due to lose of anchorage of the member (Loehr et al., 2007).

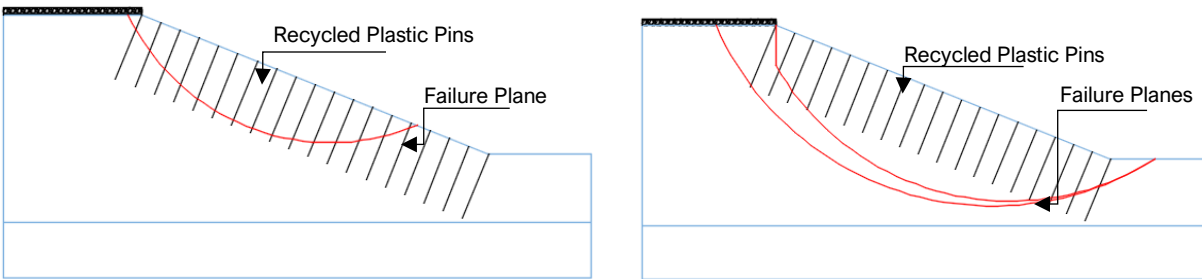


Figure 1.1 Slope Reinforced with RPP(a) Shallow Slope Failure.; (b) Deep Slope Failure.

A two layered overlap pin layout is proposed to stabilize deep slope failures with RPP. During a deep slope failure, a crest fall of about 4-6 ft is generally observed. The vertical drop can be utilized to drive reinforcement into deeper failures planes providing enough anchorage into stiffer layers providing increased resistance against deeper failures. The use of the vertical drop to drive reinforcement to deeper depths followed by backfilling and compaction, saves construction time and costs related to driving piles deeper and material for longer members. In addition, previous research has not studied any reinforcement methods which are cost effective, sustainable and time saving for deep-slope failures in highway embankments. Hence, in this study, a modified overlap pattern of using Recycled Plastic Pins to stabilize rainfall-induced deep slope failures in a highway embankment has been proposed.

1.3 Research Objective

The main objective of this study is to evaluate the performance of using Recycled Plastic Pins (RPP) in two Layers to stabilize highway embankments susceptible to deep slope failures. The specific tasks to achieve the objective of the study includes,

- Site investigation and selection of appropriate study area.

- Design of slope stabilization scheme using Recycled Plastic Pins in a novel overlapping pin design.
- Field installation of Recycled Plastic Pins in selected study areas.
- Instrumentation of stabilized slope to evaluate the performance.
- Performance monitoring of the test sections.
- Parametric study using finite element modeling to analyze the effect of construction sequence, location, spacing, number of layers and overlap depth on factor of safety and lateral deformation.
- Analytical solution to analyze the effect of pin overlap on lateral limit resistance and development of design methodology to obtain the resistance provided by the reinforcement.

1.4 Dissertation Organization

The dissertation is organized as follows. The summary is presented below;

Chapter 1 presents the background, problem statement, and objective of the current study.

Chapter 2 summarizes the past studies conducted in the field of using reinforcement similar to Recycled Plastic Pins (RPP) for slope stabilization. The common methods of slope stabilization for shallow and deep slope failures are discussed in addition to case studies of the use of RPP for shallow slope failures. Finally, the limitations of the past studies are discussed.

Chapter 3 discusses the field investigation of two highway embankments located in Interstate 820 and highway 67 conducted for this study. The initial site reconnaissance,

site investigation, laboratory testing results are discussed. The site investigation results are analyzed to understand the cause of failure and the slope stability analysis was conducted to back calculate the strength parameters at failure.

Chapter 4 focuses on the mechanism of slope stabilization and selection of materials. The chapter also discusses the selected slope stabilization scheme and the details of the field installation incorporating a two-layer design.

Chapter 5 presents the instrumentation conducted to monitor the field performance of the reinforced sections. The results of periodic monitoring of the test sites are presented in this chapter.

Chapter 6 discusses the numerical study conducted to analyze the performance of the reinforced slopes. Parametric study on the effect of overlap depth, number of deep pin layers, and spacing on factor of safety was presented in this chapter.

Chapter 7 describes the development of design methods. Three limiting criteria were used to determine the limit resistance. Numerical data and modified equation was statistically analyzed to determine equations incorporating overlap depth. In addition, this chapter introduced the design steps and calculation of factor of safety for a given slope.

Chapter 8 summarizes the main findings of this study and presents future recommendations.

CHAPTER 2

LITERATURE REVIEW

2.1 Slope Failures

The gradual or rapid downslope movement of soils under the gravitational stress is called a slope failure (American Geological Institute). Slope failures are frequently seen in Texas and across the United States in highway embankments. The occurrence of slope failures disrupts traffic flow in addition to damage caused to public and private property (Sindlinger, 2009). Highway agencies around the United States spend millions of dollars to maintain and repair highway embankment slopes (Loehr et al., 2002; Sindlinger, 2009). Total direct costs for maintenance and repair of landslides involving major U.S. highways alone (roughly 20% of all U.S. highways and roads) were estimated to exceed \$100 million annually (Turner & Schuster, 1996).

Slope failures occur due to the decrease in shear strength of the soil, or the increase of the shear stress required for the equilibrium of the slope. The increase in pore water pressure, cracking, swelling and long-term creep behavior due to wet-dry cycles causes the reduction of strength of the soil (Duncan et al., 2014). The shear stress required for equilibrium can increase due to water filled in cracks at the crest of the slope and due to the increase of the weight of soil due to saturation (Duncan et al., 2014).

2.1.1 Expansive Soils

North Texas region mostly consists of high plastic clays with expansive behavior. There are three types of clay minerals: kaolinite, illite and montmorillonite. The clay minerals are classified as high or low plastic clays due to its ability to attract water. Kaolinite and illite

has less surface area and attract less water while montmorillonite has a higher surface area, attracting a higher volume of water (Reddy 2012, Khan 2014). Due to its ability to attract high volume of water, these kinds of soil also show expansive behavior. Fine grained clay rich soil become sticky and heavy after absorbing water (Mokhtari & Masoud , 2012). The soil becomes very dry and hard due to evaporation of water which leads to shrinkage cracking. The shrinkage potential increases with higher plasticity index (Asuri and Keshavamurthy, 2016).

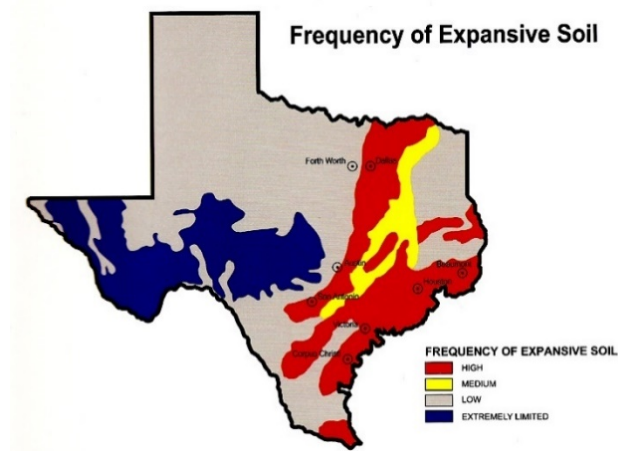


Figure 2.1 Soil Map of Texas (www.tellafirmafoundaions.com).

The cyclic wetting and drying of the soil lead to the decrease of soil strength over time which is known as the softening of expansive clay (Wright, 2005). The cracks caused by the shrink swell behavior aids this process by letting the water diffuse through the fissures into the slope. The clay diffused by the infiltrated water allows the particles to swell under zero confining pressure (Castellanos 2016). This process weakens the strength of the soil over time allowing the formation of more cracks extending deeper into the slope (Sun et al., 2009; Castellanos 2016).

The slopes are more susceptible to failure at the fully softened state. The concept was first introduced by Skempton (1977) for natural and excavated slopes in London. The fully softened strength is between the residual strength and the peak strength of the soil. The soil reaches this state due to the loss of strength after undergoing several cycles of wet and dry periods. But when the material fails, it experiences considerable strains, the peak strength parameters are reduced to residual values (Al-Homoud et al., 1997).

Slope failures can be categorized into two types: shallow and deep failures. Shallow failures are typically less than 6 ft in depth and deep failures are slope failure above 6 ft depth. Although shallow slope failures are typically seen in highway embankments, deep seated failures are also probable.

2.2 Shallow Slope Failures

Shallow slope failures are typically seen on highway embankments. Shallow slope failures occur as a result of rainwater infiltration into the slope surface and the cyclic weather conditions in the Texas region. Depth of shallow slope failures are usually between 3-6 ft. (Kim et al., 2004; Khan et al., 2017). Shallow failures are more frequent since the top few feet of the slope are more susceptible to moisture variations than deeper soil layers (Khan et al. 2017).



Figure 2.2 Shallow Slope Failure (Rauss, 2019).

2.2.1 Methods of Repair for Shallow Slope Failures

Slope repair techniques vary depending on several factors. Site accessibility, availability of funds, experienced labor, time sensitivity and availability of equipment affect the selection of repair technique.

Robert Day (1996) discussed several methods of design and repair of surficial slope failures. The most typical method used is the rebuilding of the failure area by removing the failure debris such as grass and roots and recompacting. This is considered as an easy and economical solution but is observed to be quite ineffective due to the swelling in the wet season leading to the loss of the benefit from compaction (Day, 1996). Other typical methods of slope repair are geogrid repair, soil-cement repair and the use of pipe piles and wood lagging are presented below.

2.2.1.1 Rebuilding/Regrading the Slope

Regrading of the slope involves air-drying the failed soil, pushing back and compaction of the failed soil after failure. Although this method is the most economical and is being performed by DOTs around the U.S. as a routine maintenance, it is not very effective. The shear strength especially in clay does not increase much due to compaction. Re-wetting of the soil during rainfall will decrease its strength again which ultimately leads to failure (Titi & Helwany, 2007).

In comparison to regrading the slope, the soil is often removed and replaced entirely with improved material. The slope is filled with soil and aggregates will provide sufficient dead weight at the toe of the slope to prevent the driving force of the failure (Bowders et al., 2003). Rebuilding the slope is comparatively costlier.

2.2.1.2 Geo-grid repair

Geo-grid is used as a soil reinforcement to stabilize failed slopes. They are composed of high-density polyethylene resins. The reinforcement effect provided by the geo-grids by allowing the interlock of granular particles is similar to the reinforcement provided by plant roots. The type and vertical spacing of the geogrid were the main design requirements. The results showed that the shear strength of the import fill, the slope inclination, and the thickness of the potential failure mass effect the design (Day, 1996). The steps followed for design are as follows (Day, 1996) (Figure 2.3),

1. Removal of the failure mass.
2. Cutting benches into the hillside into the underlying undisturbed soil. This process increases the friction between the new soil mass and the horizontal portion of the bench.
3. Drains are installed into the benches. These drains collect water off site.
4. Rebuilding the slope. Layers of geogrid and compacted fill were used in the rebuilding process.
5. The slope was covered with an erosion control fabric and backfilled.

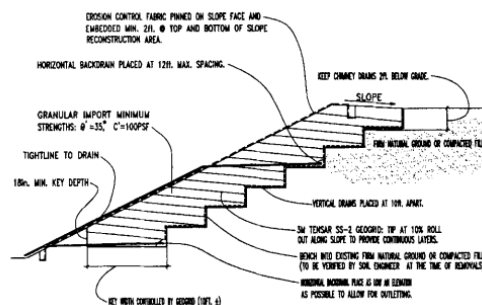


Figure 2.3 Geogrid Repair (Day, 1996).

The use of geo-textile as a reinforcing method is similar to the use of geo-grid. The effect of soil-geotextile interaction with respect to allowable compatible strain for the geotextile is considered in design. Figure 2.4 shows the typical placement of geotextile in the slope. The allowable strains can be obtained from design charts and will depend on the foundation stiffness, the embankment geometry, the deposit depth, the unit weight of the fill, and the critical height of an unreinforced embankment (Rowe & Soderman, 1985).

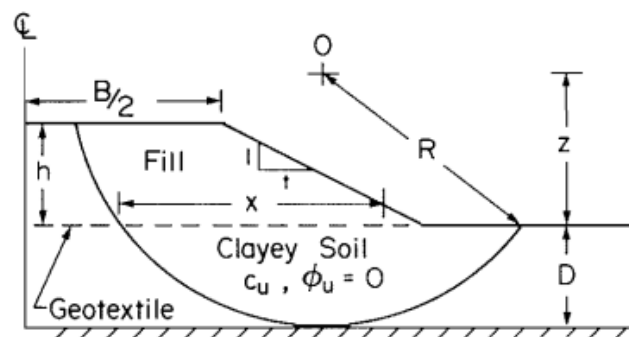


Figure 2.4 Geotextile Slope Repair (Rowe & Soderman, 1985)

2.2.1.3 Pipe piles and wood lagging

According to Day (1996), pipe piles and wood lagging is frequently used as a slope stabilization method. The failed soil debris is removed, and benches are cut into the slope intersecting the failure plane. A hollow galvanized steel pipe pile is either driven or placed in predrilled holes that are filled with concrete. Wood lagging is placed behind the piles followed by the drainage system. The slope is then backfilled and compacted with the selected fill (Titi & Helwany, 2007). Figure 2.5 shows typical design of pipe pile and wood lagging.

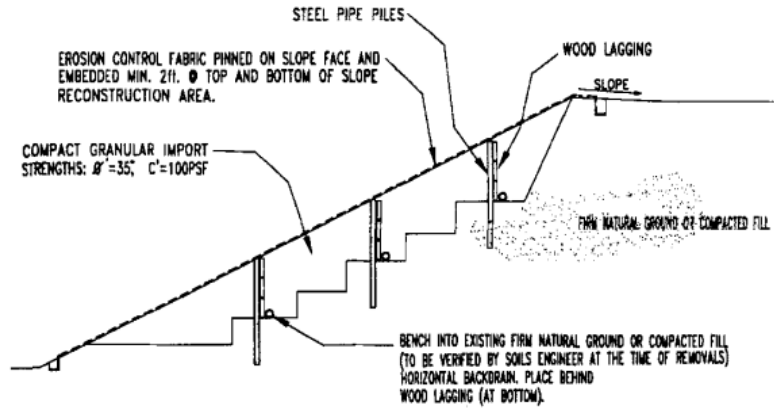


Figure 2.5 Pipe Pile and Wood Lagging (Day, 1996).

In this design, the lateral soil pressure is directly transferred to the wood lagging. The structural capacity of the wood is comparatively low; therefore, the members often fail in bending (Titi & Helwany, 2007). Another disadvantage of using this method is that it is not designed but done according to the contractor's experience, often leading to overstressed piles and ultimately slope failure (Day, 1996).

2.2.1.4 Soil Cement Repair

The soil cement repair is similar to geo-grid repair. The failed soil is completely removed and replaced with soil-cement. Granular soil is mixed with 6% cement and compacted into the slope (Figure 2.6) (Day, 1996). This method increases the shear strength aiding against failure.

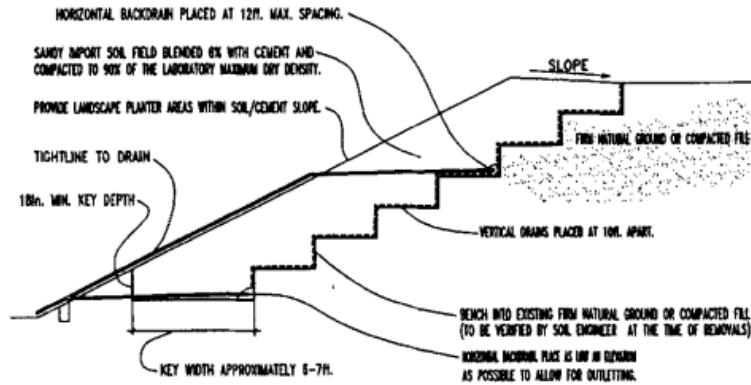


Figure 2.6 Soil- Cement Repair (Day, 1996)

2.3 Deep Slope Failures

Deep slope failures extend deeper into the slope than the shallow slope failures which are generally less than 6 ft in depth. Shallow slope failures are often rainfall induced and the active zone due to rainfall is limited to the surface of the slope (Sapkota, 2019). But infiltration of water into the slope during rainfall also plays a major role in deeper slope failures. Xu et al., 2014 conducted research on a landslide in China which had a depth of 3 m (10 ft). SEM analysis conducted by Xu et al., 2014 indicated the presence of small macro fractures due to the shrink-swell behavior of clay minerals and presence of large pores at the slip surface. Following these observations and the research of others stating that the fractures and large pores increases the water infiltration into the slope, Xu concluded that the rainfall infiltrates into the slope through the cracks and improves the permeability of the soil at deeper depths extending the active zone.

Presence of macropores in the soil provides a preferential path for water flow deeper into the slope therefore the presence of fissures must be taken into consideration for deep slope failures (Sun et al., 2009).

Deeper slope failures can occur progressively after shallow slope failures. Cracking influences the rate at which the water enters and leaves the slope, and the cracks provide sites for stress concentration that can lead to local movement and then progressive failure as the soil moves towards residual strength (Stirling et al., 2021). Research conducted by Duncan et al. 2014 portrays a case study of a landslide in Tuve, Sweden where the failure started with a small failure and progressed over time with many small failures finally extending into a deeper failure.

The shallow slope failures prevalent in Texas highway embankments could extend to deeper failure plane over time if left unreinforced. The following section presents few common deep slope failure repair methods.

2.3.1 Methods of Repair for Deep Slope Failures

Ground improvement techniques such as stone columns, geofabric, micropiles, deep mixed columns, drilled shafts, rammed aggregate pier reinforcement and deep patch repair have been used to prevent and repair deep-seated slope failures.

2.3.1.1 *Stone Columns*

Stone columns have been commonly used as an alternative to solve deep-seated slope stability problems. Stone column have been in use since 1960s to increase the bearing capacity, reduce settlement, and accelerate consolidation. The two methods of installing stone columns are the dry method and the wet method. The wet method involves a jet of

water forming holes in the ground and a vibratory probe, with a backfill of stones. The dry method uses a jet of air and a probe to insert stone to the bottom of the hole.

Stone columns reinforce the ground by increasing the strength of the ground. Figure 2.7 shows a typical schematic of stone columns installed as slope stabilization. The most important design criteria are the stiffness of the column and the load sharing between the column and the soil (Abusharar & Han, 2011).

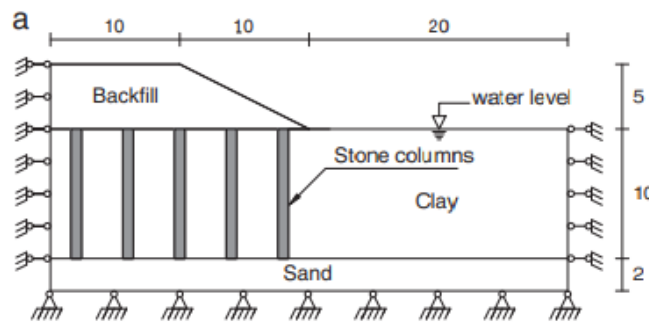


Figure 2.7 Stone Column Reinforced Embankment (Abusharar & Han, 2011).

Abusharar and Han (2011) presented results of a two-dimensional modeling of a stone column reinforced embankment. Figure 2.8 shows the variation of cohesion of the soil, height of the embankment and spacing of the columns with factor of safety.

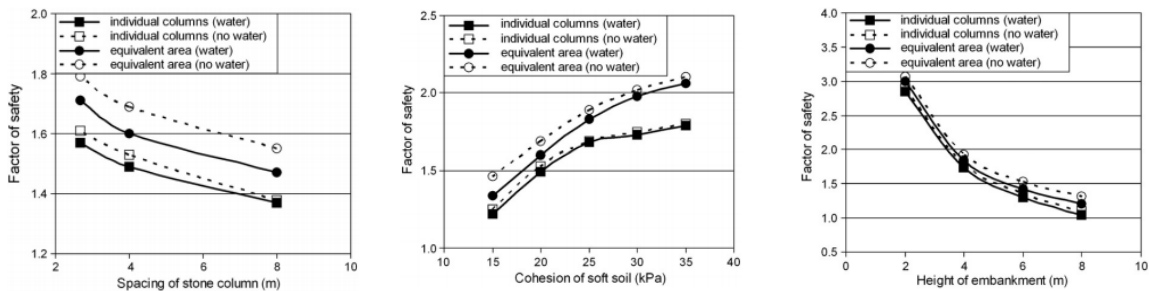


Figure 2.8 Variation of Spacing, Cohesion and Height with FOS (Abusharar & Han, 2011).

According to the results, FOS decreases with the increase of spacing between the columns and the height of the embankment. But the FOS increases with the increase of cohesion of the soil. In addition, the FOS increased with the increase of thickness of the stone column.

2.3.1.2 Geo-Foam Repair

The use of expanded polystyrene (EPS) geofom blocks to treat an unstable roadway embankment slope with clay soil was discussed by Jutkofsky et al. (1999). Blocks of 2 by 4 by 8-ft weighing about 80-lbs per block were installed at a site located in Route 23A in New York State.

A deep-seated failure was assumed after embankment started moving shortly after construction. An inclinometer installed showed that the failure plane was about 36-40 ft. below the ground surface. Stabilizing treatments such as including a berm, lowering the grade, realignment away from the failure area, lightweight aggregate, and stone columns, were considered but deemed impractical, environmentally sensitive and cost prohibitive. As an alternative, geofom was chosen to be used because of its drainage capacity and the ability to act as an insulator.

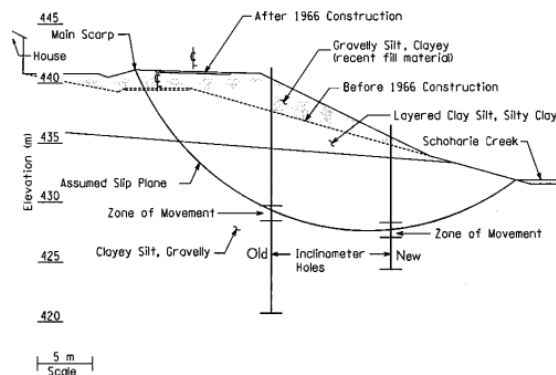


Figure 2.9 Failure Plane for Route 23A, NY (Jutkofsky et al., 1999).

Construction of this section included installing a temporary sheet pile wall, excavating the soil in front of the sheet, installing drainage system, geofoam quality control check, placing the geofoam blocks, backfilling, concrete capping, subbase placement and finally paving. Inclinometers and extensometers were installed to monitor movement.

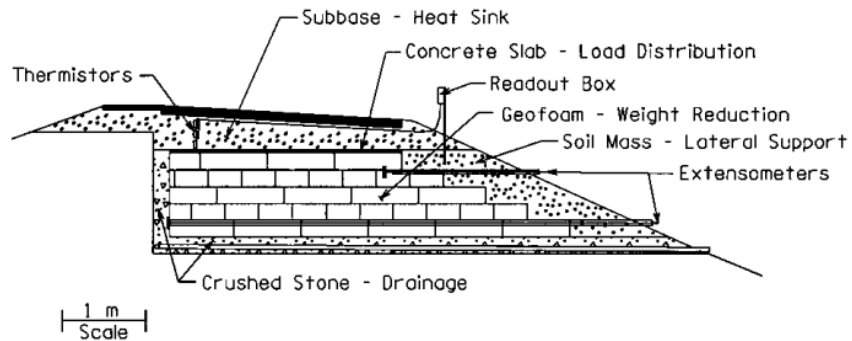


Figure 2.10 Geofoam Repair (Jutkofsky et al.,1999).

Inclinometer results showed that the movement after the initial construction has been negligible (Figure 2.11). Use of geofoam as a slope stabilization method has proven to be effective since no movement has been observed and no problems due to differential icing has occurred.

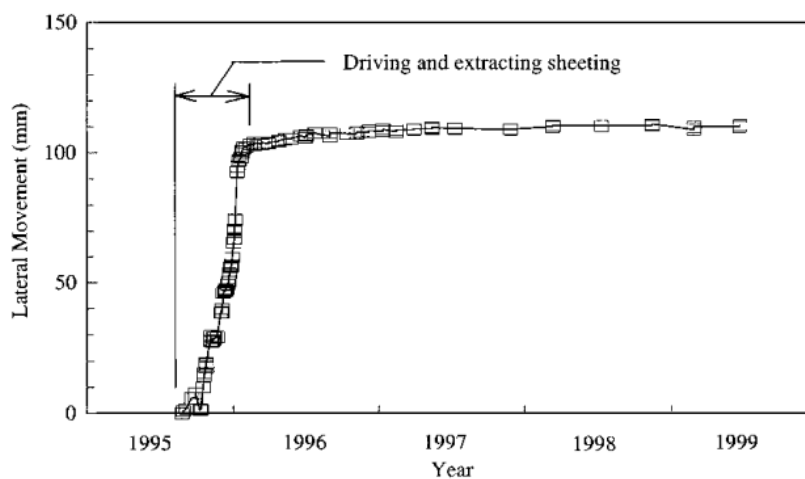


Figure 2.11 Inclinometer Results (Jutkofsky et al.,1999).

2.3.1.3 Micropiles

Sun et al. (2013) discussed the use of micropiles for slope stabilization in a test site in China. Micropiles are small in diameter, drilled and grouted non-displacement piles. The diameter of a typical micropile is limited to less than 300 mm. Micropiles can be easily installed with minimum disturbance to the equilibrium of the slope. The length of the micropiles used in this test ranged from 15 m to 18 m (Sun et al., 2013). This method can be easily implemented to stabilize deep seated failures. A test site in Qinghai Province in China was installed with micropiles. The slope failed after a storm, 30 years after construction with a slip surface of approximately 10 m. Three rows of micropiles were installed. The first row of piles was inclined at 10 deg, the middle vertical and the third row inclined at 21 deg. A total of 123 micropiles were used.

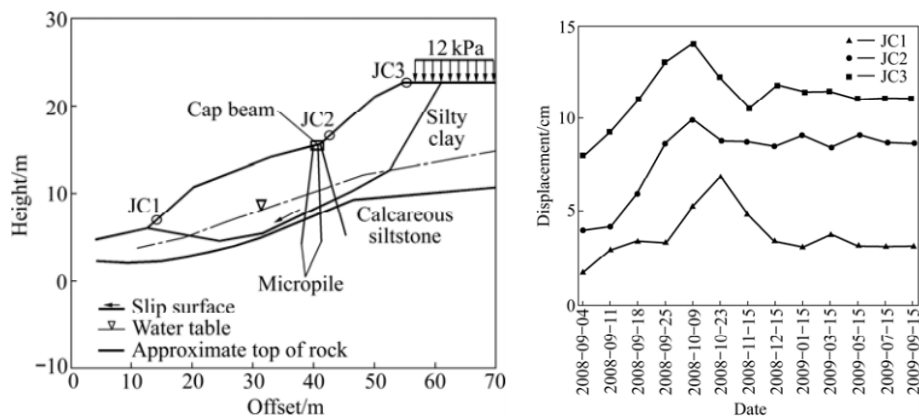


Figure 2.12 Installation of Micropiles and Results (Sun et al., 2013).

The measured displacements showed that the values increased at the beginning of construction and decreased slightly over time. The maximum horizontal displacement was about 15 cm. After 2 months of construction the displacements remained constant,

therefore, micropiles were deemed effective in reducing slope movement (Sun et al., 2013).

2.3.1.4 Drilled Shafts

A case study in Lake Ridge Parkway Station 248, Grand Prairie, TX was shown by Gregory (2011) to show the effect of drilled shafts to stabilize an embankment against deep slope failure. The embankment was constructed of residual fat clays of eagle ford geological formation. Many shallow slope failures occurred and was repaired using fiber-reinforced soil. During repair a much deeper failure was discovered and found to be a creep type failure: a soil mass sliding along a soft bentonite seam within the underlying shale (Gregory, 2011).



Figure 2.13 Construction of Drilled Shafts.

Geotechnical analysis on the drilled shafts were done using p-y (load-deformation curves) method and L-PILE. The analysis resulted in 0.9 m (36 inch) diameter drilled shafts placed 1.8 m (6 feet) on center with a penetration depth below the bentonite seam of 4.6 m (15 feet). The calculated deflection was 30 mm (1.2 inches). The project required 25 drilled

shafts at 1.8 m spacings. Drilled shafts were installed in 2011 preventing a catastrophic failure (Gregory, 2011).

2.3.1.5 Rammed Aggregate Pier Reinforcing Elements

Two sites which experienced deep seated rotational slide in Louisiana and Arkansas is discussed by Parra et al., (2007). Site in US-71 highway over Bayou Des Glaises experienced a slope failure with a scrap of 1.2 m (4 ft.) with a failed mass displacement of 3m to 4.5 m (10-15 ft). The boring results of the site indicated the presence of soft to medium stiff, high plastic clay. A similar site in US-167 also experienced movement in a 91 m active slide.

Both sites were repaired using Rammed Aggregate Piers (RAP). The installation of RAP involves drilling 760 mm (3 inches) diameter holes ranging between 2.0 and 7.6 m (7 to 25 ft). The holes are filled with aggregate stone in controlled lifts (0.3 m/1 ft) and compacted using a high-energy beveled impact tamper. The bottom of the excavated shaft has a beveled shape which helps in increasing the lateral stress in the matrix soil. Figure 2.14 shows the installation procedure. The post-monitoring results of the two sites indicated reduction in lateral displacement.

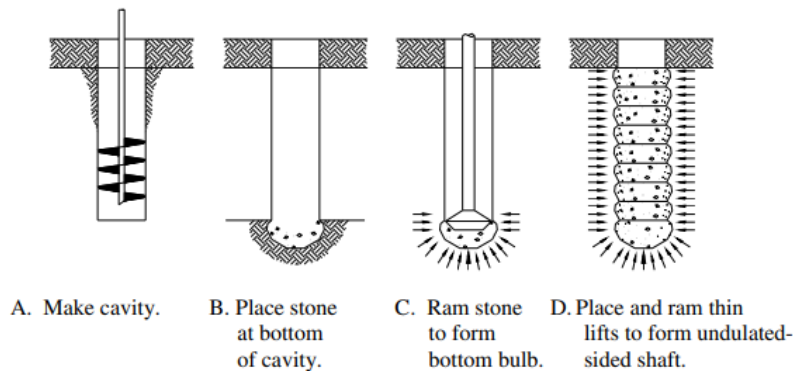


Figure 2.14 Installation Procedure (Fox & Cowell, 1998).

2.3.1.6 Deep-Patch Repair Technique

A landslide repair method known as the USFS deep-patch technique was developed by the U.S. Forest Service (USFS) to repair shallow and long (skin flow) landslides. These kinds of failures are often observed in loosely compacted cut and fill slopes. Depths of failures were typically up to 1 to 2 m deep (3.3-6.6 ft.) at the crest and as much as 15 to 20 m long (49.2-65.6 ft.) parallel to the face of the slope (Wu & Helwany, 2001). This method involved excavating past the failure depth and layering with geosynthetics. A test apparatus was manufactured by the Colorado Transportation Institute to investigate the effectiveness of the geosynthetic reinforcement in the USFS deep-patch technique.

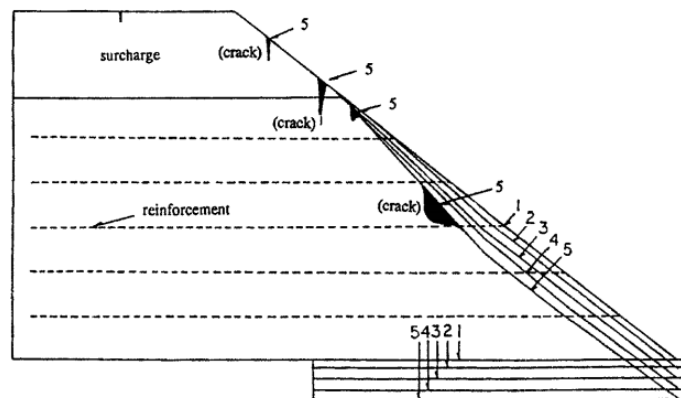


Figure 2.15 Mitigation of Cracks Due to Reinforcement (Wu & Helwany, 2001).

According to the results presented by Wu and Helwany (2001), the reinforced section was intact during the test. As seen on figure 2-8, propagation of cracks was stopped by the geosynthetic reinforcement. Therefore, it indicated that the geosynthetic reinforcement can be very effective in alleviating the development of major cracks caused by subsequent failure underneath the patched slope (Wu & Helwany, 2001).

2.4 Recycled Plastic Pins (RPP)

Recycled Plastic Pins (RPP)/ Recycled Plastic Lumber which are commercially produced in the size of 3.5 in by 3.5 in by 10 ft., has successfully been used to stabilize shallow slope failure in recent times. RPP has proven to be a cost effective and sustainable solution to slope stabilization.

2.4.1 Manufacturing Process of Recycled Plastic Pins

Recycled Plastic Pins (RPPs) are made out of recycled plastic and waste materials (polymers, sawdust and fly ash) (Khan et al., 2015, Chen et al.,2007). RPP is composed of 55-70% of high-density polyethylene (HDPE), 5-10% of low-density polyethylene and 2-10% of other types of plastics (McLaren 1995). Additives (0-5%) like fiberglass, wood fibers are combined with the melted plastic and polyolefin is used as the binding adhesive. Due to the composition of the pins, they are less susceptible to chemical and biological degradation (McLaren, 1995). The use of these plastics to manufacture reinforcing members helps in the global issue of recycling plastics. In recent times due to the COVID-19 pandemic, plastic generation has increased by 17% (Aurpa, 2021). Therefore, recycled plastic pins becomes a sustainable solution.

The manufacturing of Recycled Plastic pins includes pulverizing, blending, heating, partially melting and compressing into molds of plastic materials forming plastic lumber (Loehr et al., 2000). Two methods of production were mentioned by Bowders et al. (2002) as compression molding and extrusion forming. In the process of compression molding, the plastics are pulverized, melted, and is compressed into desired shapes in molds. In comparison, extrusion forming involves forcing the material through a die of desired

cross-section. Extrusion process is more advantageous since any length of the pins can be easily produced without a mold.



Figure 2.16 Stack of Recycled Plastic Pins (RPP)

2.4.2 Engineering Properties of Recycled Plastic Pins

Several tension and compression tests were done on RPPs, and it was found that they show an average compressive strength of 21 MPa and a tensile strength of 13 MPa.

Tests were done on samples from different manufactures to determine the variation of strength. Extruded specimens showed strengths lower than the compression molded specimens (Bowders et al., 2002). Negligible strength reduction after being exposed to UV lighting, freeze-thaw conditions, wet-dry cycles and acidic or hydrocarbon environments was observed. Although it is resistant to all these conditions, RPPs are prone to creep.

Study done on the creep behavior of RPPs showed that the flexural creep or the bending behavior at a sustained load was an important property. It was found that as the temperature increased, the time for failure decreased with the same load applied (Chen et al., 2007). Results showed that the loading levels along with the temperature affect the

creep behavior of the specimen (Figure 2.17). Chen and others also verified that the measured strength of the specimen depends on strain or deformation rate used. Flexure Strength results from a four-point flexure test showed strengths ranging from 9-18 MPa for extruded specimens (Bowders, et al., 2002)

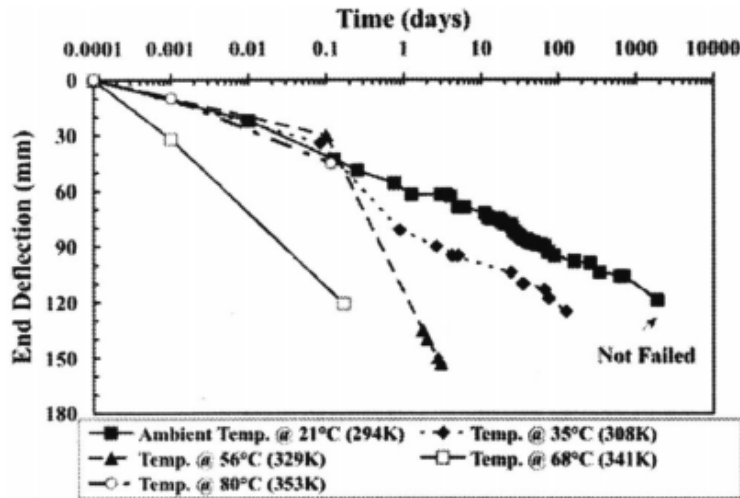


Figure 2.17 Deflection Versus Time Response for RPP loaded with 222 N at free end (Chen et al., 2007).

Common slope stabilization techniques use soil nails, guardrail post and railroad rails which are made out of iron, steel or concrete which have a higher strength capacity, but they are susceptible to environment conditions and are prone to corrosion. Therefore, although the strength capacity of RPP is not high, it is an economical and sustainable solution for slope stabilization.

2.5 Design for stabilizing slopes with Recycled Plastic Pins

2.5.1 General Approach

The stability of a slope is generally evaluated by considering a potential sliding surface and then calculating the factor of safety of the specified failure surface. The factor of safety can be calculated as below.

$$F = \frac{\int S}{\int \tau}$$

Where, “F” is the factor of safety, “S” is the shear strength from soil at the sliding surface and “τ” is the mobilized shear stress to maintain equilibrium. The most common approach in slope stability analysis is the method of slices using Mohr Coulomb failure envelop. This method separates the slip surface into a number of slices and each slice is considered individually to determine the factor of safety (FOS) for the sliding surface (Figure 2.18). The sliding surface with the lowest FOS is considered as the critical sliding surface.

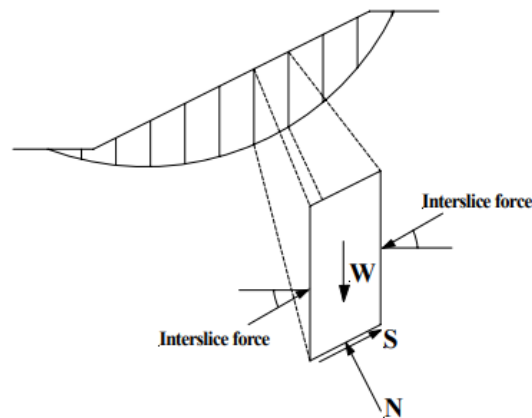


Figure 2.18 Method of Slices (Loehr et al.,2014)

Installation of RPP provides a direct resistance (F_R) along the slip surface. This resisting force will be used in calculating the FOS for the critical sliding surface. Due to the increase in resistance the factor of safety increases (Figure 2.19).

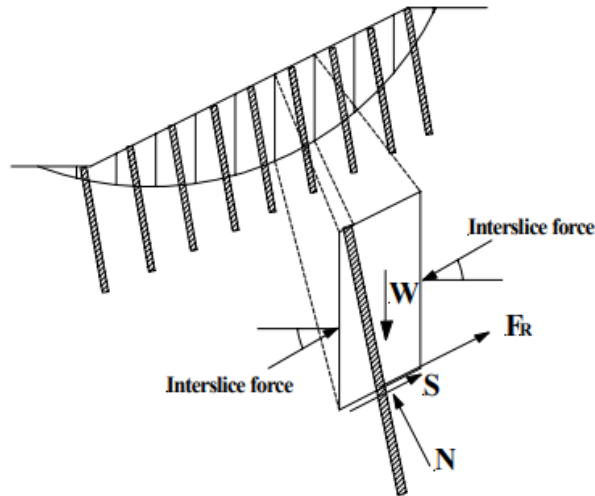


Figure 2.19 Addition of Resisting Forces into the Method of Slices (Loehr et al.,2014).

Loehr et al., (2014) developed limiting resistance curves to understand the effect of different failure criteria on the resisting force applied by the reinforcing member. The resisting force will differ according to the position of the sliding surface intersecting the reinforcing member (Loehr et al. 2014). Three failure modes were considered to develop the curve; failure of the soil around or between members (failure mode 1), insufficient anchorage length (failure mode 2) and structural failure of the reinforcing members due to loads applied from the soil mass (failure mode 3) was considered.

The limiting resistance curves for the three failure modes were combined to one curve which is used in conventional slope stability analysis software to determine the factor of safety for a reinforced slope (Figure 2.20).

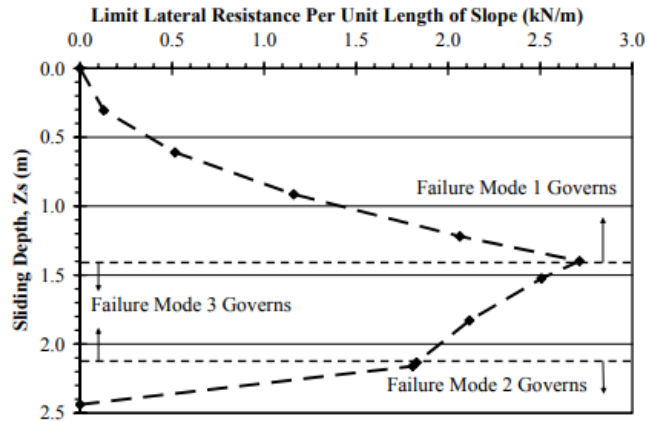


Figure 2.20 Composite Limit Resistance Curves for RPP (Loehr et al., 2014).

According to the composite limiting resistance curve, it was observed that the failure modes 1 & 2 governs the limiting resistance for sliding surfaces passing through the top and bottom of the reinforcing members. Loehr et al. (2014) concluded that the capacity of the reinforcing member and the FOS will only be affected if the sliding surface passes through the middle of the member.

2.5.2 The Effect of Pile Characteristics on the Resisting Force

The effect of piles with different spacing, diameter and length were studied by several authors. Figure 2.21 shows the variation of spacing, diameter and length with the resistance developed by the pile. The resistance provided by the piles increases with the decreasing of pile spacing and the increasing of pile length. The resistance also increased with the increase of pile diameter (Poulos, 2011). Increasing of the resistance suggests the increase of FOS.

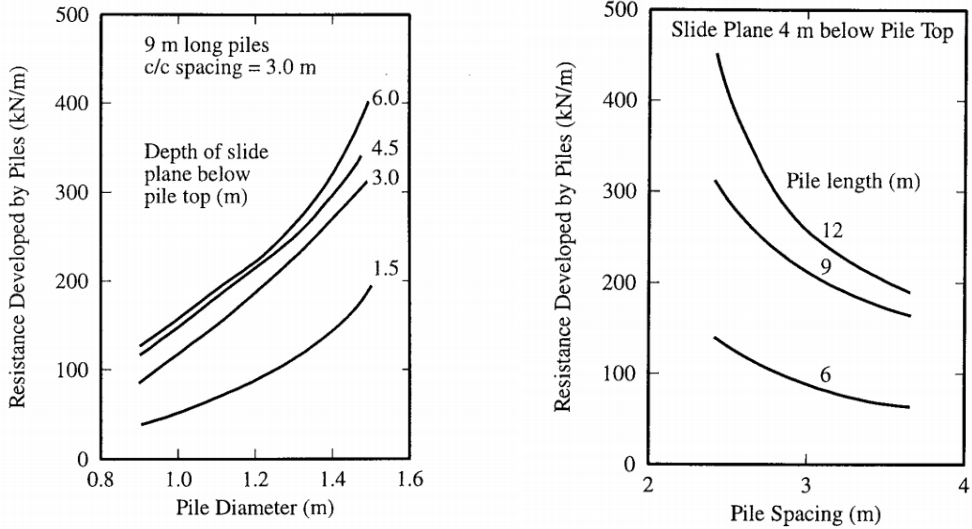


Figure 2.21 Variation of Resistance Developed by Piles with Pile Spacing and Pile Length (Poulos, 2011).

Research done on soil nails by Altalhe and Abdalfthah (2019) also showed similar results.

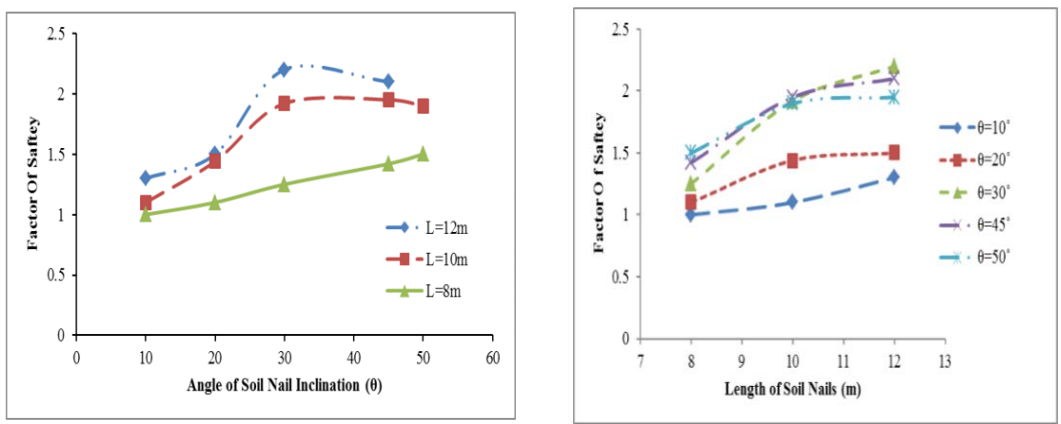


Figure 2.22 Variation of FOS With Angle of Soil Nail Inclination and Length of Soil Nails (Altalhe and Abdalfthah, 2019).

Figure 2.23 shows the variation of FOS with the angle of inclination and the length of the nails. The FOS increases with increase of the length suggesting better anchorage.

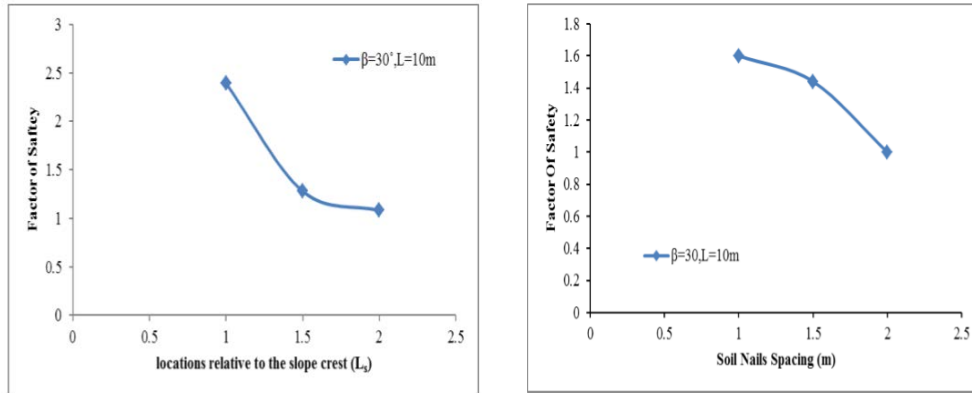


Figure 2.23 Variation of FOS with Location of the Pin and the Spacing (Altalhe and Abdalftah, 2019).

Similar to Poulos (2011), FOS decreased with the increase of spacing between the nails suggesting less resistance force is applied. Altalhe and Abdalftah (2019) also suggested that installation of nails at the crest of the slope is the most effective.

A case study done in India by Idiculla and Dasaka using discrete piles showed similar results. Piles of different diameters, spacing were installed at different distances from the crest to obtain the optimum installation criteria. Piles were also installed in staggered fashion to reduce the shadow effect and increase the resistance to soil movements (Idiculla & Dasaka). Figure 2.24 & Figure 2.25 shows results obtained.

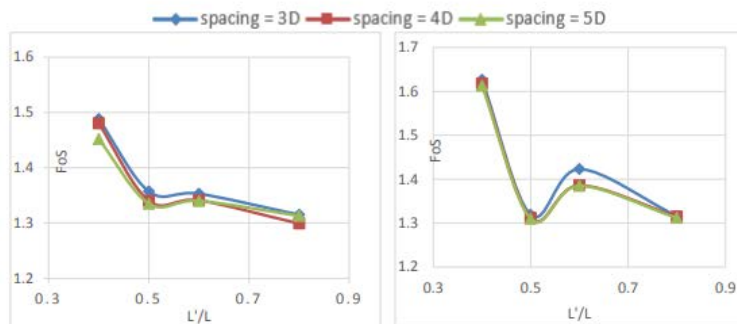


Figure 2.24 Variation of FOS with Location of Pile and Spacing (Idiculla & Dasaka).

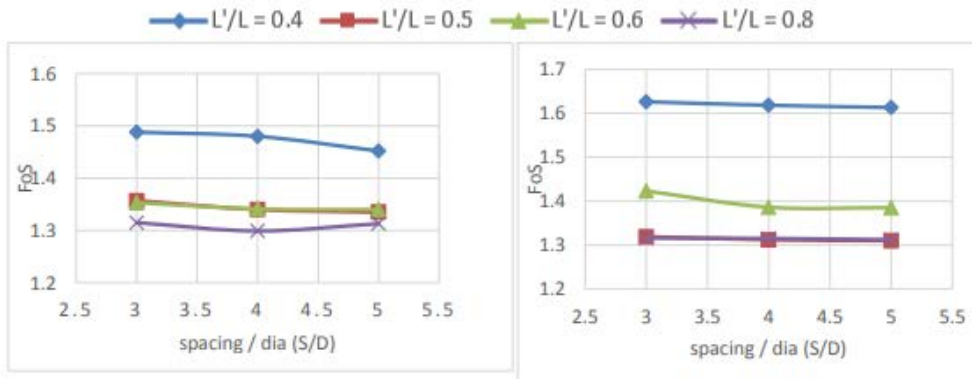


Figure 2.25 Variation of FOS with Location of the Pile and Diameter (Idiculla & Dasaka).

Similar to other literature, the FOS decreased with the increase of spacing between the piles. It was observed that the FOS decreases as the distance from the crest increases.

The optimum distance for the piles to be installed was at L'/L ($L-L'$ = distance from crest to the pile) ratio of 0.4 with 4D center-to-center spacing (Idiculla & Dasaka).

Hassiotis et al., (1997) discussed the variation of FOS with the distance from the toe of the slope. 'S' was classified as the distance from the toe of the slope. The FOS was found to be low at the toe and increased with distance away from the slope. For a maximum factor of safety, it was found that the piles must be placed in the upper middle part of the slope. Generally, they must be located closer to the top of the steeper slopes than of the shallower ones (Hassiotis et al., 1997).

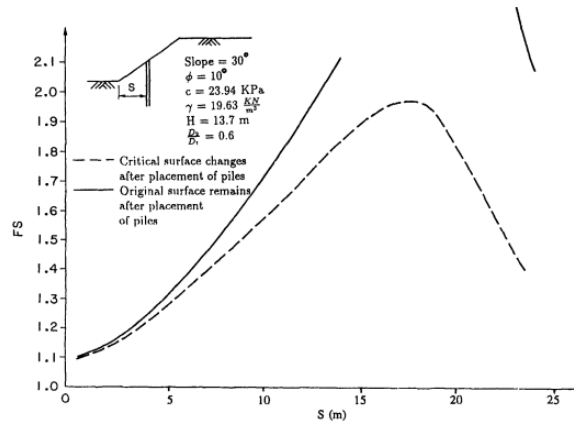


Figure 2.26 Effect of Pile Location on FOS.

Parametric study done by Khan et al., (2014) for RPPs also showed similar results.

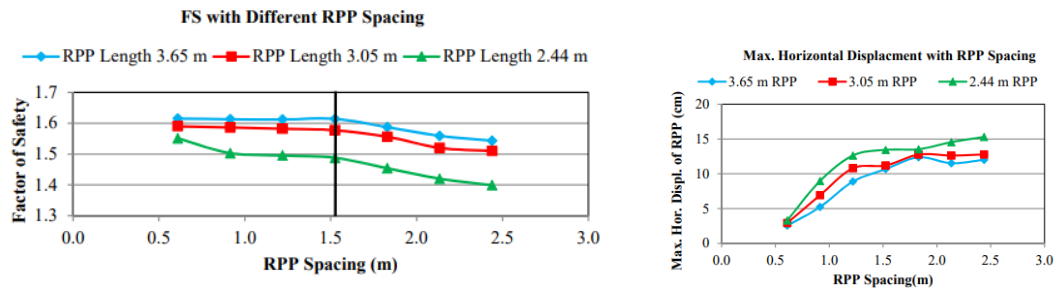


Figure 2.27 Variation of FOS and Maximum Horizontal Displacement with RPP Spacing (Khan et al., 2014).

Results showed that FOS decreases with the increase of RPP spacing similar to all other literature. It was also verified that maximum horizontal deformation increase with the RPP spacing at the crest (Khan et al., 2014). Although having larger spacing is economical, the deformation will be significantly high.

2.6 Field Studies

2.6.1 Emma I-70

The case study of the field performances of a site located in Emma I-70, Missouri was presented by Parra et al. (2003). The site was dominantly composed of clayey soil with recurring surficial failures of depths between 3 ft and 5 ft.

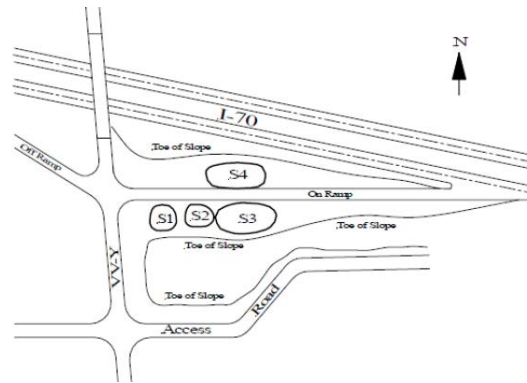


Figure 2.28 Location of Slide Areas in I-70 (Parra et al., 2003).

The first site was located in Emma (I-70), Missouri and was stabilized using 3.5-inch by 3.5-inch members of 8-ft length. 3-ft center to center staggered design was used and the site was instrumented with inclinometers which showed minimal displacement of about 1 inch (Loehr et al., 2002).

The results for the site were presented by Parra et al. (2003). It was observed that the movements were generally minimal for the first year following installation of the reinforcement, after which the movements increased to a maximum of approximately 20 mm (0.8 in.) over the next 6 months (Parra et al., 2003). Maximum movement was observed in the crest. The movements observed are deemed tolerable and are believed to be movements that are required to mobilize the resistance in the reinforcing members rather than movements indicating potential instability.

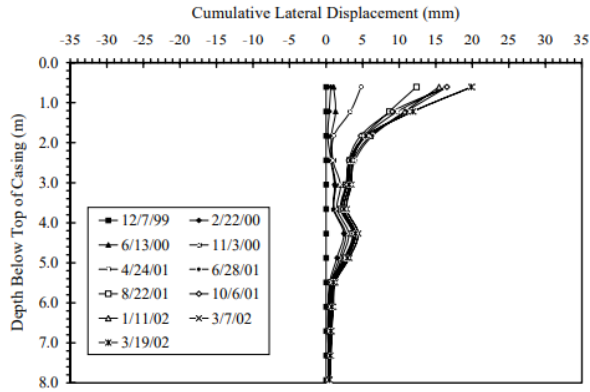


Figure 2.29 Inclinometer results for site Emma, I-70 (Parra et al., 2003).

Site 3 was stabilized using different orientation of reinforcing members and was presented by Loehr and Bowders (2007) (Figure 2.30). Closer and wider spacing was used to stabilize the failed section. The authors observed failures in sections B and C after 2 years of monitoring. Section D was also assumed to have experienced large deformations although it was not observed at site due to lower slope height.

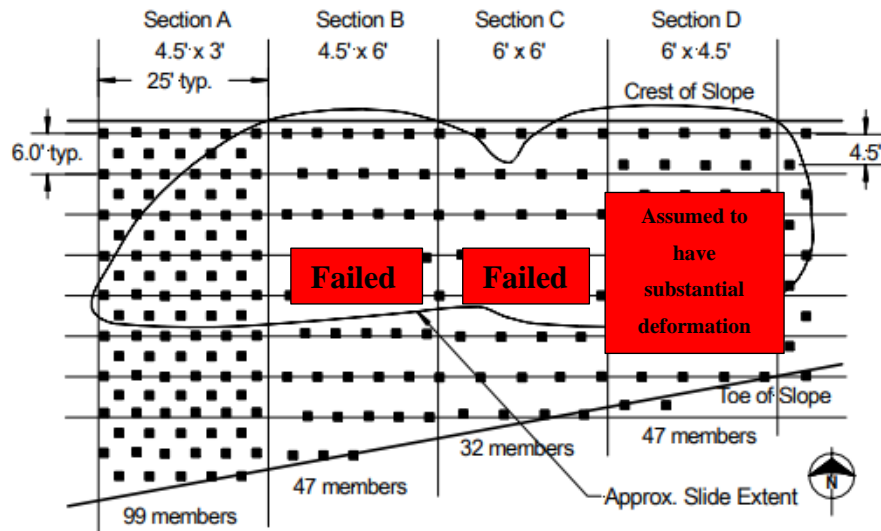


Figure 2.30 Stabilization Scheme for I-70 Emma- Section 3 (Loehr & Bowders, 2007).

2.6.2 I-435 & Wornall Road

Another case study of the field performances of a site located in Wornall I-435, Missouri was presented by Para et al. (2003). The site was dominantly composed of clayey soil with recurring surficial failures of depths between 3 ft and 5 ft. The slope failure initiated from the middle of the slope.

The site was located at the intersection of I-435 and Wornall Road in Southern Kansas City, Missouri. The slope was approximately 31.5 ft in height with a slope geometry of 2.2(H): 1(V). It consisted of a mix of mixed lean-to-fat clay overlying stiffer compacted clay shale. The site was reinforced with 616, 3 ft RPP in a staggered pattern. The inclinometer results are shown in Figure 2.31. The results presented by Parra et al., (2003) shows that the displacements were negligible over a period of several months after installation. The maximum displacement was observed to be 1.2 inches.

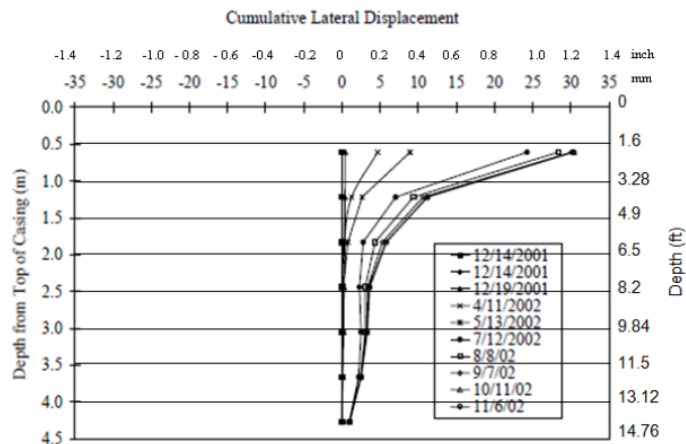


Figure 2.31 Cumulative Displacement Plot of Inclinometer I-2 at I-435 Site (Parra et al., 2003).

2.6.3 U.S 54 - Fulton

Another field study was conducted by Loehr and Bowders (2007) near U.S highway 54 in Fulton, Missouri. This slope was observed to have experienced a failure in the lower 2/3 of the slope. Site investigations showed the presence of lean-to fat clay. The slope was separated into 5 sections and reinforced with Recycled Plastic Pins with different orientations.

Lateral deformation was monitored in this site using inclinometers and it was observed that the deformations are occurring between depths of 10-15 ft (Figure 2.32). According to the author, large displacements were observed at deeper depths because the failure planes in this slope is extending under the reinforcing members. A dip at the crest of the slope and a bulge at the top of the slope was observed but no failure was reported.

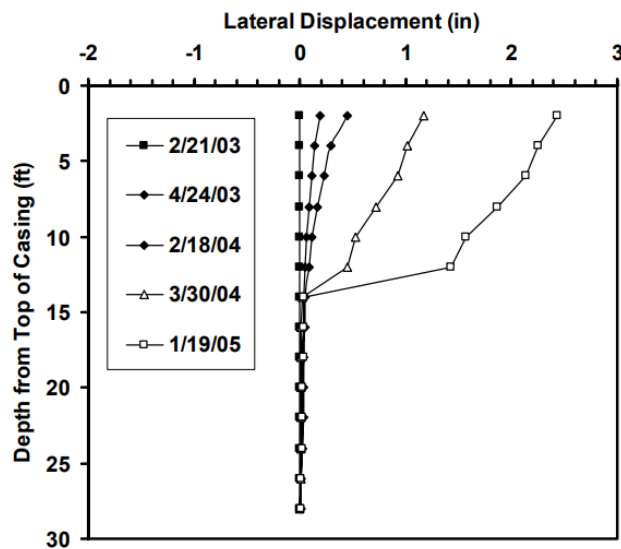


Figure 2.32 Inclinometer readings for Section C of U.S 54-Fulton Site (Loehr & Bowders, 2007).

Although the failure planes were not intersecting the reinforcing members, the strain gauges in the instrumented RPP in this section showed bending moment. The authors

stated that this observed bending moment signifies that the RPP is providing some resistance against shallow failures even if the pin is not being intersected by the failure plane.

2.6.4 U.S 287 - Midlothian

A field study was also conducted in Texas by Khan in 2011. The site was located in U.S 287, Midlothian Texas. The site showed surficial movement and large cracks on the shoulder before repair. The slope was 35 ft. in height with a geometry of 3H: 1V. The main cause of surficial failure was accounted to the rainwater infiltration into the slope through the cracks. The site was reinforced with RPPs of different lengths and different spacings. Ten feet RPPs were used at the crest with closer spacing, and wider spacing at the toe. Different sections with variation of spacing and length is shown in Figure 2.33 (Khan et al., 2015).

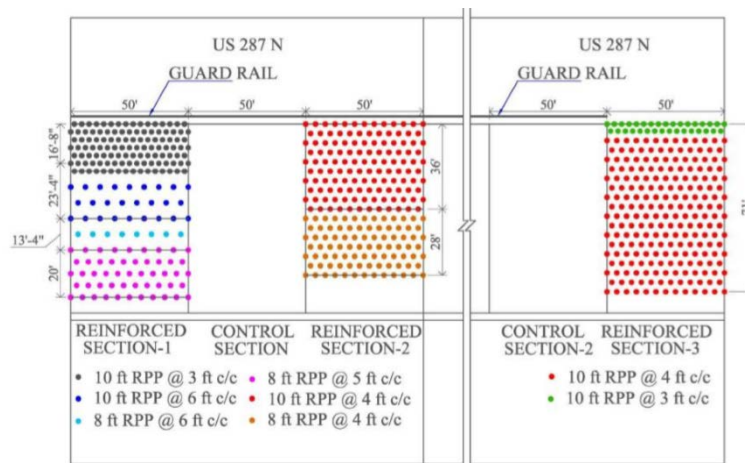


Figure 2.33 Layout of RPP for US287 (Khan et al., 2015).

U.S 287 site was monitored monthly using inclinometers and topographic survey to monitor the lateral and vertical movement of the slope. The inclinometer results showed that the maximum horizontal displacement took place at the surface of the slope and

reduced with depth. The topographic survey showed that the control sections had large settlements while the settlement of the reinforced sections were reduced (maximum settlement 5.1 inches).

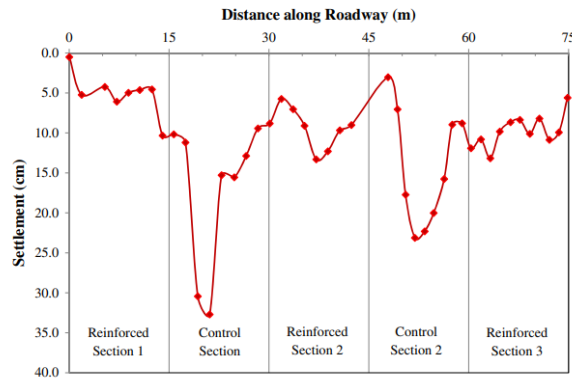


Figure 2.34: Topographic Survey Results (Khan et al., 2015).

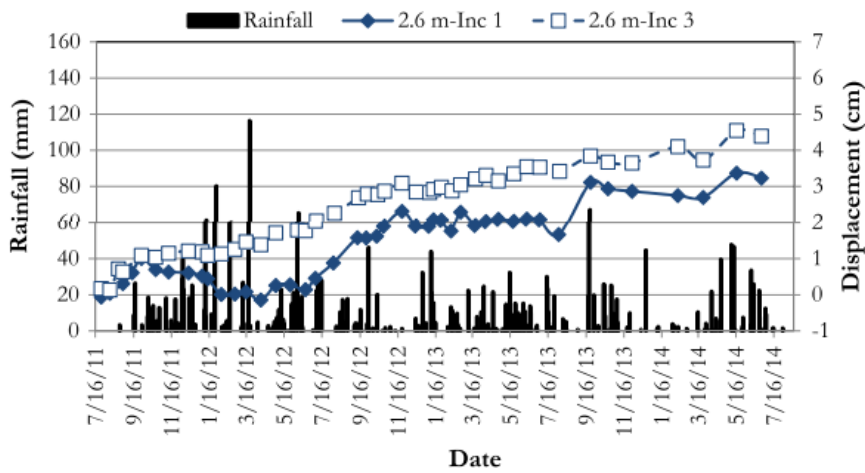


Figure 2.35 Inclinomometer Results (Khan, Hossain, & Kibria, 2015).

Number of failures were observed in the control sections near the reinforced slope throughout the five-year monitoring period. The following figure shows the schematics and the failures that occurred adjacent to the reinforced sections. None of the reinforced sections showed any failures.

Failure Location	Time
Failure Location-1	October 2013
Failure Location -2	October 2013
Failure Location-3	June 2015
Failure Location-4	June 2015



Figure 2.36 Slope failures observed in Northbound Control Slope (Khan, 2017)

2.7 Limitations of Previous Studies

The previous studies using Recycled Plastic Pins (RPP) are all related to stabilization of shallow slope failures. It was observed that large movements could occur even in slopes reinforced against shallow failure if the sliding surfaces extend beyond the length of the reinforcing members. Therefore, it is important to study the use of recycled plastic pins as a cost effective and sustainable solution for failures extending deeper than a shallow slope failure.

CHAPTER 3

SITE INVESTIGATION AND SLOPE STABILIZATION PLAN

3.1 Background

The objective of the current study was to establish a cost effective and sustainable slope stabilization method using Recycled Plastic Pins to stabilize deep slope failures. Generally, slope failures in highway embankments are shallow in nature but deeper cracks due to cyclic wetting and drying periods extends failures planes into deeper layers. Therefore, two highway slopes located in the North Texas region was selected for this study. The first slope was located in the intersection of Interstate 820 and Rosedale Street in Fort Worth, Texas and the second slope is located near U.S highway 67 in Alvarado, Texas. Both sites experienced failures with large crest deformation indicating deeper slope failures. The details of the site investigation program are presented in this chapter.

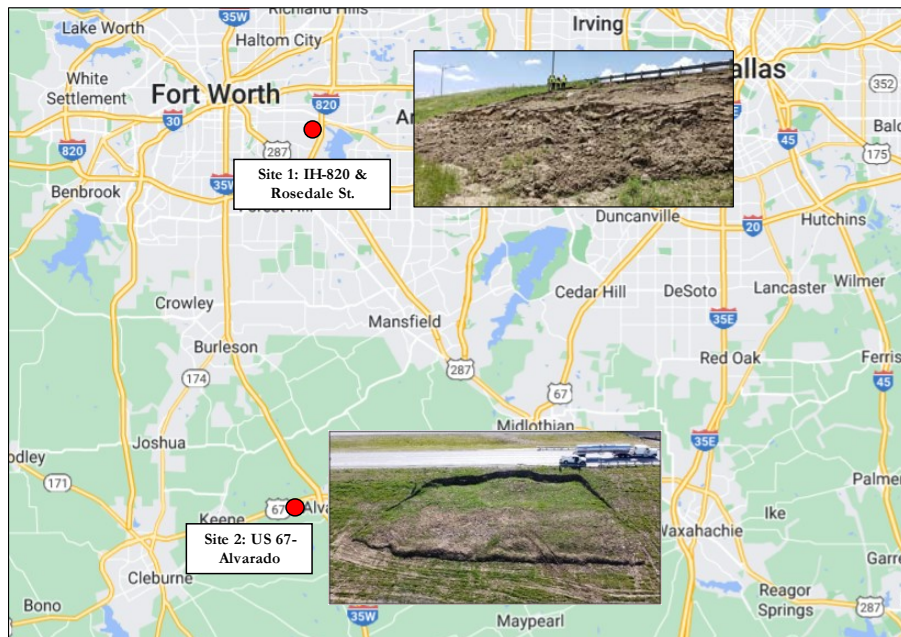


Figure 3.1 Location of Project Sites.

3.2 Site 1: IH-820 & Rosedale Street

3.2.1 Site Investigation

The project site for this study was located in the intersection between E Rosedale Street and East Loop 820 South in Fort Worth, Texas (Figure 3.2). The slope was 25 ft in height with a slope geometry of 1(V):2.5(H). The slope was reported to fail on numerous occasions before the slope failure investigated in this study. The length of the failure section was 120 feet with a 60 feet section in the center with increased head scrap averaging 5.5 feet (Figure 3.3 (b)). The soil debris from the failure was observed to bulge from lower third of the slope (Figure 3.3 (a)).



Figure 3.2 Site Location: IH-820 & Rosedale Street Site.



(a)

(b)

Figure 3.3 Slope Failure at IH-820 & Rosedale Street (a) Soil Debris Bulging at the Bottom of the Slope (b) Head Scrap at the Crest of the Slope.

Two borings were advanced up to a depth of 30 feet as shown in Figure 3.4 to investigate the subsurface conditions of the project site. Subsurface exploration and geophysical testing using 2D electrical resistivity imaging (ERI) were conducted in July 2019 (Figure 3.4).

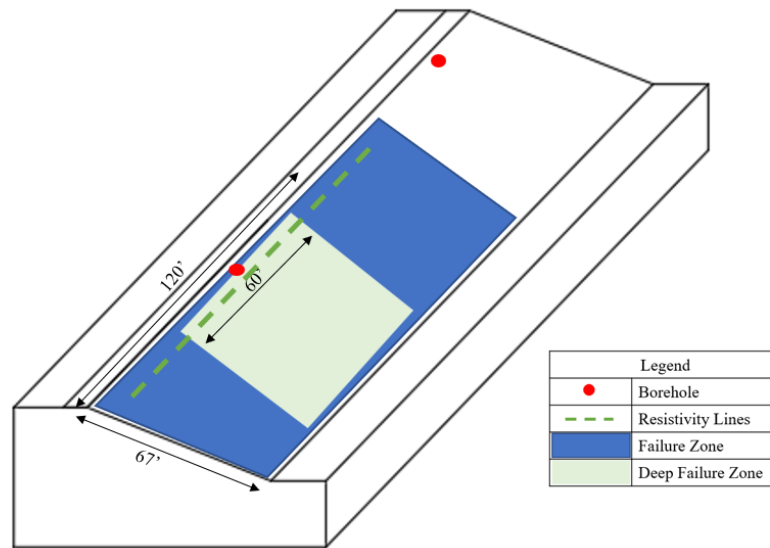


Figure 3.4 Schematic of 2D Electrical Resistivity Imaging Location

3.2.2 Geotechnical Investigation

Two soil test borings were conducted in the reinforced section and control section for the sub-surface sample collection. Both soil test boreholes were located at the crest of the slope. Truck mounted drilling rig was used for the drilling. Hollow-stem augers with 5-inch diameter was used. Disturbed and undisturbed samples were collected throughout the two boreholes. Undisturbed samples were collected at intervals of 5 ft, using 3-inch diameter thin-walled Shelby tube sampler. Similarly, Disturbed Samples were collected

at 5 ft intervals. The Shelby tube samples obtained from the first 15 ft were not continuous due to the presence of small stones and sand.



Figure 3.5 Collection of Samples



(a)

(b)

Figure 3.6 Shelby Tube Samples (a) Depth 5 ft; (b) Depth 10 ft

The American Society of Testing Materials (ASTM) standards were followed to conduct the laboratory tests on collected samples to determine the physical properties. The tests conducted are as follows.

3.2.2.1 Grain Size Distribution

The Grain size distribution test was performed using mechanical sieve analysis for grain sizes over 0.075 mm and hydrometer analysis for grain sizes less than 0.075 mm according to the American Society of Testing and Materials (ASTM) D6913 code for Standard method for particle size distribution (Gradation) of soils using sieve analysis to obtain the full-range grain distribution curve. Standard sieves #4, #10, #30, #40, #80, #100

and #200 were used in the mechanical sieve analysis. Additionally, hydrometer tests were done for samples with grain size less than 0.075 mm (passing No. 200 sieve). Table 3.1 summarizes the percentages of gravel, sand, silt, and clay from disturbed samples collected at different depths. Figure 3.7 shows the gradation curve. The fine content of the sample was observed to be more than 80%.

Table 3.1 Summary of Grain Size distribution.

Depth (ft.)	Gravel (%)	Sand (%)	Silt (%)	Clay (%)	Classification
5	0	19.6	20.43	59.9	Fat Clay with Sand
7	0	19.5	20.45	60.05	Fat Clay with Sand
9	0	35	17.20	47.80	Sandy Fat Clay
12	0	10	23.9	66.1	Fat Clay
17	0	17	23.0	60.0	Fat Clay with Sand
22	0	19.5	22.5	58.0	Fat Clay with Sand

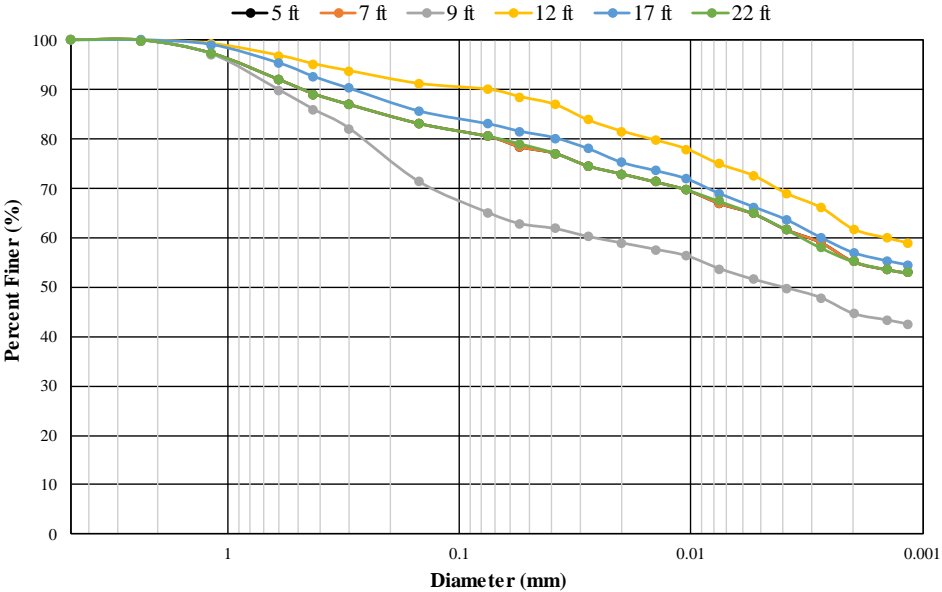


Figure 3.7 Grain Size Distribution Curve

3.2.2.2 Atterberg Limit Test

The Atterberg test was conducted on the undisturbed samples using the ASTM code D 4318 the standard test method for liquid limit, plastic limit, and plasticity index of soils. The liquid limits and plasticity indices of the samples ranged between 50-60 and 30-40, respectively. Figure 3.8 represents the plasticity chart. Based on the laboratory investigation results, the soil was classified as high plastic clay (CH) with Sand according to the Unified Soil Classification System (USCS).

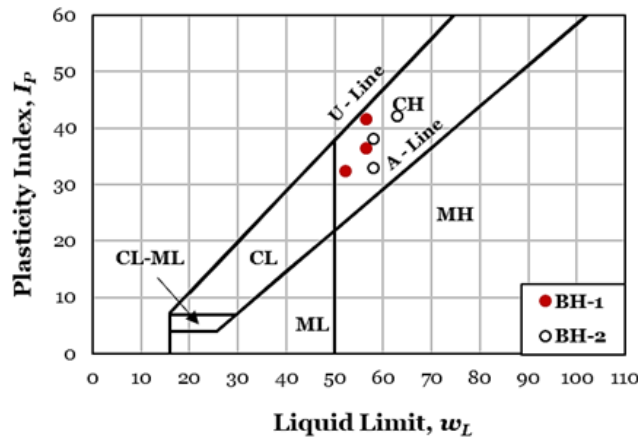


Figure 3.8 Plasticity Chart for Collected Soil Samples.

3.2.2.3 Shear Strength Test

Undisturbed samples obtained were further investigated to obtain strength parameters of the soil. Undisturbed samples obtained from the first 15 ft were not continuous due to presence of small rocks and sand. Therefore, Direct Shear tests were carried out to determine the peak strength parameters of the soil in the slope under ASTM D3080, the standard test method for direct shear test of soil under consolidated drained conditions. Undisturbed Shelby tube samples were used with a loading rate of 5%. Continuous undisturbed sample was obtained in the last 10 ft. Therefore, Unconfined Compressive

Strength (USC) test was done under ASTM code D2166, the standard test method for Unconfined Compressive Strength of cohesive soil.

Table 3.2 Shear Strength Test Results.

Sample Depth (ft.)	Test Type	Cohesion (psf)	Friction Angle (°)
0-5	DS*	250	14
5-10	DS*	550	18
10-15	DS*	260	15
15-30	DS/UCS*	700	20

*Note: DS = Direct Shear Test; UCS = Unconfined Compressive Strength Test

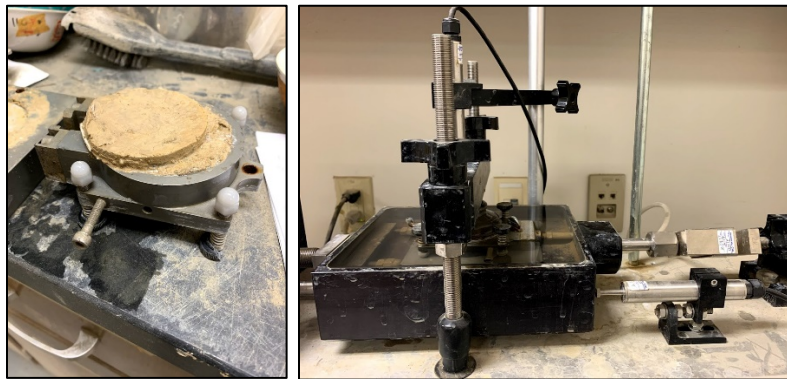


Figure 3.9 Direct Shear Testing.

3.2.2.4 Moisture Content Tests

Moisture contents were conducted to observe the variation of moisture with depth. American Society of Testing Materials (ASTM) manual D2216 for standard test methods for laboratory determination of water (Moisture) content of Soil and Rock by mass was followed. The moisture variation with depth is shown in Figure 3.10 (a). The moisture variation is observed to be within 9-22%. The maximum moisture contents are observed 10-25 ft.

Texas Cone Penetration (TCP) Test was done in 5 ft. consecutive intervals to determine the allowable shear values of existing materials. The results are show below in Table

3.3. The TCP values of both boreholes fall into the range of 8 to 20 which is classified as loose/soft soil (TxDOT, 2000).

Table 3.3 TCP Results for I-820 & Rosedale St.

Depth (ft.)	TCP Results	
	Blow Count (N Value) BH-1	Blow Count (N Value) BH-2
5	12	4
10	17	12
15	7	9
20	17	14
25	17	16
30	18	17

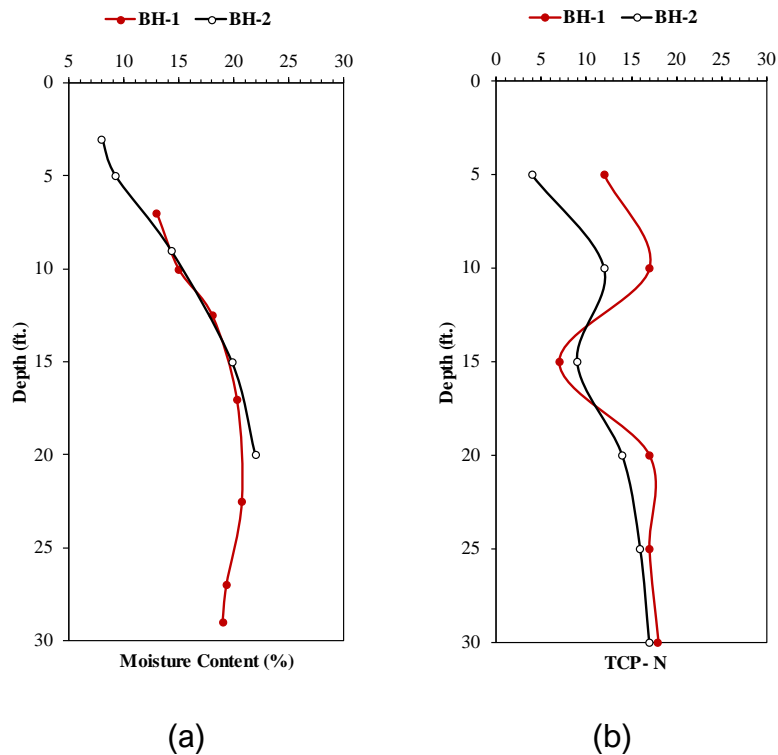


Figure 3.10 (a) Variation of Moisture Content (b) Variation of TCP-N Blow Count with Depth

3.2.2.5 Geophysical Testing

Geophysical testing was performed using 2D electrical resistivity imaging (ERI). ERI uses a multi-electrode array system and inversion modeling to provide a continuous image of the subsurface. Resistivity Imaging (RI) was conducted at the crest of the slope along the failed section to determine the moisture variation in the slope (Figure 3.12).



Figure 3.11 Location of Resistivity Imaging.

Moisture content and resistivity is inversely related. Electric resistivity decreases with the increase of moisture (Siddiqui and Osman 2013). Low resistivity was observed across the profile indicating high moisture levels and saturated soil conditions. Resistivity has also been observed to be low in soil with fine grained particles due to the ion exchange property of clay ions which facilitates the flow of electric current (Zhdanov and Keller 1994). Resistivity values for clay is less than 10 Ohm-m (Sudha et al. 2009). Values ranging between 3-8 ohm-m was observed across the slope indicating the presence of clayey soil which was verified during soil investigation. Higher resistivity pockets at the surface shows the presence of voids and cracks.

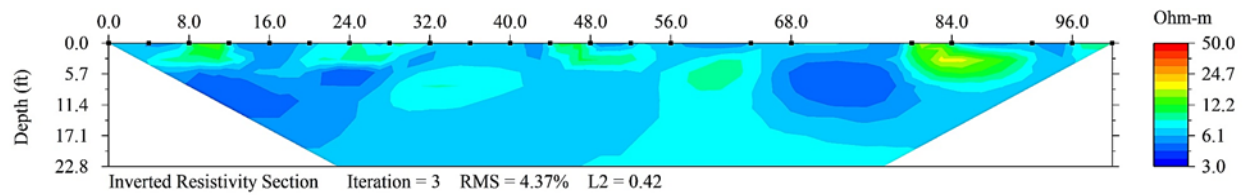


Figure 3.12 Result of Resistivity Imaging.

3.2.3 Analyses of Site Investigation Results

The subsurface investigation of the project site indicated that the slope was constructed using high plastic clay. The presence of high plastic clay makes the slope highly susceptible to slope failure due to the swelling and shrinkage during the wet and the dry seasons. The swelling and shrinkage behavior of the soil reduces the strength of the soil in the active zone (less than 6 feet (Sapkota 2019)) and causes shallow slope failures. The project site slope was observed to fail on numerous occasions before the failure described in this study which caused shoulder cracks at the crest of the slope. After each shallow failure, the slope was reported to be pushed back and compacted by TxDOT officials, but the strength of the soil does not increase considerably by compaction (Titi and Helwany, 2007). Instead, this process created low strength layers with existing cracks beneath the surface of the slope. The low strength/ low permeable soil combined with the cracks at the crest of the slope aided the infiltration of rainwater deeper into the slope during wet-dry cycles. The voids and cracks up to depths of 5 feet were also observed in the resistivity imaging with high moisture zones up to depth of 10 feet indicating the presence of a deeper active zone. The increase of saturation extending deeper into the slope increased the driving force thereby decreasing the factor of safety causing failure.

According to Duncan (2014) the head scarp indicates the extent of the movement of the slope. The head scarp during failure in IH-820 & Rosedale Street extended up to 5.5 ft which indicated the occurrence of large slope movements (Figure 3.13 (b)).



Figure 3.13 IH-820 & Rosedale St. (a) Slope Failure; (b) Head Scarp.

3.2.4 Slope Stability Analysis

Elasto-plastic finite element method (FEM) is an accurate, robust and simple method for slope stability. Slope stability analysis for this study was conducted using the FEM program, PLAXIS. Mohr Coulomb failure criterion was also used where the soil model is linearly elastic perfectly plastic soil model (Alkasawne et al., 2008). The FEM analysis was done using triangular elements with 15 nodes. Rawat and Gupta (2016) stated that when reinforcements are incorporated in analysis, 15-noded elements give more accurate and reliable results compared to six-noded elements.

The analysis was carried out considering the initiation of slope failure at a limiting factor of safety at 1. It is common practice to assume the depth of wetting as 7 to 10 feet (Nelson et al., 2001) and according to Hughes et al., 2009 the reduced strength should be used in the upper 10 feet for failure surfaces extending deeper into the slope. In this study, the top 8 ft at the crest (Soil 1) with decreasing depth of zone (Soil 2) was considered as the

failure zone with residual strength (Figure 3.14). Residual strength parameters were considered since this slope experienced several failures before the failure discussed in this study (Al-Homoud et al., 1997). The soil parameters for the remaining layers were obtained using the soil test results done during site investigation. The soil profile is shown below (Figure 3.14). Several iterations were carried out during the analysis to calibrate the soil model to represent failure as observed at site. The residual parameters for the top 8 feet were back calculated to stimulate the failure at a factor of safety of 1. Head scrap of 5 ft and bulging initiating from the middle of the slope was observed in the model as well as the field after failure (Figure 3.15 (a)). The soil parameters that yielded a factor of safety of 1.00 is shown in Table 3.4.

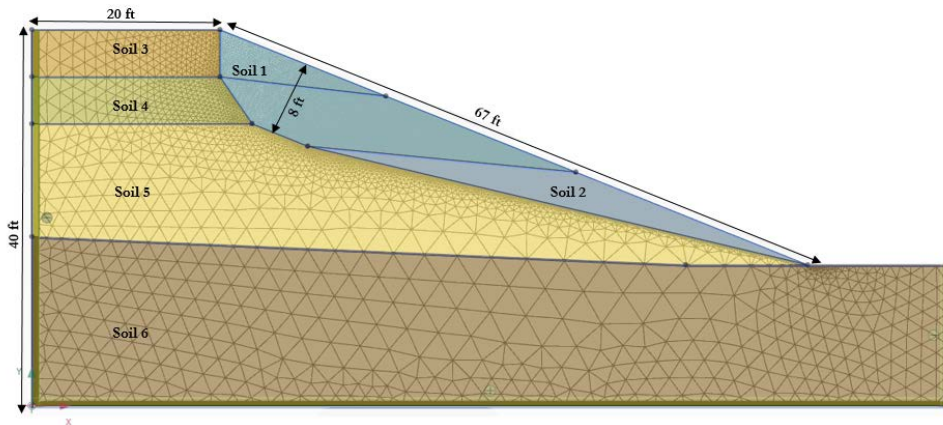


Figure 3.14: Soil Profile

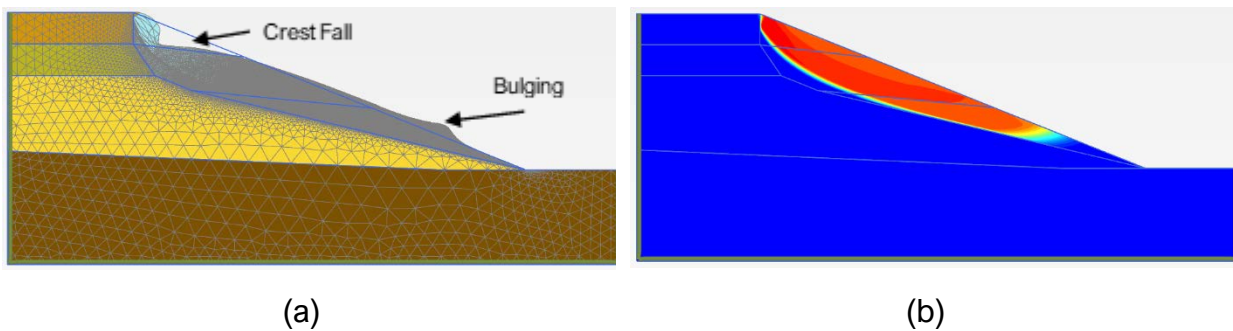


Figure 3.15 (a) Deformed Mesh Showing Crest Fall and Bulging, (b) Slip Circle: FS=1.00.

Table 3.4 Parameters for FE Analysis.

Layer	Unit Weight (pcf)	Elastic Modulus E (psf)	Poisson Ratio v	Cohesion c (psf)	Phi (°)
1	120	9000	0.39	60	12
2	120	11E3	0.35	70	13
3	125	38E3	0.30	250	14
4	130	82E3	0.30	550	18
5	120	39E3	0.32	260	15
6	130	110E3	0.2	700	20

The FEM analysis showed the presence of slip surfaces extending deeper than surficial failures. Therefore, remedial measures to stabilize deeper failures was required.

3.3 Site 2: U.S 67 – Alvarado

3.3.1 Site Investigation

The project site for this study was located beside U.S 67 highway near the intersection with Interstate highway 35 by Alvarado (Figure 3.16). The slope was 37 feet in height with a slope geometry of 1(V): 3(H). The length of the failure was observed to be 180 feet with a width of 115 feet. The failure originated approximately 10 feet from the crest of the slope with a head scrap averaging 4 to 5 feet indicating deeper failure planes. The failure debris was observed to extend from the crest of the slope to the lower third of the slope.



Figure 3.16 Site Location: U.S 67 Alvarado.



(a)

(b)

Figure 3.17 U.S 67 Alvarado (a) Slope Failure (b) Saturated Soil.

Two borings were advanced up to a depth of 30 feet at the crest of the slope as shown in Figure 3.18 to investigate the subsurface conditions of the project site. Subsurface exploration and geophysical testing using 2D electrical resistivity imaging (ERI) were conducted in March 2021.

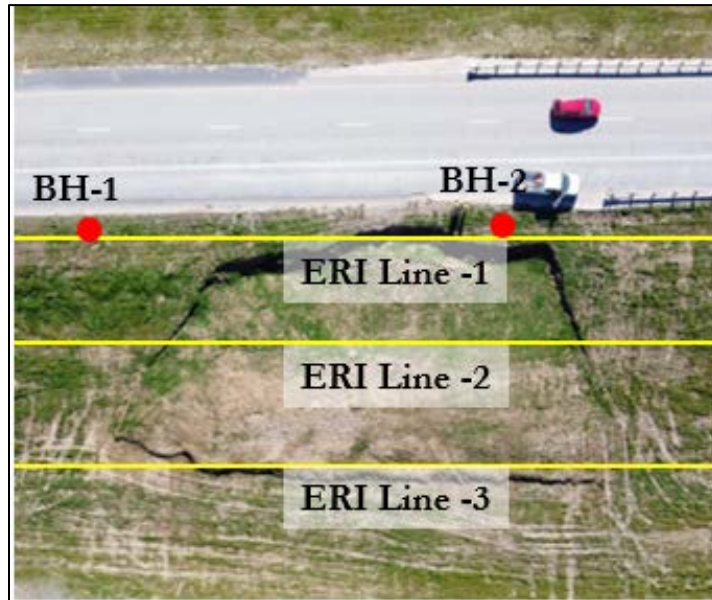


Figure 3.18 Location of Boreholes and ERI Lines.

3.3.2 Geotechnical Investigation

Two soil test borings were conducted in the reinforced section and control section for the sub-surface sample collection. Both soil test boreholes were located at the crest of the slope. Truck mounted drilling rig with hollow-stem augers of 5-inch diameter was used. Each auger was 5 ft in length. Disturbed and undisturbed samples were collected throughout the two boreholes. Undisturbed samples were collected at intervals of 5 ft, using 3-inch diameter thin-walled Shelby tube sampler. Similarly, Disturbed Samples were collected at 5 ft intervals.

The American Society of Testing Materials (ASTM) standards were followed to conduct the laboratory tests on collected samples to determine the physical properties. The tests conducted are as follows.

3.3.2.1 *Atterberg Limit Test*

The Atterberg test was conducted on the undisturbed samples using the ASTM code D 4318 the standard test method for liquid limit, plastic limit, and plasticity index of soils. The liquid limits and plasticity indices of the samples. Based on the laboratory investigation results, the soil at 5-20 ft depth was classified as low plastic clay (CL) and soil from 20-30 ft depth was classified as high plastic clay (CH) according to the Unified Soil Classification System (USCS).

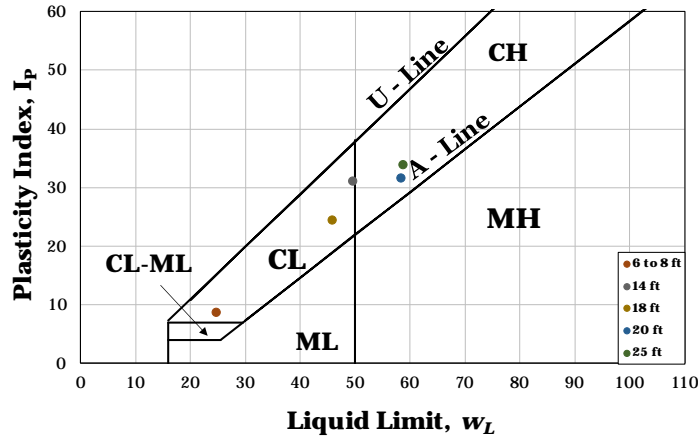


Figure 3.19 Plasticity Chart for Collected Soil Samples.

3.3.2.2 Shear Strength Test

Undisturbed samples obtained were further investigated to obtain strength parameters of the soil. Unconfined Compressive Strength (USC) test was done under ASTM code D 2166, the standard test method for Unconfined Compressive Strength of cohesive soil.

Table 3.5 Shear Strength Test Results.

Sample Depth (ft.)	Test Type	Cohesion (psf)	Friction Angle (°)
0-5	UCS*	500	15
5-15	UCS*	350	16
15-25	UCS*	460	14
25-30	UCS*	950	25

*Note: UCS = Unconfined Compressive Strength Test

3.3.2.3 Moisture Content Tests

Moisture contents were conducted to observe the variation of moisture with depth. American Society of Testing Materials (ASTM) manual D2216 for standard test methods for laboratory determination of water (Moisture) content of Soil and Rock by mass was followed. The moisture variation with depth is shown in Figure 3.20. The moisture variation is observed to be within 19-26%. The maximum moisture contents are observed 10-25 ft.

Texas Cone Penetration (TCP) Test was done in 5 ft. consecutive intervals to determine the allowable shear values of existing materials. The results are shown below in Table 3.6.

The TCP values of both boreholes fall into the range of 8 to 31 which is classified as loose/soft – Medium stiff soil (TxDOT, 2000).

Table 3.6 TCP Results for U.S 67 & Alvarado

Depth	TCP Blow Count (N- Value)	
	BH-1	BH-2
5	11	13
10	8	9
15	9	10
20	11	12
25	17	20
30	29	31

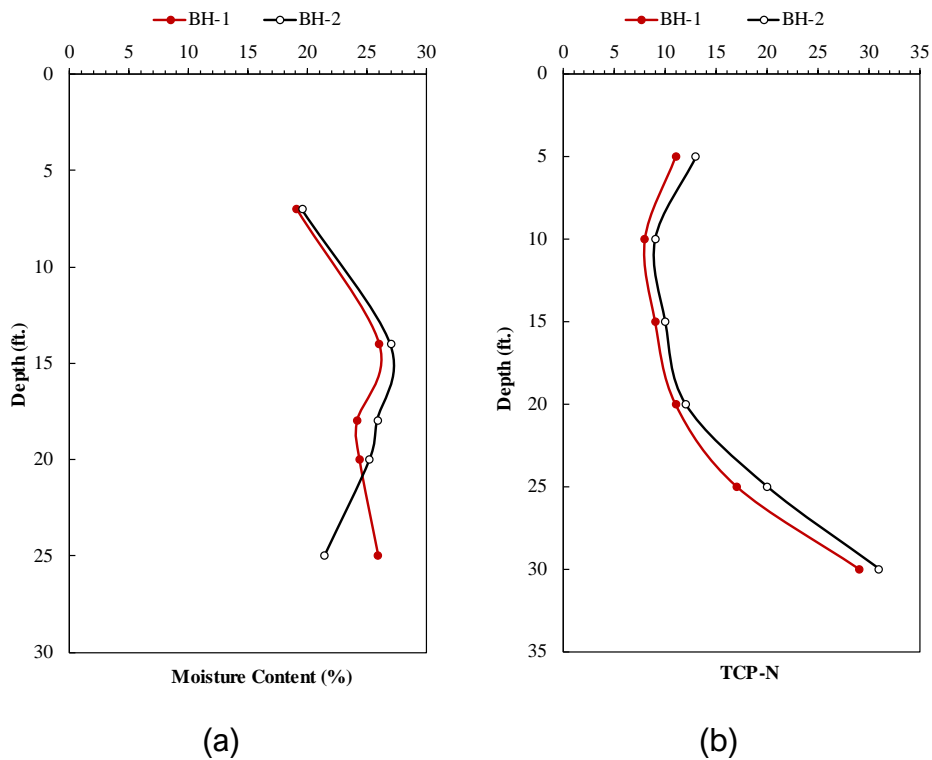


Figure 3.20 (a)Variation of Moisture Content (b) Variation of TCP Blow Count with Depth

3.3.2.4 Geophysical Testing

Geophysical testing was performed using 2D electrical resistivity imaging (ERI). ERI uses a multi-electrode array system and inversion modeling to provide a continuous image of the subsurface. Resistivity Imaging (RI) was conducted at the crest, middle and toe of the slope along the failed section to determine the moisture variation in the slope (Figure 3.22).

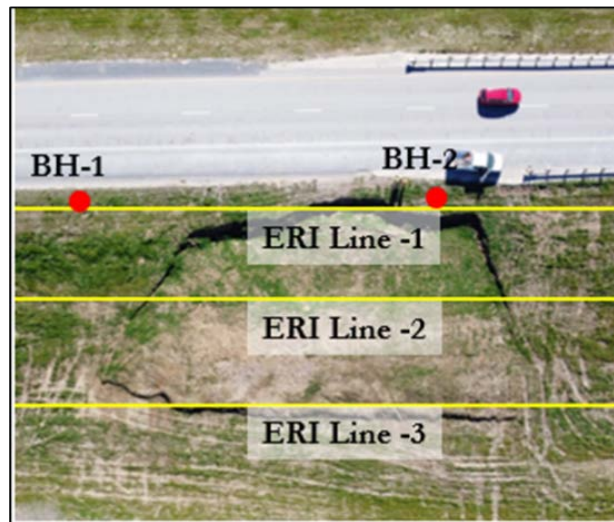


Figure 3.21 Location of ERI Lines.

Moisture content and resistivity is inversely related. Electric resistivity decreases with the increase of moisture (Siddiqui and Osman 2013). Low resistivity was observed across the profile indicating high moisture levels and saturated soil conditions. Resistivity has also been observed to be low in soil with fine grained particles due to the ion exchange property of clay ions which facilitates the flow of electric current (Zhdanov and Keller 1994). Resistivity values for clay is less than 10 Ohm-m (Sudha et al. 2009). Values ranging between 3-8 ohm-m was observed across the slope indicating the presence of

clayey soil which was verified during soil investigation. Higher resistivity pockets at the surface shows the presence of voids and cracks.

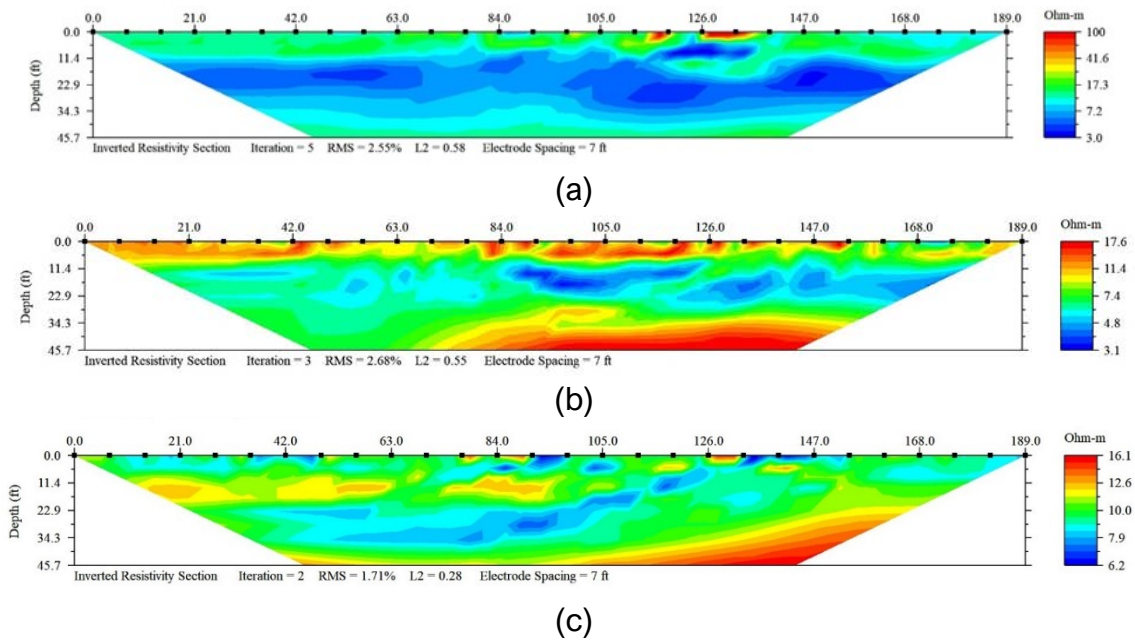


Figure 3.22 Result of Resistivity Imaging; (a) Crest (b) Middle (c) Toe.

3.3.3 Analyses of Site Investigation Results

The subsurface investigation of the project site indicated that the slope was constructed using low plastic clay. High moisture conditions were observed at this project site in both lab testing results and electrical resistivity results. Saturated surface conditions in the middle of the slope were observed during site reconnaissance. A water body is located on the opposite side of the highway embankment. Therefore, the ground water level was projected to the failed section to understand the effect of the groundwater on the saturation of the slope (Figure 3.23).

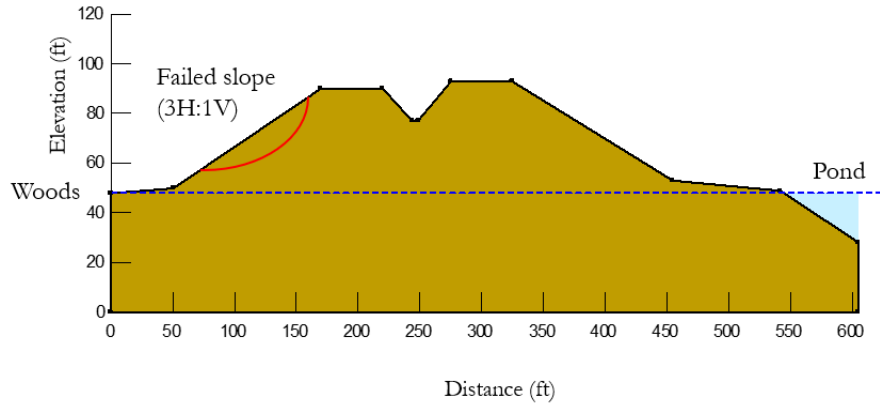


Figure 3.23 Cross Section of the Slope Embankment.

The failure of this site was observed to originate approximately 10 feet from the crest of the slope. During the site investigation high moisture and low strength soil was observed at depths of 10-20 feet. Rise of the ground water table and the infiltration rainwater into slope increases the weight of the soil driving the failure. In addition, the strength of the soil is decreased over time due to the wet dry cycles.

The head scrap observed during the failure averaged between 4 to 5 feet. The increased depth of the head scrap indicated large movements and failure planes extending deeper into the slope.

3.3.4 Slope Stability Analysis

Elasto-plastic finite element method (FEM) is an accurate, robust and simple method for slope stability. Slope stability analysis for this study was conducted using the FEM program, PLAXIS. Mohr Coulomb failure criterion was also used where the soil model is linearly elastic perfectly plastic soil model (Alkasawne et al., 2008). The FEM analysis was done using triangular elements with 15 nodes.

The analysis was carried out considering the initiation of slope failure at a limiting factor of safety at 1. In this study, the top 10 ft at the crest (Soil 1) with decreasing depth of zone

(Soil 2) was considered as the failure zone with residual strength (Figure 3.14). Fully softened soil parameters were used for the soil over the assumed failure plane. The soil parameters for the remaining layers were obtained using the soil test results determined during site investigation. The soil profile is shown below (Figure 3.24). Several iterations were carried out during the analysis to calibrate the soil model to represent failure as observed at site. The fully softened parameters for the top 10 feet were back calculated to stimulate the failure at a factor of safety of 1. Head scrap of 5 ft originating approximately 10 ft into the slope face and bulging initiating from the middle of the slope was observed in the model as well as the field after failure (Figure 3.25 (a)). The slip circle in the model was observed as expected originating at failure initiation point and ending 3/4th into the slope. The soil parameters that yielded a factor of safety of 1.00 is shown in Table 3.7.

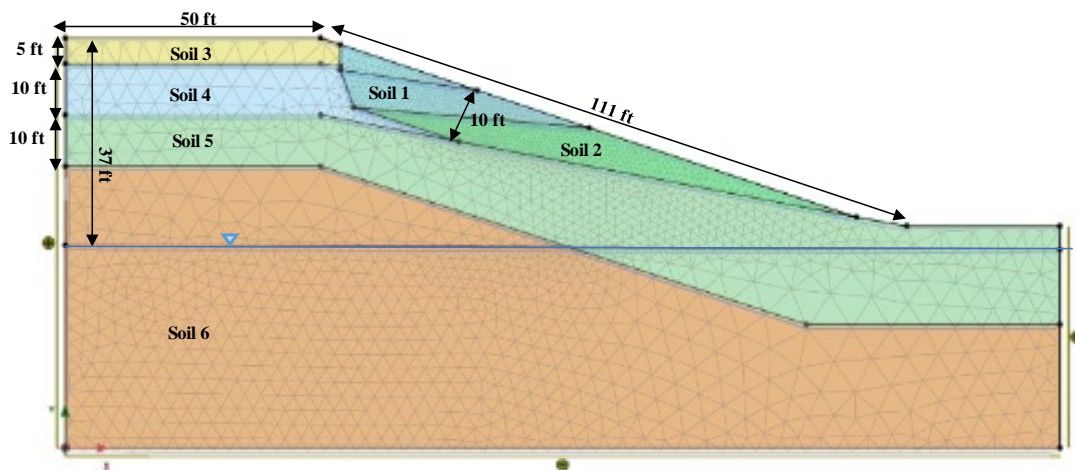


Figure 3.24 Soil Profile.

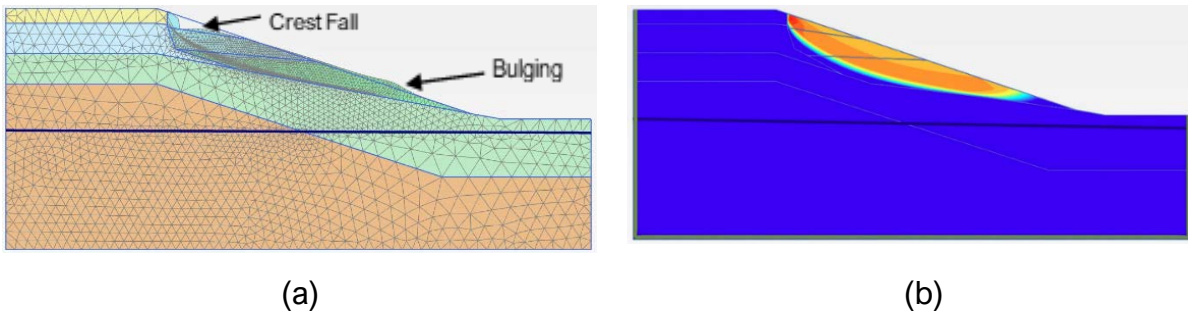


Figure 3.25 (a) Deformed Mesh Showing Crest Fall and Bulging, (b) Slip Circle: FS=1.00.

Table 3.7 Parameters for FE Analysis

Layer	Unit Weight (pcf)	Elastic Modulus E (psf)	Poisson Ratio ν	Cohesion c (psf)	Phi ($^{\circ}$)
1	120	9000	0.39	60	12
2	120	11E3	0.35	70	13
3	125	67E3	0.30	450	16
4	130	52E3	0.35	350	15
5	125	68E3	0.32	450	18
6	130	140E3	0.2	950	25

The FEM analysis showed the presence of slip surfaces extending deeper than surficial failures. Therefore, remedial measures to stabilize deeper failures was required.

CHAPTER 4

SLOPE STABILIZATION USING RECYCLED PLASTIC PINS

4.1 Mechanism of Slope Stabilization

Recycled Plastic Pins (RPP) are used as piles driven into stable soil below the assumed sliding surface to provide reinforcement against the sliding mass. The reinforcing members intersect the failure plane perpendicularly and add an additional resisting force against the driving force of the weight of the soil. The general factor of safety equation is the ratio of the resisting moment (M_r) to the driving moment (M_d). The shear strength of the soil provides the resisting moment in an unreinforced slope where the weight of the soil provides the driving moment. The reinforcement adds the extra resisting moment of (ΔM_r), thereby increasing the factor of safety.

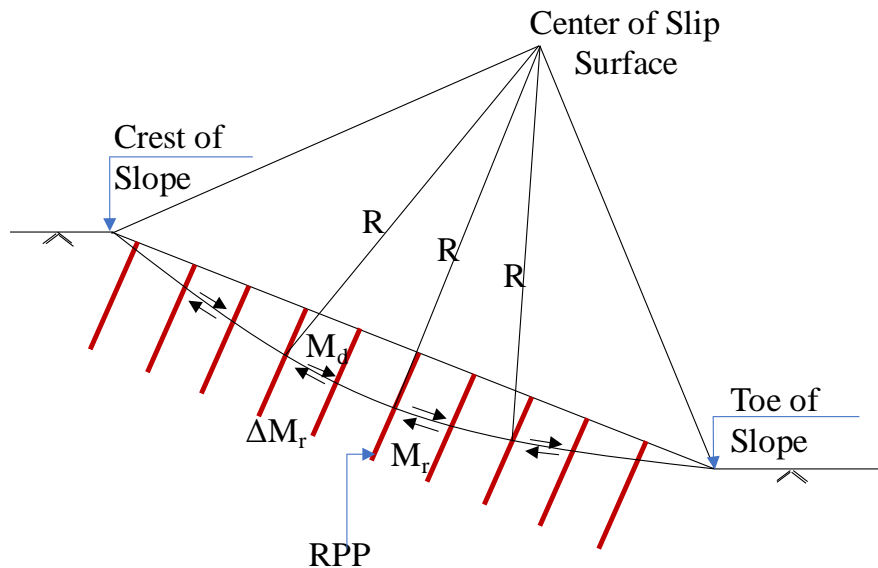


Figure 4.1 Schematic of Mechanism of Slope Failure

The resisting force provided by the reinforcing member is based on the location of the intersection of the sliding surface (Titi and Helwany 2007; Loehr and Bowders, 2007). The

section of the reinforcing member extending beyond the limits of the slip surface provides an anchoring mechanism for the section above the slip surface which acts as a cantilever beam (Loehr et al., 2004). Therefore, the reinforcement that intersects the potential failure surfaces are assumed to increase the resisting moment or force (Strata Systems). Therefore, adequate anchorage into stiffer strata is required to provide sufficient anchorage against failure.

4.2 Selection of Materials

Recycled Plastic pins (RPP) are commercially produced as a pile with a 3.5 inch² cross-section and a length of 10 feet. Deeper slope failures extend to depths greater than 6 feet. Therefore, either longer reinforcing members or a different installation scheme must be utilized to stabilize a deep slope failure.

Recycled Plastic Pins are a cost-effective slope stabilization method (Khan 2013). Therefore, associated cost is an important consideration in the selection of length of RPP. Figure 4.2 shows the relationship between the cost and length of RPP. The cost and length are linearly related.

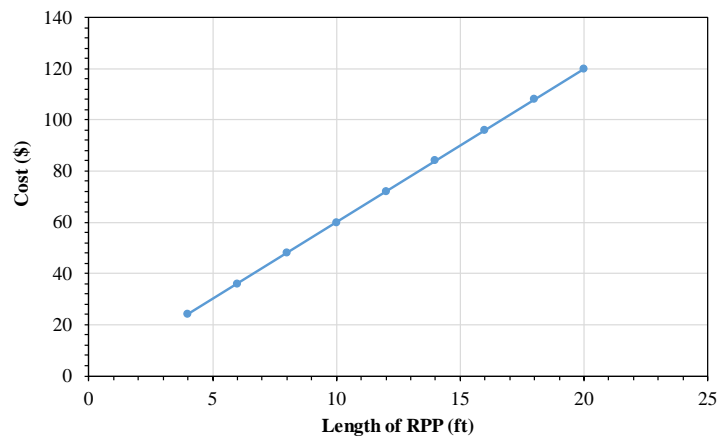


Figure 4.2 Relationship between Cost and Length of RPP.

The use of longer reinforcing members poses problems associated with buckling during installation (Bhattacharya et al., 2005). The slenderness ratio (L/D) provides a relationship between the length and the diameter of the reinforcing member to resist failure due to buckling. According to the U.S Army field manual, an L/D ratio of less than 40 is adequate to avoid extremely slender piles being subjected to buckling. Figure 4.3 presents the L/D ratio of a 3.5-inch by 3.5-inch RPP. The length of RPP must be less than 12 feet (L/D<40) to prevent buckling. Therefore, the commercially produced 10 feet RPP is selected for this study.

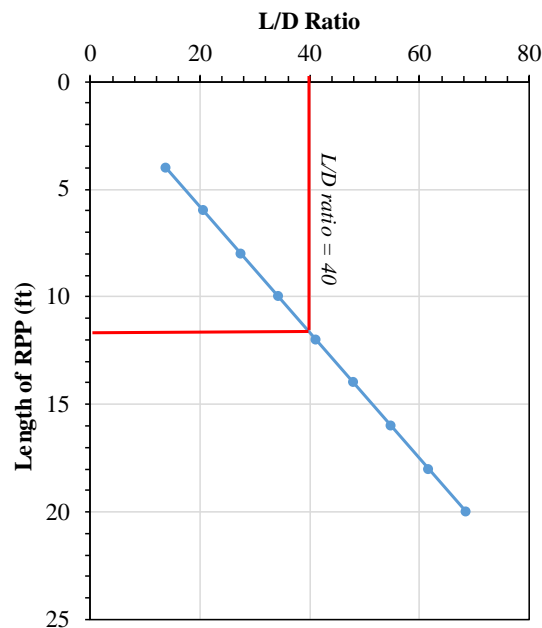


Figure 4.3 Relationship between L/D ratio and Length of RPP.

A modified stabilization scheme is required in order to use 10 feet RPP to stabilize deep slope failures. A two layered design is proposed so that one layer will intersect deeper slip surfaces. The objective of this study is to determine the effectiveness of using a two-

layered layout to stabilize deep slope failures. Two sites in Texas have been selected to satisfy this objective and are presented in the following sections.

4.3 Design of Slope Stabilization Scheme: IH-820 & Rosedale Street.

The site investigation results, and the nature of the slope failure observed at site was considered for the design of the slope. A 120 ft failed section was selected to be reinforced with RPP and a section adjacent to the failed section was designated as a control section. The middle of the failed section (60 ft) where the failure was observed to be the deepest was selected to be reinforced with two layers.

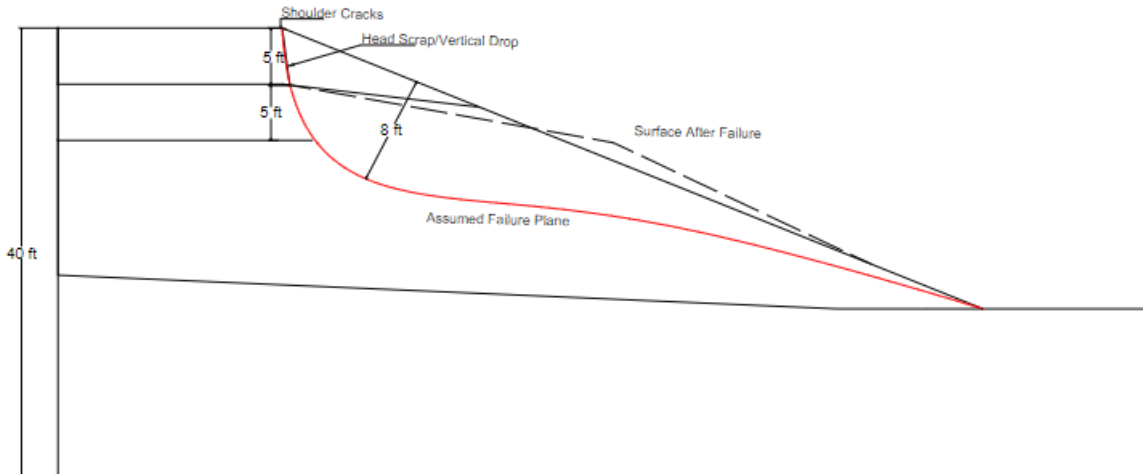
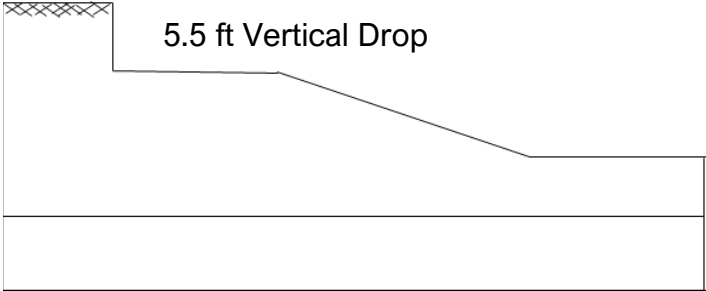


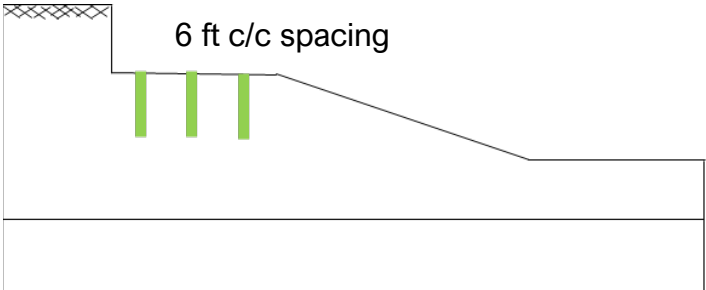
Figure 4.4 Cross-sectional view of the Slope and Possible Failure Plane.

The vertical drop/ crest fall observed after the failure of the slope was utilized to drive in reinforcement that will advance deeper into the slope and intersect deeper failure planes. The depth of the vertical drop averaged about 5.5 ft from the crest of the slope (Figure 4.5 (a)). The slope profile was created and three lines at 6 ft c/c spacing was designed into the failure section. This spacing was selected as the slope would be backfilled and

reinforced with the second layer of RPP at 6 ft c/c spacing (Figure 4.5 (b)). The combined spacing in the section is 3 ft c/c.



(a)



(b)

Figure 4.5 Schematic of (a) Benched and Compacted Slope, (b) First Layer of Reinforcement (Deep Layer)

A 120 feet section was designed to be stabilized with 517 pins. Optimum spacing was selected as 3 ft c/c at the crest, 5 ft c/c in the middle and 4 ft c/c at the toe considering that closer spacing is needed to reinforce the initiation point of failure at the crest and the bulge observed at the toe. The cross-section and proposed layout are shown below (Figure 4.7, Figure 4.6).

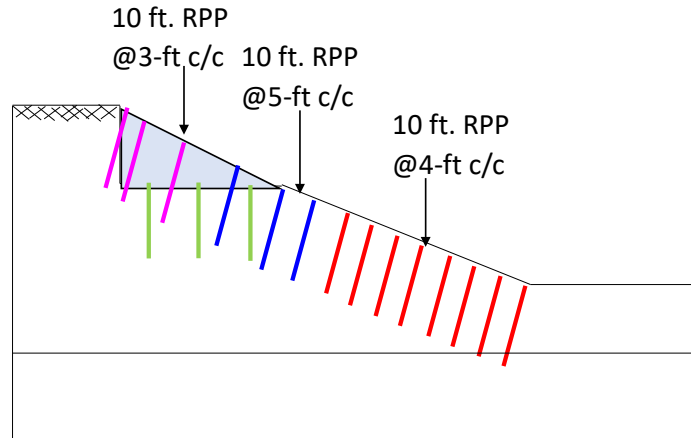


Figure 4.6 Cross-section Design Layout

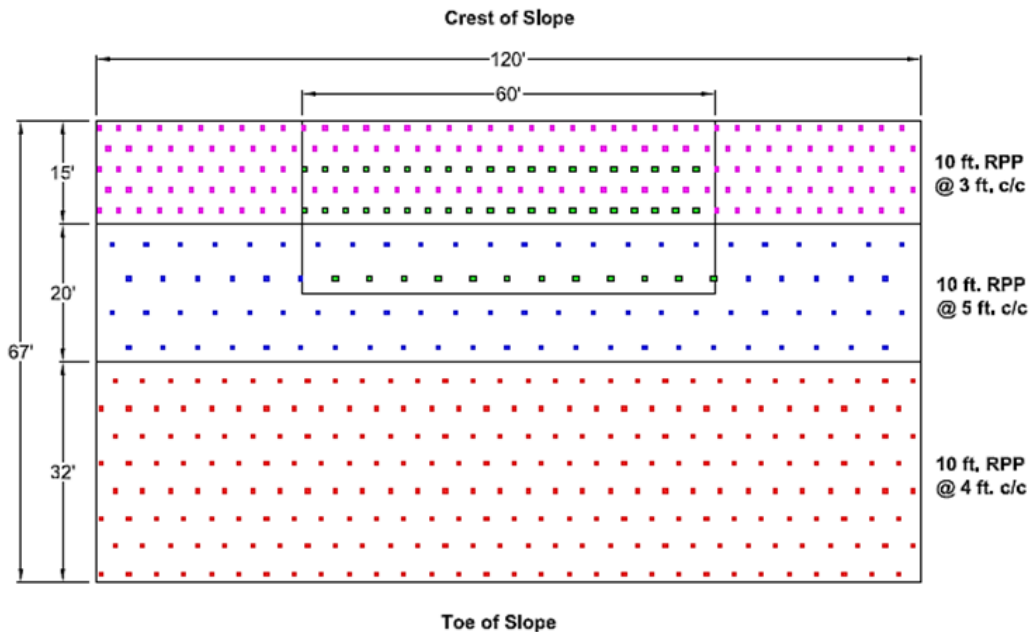


Figure 4.7 Proposed RPP Layout at IH-820 & Rosedale Street.

Slope stability was conducted using the initial model in PLAXIS 2D. The RPP was incorporated into the model using a plate element. Based on the proposed design slope stability analysis was conducted using PLAXIS 2D to evaluate the factor of safety of the reinforced section. The factor of safety for the section was observed as 1.61. The slope profile with the slip circle is shown in Figure 4.8.

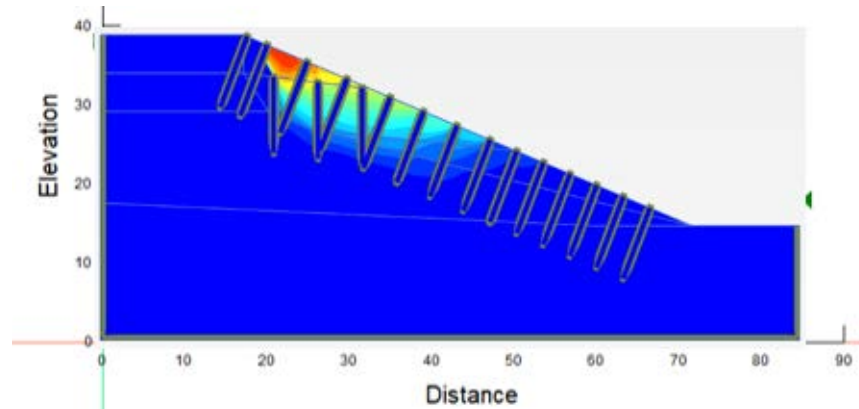


Figure 4.8 Slope Stability Analysis using RPP: Slip Circle: FS = 1.61

4.4 Installation of RPP: IH-820 & Rosedale Street.

Research was conducted in Missouri to understand the effectiveness of different construction methods for installing Recycled Plastic Pins (RPP). Sommers et al., (2000) stated that the equipment to be used must be simple, easily modifiable to conventional equipment, and have an installation rate which is cost effective with minimum damage to RPP. Methods by pseudo vibratory hammers mounted on skid loaders and hydraulic hammers mounted on a backhoe and drilling rigs were evaluated. During the field demonstration for the pseudo vibratory hammer mounted on skid loader, it was observed that the penetration ranged between 12 ft/min to 0.8 ft/min but the skid loader was unstable on the slope and did not have enough capacity to drive in a full length RPP.

The research was continued to use an energy class hydraulic hammer mounted on a backhoe, but this method was unsuccessful due to the difficulty of maneuvering in the slope and excessive rutting due to the rubber tires of the backhoe. The research was further resumed using mast mounted drilling rig. This method was more advantageous than the other methods with less installation times, easy maneuvering in the slope and effective installation.

Following the results obtained from research done by Sommers et al., (2000) and the site observations during other installation done in sites in Texas an excavator (Komatsu PC200 LC) equipped with a hydraulic hammer (NPK GH-15) was used in the RPP installation for this study.



Figure 4.9 RPP Installation Equipment; Excavator Equipped with Hydraulic Hammer, (b) Hydraulic Hammer

During a slope failure that extends deeper than a shallow failure, a deeper vertical drop/head scrap is observed at the crest of the slope after failure (Duncan et al., 2014). This vertical drop will be used to drive in reinforcement that will advance deeper into the slope and intersect deeper failure planes. The vertical drop/crest fall observed at IH-820 & Rosedale St. site during failure was approximately 5.5 ft. The section was initially benched and compacted so that the equipment could easily install the first layer of reinforcement (Figure 4.10). The three lines of deep pins (layer 1) was installed as shown in Figure 4.11. The deeper pins were installed vertically flush to the ground. This layer of pins will be at depths of 15-16 ft from the top of the slope (at grade) after backfilling of the slope.



Figure 4.10 Benching and Compaction of the Crest of the Slope.



Figure 4.11 Installation of Deeper Pins.

In the next phase of construction, the slope was backfilled over the first layer of RPP and compacted (Figure 4.12 (b)). This process was followed by the installation of shallow pins (layer 2), flush to the ground (Figure 4.12 (b)).



(a)



(b)

Figure 4.12 (a) Backfilling of the Slope; (b) Installation of Shallow Pins (at grade).



Figure 4.13 Fully Reinforced Section.

The design was altered during installation according to site conditions. Closer spacing section was extended for better reinforcement. The slope was completely reinforced with a total of 548 RPP as shown in Figure 4.14.

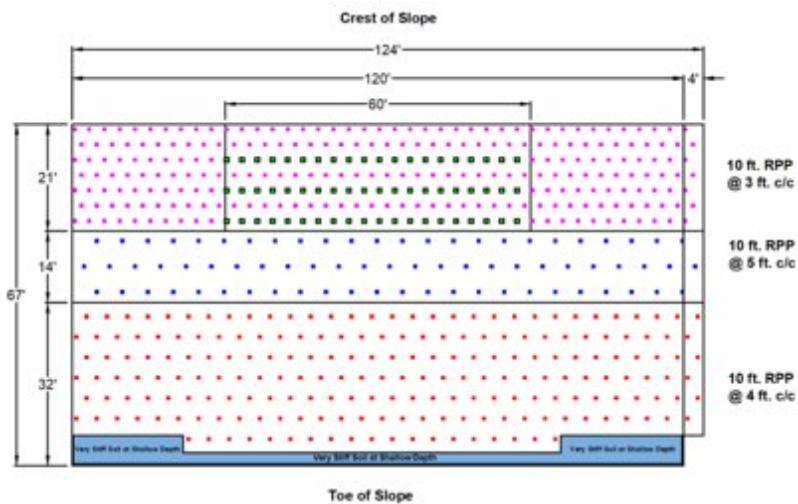


Figure 4.14 As-built Design

The average driving time was recorded during the installation. The average driving time was recorded as 8.83 ft /min. The project was completed in seven days.

Table 4.1 Summary of RPP Driving Time

	Line	Average Total Time per pin (min)	Length of Pin (ft.)
Crest	1	1.26	10
	2	1.02	
	3	1.24	
	4	1.14	
Middle	7	1.13	
	8	1.04	
	9	1.13	

4.5 Design of Slope Stabilization Scheme: U.S 67- Alvarado

The site investigation results, and the nature of the slope failure observed at site was considered for the design of the slope. A 180 ft failed section was selected to be reinforced with RPP and a section adjacent to the failed section was designated as a control section. The middle of the failed section (140 ft) where the failure was observed to be the deepest was selected to be reinforced with two layers.

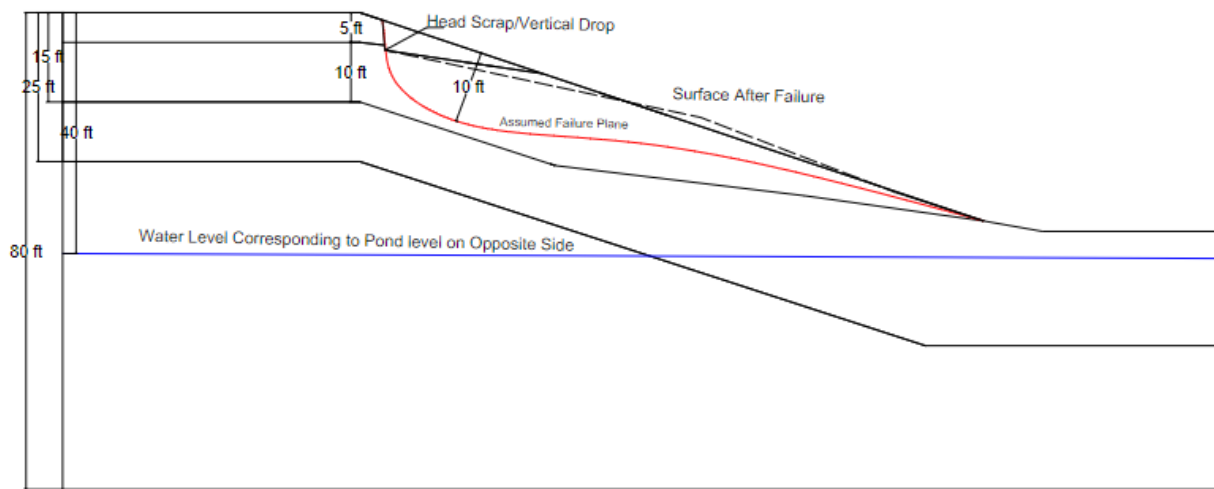
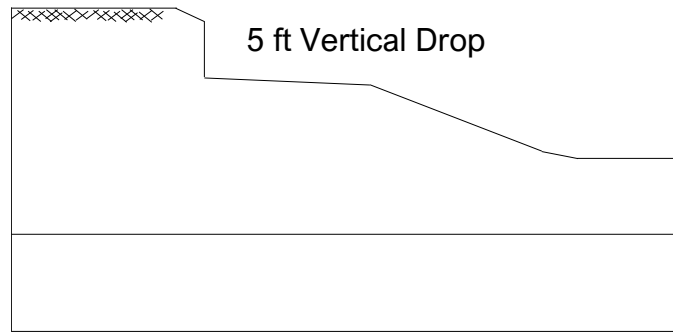
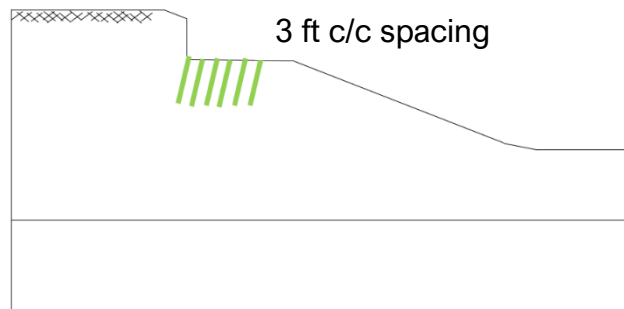


Figure 4.15 Cross-sectional Slope Profile.

The vertical drop/ crest fall observed after the failure of the slope was utilized to drive in reinforcement that will advance deeper into the slope and intersect deeper failure planes. The depth of the vertical drop averaged about 4 to 5 ft from the crest of the slope. The slope profile was created and three lines at 3 ft c/c spacing was designed into the failure section. This spacing was selected as the slope would be backfilled and reinforced with the second layer of RPP which will also be at 3 ft c/c spacing. The combined spacing between the layers would be 1.5 ft c/c. Closer spacing was selected for this site due to the observation of saturated surface conditions.



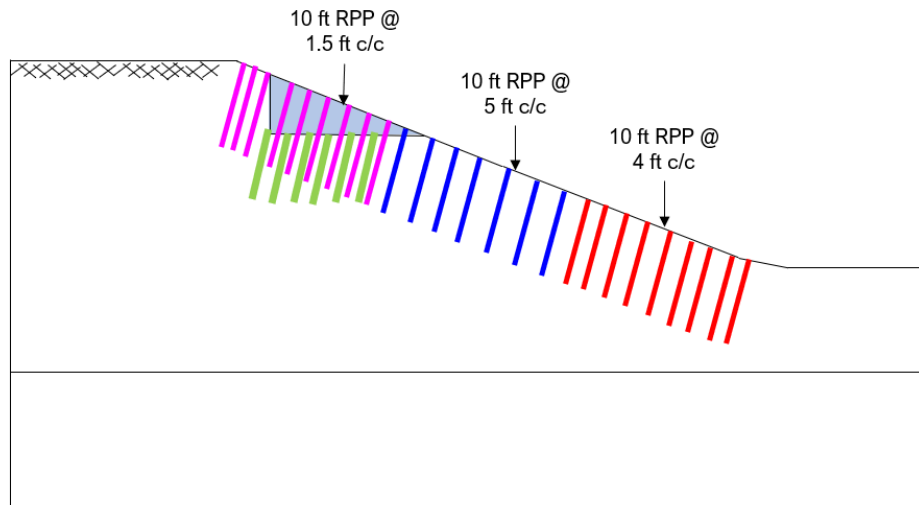
(a)



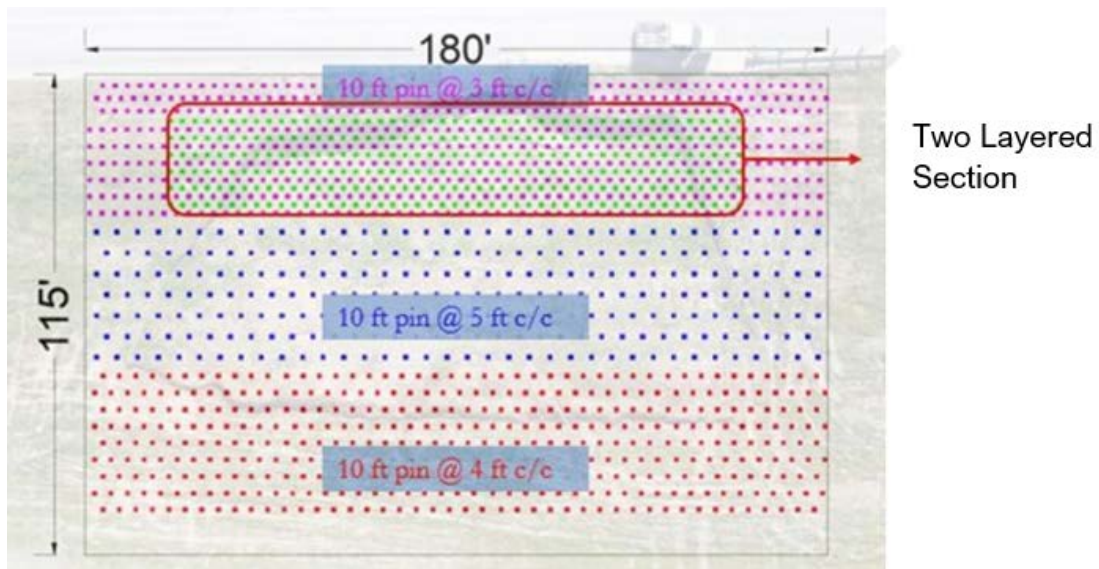
(b)

Figure 4.16 Schematic of (a) Benched and Compacted Slope, (b) First Layer of Reinforcement (Deep Layer)

A 180 feet section was designed to be stabilized with 1438 pins. Optimum spacing was selected as 3 ft c/c at the crest, 5 ft c/c in the middle and 4 ft c/c at the toe. The layout for RPP installation is presented in Figure 4.17 (a)/(b).



(a)



(b)

Figure 4.17 (a) Cross-sectional Design Layout; (b) Design Layout

Slope stability analysis for the proposed design was conducted using PLAXIS and the factor of safety was observed as 1.67 and suitable for slope stabilization design.

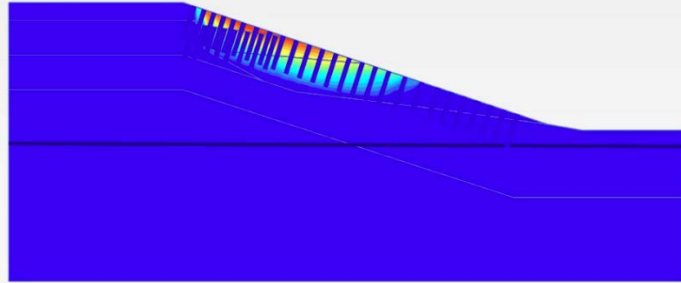


Figure 4.18 Slope Stability Analysis using RPP: Slip Circle: FS = 1.67

4.6 Installation of RPP: U.S 67- Alvarado

An excavator equipped with a hydraulic hammer was utilized to install the RPP. This equipment is suitable for the installation process over the slopes since no additional anchorage is required to maintain the stability of the equipment. RPP installation was conducted in June 2021. Initially, the locations for the RPPs were flagged according to the design layout. An 8 ft steel pin was used to create a hole at each marked location to increase the efficiency of installation. The process of RPP installation in two layers is presented in Figure 4.19 and Figure 4.20.

The crest drop was benched and compacted to install the first layer of RPP followed by the backfilling and compaction to match the existing grade (Figure 4.19). The second layer of RPP was installed flush to the ground over the backfilled slope (Figure 4.20 (b)).

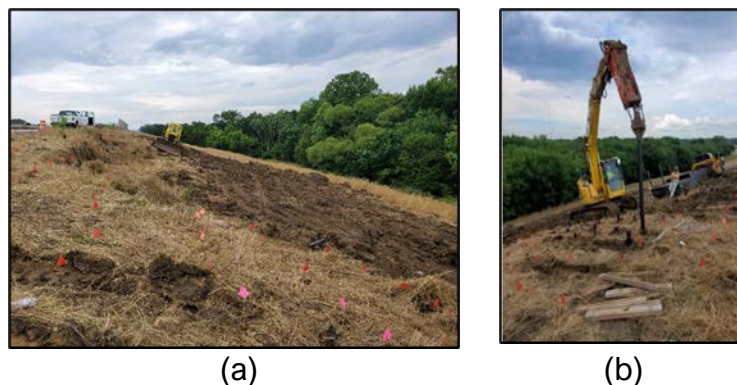


Figure 4.19 (a) Benching and Compaction (b) Installation of the First Layer of RPP



(a)



(b)

Figure 4.20 (a) Backfilling of Slope and (b) Installation of Second Layer of RPP

A 180 ft. long section was reinforced with 10 ft. long RPPs with 3 ft. c/c, 4 ft. c/c and 5 ft. c/c spacing. The spacing of RPP was changed due to the observation of seepage of water from the mid-slope to provide additional resistance. A total of 1454 RPPs were installed as shown in Figure 4.21.

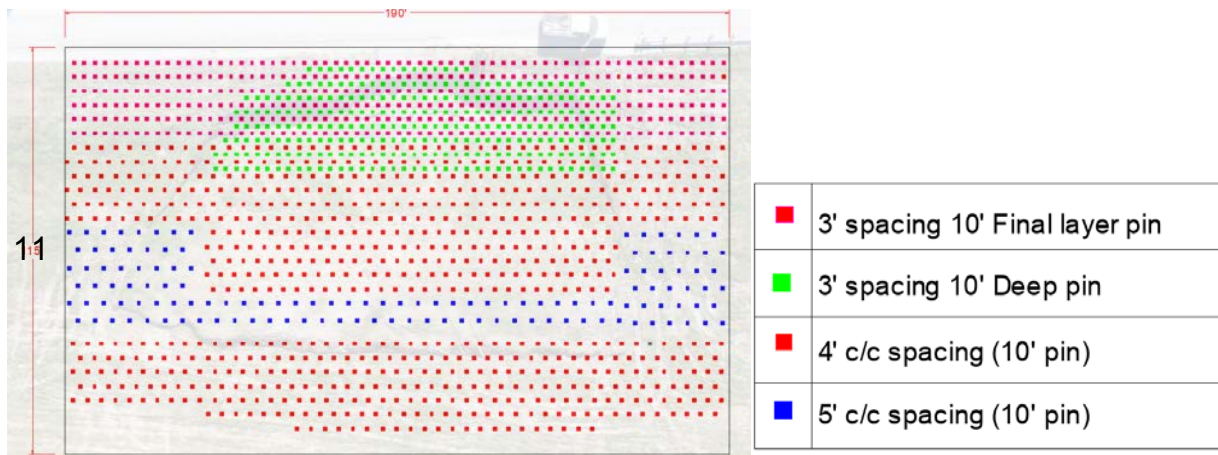


Figure 4.21 As-built drawing of RPP Installation

According to Khan (2014), installation time per RPP is the summation of the time required to install and to maneuver the drilling equipment to the next location. During the installation process, the RPP driving time was measured. Average driving time ranged from 5-10 ft./min.

The soft soil present at site created issues for the installation process. The soil was observed to be extremely soft after rainfall events. The installation equipment had difficulties maneuvering and installing pins due to soft and clayed soil present at site (Figure 4.22).



(a)



(b)



(c)



(d)

Figure 4.22 (a) Geotechnical Drill Rig delivery truck stuck, (b) Excavator stuck at the toe of the slope, (c) Visible perched water in the middle of the slope and (d) Installation equipment stuck due to the extremely soft soil.

4.7 Cost Analysis

The costs associated with slope stabilization depend on site conditions, site accessibility, cost of materials, cost of mobilization, and cost of site preparation (Khan 2013). The cost estimate for the sites in this study was calculated considering only the cost for RPP and the cost for field installation. The average cost to stabilize a slope with RPP is \$7/ft² of slope.

Table 4.2 Cost Analysis

Site	Total Cost (\$)	Area (ft ²)	Cost (\$/ft ² of Slope)
IH-820 & Rosedale Street	54,294	7,200	7.54
U.S 67- Alvarado	139,140	20,900	6.68

The comparison of costs for common slope stabilization methods are presented in Figure 4.23. The cost of slope stabilization with the stabilization methods mentioned in the figure below is 10% to 80% more than the cost for slope stabilization with RPP.

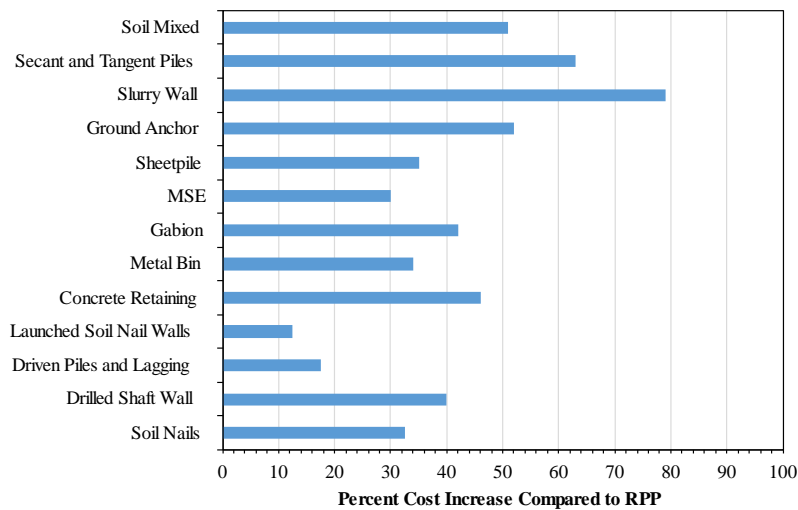


Figure 4.23 Cost Comparison for Slope Stabilization Methods (Redrawn using data from Kioussis et al., 2010, Sabatini et al., 1997 cited in Lazarte et al., 2003)

CHAPTER 5

INSTRUMENTATION AND PERFORMANCE MONITORING

Instrumentation was conducted to monitor the performance of the reinforced slopes. Vertical Inclinerometers and Topographic survey were conducted on a regular basis. The details of the instrumentation and performance monitoring conducted is discussed in this chapter.

5.1 Instrumentation in IH-820 & Rosedale Street

The performance of the reinforced section was monitored monthly using vertical inclinometers and topographic survey. The details of the instrumentation and performance monitoring is presented below.

Vertical Inclinerometer

Vertical inclinometers are primarily used to monitor the lateral deformation of soil and rock in different geotechnical applications. There are two types of inclinometers: in-place sensor systems and portable inclinometers. The inclinometer used in this study is a portable vertical inclinometer by Slope Indicators.

The system consisted of a guide casing embedded in the ground which deforms with the soil. The bi-axial wheeled probe is connected to the control cable and guided into the casing. The probe is sent through the casing measuring the deflection of the casing. The data is acquired using a data acquisition system (Figure 5.1).

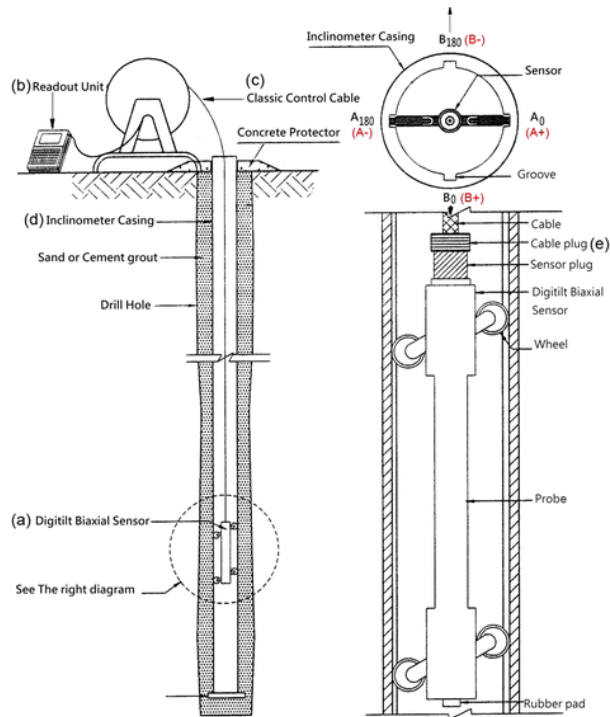


Figure 5.1 Vertical Probe Inclinerometer (Jeng, 2017)

Topographic Survey

Topographic survey was conducted by the use of a Total station (Leica Geosystems) (Figure 5.2). Three permanent objects around the test site are selected as fixed/anchor points. The survey is conducted using a reflector held at each pre-determined location. The data collected on a monthly basis is compared to the baseline reading to determine the vertical displacement of the slope.



Figure 5.2 Total Station

5.1.1 Inclinerometer

Vertical inclinometer casings to monitor the lateral movement of the slope were installed on 1st October 2019. Two inclinometer casings with depths of 30 ft. were installed vertically in the middle of the reinforced section and the control section (Figure 5.3). Two 30 ft. boreholes were drilled using an 8-inch hollow stem auger to insert the inclinometer pipes into the slope (Figure 5.4). Three 10 ft. commercially available inclinometer casings were connected to get a total length of 30 ft. The bottom of the casing was sealed with a bottom cap and inserted into the pre-drilled borehole. The top of the pipe was fixed with bentonite. The top of the inclinometer casing was cut to be about 1 foot from the ground surface as shown in Figure 5.4 (b).

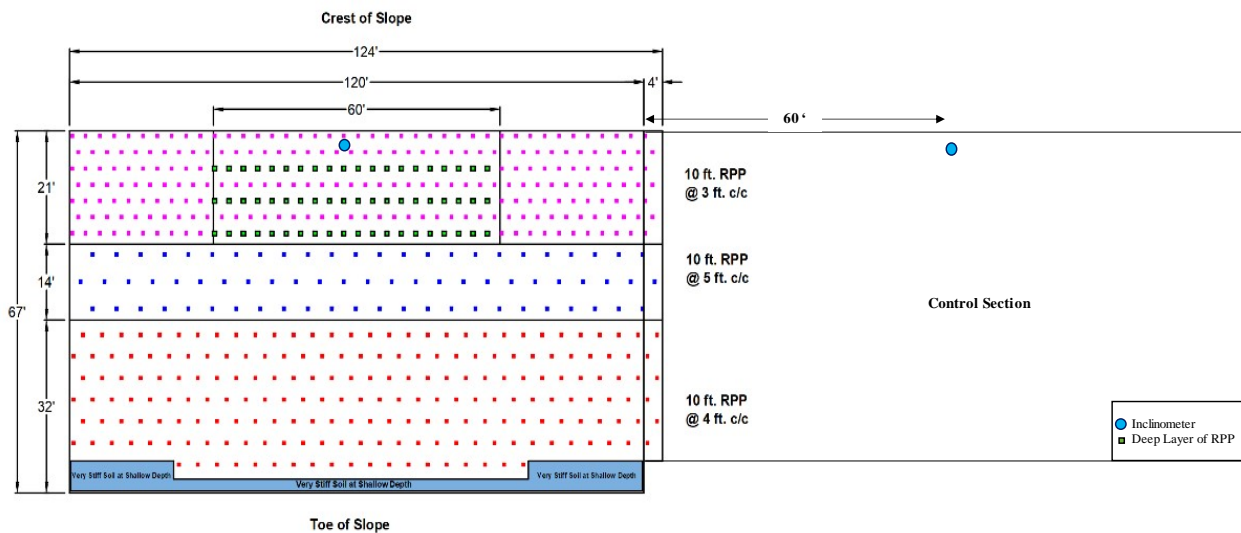


Figure 5.3 Inclinerometer Location



(a)



(b)

Figure 5.4 Inclinometer Casings Installation: a) Drilling and Placing Inclinometer Casing, b) Inclinometer Casing After Installation.

5.1.2 Topographic Survey

Topographic survey was conducted to monitor the vertical movement of the slope after reinforcement. The first survey was conducted in September 2019 after the RPP installation. Topographic survey of 160 points were carried out monthly to monitor the vertical settlement of the slope.

Aligning of survey data was carried out using three points on fixed locations around the survey area. Two fixed points were located at bridge and light pole at the crest of the slope while the third point was located at the traffic signal at the bottom of the slope. Two lines of surveys were done at the crest and the middle of the slope. Eighty (80) points were surveyed on the first line of reinforced section at the crest of the slope with 3 ft. c/c spacing and 80 survey points on the 7th line with 3 ft. c/c spacing as shown in Figure 5.5.

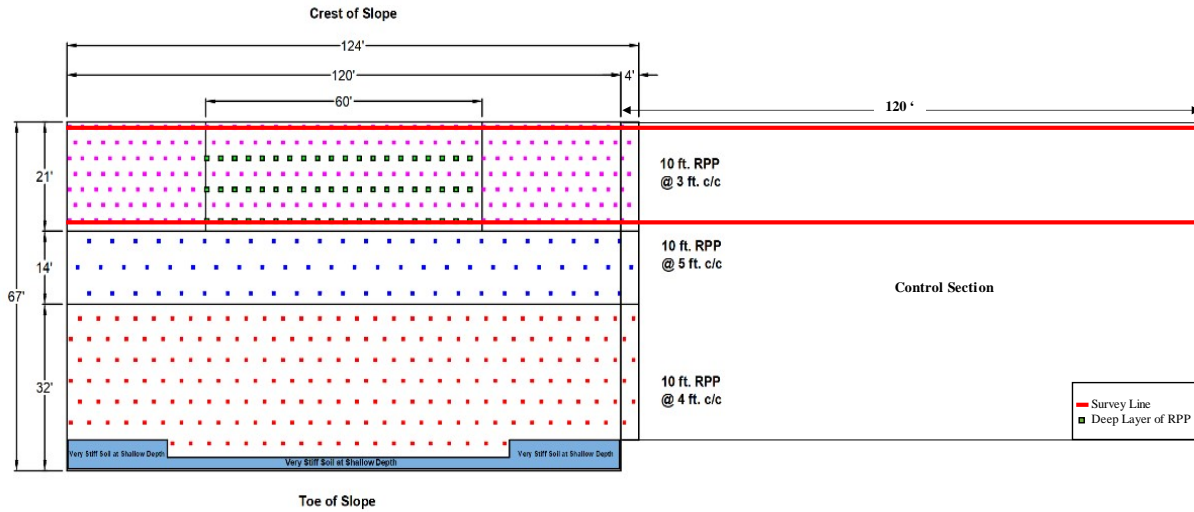


Figure 5.5 Schematic of Topographic Survey Lines.

5.2 Performance Monitoring Results: IH-820 & Rosedale Street.

The study site was monitored monthly. The results of the inclinometer and survey is discussed in the following section.

5.2.1 Inclinometer Monitoring

The variation of lateral movement of the slope was monitored monthly. The variation of lateral displacement of the slope with depth and rainfall is shown in Figure 5.8 and Figure 5.6 for the reinforced and control sections, respectively. The baseline reading was taken on 18th October 2019 after two weeks adjustment period for casing stabilization and monitoring was continued monthly. The maximum displacement for both sections were observed at the crest. The lateral movement variation in the control section is shown in Figure 5.6. Maximum displacement of 1.03 inches was observed in October 2021 with movement up to a depth of 10 feet. The cyclic behavior of the slope was observed in the results where the dips and peaks in movement was observed with the rainfall patterns.

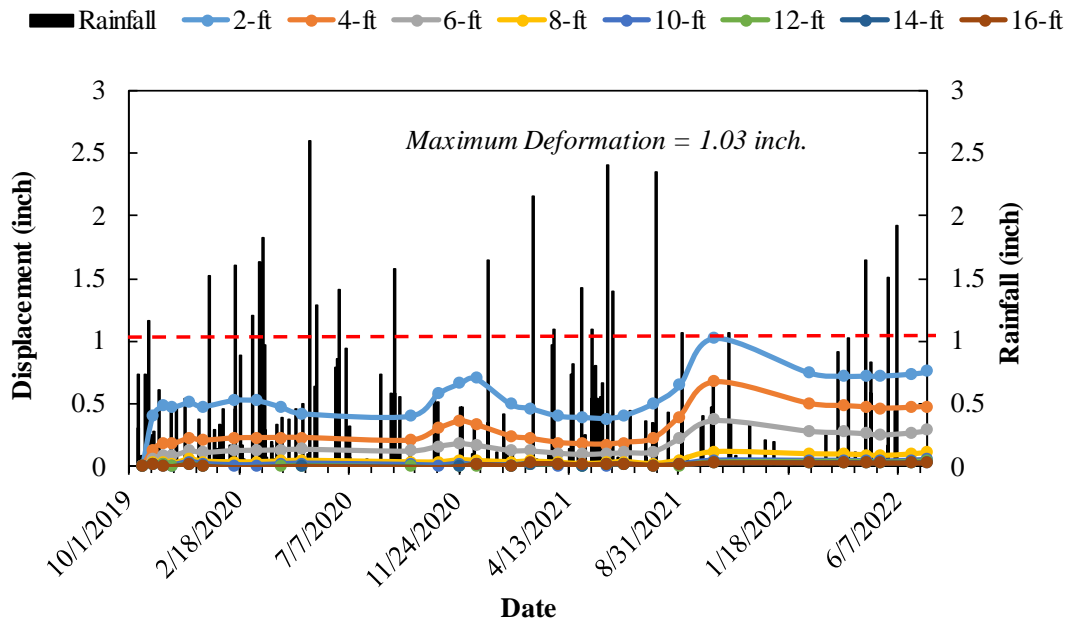


Figure 5.6 Lateral Movement in the Control Section.

The lateral movement variation in the section reinforced with RPP is shown in Figure 5.8. Initial displacement of 0.2 inches was observed after installation. A maximum deformation of 3.29 inches was observed over a monitoring period of 33 months in July 2022. One month after the installation, considerable surface erosion was observed in the reinforced section due to the absence of vegetation and low compaction after installation. According to Kentucky Construction Site manual, erosion is 30% more in compacted and smooth slopes and erodibility is very high in slopes with fine grained soil. Figure 5.7 shows the trenches formed in the reinforced section due to rainfall runoff from the top of the slope. The rill erosion developed into gullies after months of lack of grass cover. The unrepaired shoulder cracks (Figure 5.7 (a)) aided the process and created a drainage channel/gully for the rainwater runoff from the slope over the slope.

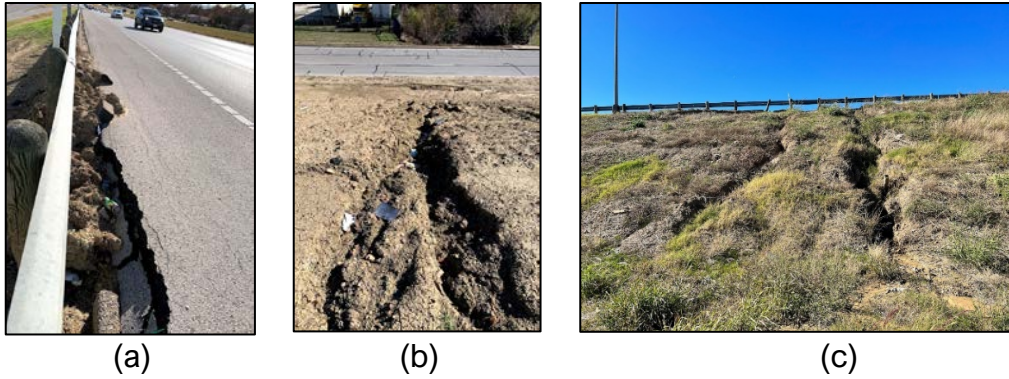


Figure 5.7 Surface Erosion (a) Unrepaired Shoulder Cracks, (b) Surface Erosion, (c) Rill Erosion in the Reinforced Section.

The effect of the formation of the drainage channel and increased infiltration of rainwater into the slope was observed in the inclinometer readings after 20 months. The lag in the effect observed in the results is because the soil strength takes cycles of wet and dry patterns to lose strength and initiate movement. It must be noted that even with the effect of erosion the movement in the reinforced section was limited to the top 6 feet while the control section showed movement depths greater than 10 feet. Therefore, the two layered design is aiding in minimizing movement at deeper depths.

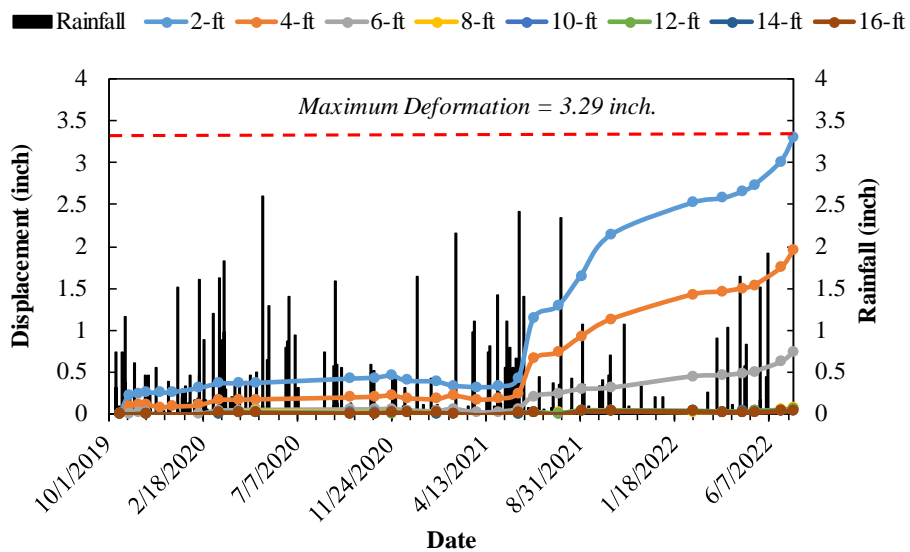


Figure 5.8 Lateral Movement in the Reinforced Section.

The monitoring period prior to the observation of the effect of surface erosion and drainage channel on the results were separated for analysis of the effect of the two layered RPP as a reinforcement method. The movement at the crest of the slope for the reinforced section and the control section was compared (Figure 5.9). The slope is initially stable after installation due to low porewater pressures (Loehr et al., 2014). But with the first rainfall season, pore water pressure increases and the slope initiates movement. The reinforcing members are mobilized against this movement and provide resisting loads until equilibrium of the slope is reached. Additional movement is resisted by the reinforcing members after this point. Further movement would be observed if the pore pressure increases beyond the previously experienced allowing the members to mobilize increased resistance. The initial movement observed after installation in the reinforced section is accounted for the mobilization of the RPP against failure.

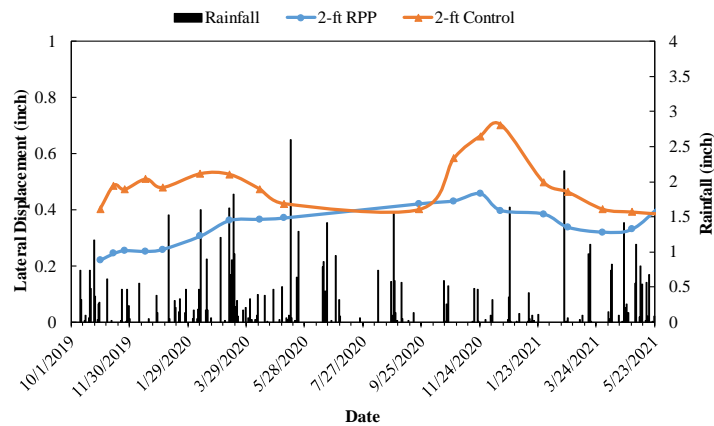


Figure 5.9 Comparison of Lateral Displacement of the Crest in the Reinforced Section and the Control Section.

The comparison of the incremental displacement observed over time at the crest in the reinforced section and the control section is shown in Figure 5.10. The variation in the

control section is significant compared to the reinforced section. The movement of the slope due to the swell and shrink behavior is observed in these results. The soil is observed to swell after periods of rainfall and shrink after periods of reduced rainfall. The low peak observed in January 2021 after a period of low rainfall can be accounted for the movement due to the shrinkage effect of the soil. In comparison, the reinforced section shows minimum variation since the reinforcing members are providing resisting loads against the movements.

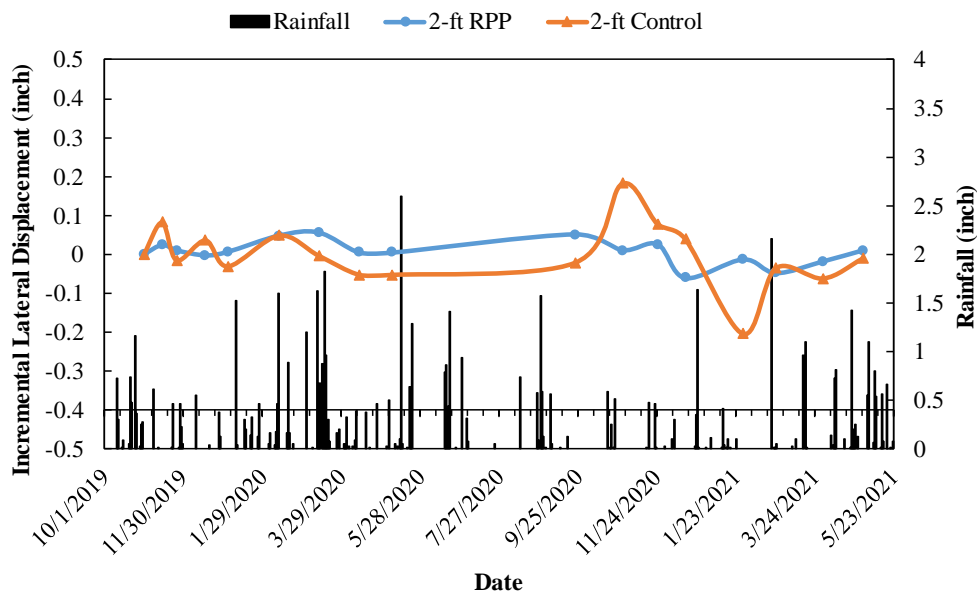


Figure 5.10 Comparison of Incremental Lateral Displacement of the Crest in the Reinforced and Control Section.

The maximum cumulative lateral displacement with depth for a monitoring period of 20 months is shown in Figure 5.11. The movement in the reinforced section is observed to be limited to the top 6 feet while the movement in the control section at deeper depths. The two layered RPP is providing resistance against movement at deeper depths.

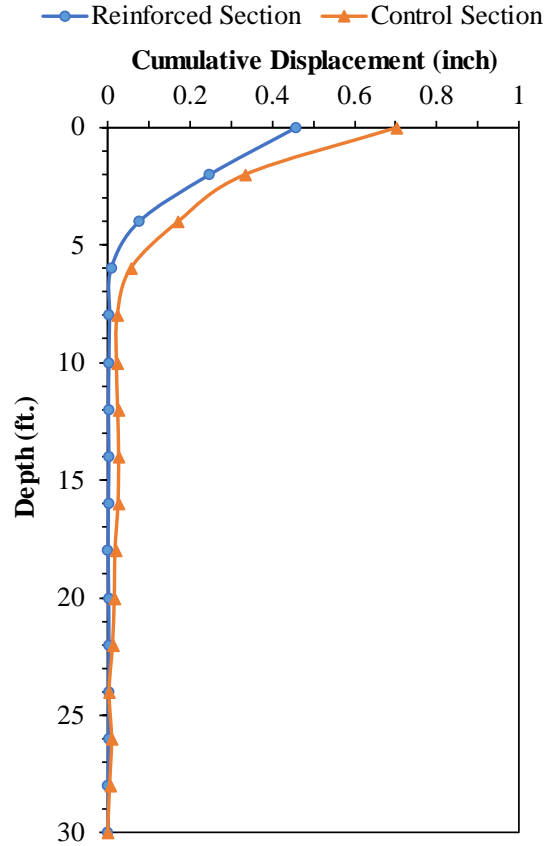


Figure 5.11 Cumulative Lateral Displacement with Depth for Reinforced and Control Sections.

Monitoring period of 20 months indicated a 40% reduction in lateral movement of the slope (Figure 5.12). The reduction in lateral displacement indicate the effectiveness of the use of Recycled Plastic Pins to stabilize deep slope failures.

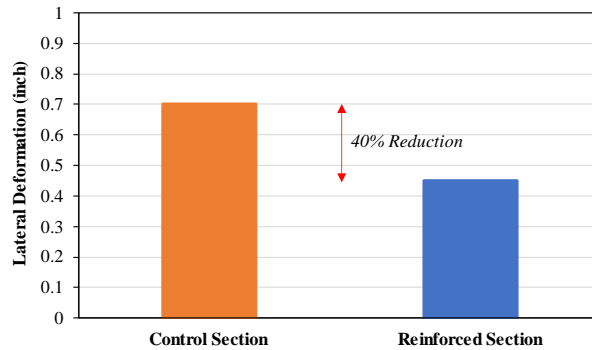


Figure 5.12 Percentage Reduction of Lateral displacement due to the Layered Design.

5.2.2 Topographic Survey Monitoring

Topographic survey was conducted monthly to monitor the vertical movement of the slope. Figure 5.13 and Figure 5.14 show the variation of vertical displacement with distance along the slope for the two survey lines. The maximum vertical settlement in the reinforced section was observed to be 2.46 inches and 2.66 inches in the crest and middle of the slope, respectively. The control section has a maximum settlement of 0.60 inches and 0.74 inches in the crest and middle of the slope, respectively.

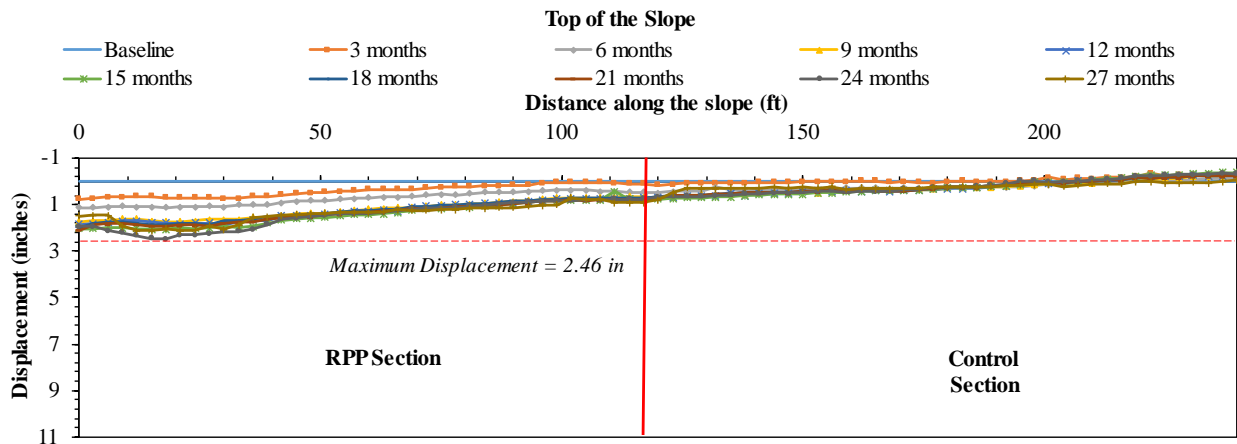


Figure 5.13 Vertical Displacement on the Crest of the Slope.

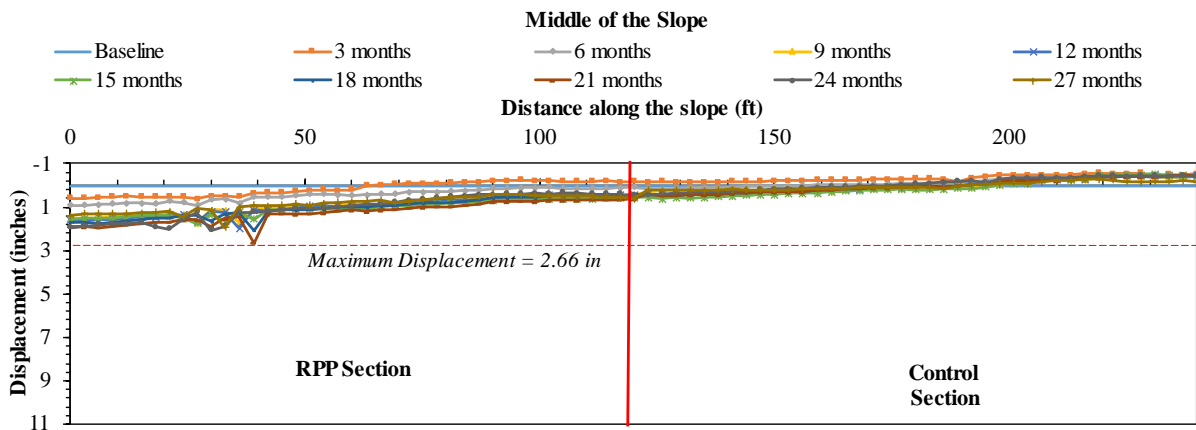


Figure 5.14 Vertical Displacement in the Middle of the Slope.

The increased settlement observed in the reinforced section can be accounted to the surface erosion. The control section had constant grass coverage over the monitoring

period which reduces the surface erosion resulting in decreased vertical ground settlement. In comparison the reinforced section has negligible grass cover for over a year after the installation (Figure 5.16).



Figure 5.15 Surface Erosion in December 2021 exposing the RPP at the Crest.



Figure 5.16 Grass Cover in the Reinforced Section and Control Section in November 2021.

In December 2021, the trenches were backfilled and the compacted to prevent further soil erosion. Figure 5.17 shows the backfilling process by TxDOT. Biodegradable erosion was placed as an erosion control method as shown in Figure 5.18.



Figure 5.17 Backfill of Slope.



Figure 5.18 Biodegradable erosion control

5.3 Instrumentation in U.S 67: Alvarado

The performance of the reinforced section was monitored monthly using vertical inclinometers and topographic survey. The details of the instrumentation and performance monitoring is presented below.

5.3.1 Inclinometer

Vertical inclinometer casings to monitor the lateral movement of the slope were installed in September 2021. Two inclinometer casings with depths of 30 ft. were installed vertically in the middle of the reinforced section and in the control section (Figure 5.19). Two 30 ft. boreholes were drilled using an 8-inch hollow stem auger to insert the inclinometer pipes into the slope. Three 10 ft. commercially available inclinometer casings were connected to get a total length of 30 ft (Figure 5.20 (a)). The bottom of the casing was sealed with a bottom cap and inserted into the pre-drilled borehole (Figure 5.20 (b)). The top of the pipe was fixed with bentonite (Figure 5.20 (c)).

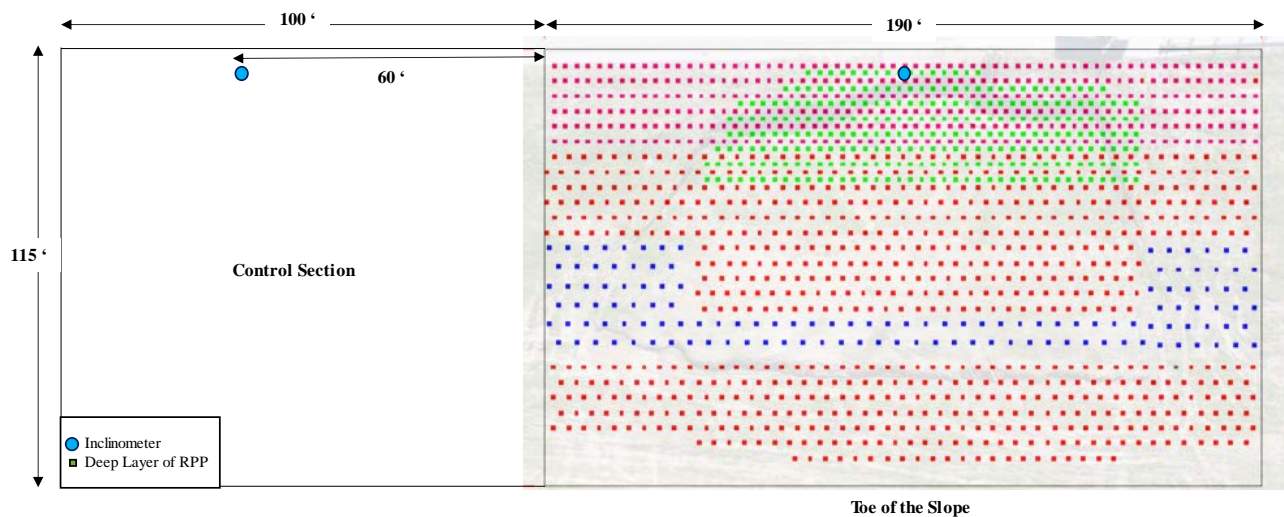
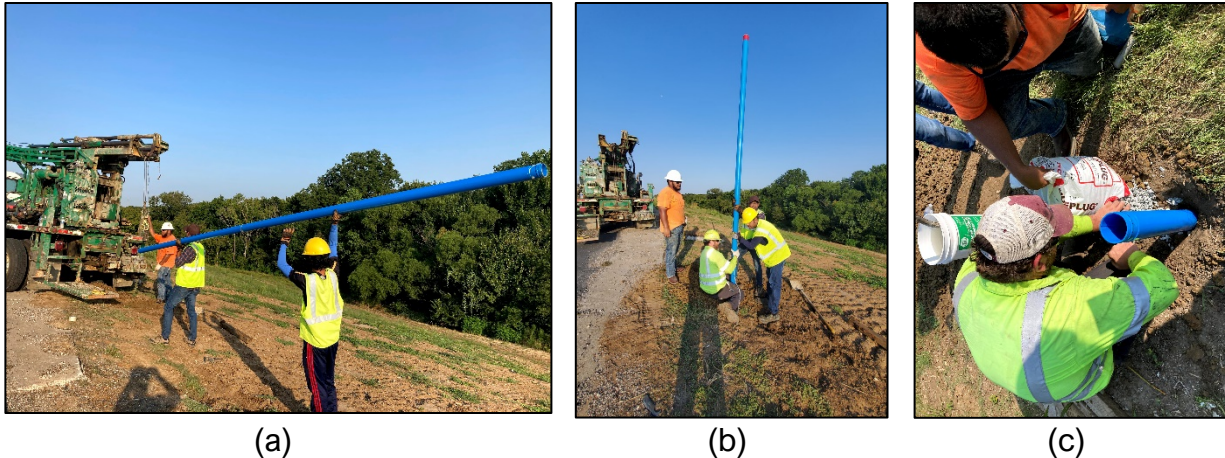


Figure 5.19 Inclinometer Location



(a) (b) (c)
Figure 5.20 Inclinometer Installation at U.S 67- Alvarado (a) Connected Inclinometer casings (b) Inserting the casing into the borehole (c) Fixing the top with bentonite.

5.3.2 Topographic Survey

Topographic survey was conducted to monitor the vertical movement of the slope after reinforcement. The first survey was conducted in August 2021 after the RPP installation. Topographic survey of 120 points were carried out monthly to monitor the vertical settlement of the slope.

Aligning of survey data was carried out using three points on fixed locations around the survey area. Two lines of surveys were done at the crest and the middle of the slope. Sixty (60) points were surveyed on the first line of reinforced section at the crest of the slope with 5 ft. c/c spacing and 60 survey points on the 13th line with 5 ft. c/c spacing as shown in Figure 5.21.

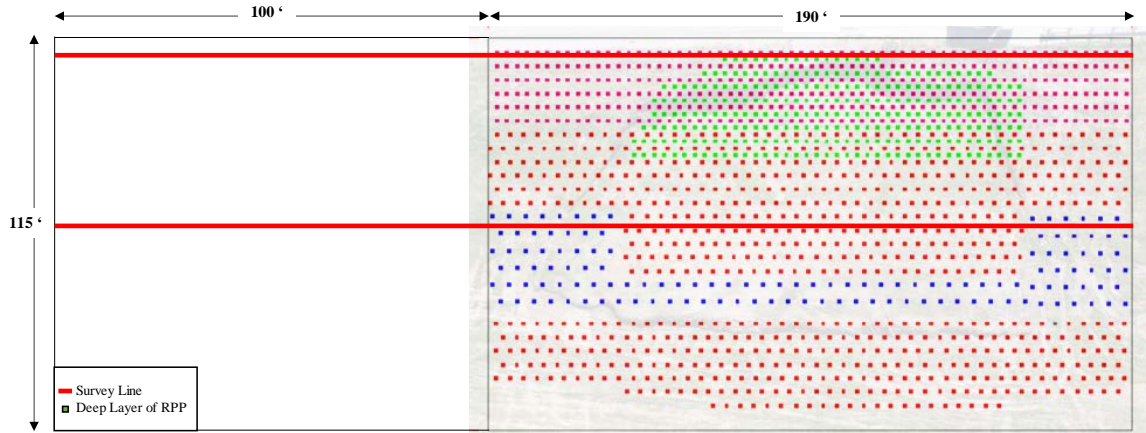


Figure 5.21 Survey Line Location

5.3.3 Piezometer

Standard piezometers (Model 4500) are used to measure ground water elevations and pore pressures. The piezometers are directly buried within the slope to measure the fluctuation of water levels within the slope. One piezometer was installed in the reinforced section at a depth of 30 feet (Figure 5.22 (b)). This site was selected to be installed with a piezometer due to the observation of extremely soft soil and surface seepage.

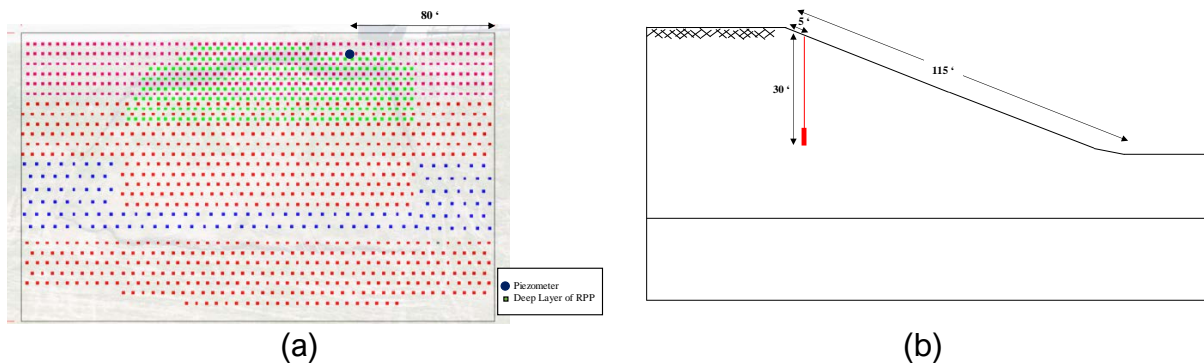


Figure 5.22 (a) Piezometer Location, (b) Cross sectional view of piezometer location

A 30 feet borehole was drilled using an 8-inch hollow stem auger. Sand was poured to the bottom of the borehole to make a pad to embed the piezometer. The piezometer was calibrated with water and inserted into the hole using a long rod. The borehole was

backfilled with sand to surround the apparatus and filled with soil cuttings to surface level. The piezometer was connected to a data logger which records data at 6-hour intervals.

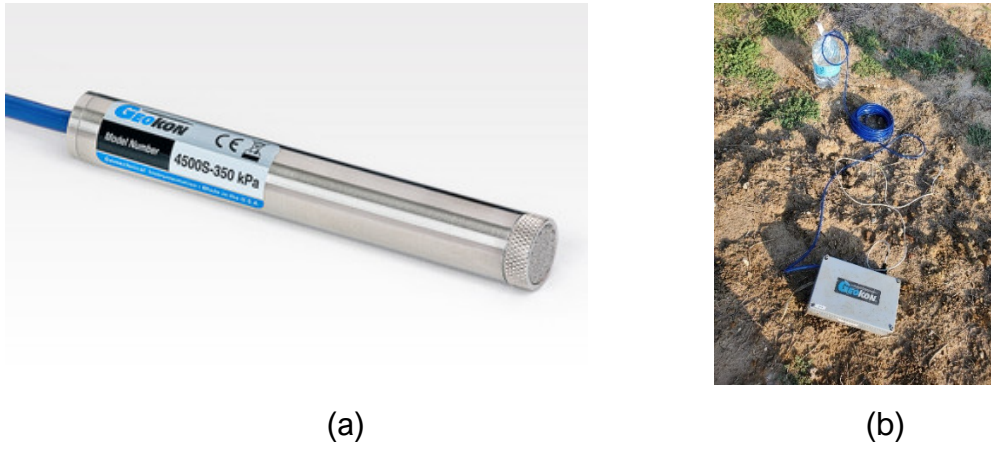


Figure 5.23 (a) Standard Piezometer (Model 4500) (b) Installation of Piezometer and Data Logger.

5.4 Performance Monitoring Results: U.S 67: Alvarado

The study site was monitored monthly. The results of the inclinometer and survey is discussed in the following section.

5.4.1 Inclinometer Monitoring

The variation of lateral displacement of the slope with depth is shown in Figure 5.24 and Figure 5.25 for the reinforced and control sections, respectively. The baseline reading was taken on September 2021 after two weeks adjustment period for casing stabilization and monitoring was continued monthly. The maximum displacement for both sections were observed at the crest. The lateral movement variation in the section reinforced with RPP is shown in Figure 5.24. The displacement of 0.61 inches was observed in August 2022.

The slope is initially stable after installation due to low porewater pressures (Loehr et al., 2014). But with the first rainfall season, pore water pressure increases and the slope

initiates movement. The reinforcing members are mobilized against this movement and provide resisting loads until equilibrium of the slope is reached. Additional movement is resisted by the reinforcing members after this point. Further movement would be observed if the pore pressure increases beyond the previously experienced allowing the members to mobilize increased resistance. The initial higher movement observed after installation in the reinforced section is accounted for the mobilization of the RPP against failure.

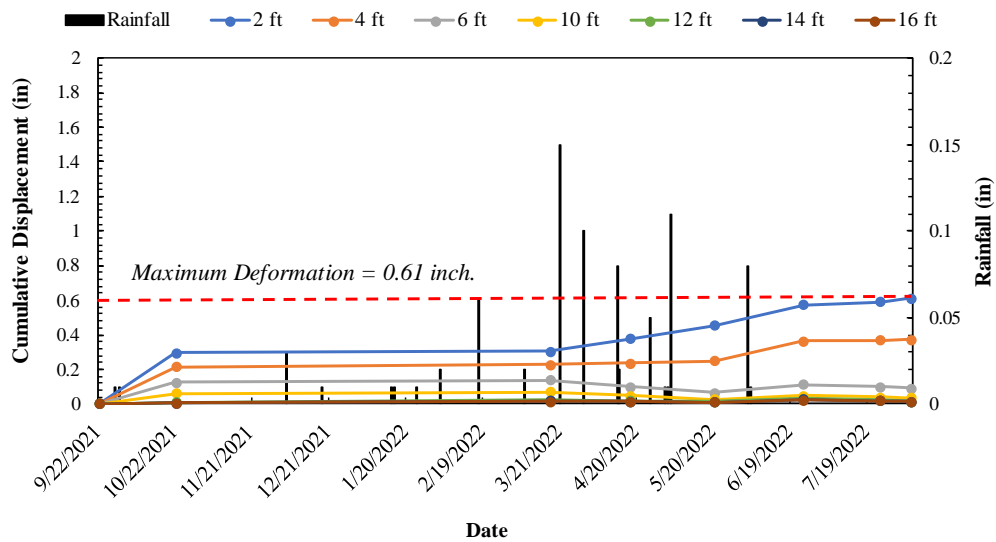


Figure 5.24 Variation of Lateral Displacement with Rainfall in the Reinforced Section. The lateral movement variation in the control section is show in Figure 5.25. Maximum displacement of 1.00 inches was observed in August 2022 with movement up to a depth of 10 feet. The period between October 2021 and March 2022 was not monitored due the inclinometer being repaired.

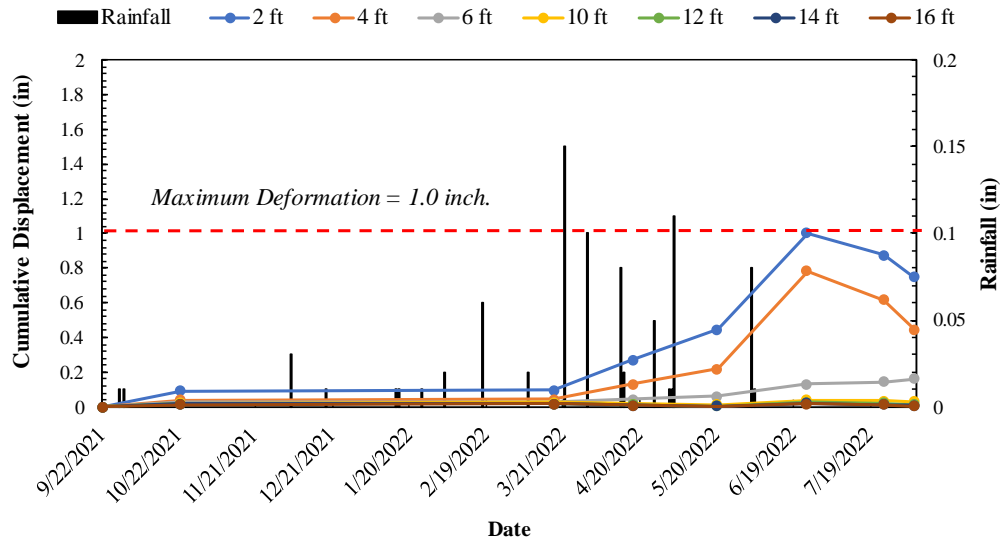


Figure 5.25 Variation of Lateral Displacement with Rainfall in the Control Section.

The maximum cumulative lateral displacement with depth for a monitoring period of 6 months is shown in Figure 5.26. The movement in the reinforced section is observed to be limited to the top 6 feet while the movement in the control section is observed up to a depth of 10 feet. The two layered RPP is providing resistance against movement at deeper depths.

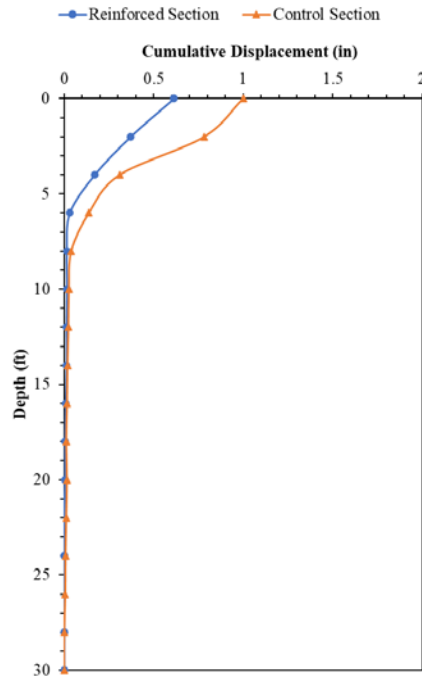


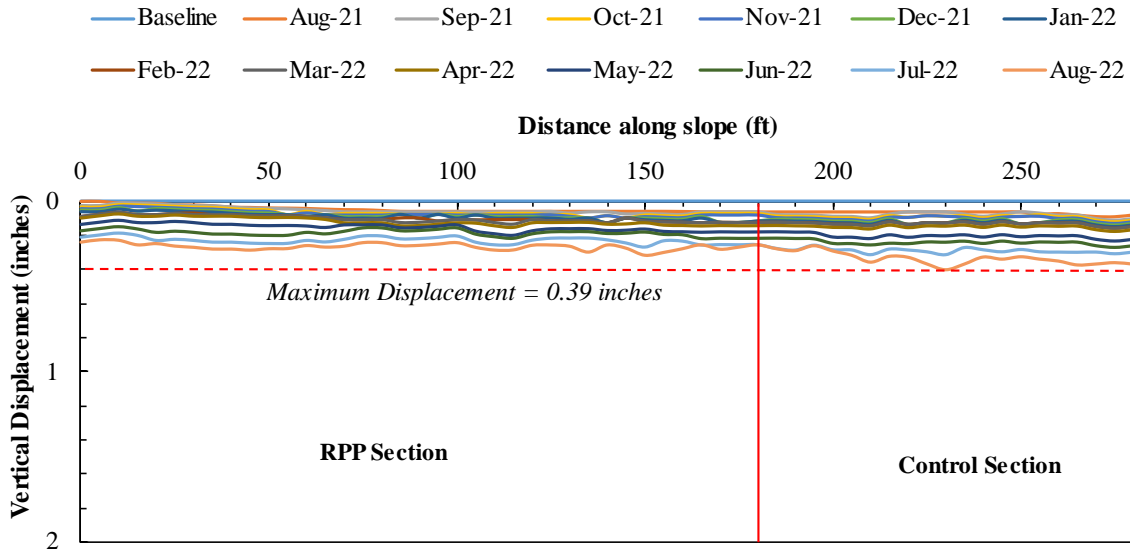
Figure 5.26 Cumulative Lateral Displacement with Depth for Reinforced and Control Sections.

5.4.2 Topographic Survey Monitoring

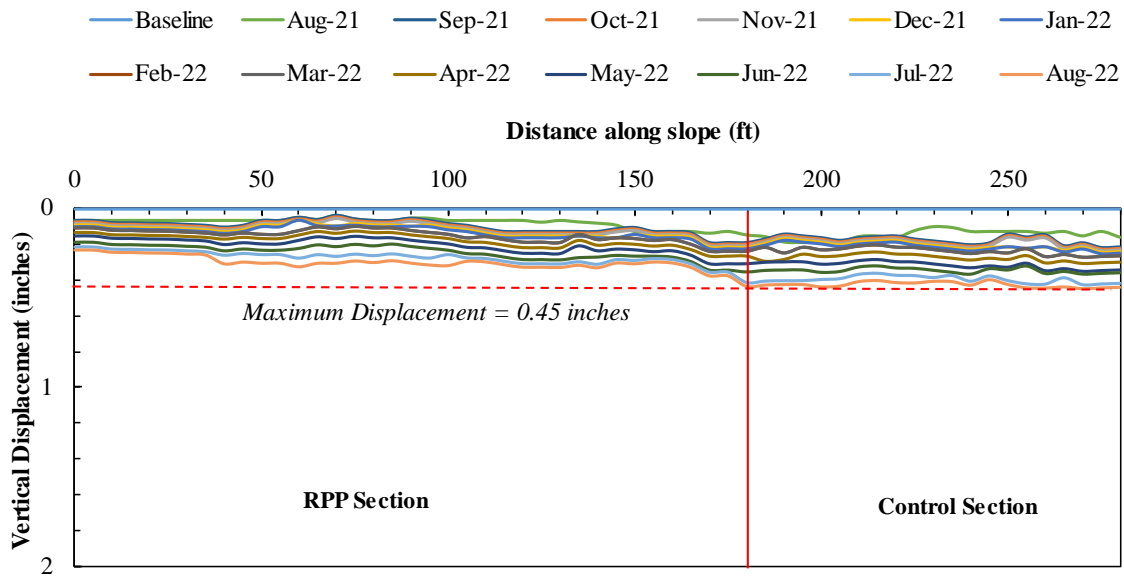
Topographic survey of 160 points is carried out monthly to monitor the vertical settlement of the slope. Two lines of survey are done at the crest and the middle of the slope (Figure 5.21). The variation of vertical displacement of the crest along the slope is shown in Figure 5.27 (a). A settlement of 0.39 inches was observed in the control section while the reinforced section showed a vertical settlement of 0.28 inches.

Figure 5.27 (b) shows the variation of vertical displacement of the middle of the slope. A maximum settlement of 0.45 inches was observed in the control section while the reinforced section showed less amount of settlement. The settlement in the middle of the slope was higher compared to the crest. This is expected since saturated soil was observed in the middle of the slope. The vertical settlement in the reinforced section for

both the top and middle section is observed to be less than the control section. Therefore, it can be observed that the reinforcement is aiding in stabilizing the slope.



(a)



(b)

Figure 5.27 Variation in Vertical Displacement at the (a) Crest & (b) Middle of the Slope

5.4.3 Piezometer Monitoring

Fluctuation of average daily pore water pressure with rainfall is represented in Figure 5.28. Average pore water pressure is observed to increase with rainfall events. The maximum pressure over the monitoring period of 9 months is 530 psf with water levels fluctuating between 22 to 26 feet below ground surface. This depth corresponds the middle of the slope. The saturated soil observed in the middle of the slope can be accounted for the fluctuating moisture detected by the piezometer. The increased vertical deformation in the middle of the slope can be related to the presence of high moisture and fluctuating pore pressures in this region.

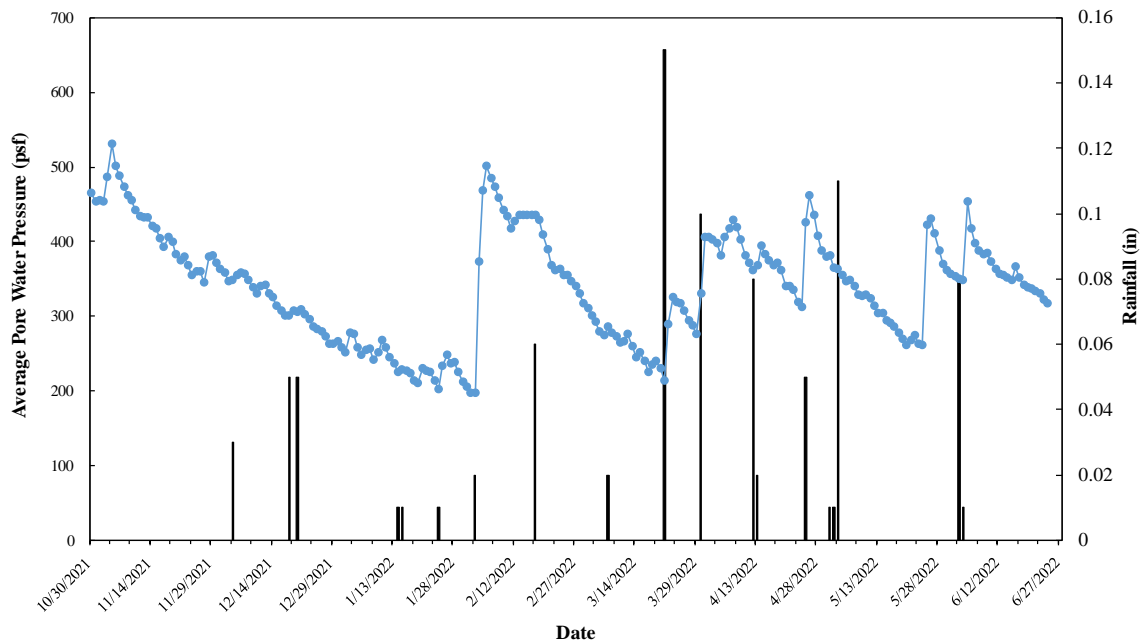


Figure 5.28 Variation of Average Pore Water Pressure with Rainfall.

Temperature variations recorded by the temperature sensor in the piezometer and the daily average temperature obtained using NOAA (National Oceanic and Atmospheric

Administration) with rainfall is shown in Figure 5.29. The ground temperature and the atmospheric temperature is showing close correlation.

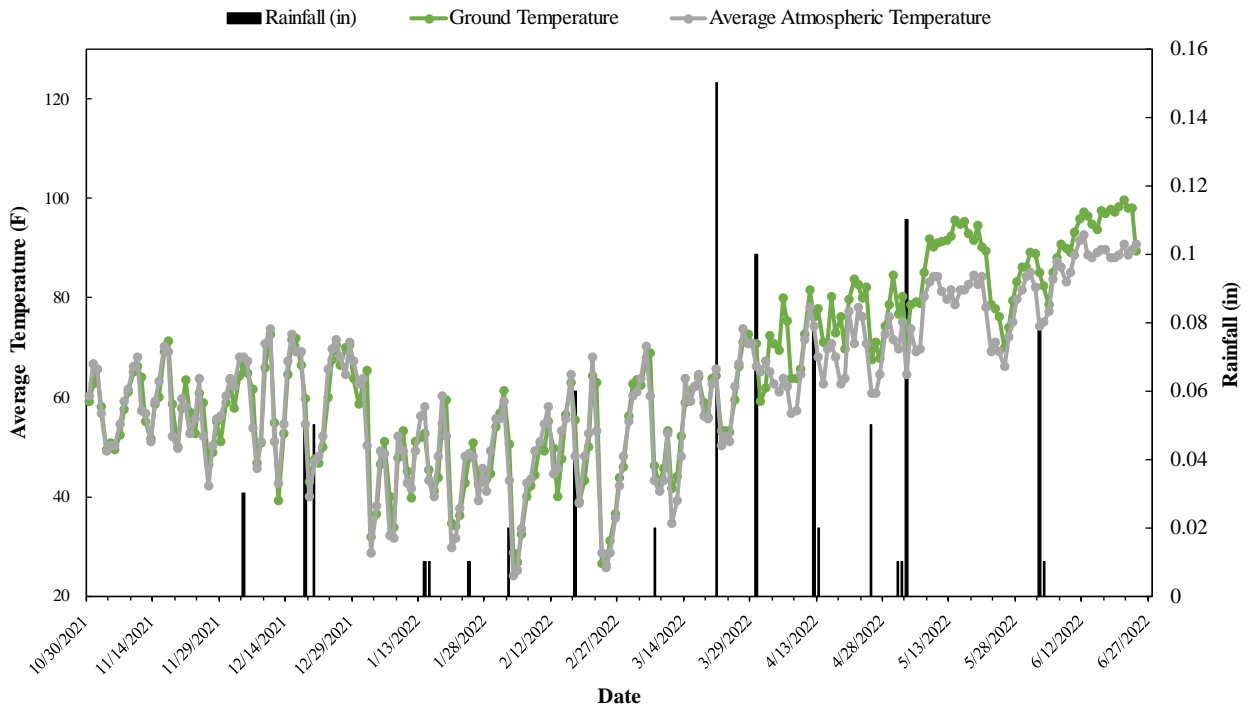


Figure 5.29 Variation of Average Ground and Atmospheric Temperature.

The variation of average pore water pressure in the slope with the ground temperature is shown in Figure 5.30. It is observed that the pore water pressure decreases with the increase of temperature. Both the temperature and rainfall are affecting the fluctuation of porewater pressure in the slope. The temperature drops and rainfall events occur, the porewater pressure increases due to less evaporation, more infiltration and increased retention in the soil.

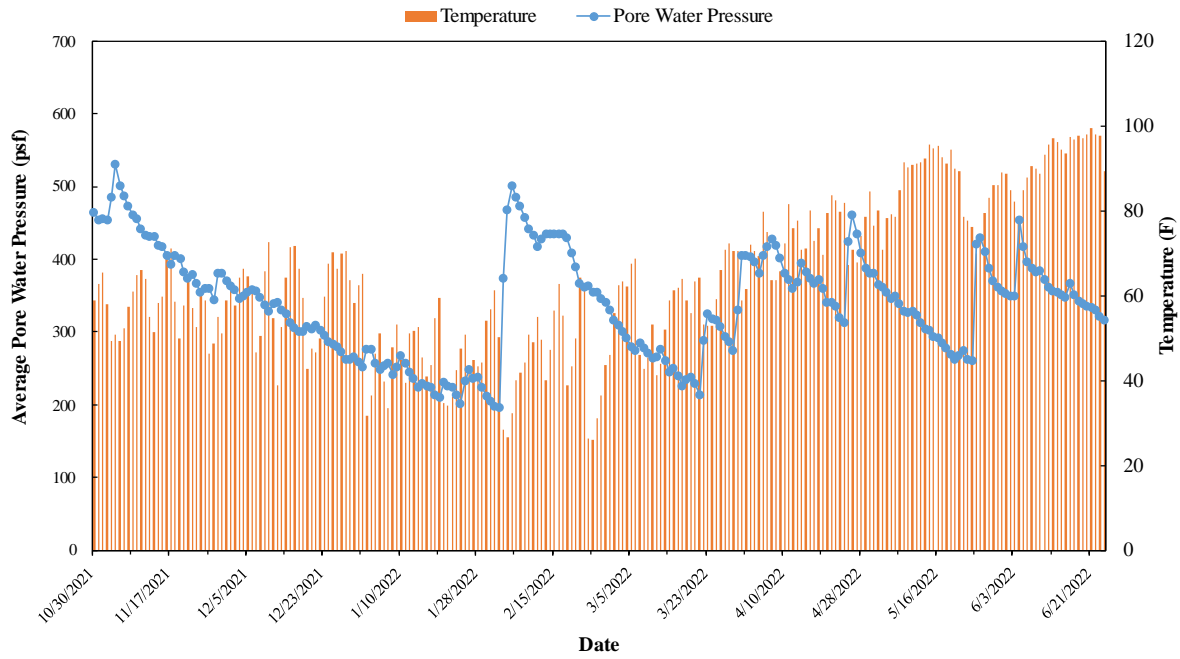


Figure 5.30 Variation of Pore Water Pressure with Ground Temperature.

5.5 Summary

Test sites at IH-820 & Rosedale Street and U.S 67- Alvarado was instrumented and monitored to evaluate the effect of the reinforcement on lateral and vertical deformations of the slope.

- IH-820 and Rosedale Street:
 - The maximum lateral deformation was observed at the crest with 1.03 inches observed in the control section and 3.29 inches observed in the reinforced section.
 - The increased movement in the reinforced section was due to increased erosion and creation of a drainage channel across the slope due to broken shoulder at the crest.
 - The lateral deformation before the effect of erosion was analyzed. The deformation in the reinforced section was observed to be limited to the top 6 feet with a maximum deformation of 0.45 inches. In comparison the control section experienced a maximum deformation of 0.7 inches. The movement was also observed up to a depth of 10 ft.
 - Increased vertical deformation was observed in the reinforced section due to severe erosion.
- U.S 67 Alvarado:
 - The maximum lateral deformation was observed at the crest. Maximum deformation of 0.61 inch and 1.0 inch was observed in reinforced section and control section respectively.

- Lateral deformation was limited to the top 6 feet in the reinforced section while movement up to a depth of 10 feet was observed in the control section.
- Higher vertical deformation was observed in the middle of the slope compared to the crest of the slope. This observation was validated by the presence of saturated soil in the middle of the slope.
- Vertical deformation less than 0.2 inches were observed in the reinforced section while the control section showed higher deformation.
- Results of the piezometer showed that the moisture fluctuates between 22-26 feet below ground surface which corresponds to the middle of the soil.
The soft soil observed at site was validated.
- The limitation of lateral deformation to the top 6 feet shows that the two layered design is reducing the deformation at deeper depths.

CHAPTER 6

NUMERICAL STUDY

6.1 Introduction

The objective of the current study is to determine the effect of the use of a two layered layout for the stabilization of deep slope failures with Recycled Plastic Pins. Field study was conducted in two highway embankments to explore this objective. The performance monitoring conducted throughout the study period of three years concluded that the two layered layout is providing sufficient reinforcement against deeper failures.

The field study was conducted with an overlap depth of 5 feet and spacing of 6 feet and 3 feet at grade. The numerical study was conducted to analyze in-depth the field performance in addition to the effect of varying overlap depths, the number of lines utilized on factor of safety and deformation. The details of the FEM analysis are presented in this chapter.

6.2 IH-820 & Rosedale Street

6.2.1 Model Calibration

Finite Element method is a very powerful computational tool in engineering used to study the stability of slopes using a failure definition similar to the traditional limit equilibrium method (Alkasawne et al., 2008). Strength reduction method associated with finite element modeling was used in this study using PLAXIS 2D. The factor of safety calculated using the shear strength reduction method divide the original shear strength parameters by the reduced shear strength parameters to bring the slope to failure (Griffiths & Lane 1999). Mohr Coulomb failure criterion was also used where the soil model is considered

to be linearly elastic perfectly plastic soil model (Alkasawne et al., 2008). The FEM analysis was done using triangular elements with 15 nodes. Rawat and Gupta (2016) stated that when reinforcements are incorporated in analysis, 15-noded elements give more accurate and reliable results compared to six-noded elements.

The analysis was carried out considering the initiation of slope failure at a limiting factor of safety at 1. It is common practice to assume the depth of wetting as 7 to 10 feet (Nelson et al., 2001) and consideration of a deeper wetting zone with residual strength in the top 10 m was suggested for deeper slope failures to account for the infiltration of water through cracks and fissures (Hughes et al., 2009). In this study, the top 8 ft at the crest (Soil 1) with decreasing depth of zone (Soil 2) was considered as the failure zone with residual strength (Figure 6.1). The soil parameters for the remaining layers were obtained using the soil test results done during site investigation. The soil profile is shown below (Figure 6.1). Several iterations were carried out during the analysis to calibrate the soil model to represent failure as observed at site. The model was stimulated to represent the 5 ft crest drop and bulging initiating from the middle of the slope as observed at field after failure (Figure 6.2 (a)). The soil parameters that yielded a factor of safety of 1.00 is shown in Table 6.1.

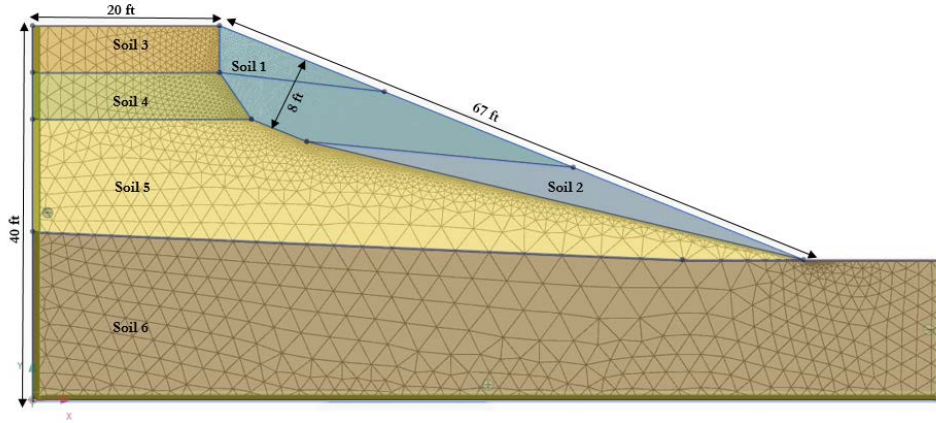


Figure 6.1 Soil Profile

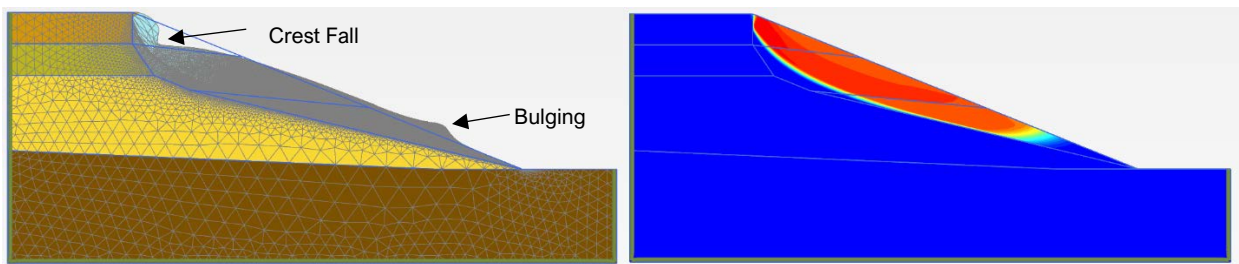


Figure 6.2 (a) Deformed Mesh Showing Crest Fall and Bulging, (b) Slip Circle: FS=1.00

Table 6.1 Parameters for FE Analysis

Layer	Unit Weight (pcf)	Elastic Modulus E (psf)	Poisson Ratio ν	Cohesion c (psf)	Phi ($^{\circ}$)
1	120	9000	0.39	60	12
2	120	11E3	0.35	70	13
3	125	38E3	0.30	250	14
4	130	82E3	0.30	550	18
5	120	39E3	0.32	260	15
6	130	110E3	0.2	700	20

Table 6.2 RPP Properties used in Numerical Model

Axial Stiffness, EA	3,200,000 lbf/ft
Flexural Rigidity, EI	29,630 lbf ft ² /ft
Specific Weight, w	1.85 lbf/ft/ft
Poisson's Ratio, ν (nu)	0.3

6.2.2 Performance Evaluation of Reinforced Section

Soil parameters calibrated from the control section was utilized in the in the reinforced section to analyze the performance of the Recycled Plastic Pins (RPP). The Recycled Plastic Pins (RPP) were modeled as plates with the properties shown in Table 6.2. Based on the deformation analysis, the maximum vertical and lateral deformation 2.40 inches and 3.11 inches was observed in the model (Figure 6.3).

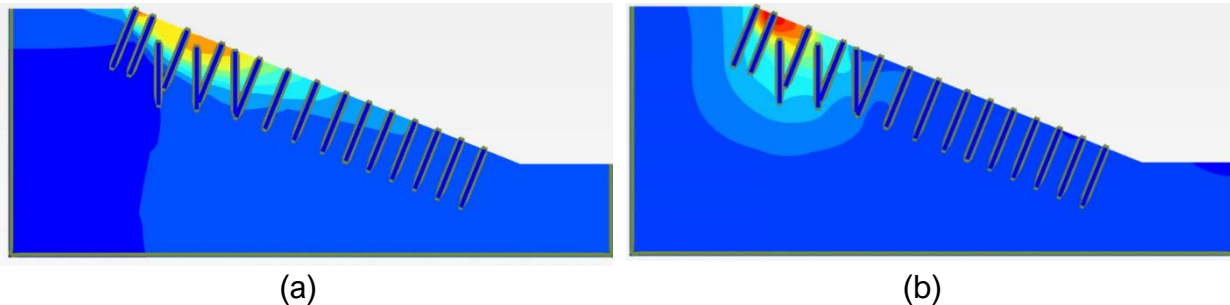


Figure 6.3 : Deformation Analysis in Reinforced Section; (a) Maximum Lateral Deformation = 2.40 inches, (b) Maximum Vertical Deformation = 3.11 inches.

Figure 6.4 shows the comparison of lateral deformation from the field and model data. The trend of deformation with depth is comparable. The model showed higher deformation than the field observations. This result is expected since the soil parameters used for the model are at residual strength while the soil at field is not. Therefore, higher deformation is expected in the model. Similar trend indicates that the model is behaving similar to the field.

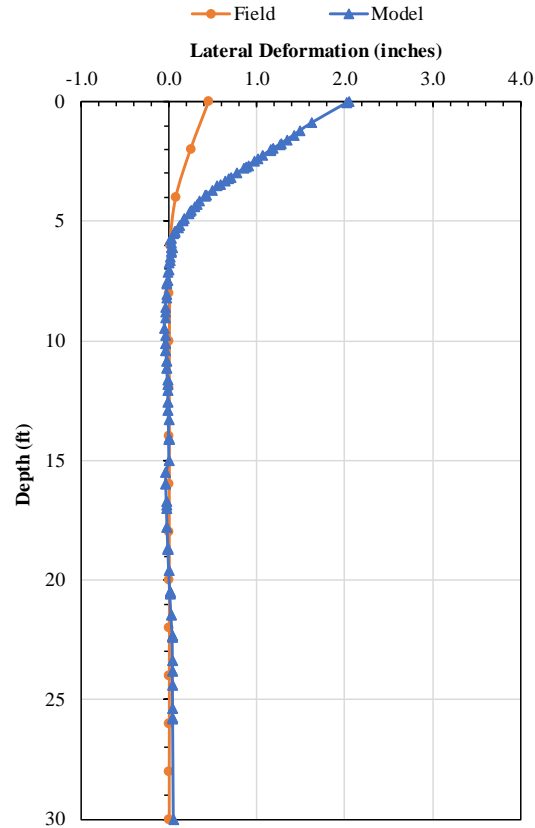
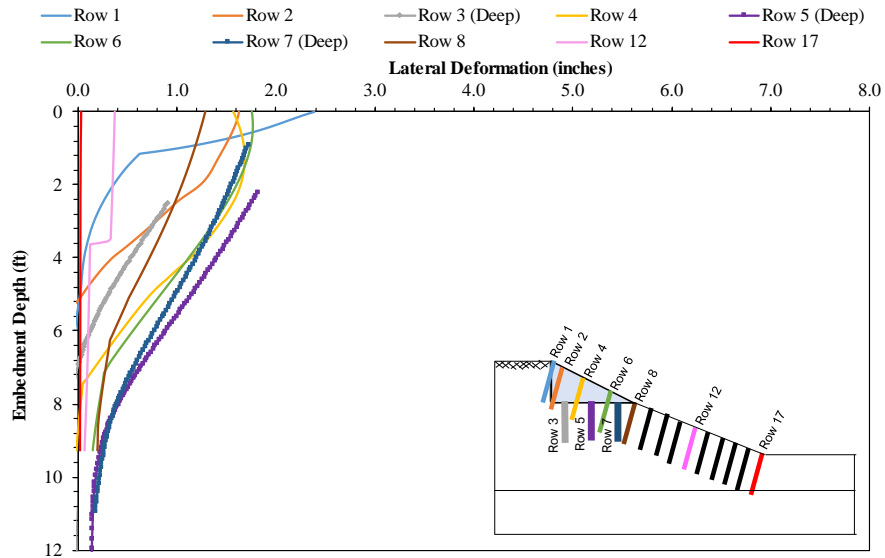
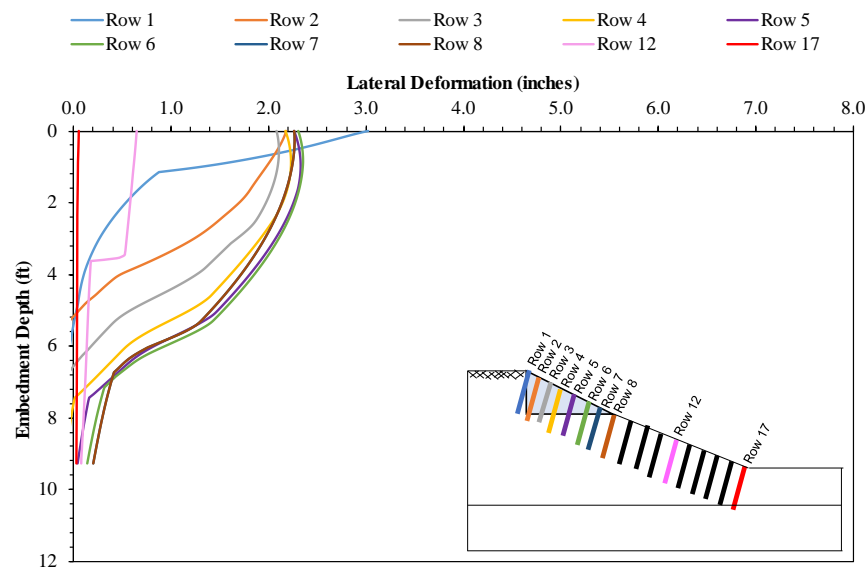


Figure 6.4 Comparison of Lateral Deformation between the Field and Model.

The calibrated model was also incorporated to build a model with the conventional layout (all pins flush to the ground) of RPP for comparison. The lateral deformation of RPP rows for the two-layer layout and conventional layout is shown in Figure 6.5 (a) and (b) respectively. The maximum deformation of the RPP beyond second row observed in the layered layout is 1.86 inches while the normal layout shows a maximum deformation of 2.26 inches. Both layouts show similar trend in deformation with the layered section reducing the deformation by approximately 15%.



(a)

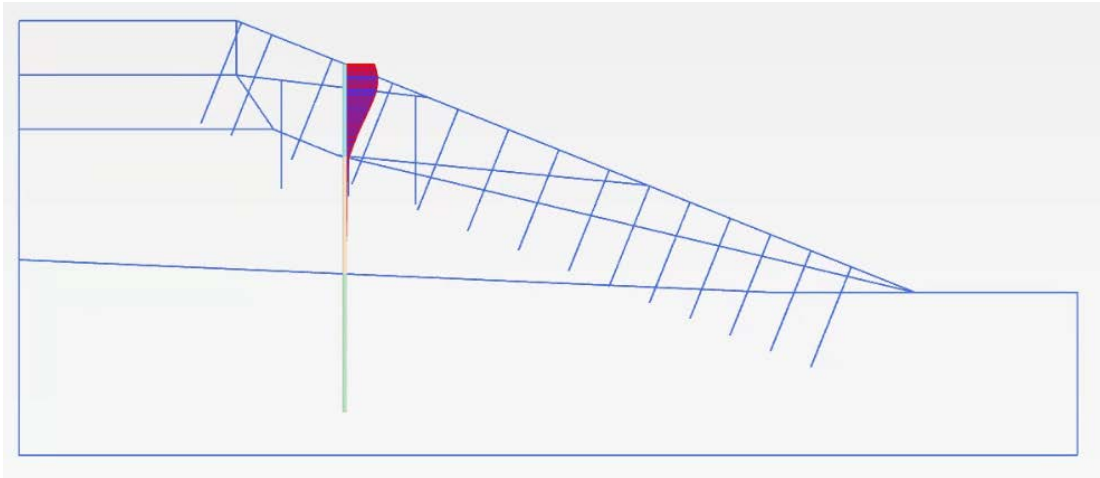


(b)

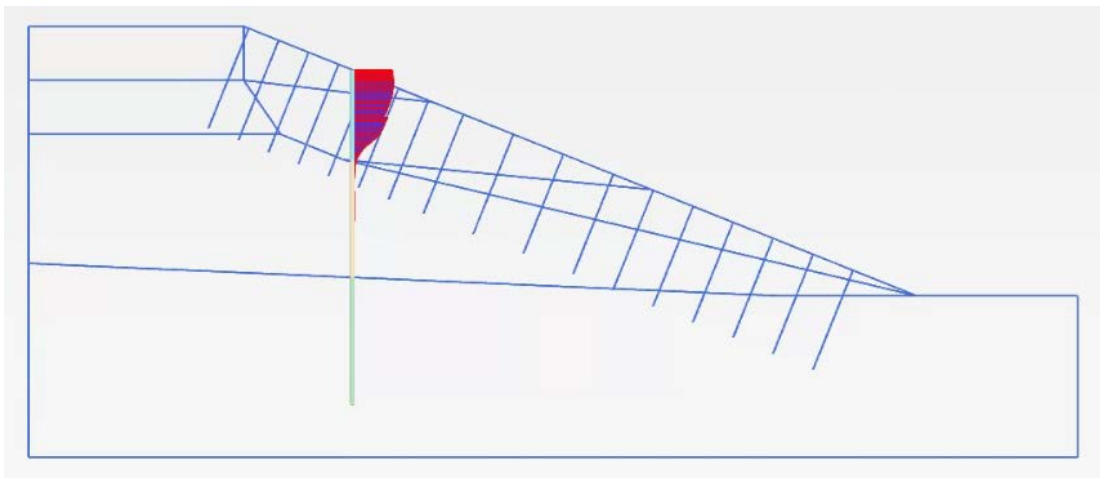
Figure 6.5 : Variation of Lateral Deformation of RPP with Depth; (a) Layered Layout, (b) Normal Layout

The section of slope with the overlap depth was considered to evaluate the effect of the two layered design. Figure 6.6 shows the lateral deformation of the slope between row 4 and 5 and Figure 6.7 shows the percentage reduction in the two sections. Similar to the

deformation in RPP, deformation of the slope in both sections showed similar trend. Lower deformation at certain depths were observed in the two layered layout indicating that the overlap is affecting the deformation.



(a)



(b)

Figure 6.6 (a) Lateral Deformation in Two Layer Layout (b) Lateral Deformation in Normal Layout

The reduction in deformation up to 45% was observed near the slip surface depth for the layered model. The two layered RPP extending deeper into the slope is reducing the slope movements at the slip surface by providing higher anchorage. In comparison, the conventional layout of RPP which extends only up to a depth of 10 feet isn't providing

sufficient resistance to minimize lateral deformation. Therefore, the two layered design is reducing lateral deformation.

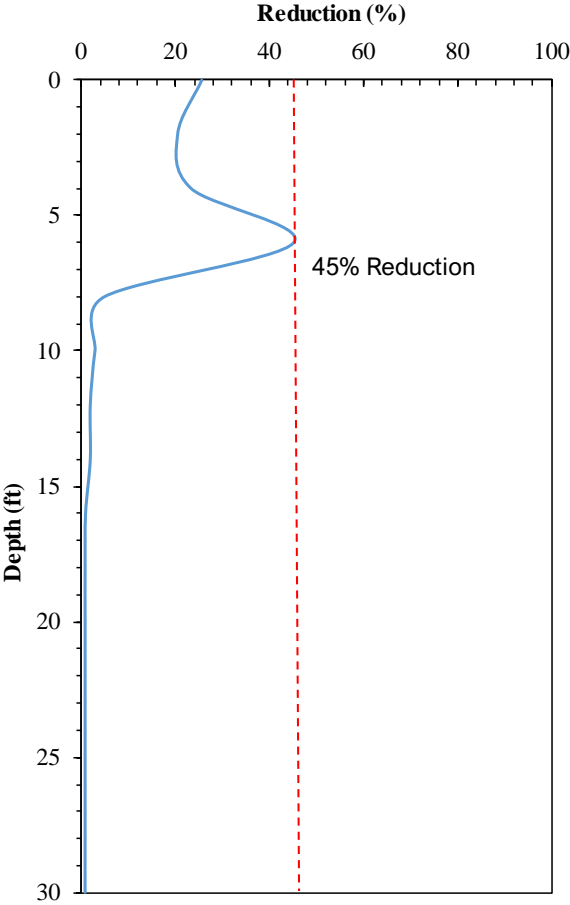


Figure 6.7 Lateral Deformation Reduction due to Two Layers with Depth

6.2.2.1 Flexural Strength of RPP

A study conducted by Bowders et al., (2003) evaluated the engineering properties of RPP and showed that the flexural strength of RPP ranged between 1.5-1.7ksi. Khan et al., 2013 showed that the ultimate flexural strength ranged between 3.1 and 4.7ksi for different loading rates. The allowable flexural strength for the RPP for this study was obtained using the technical data provided the plastic lumber manufacture- Bedford. The flexural strength was given as 1.4ksi. This result is comparable with Bowders et al., 2003 and

allowable flexural strength obtained by Khan et al. 2013. The relationship between Flexural Strength and Maximum Moment Capacity is given below:

$$\sigma_b = \frac{M_b \times y}{I}$$

M_b = Maximum Bending Moment Capacity

y = Vertical distance from the bending axis at the middle (centroid) of the cross section

I = Moment of Inertia $((1/12) \times b \times d^3)$ (b = width, d = height)

The maximum bending moment was calculated as 806 lb-ft. The bending moment of RPP of Rows 1 through 8 is shown in Figure 6.8. The maximum bending moment is observed in observed in the rows of RPP that extend deeper into the slope. The maximum bending moment of 235 lb-ft is experienced by the 5th row that extends deeper into the slope. The failure plane intersects at a depth of 6.5 feet. The other rows of RPP experience less than 30 lb-ft of maximum bending moment. This shows that the deeper RPP are providing additional reinforcement against failure and thereby reducing the deformation.

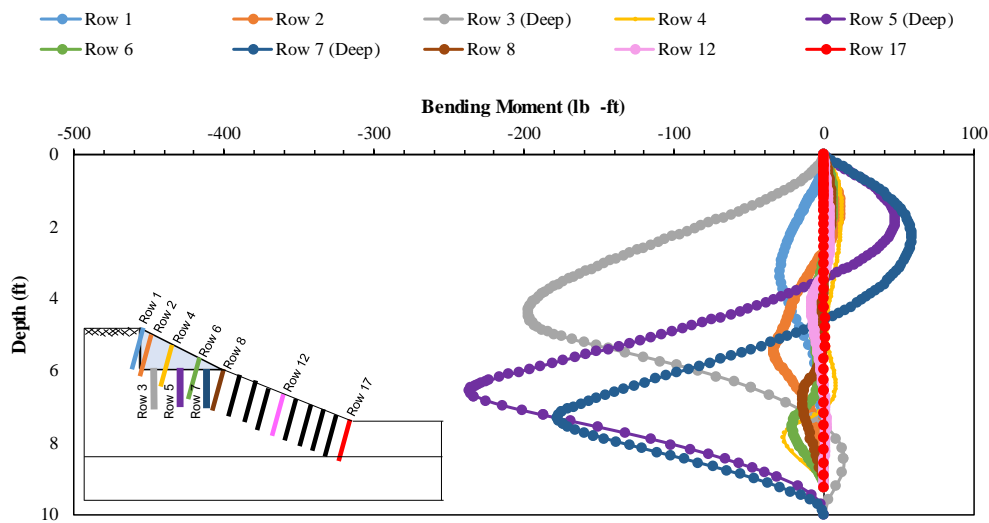


Figure 6.8 Bending Moment

6.2.2.2 Moment transfer

The amount of total capacity of RPP utilized is calculated to understand the life of RPP.

The % of moment transfer is calculated using the following equation.

$$\% \text{ Moment Transfer} = \frac{\text{Bending Moment } M \text{ of RPP}}{\text{Maximum Moment Capacity of RPP, } M_{max}}$$

Research conducted by Chen et al., 2007 showed that if the percentage of moment transfer is less than 35%, the estimated time for creep failure is more than 100 years. The percentage of moment transfer with depth of reinforcement is shown in Figure 6.9. The maximum moment transfer is less than 30% for the three rows of RPP that extend deeper into the slope and less than 7% for all other rows of RPP. Therefore, the RPP will not fail under creep for more than 100 years.

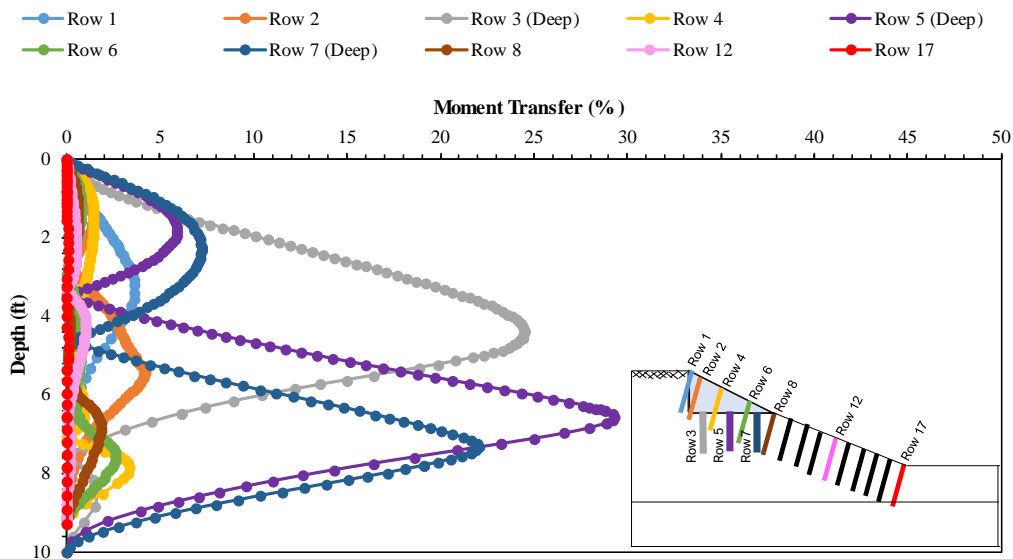


Figure 6.9 Variation of Moment Transfer with Depth of RPP

6.3 U.S 67- Alvarado

6.3.1 Model Calibration

Finite Element method is a very powerful computational tool in engineering used to study the stability of slopes using a failure definition similar to the traditional limit equilibrium method (Alkasawne et al., 2008). Strength reduction method was utilized in finite element modeling with Mohr Coulomb failure criteria using PLAXIS 2D.

The analysis was carried out considering the initiation of slope failure at a limiting factor of safety at 1. It is common practice to assume the depth of wetting as 7 to 10 feet (Nelson et al., 2001) and consideration of a deeper wetting zone with residual strength in the top 10 m was suggested for deeper slope failures to account for the infiltration of water through cracks and fissures (Hughes et al., 2009). In this study, the top 10 ft at the crest (Soil 1) with decreasing depth of zone (Soil 2) was considered as the failure zone with residual strength (Figure 6.1). The soil parameters for the remaining layers were obtained using the soil test results done during site investigation. The soil profile is shown below (Figure 6.10). Several iterations were carried out during the analysis to calibrate the soil model to represent failure as observed at site. The model was stimulated to represent the 5 ft crest drop and bulging initiating from the middle of the slope as observed at field after failure (Figure 6.11(a)). The groundwater table was modeled in correspondence with the lake level on the opposite side of the embankment. The soil parameters that yielded a factor of safety of 1.00 is shown in Table 6.3.

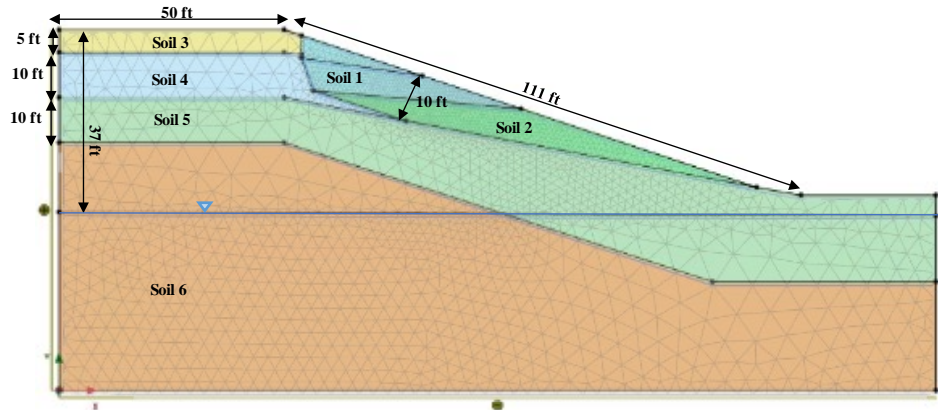


Figure 6.10 Soil Profile

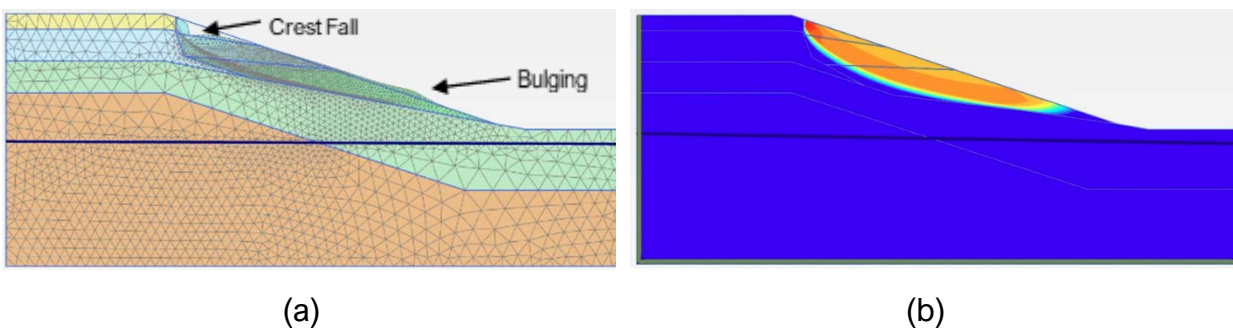


Figure 6.11 (a) Deformed Mesh Showing Crest Fall and Bulging, (b) Slip Circle: FS=1.00

Table 6.3 Parameters for FE Analysis

Layer	Unit Weight (pcf)	Elastic Modulus E (psf)	Poisson Ratio ν	Cohesion c (psf)	Phi ($^{\circ}$)
1	120	9000	0.39	60	12
2	120	11E3	0.35	70	13
3	125	67E3	0.30	450	16
4	130	52E3	0.35	350	15
5	125	68E3	0.32	450	18
6	130	140E3	0.2	950	25

Table 6.4 RPP Properties used in Numerical Model

Axial Stiffness, EA	3,200,000 lbf/ft
Flexural Rigidity, EI	29,630 lbf ft ² /ft
Specific Weight, w	1.85 lbf/ft/ft
Poisson's Ratio, ν (nu)	0.3

6.3.2 Performance Evaluation of Reinforced Section

Soil parameters calibrated from the control section was utilized in the in the reinforced section to analyze the performance of the Recycled Plastic Pins (RPP). Based on the deformation analysis, the maximum vertical and lateral deformation 1.83 inches and 1.08 inches was observed in the model (Figure 6.12). The maximum lateral deformation was observed in the middle of the slope. The increased saturation levels observed in the middle of the slope and the increased deformation observed in the middle is comparable. Maximum vertical displacement was observed in the crest of the slope in between the reinforcing members although the observations at field showed higher deformation in the middle of the slope.

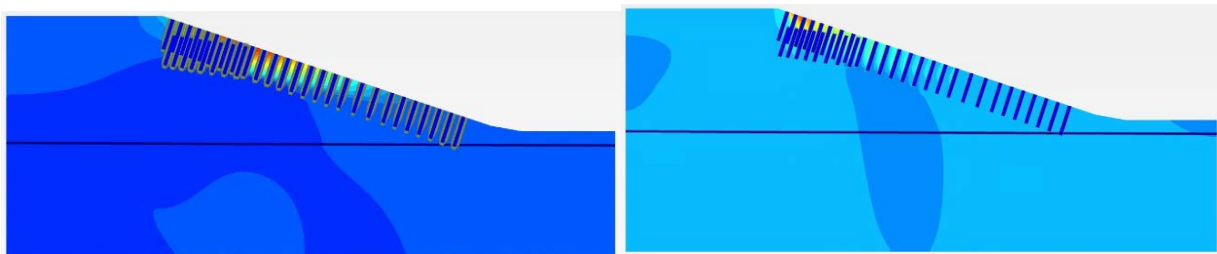


Figure 6.12 : Deformation Analysis in Reinforced Section; (a) Maximum Lateral Deformation = 2.01 inches, (b) Maximum Vertical Deformation = 1.60 inches.

The comparison of lateral deformation from the field and model data at the crest of the slope is shown in Figure 6.13. The trend of deformation with depth is comparable. The model showed higher deformation than the field observations. This result is expected since the soil parameters used for the model are at residual strength while the soil at field is not. Therefore, higher deformation is expected in the model. Similar trend indicates that the model is behaving similar to the field.

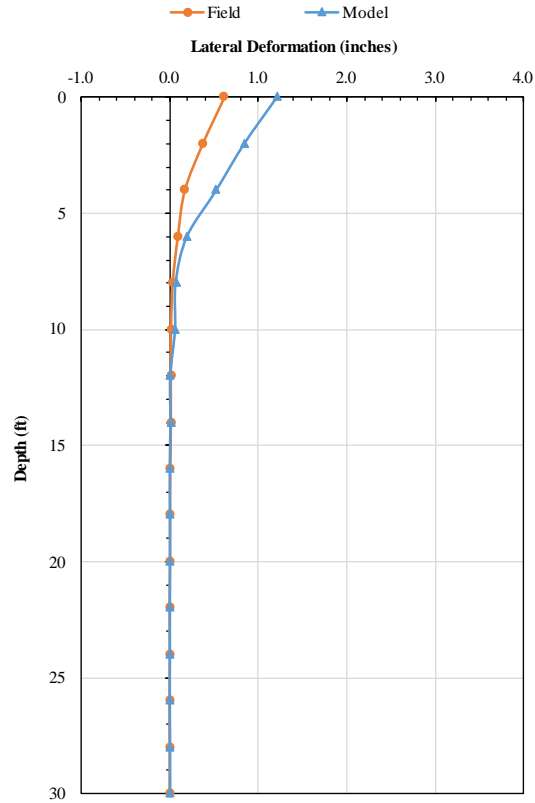
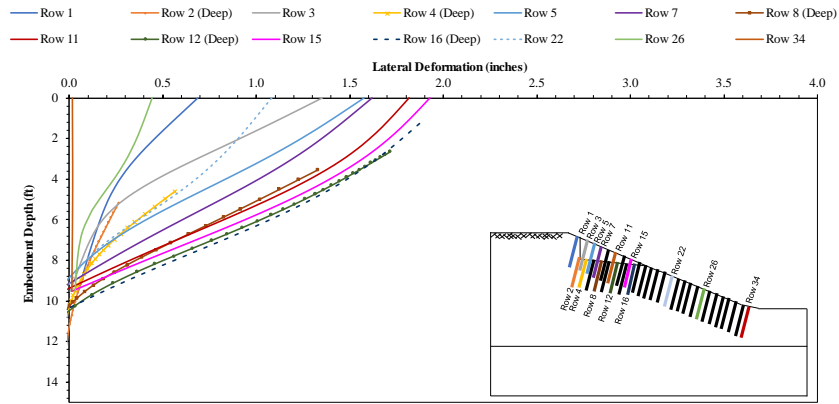
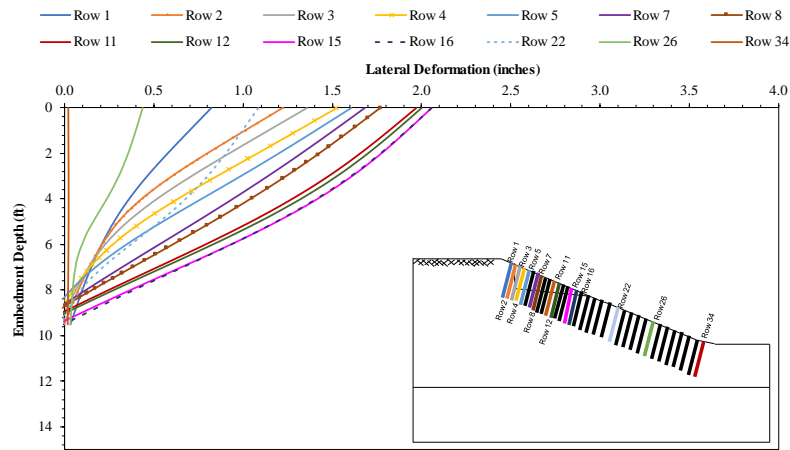


Figure 6.13 Comparison of Lateral Deformation between the Field and Model.

The calibrated model was also incorporated to build a model with the conventional layout (3 ft c/c at the crest: all pins flush to the ground) of RPP for comparison. The first 9 rows of reinforcement were considered to understand the effect of the overlap on lateral deformation of RPP. The lateral deformation of RPP rows for the two-layer layout and conventional layout is shown in Figure 6.14 (a) and (b) respectively. The deformation was observed to increase with the rows of pin since the maximum lateral displacement was observed in the middle of the slope. The maximum deformation was observed to be 2.10 inches in the normal layout compared to 1.92 inches in the two layered layout. The trend of lateral deformation was observed to be similar in both models.



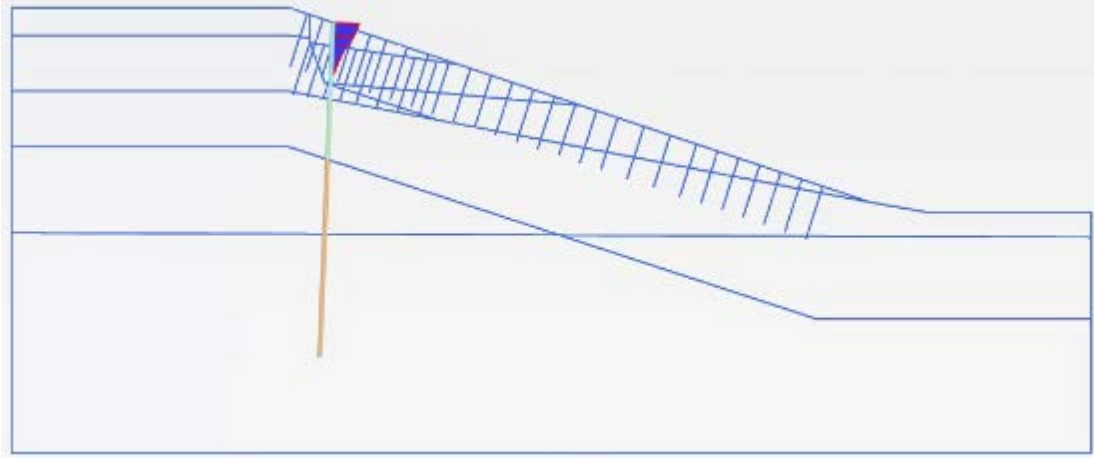
(a)



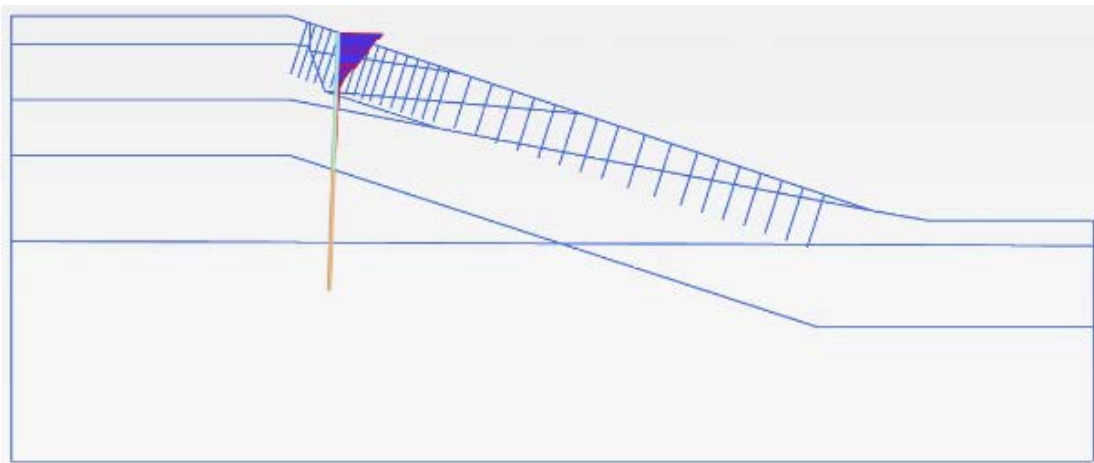
(b)

Figure 6.14 Variation of Lateral Deformation of RPP with Depth; (a) Layered Layout, (b) Normal Layout

The section of slope with the overlap depth was considered to evaluate the effect of the two layered design. Figure 6.15 shows the lateral deformation of the slope between row 4 and 5 and Figure 6.16 shows the percentage reduction in the two sections. Similar to the deformation in RPP, deformation of the slope in both sections showed similar trend. Lower deformation at certain depths were observed in the two layered layout indicating that the overlap is affecting the deformation.



(a)



(b)

Figure 6.15 (a) Lateral Deformation in Two Layer Layout (b) Lateral Deformation in Normal Layout

The reduction in deformation up to 30% was observed in the top 12 feet for the layered model. The two layered RPP extending deeper into the slope is reducing the slope movements at deeper depths lowering the deformation at the top. In comparison, the conventional layout of RPP which extends only up to a depth of 10 feet is not minimizing lateral deformation at deeper depths and has less anchorage to the stiffer strata, thereby affecting the lateral deformation.

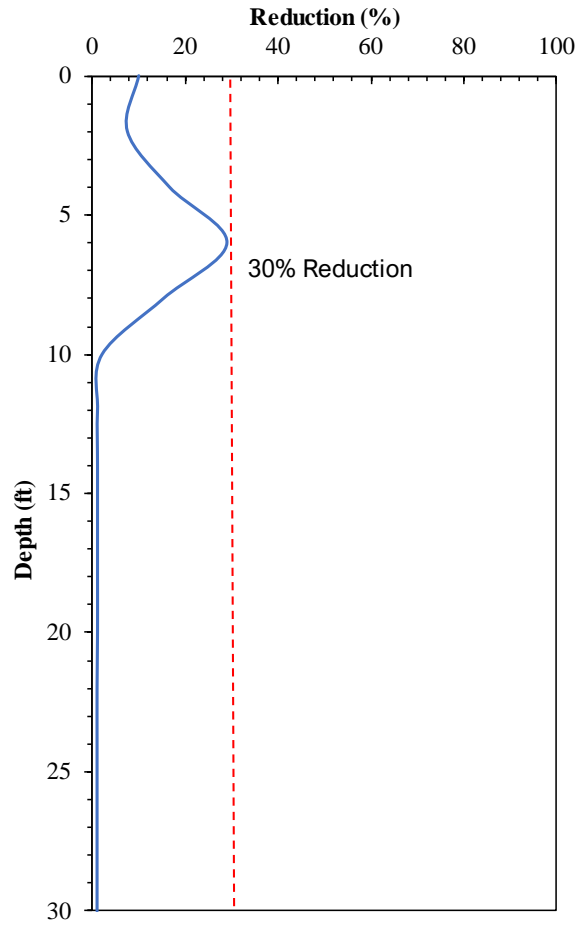


Figure 6.16 Lateral Deformation Reduction due to Two Layers with Depth.

6.4 Parametric Study

The numerical model used for IH-820 and Rosedale Street was further evaluated to conduct a parametric study to analyze the effect of construction sequence on factor of safety, effect of overlap depth on factor of safety, effect of spacing between layers on factor of safety and the effect of number of layers of deep pins on factor of safety. The parametric study was conducted using 10 feet RPP as the current field demonstration study.

6.4.1 Effect of Construction Sequence on Factor of Safety

The installation sequence followed for this study is unique. Therefore, the construction phases of the slope were stimulated using finite element modeling to understand the effect of each phase to the overall stability of the slope. Deformation and factor of safety analysis was conducted after calibration of the model for the initial slope corresponding to a factor of safety of unity.

Site observations after failure of the slope, recorded a vertical settlement/crest drop averaging 5 ft. During the first phase of construction, the section of vertical drop was compacted and flattened to create a platform for the machinery (Figure 6.17 (a)). This condition was stimulated as a cut in the model. The factor of safety was observed to increase to 1.21 and the slip circle to shift further into the slope. This phenomenon is expected since incorporating cuts/ benches into the slope is a slope stabilization method that is comparable to stabilization with a 10 ft nail (Khan & Wang 2021). The vertical deformation of the phase is shown in Figure 6.17 (b) and is observed at the bottom of the cut location.

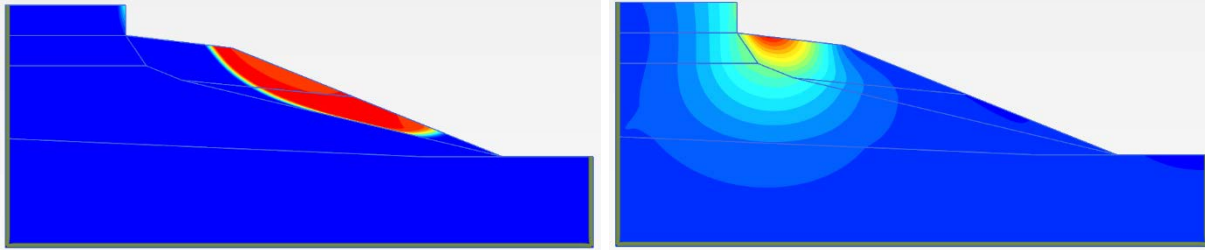


Figure 6.17 : (a) Slip circle for Cut Phase; FS: 1.21, (b) Vertical Displacement.

The installation of the second layer (Deep layer) of Recycled Plastic Pins (RPP) in the compacted and cut out section of the slope was stimulated as the next phase. Three rows of RPP were added to the model (Figure 6.18). The slip circle was observed to reduce in intensity as resisting forces were added. The factor of safety was observed to reduce to 1.19 due to addition of additional weight on to the slope.

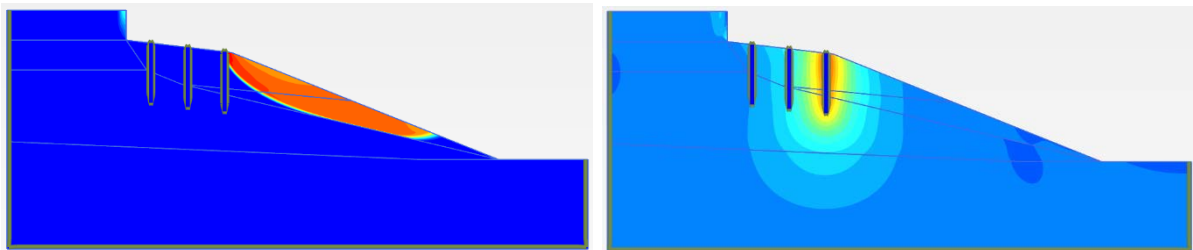


Figure 6.18 : (a) Slip circle for Deep Pin Phase; FS: 1.19, (b) Vertical Displacement.

The model was stimulated to experience fill as the next phase. The slope backfilled using the same material to stimulate worst case scenario of having backfill with fully softened parameters. The slip circle was observed to extend up to the crest and the vertical deformation was concentrated on the fill section (Figure 6.19). The factor of safety decreased to 1.17 due to the addition of extra load on to the slope.

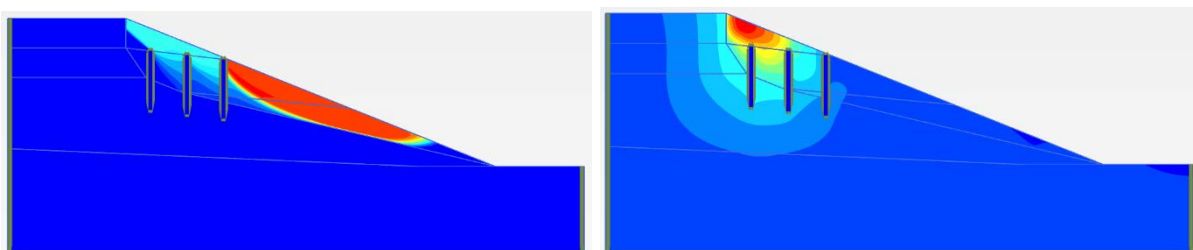


Figure 6.19 : (a) Slip circle for Fill Phase; FS: 1.17, (b) Vertical Displacement.

As the final phase of construction, the model was stimulated with shallow pin layers (layer 1). The slip circle was reduced to the crest of the slope with a factor of safety of 1.61 (Figure 6.20). In addition, the maximum vertical settlement was observed at the crest.

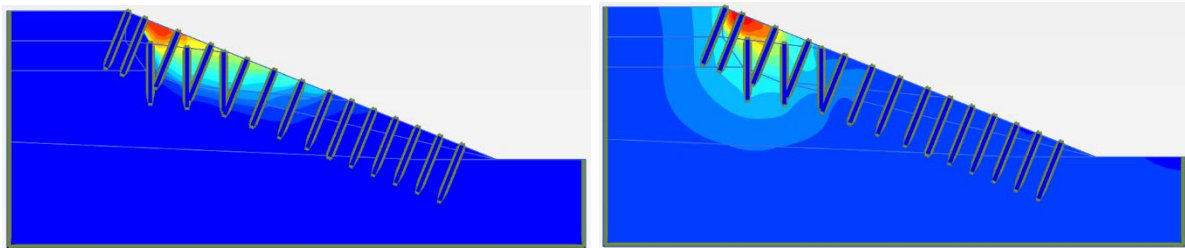


Figure 6.20 : (a) Slip circle for All Pin Phase; FS: 1.61, (b) Vertical Displacement.

The variation of factor of safety with the installation of each row of RPP was analyzed (Figure 6.21). The factor of safety was observed to increase with the addition of rows of reinforcement. Factor of safety of 1.3 was reached after the installation of the 9th row of RPP. TxDOT requires a minimum factor of safety of 1.3 for long term drained and short-term undrained conditions of a slope and requires a factor of safety of 1.5 for slopes that support abutments, utilizes and critical facilities (low tolerance for failure) (TxDOT, 2020). Therefore, the current slope in this study could have been stabilized with a minimum of 9-12 rows of RPP to reach the minimum TxDOT standard.

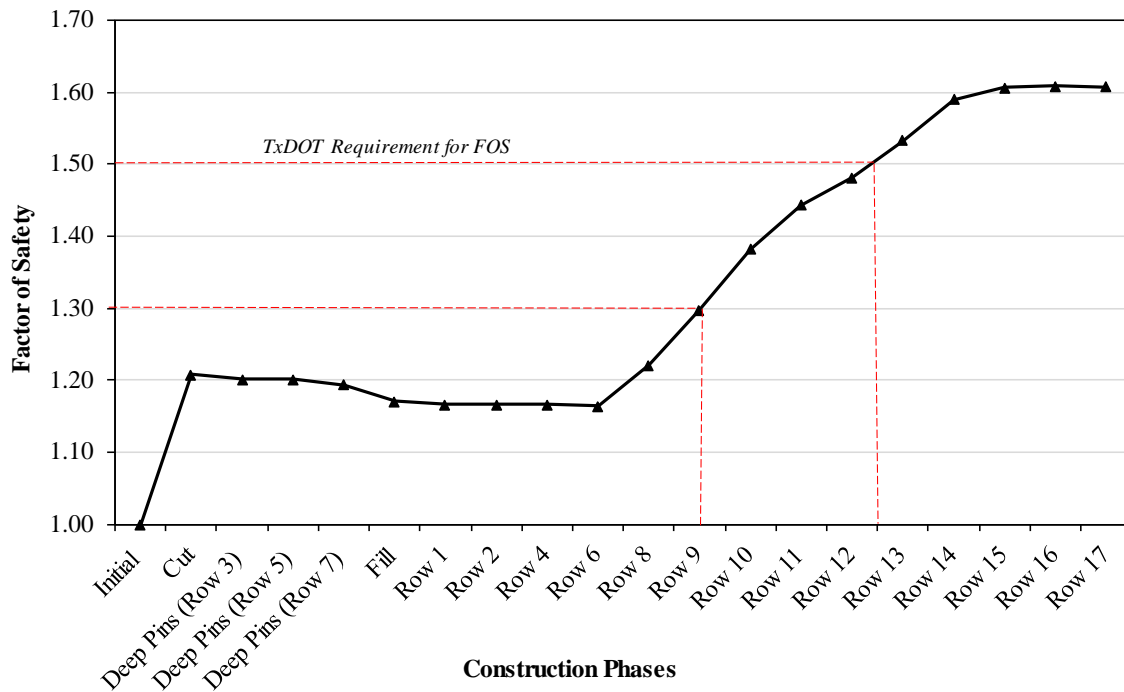


Figure 6.21 Variation of Factor of Safety with Construction Phases.

6.4.2 Effect of Location of Reinforcement on Factor of Safety

The model was further analyzed for the variation of factor of safety with the installation of reinforcement and the position of reinforcement of the slope. Wang et al., (2022) stated that the optimum position of pile arrangement is 0.55-0.65 L (L = Length of the slope) from the top of the slope and the factor of safety is to reach its maximum at the middle or the lower part of the slope. Hassiotis et al., (1997) states that the piles must be placed in the upper middle part of the slope for maximum factor of safety. In a study of statistical assessment of factor of safety of pile-reinforced slopes conducted by Trinidad et al., (2020), the optimum location was observed to move away from the toe towards the three-quarter point of the slope. In agreement with the above-mentioned studies, the factor of safety was observed to reach a satisfactory level in between 2/5 and 2/3 from the top of the slope (Figure 6.22).

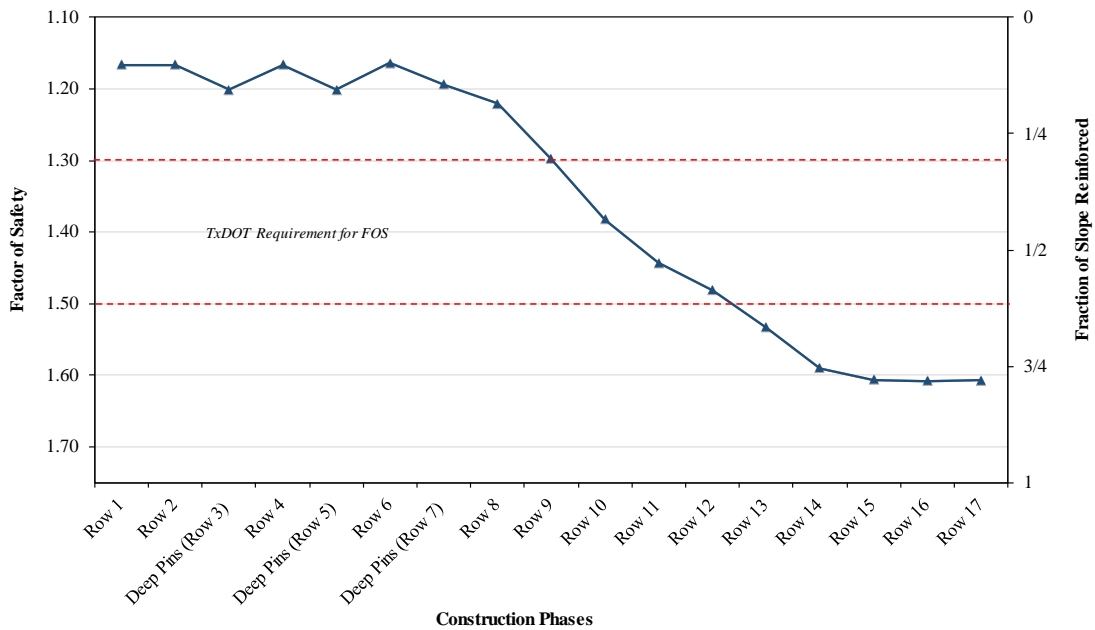


Figure 6.22 Variation of Factor of Safety by Row with Fraction of Slope Reinforced. Further analysis was conducted to determine the effect of the position of RPP in the slope. The numerical model was run with the reinforcement only active in certain sections of the slope as shown in Figure 6.23. The results showed that the highest factor of safety was obtained with reinforcement in the upper 2/3 of the slope. These results also show that reinforcing the crest of the slope is more important than the toe of the slope.

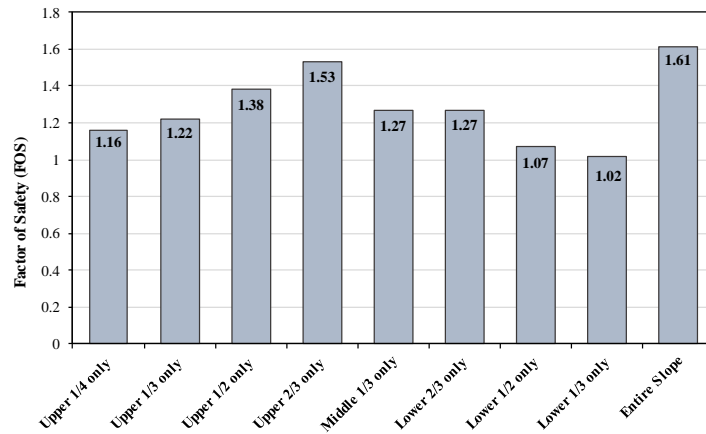


Figure 6.23 Variation of Factor of Safety with Different Reinforced Sections.

The factor of safety results from the current study was compared with other studies with RPP reinforcement for verification. Two sites in Missouri analyzed by Loehr and Bowders (2007) was compared. US-54 Fulton and I-435 Wornall Road was stabilized and analyzed with different positioning of RPP. The comparison results showed that the current study results follow the same trend of factor of safety.

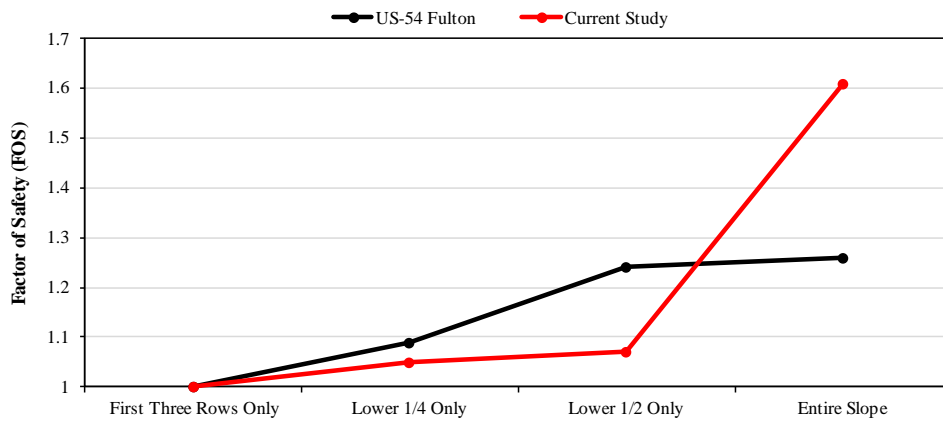


Figure 6.24 Comparison of Factor of Safety with U.S-54 Fulton Site (Loehr & Bowders, 2007)

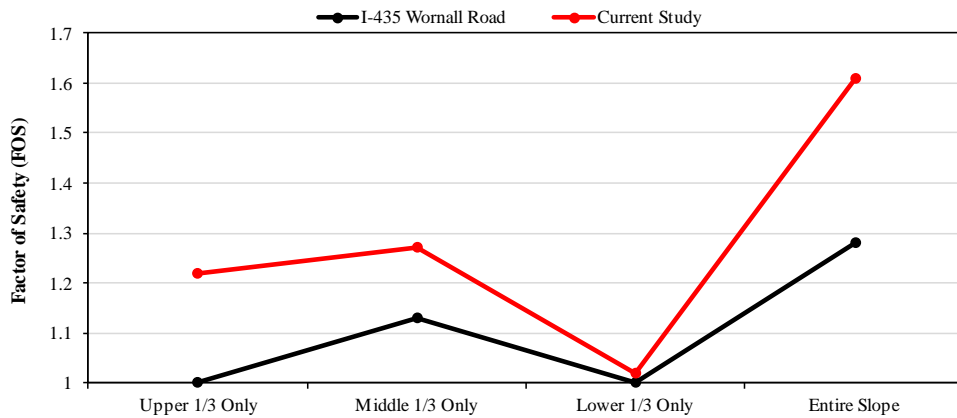


Figure 6.25 Comparison of Factor of Safety with I-435 Wornall Site (Loehr & Bowders, 2007)

6.4.3 Effect of the Number of Deep Layers on Factor of Safety

The number of lines used in the layer 1 depends on the failure. The ground surface after failure can be cut and prepared for the first layer before backfilling and compaction so that this layer will be deeper than the RPP installed flush to the ground. In order to incorporate more lines in the second layer, the spacing will have to be reduced to optimize the space. The parametric study was conducted to understand the effect of only the number of lines extending deeper. The spacing and overlap depth was kept constant at 6 ft c/c and 5 feet. The variation of the number of lines of reinforcement in the deep layer with sliding depth is shown in Figure 6.26. A schematic of the positioning of three (3) lines is shown in Figure 6.27.

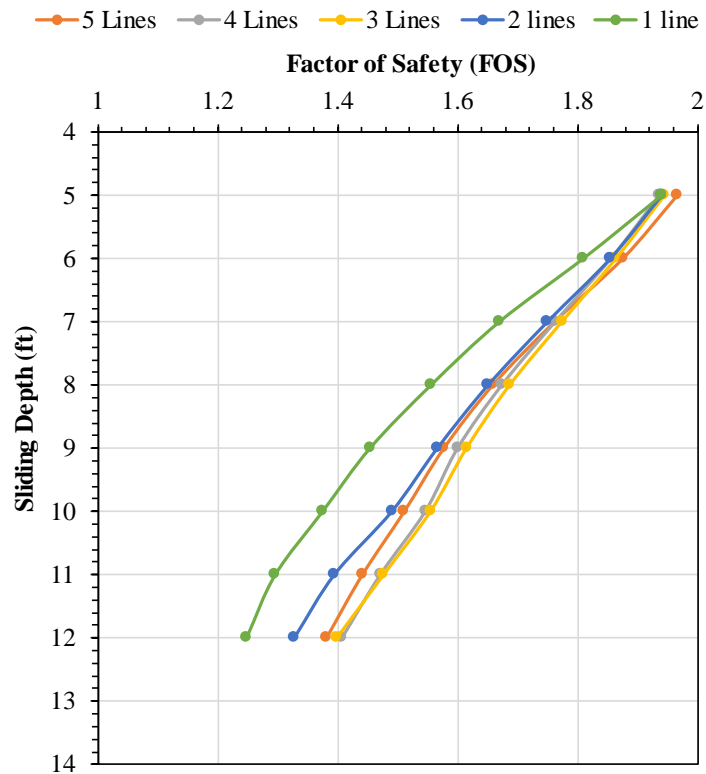


Figure 6.26 Variation of factor of safety with the number of deep layers

The trend for the variation of factor of safety was constant for all combinations. As expected, the model with 1 line of reinforcement extending deeper into the slope showed comparatively less factor of safety. Including 5 lines of RPP, showed better results for lower sliding depths but factor of safety was comparatively lower for deeper sliding depths. Although the reinforcement is providing higher anchorage, having 5 lines extend into the middle of the slope which does not significantly affect the factor of safety as the rows at the crest of the slope. Best results for this study were observed in having 3 lines of reinforcement. It has to be noted that this result may change with the change of geometry of the slope and the available space for the installation of the first layer after the failure.

6.4.4 Effect of Spacing between Layers on Factor of Safety

The effect of spacing between the first and the second layer is considered in this study. The spacing between the reinforcement flush to the ground is higher than the spacing between the first and second layer at overlap depth. The reinforcement is installed between the second layer (Figure 6.27). Field study was done using two different spacing. IH-820 & Rosedale Street was installed with 6 feet spacing in the second layer and 3 feet between the two layers. U.S 67 and Alvarado was installed with 3 feet spacing in the second layer and 1.5 feet spacing between the two layers. Both spacing was only studied for one assumed slip surface. The parametric study was conducted to include 4&2 feet spacing in addition to 6&3 feet and 3&1.5 feet.

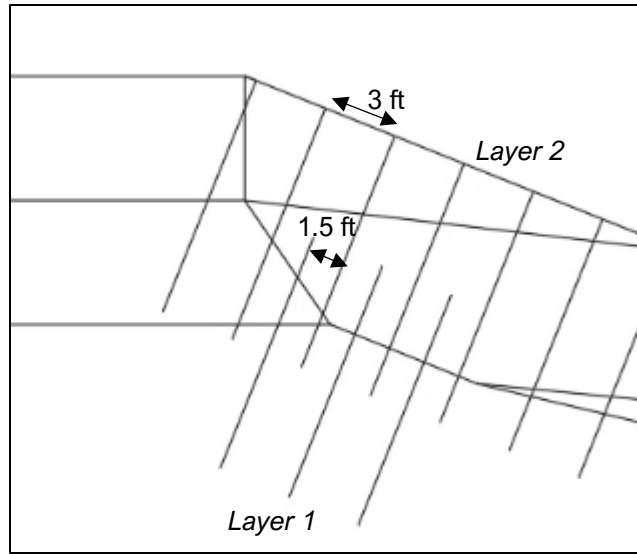


Figure 6.27 Spacing between Reinforcement.

The model was analyzed with 3 layers of deep pins and 5 feet overlap with alternating spacing between reinforcement. The results for the spacings considered showed negligible variation of factor of safety with sliding depth. All spacing followed similar decreasing trend with the increase of sliding depth. It can be concluded that the spacing between the layers has no effect on the factor of safety. This was observed since the maximum spacing considered between the two reinforcing layers was 3 ft at the intersection of 8 ft slip surface. Therefore, lower spacing is not providing any significant change.

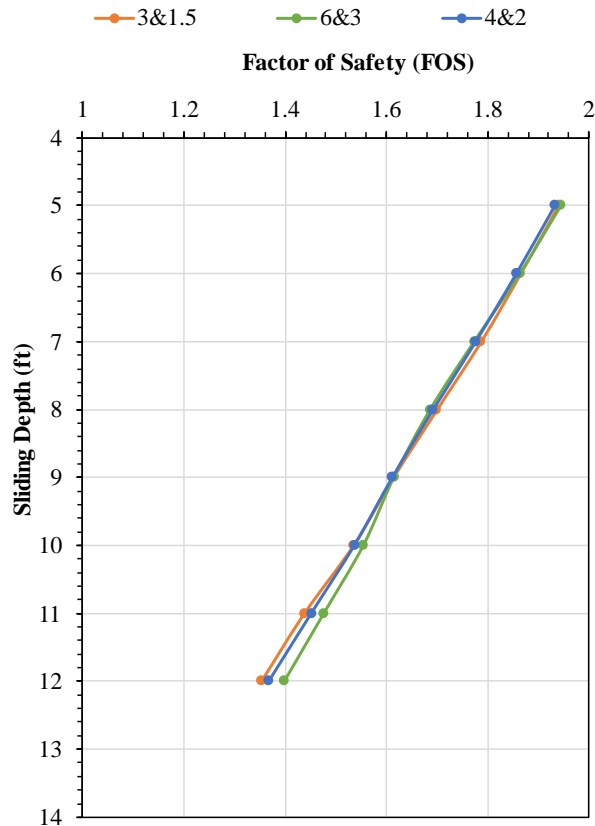


Figure 6.28 Variation of Factor of Safety with the Spacing Between Layers.

6.4.5 Effect of Overlap Depth on Factor of Safety and Lateral Deformation

The numerical model was further evaluated to conduct a parametric study to analyze the effect of overlap depth on factor of safety. Overlap depth is the depth the two layers of reinforcement overlap each other. For example, with the use of a 10 feet RPP and overlap of 5 ft, the second layer of reinforcement will be 5 feet below ground surface. The maximum depth of embedment for the reinforcement will be 15 feet below the ground surface (Figure 6.29). Loehr and Bowders (2007) conducted a study to analyze the effect of inclination of the reinforcement, and it was found that the effect is negligible since the overburden pressure at any given depth below ground surface is the same irrespective

of inclination. Therefore, the layer 1 reinforcement was modeled perpendicular as opposed to field study for the ease of altering the overlap depth between layers.

Table 6.5 Details of Overlap

Overlap Depth (ft)	Total Embedment Depth (ft)	Overlap starts at Depth below ground surface (ft)
1	19	9
2	18	8
3	17	7
4	16	6
5	15	5
6	14	4

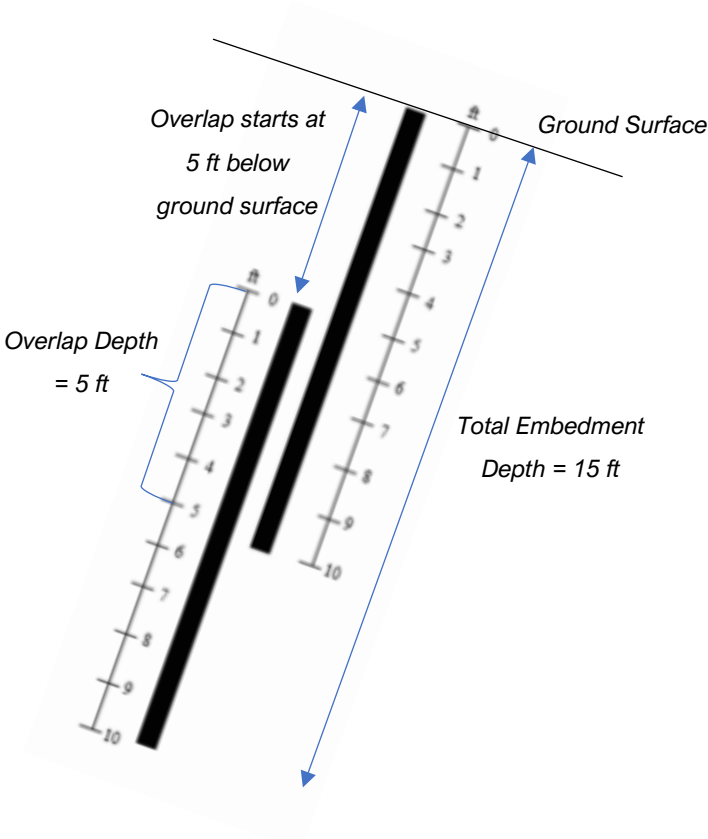


Figure 6.29 Schematic of 5 feet Overlap

The field study included only overlap depth of 5 feet with a sliding depth of 8 feet. Therefore, overlap depths of 1 ft to 6 ft were considered with sliding depth of failure ranging from 5 ft to 12 ft in the parametric study for spacing of 6 ft c/c. Soil parameters were kept constant.

Table 6.6 Numerical Model Matrix for Overlap Depth Analysis

Slip Surface Depth (ft)	Overlap Depth (ft)	Type of Analysis
5	1 ft, 2 ft, 3 ft, 4 ft, 5 ft, 6 ft	Factor of Safety
		Deformation Analysis
6	1 ft, 2 ft, 3 ft, 4 ft, 5 ft, 6 ft	Factor of Safety
		Deformation Analysis
7	1 ft, 2 ft, 3 ft, 4 ft, 5 ft, 6 ft	Factor of Safety
		Deformation Analysis
8	1 ft, 2 ft, 3 ft, 4 ft, 5 ft, 6 ft	Factor of Safety
		Deformation Analysis
9	1 ft, 2 ft, 3 ft, 4 ft, 5 ft, 6 ft	Factor of Safety
		Deformation Analysis
10	1 ft, 2 ft, 3 ft, 4 ft, 5 ft, 6 ft	Factor of Safety
		Deformation Analysis
11	1 ft, 2 ft, 3 ft, 4 ft, 5 ft, 6 ft	Factor of Safety
		Deformation Analysis
12	1 ft, 2 ft, 3 ft, 4 ft, 5 ft, 6 ft	Factor of Safety
		Deformation Analysis

6.4.5.1 Factor of Safety Analysis

The variation of factor of safety with overlap depth for varying failure depths are shown in Figure 6.30. The factor of safety is observed to increase with overlap depth for slip surfaces less than 8 feet. The relationship is observed to change after the slip surface depth of 8 feet. As the slip surface extends closer to the end of RPP in layer one, the anchorage provided becomes insufficient. Therefore, the factor of safety decreases with

the decrease of anchorage depth. One feet overlap is shown to have the best results for a slip surface of 12 feet.

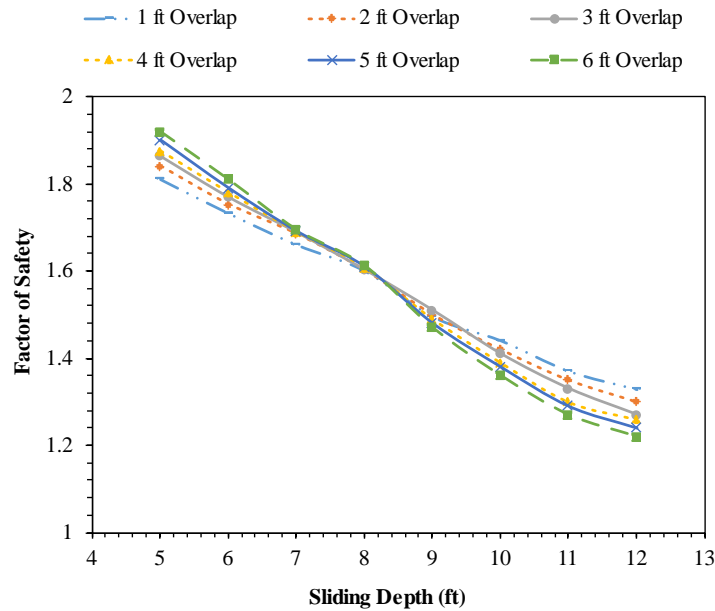


Figure 6.30 Variation of Factor of Safety with Sliding Depth of Failure for Different Overlap Depths.

6.4.5.2 Deformation Analysis

Deformation analysis was conducted to analyze the variation of lateral deformation with overlap depth.

The variation of lateral deformation with overlap depths for a slip surface of 5 ft and 8 ft are shown in Figure 6.31. At 5 ft failure, the slip surface will only intersect both layers of reinforcement for an overlap depth of 6 feet. It is observed that 6 ft overlap is the most effective in reducing the lateral deformation. At shallower depths, the spacing between the reinforcing members reduces the deformation and has higher influence than the effect from anchorage since all reinforcing members have adequate anchorage. Similar trend was observed for a failure at 8 ft, where the slip surface will intersect both layers of

reinforcement for overlap depths of 3 feet to 6 feet and intersect only the first layer for overlap depths of 1 foot and 2 feet. Higher resistance is mobilized when the slip surface intersects both layers of reinforcement, thereby decreasing the deformation. This effect is observed where higher overlap depths have reduced deformation at the slip surface depth. For example, 1 ft overlap for an 8 ft slip surface is not positively affecting the deformation because the slip surface does not intersect both rows of reinforcement, therefore, the resistance is not fully mobilized against failure.

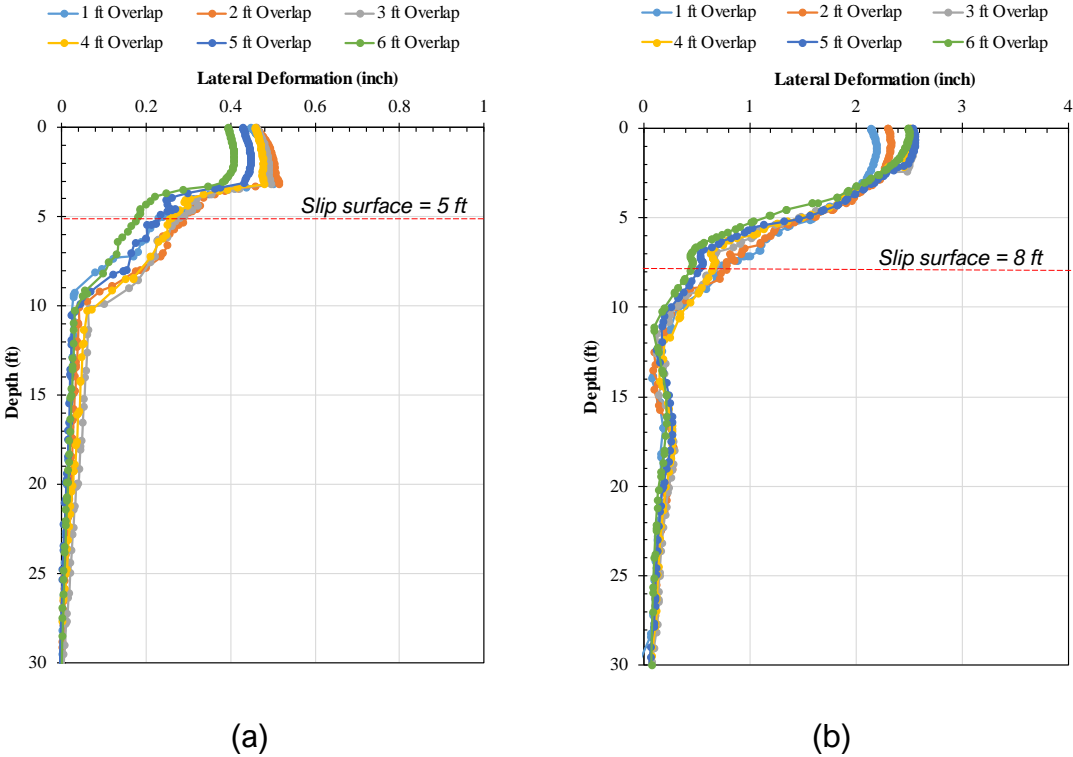


Figure 6.31 Variation of Lateral Deformation with Overlap Depth for Sliding Depth of; (a) 5 ft Failure (b) 8 ft Failure

In comparison, the variation of lateral deformation with overlap depths for a slip surface of 12 ft is shown in Figure 6.32. This slip surface does not intersect both layers of reinforcement for any of the overlap depths. Therefore, the anchorage provided is observed to take precedence over overlap depth. The deformation under the slip surface

is similar for all overlap depths but it is observed that 1 foot overlap has the least lateral deformation at the failure depth and 6 ft overlap has the most, which indicates that the higher anchorage is reducing the deformation. The deformation at the crest is observed to decrease with decrease of overlap depth as observed for 8 ft slip surface. The results indicate that for deeper failure planes, higher anchorage is positively affecting the stability of the slope.

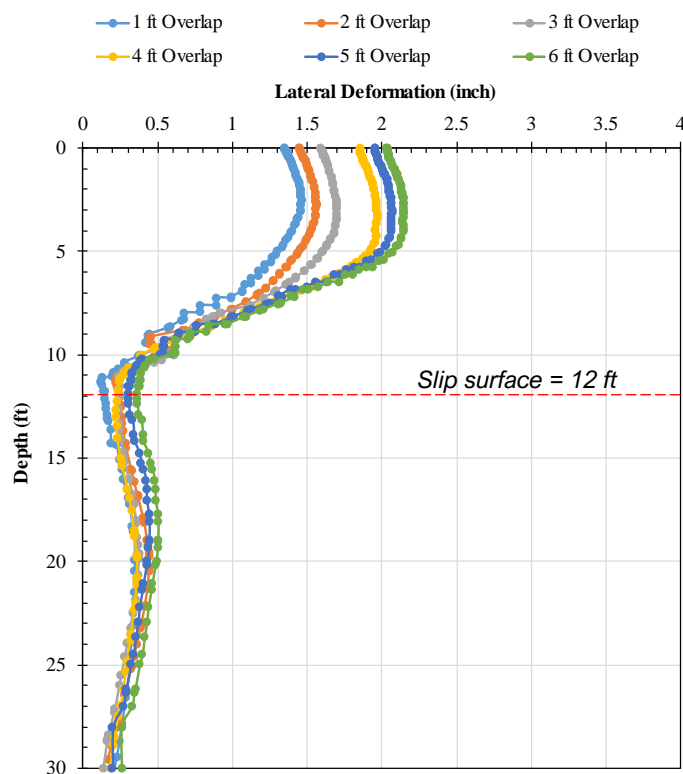


Figure 6.32 Variation of Lateral Deformation with Sliding Depth of 12 ft Failure for Different Overlap Depths.

According to Yang et al., (2015), better reinforcement is achieved if the reinforcement is applied in the region of high stress and large deformations, which is at or above the sliding depth. The results of the deformation analysis indicates that when the slip surface depths are less than 10 ft, the deformation decreases when the slip surface intersects both layers of reinforcement. But if the slip surface extends below the first layer (>10 ft), the

anchorage provided by the second layer takes precedence and decreases the lateral deformation.

Considering the factor of safety analysis and the deformation analysis for the effect of overlap depth, the optimum factor of safety can be inferred as shown in Table 6.7. The overlap depth is selected to give sufficient resistance against both failure of soil above the slip surface and failure due to loss of anchorage.

Table 6.7 Optimum Overlap Depth

Slip Surface Depth (ft)	Overlap Depth (ft)
<8	>4
8-10	4
>10	<4

6.5 Summary

- Numerical analysis was conducted using finite element modeling software PLAXIS 2D.
- The unreinforced slope was calibrated to failure with a factor of safety of 1. Soil parameters with residual strength was used.
- The maximum deformation of the reinforced slope with the calibrated model was 2.4 inches. This value is higher than the field observation due to the use of residual soil parameters.
- The trend of variation of lateral deformation with depth in the model was comparable with the field observations.
- Conventional layout of RPP and the two-layered design was compared in the numerical model.
 - Lateral deformation of RPP at the crest showed 15% reduction due the layered design.
 - Lateral deformation of the slope at failure plane showed 45% reduction due to overlap design.
 - Overlap reduced deformation at deeper depths.
- Maximum bending moment was observed for RPP in the second layer. The RPP having deeper anchorage provided higher resistance thereby decreasing the deformation.
- Parametric study was conducted to analyze the effect of construction sequence, overlap depth, number of lines and the spacing between layers on factor of safety.

- The effect of construction sequence on factor of safety.
 - FOS increase with the benching of the slope
 - FOS decreases with the addition of the first layer of reinforcement
 - FOS decreases with the backfill layer
 - FOS increases with addition of the second layer
 - FOS reached 1.3 at 9th row
- Factor of Safety was observed to reach adequate level in between 2/5 and 2/3 from the top of the slope.
- Highest factor of safety with reinforcement at top 1/3 of the slope.
- Optimum number of lines for this study was found to be 3 lines as done in the field demonstration but will differ depending on the dimensions of the slope.
- Spacing between layers showed no effect on factor of safety since the combination spacing varied was less than 3 ft c/c.
- Factor of safety analysis for effect of overlap with sliding depth,
 - FOS increases with increase of Overlap Depth up to sliding depth of 8 feet.
 - Overlap depths less than 4 feet yielded higher factor of safety for deeper depths (> 8 feet).
- Deformation analysis for overlap depth showed that the deformation is reduced when the sliding surface intersects both layers of reinforcement. It was also observed that at deeper depths, anchorage take precedence over overlap depth.

CHAPTER 7

DEVELOPMENT OF DESIGN CHARTS

7.1 Introduction

The stability of a slope is conventionally evaluated using an assumed potential failure surface. The factor of safety of the sliding surface is calculated by considering the equilibrium of the sliding mass. The factor of safety is generally defined as;

$$\text{Factor of Safety, } FOS = \frac{s}{\tau} \quad (7-1)$$

Where, s is the available shear strength in the sliding soil mass and τ is the equilibrium shear strength required to maintain a stable slope.

The limit equilibrium procedure that is generally used to evaluate the stability of the slope, reduces the available shear strength (s) by a factor of safety (s/FOS). At this state, the mobilized shear strength (τ) is just at the state of equilibrium with the available shear strength (s) (Titi & Helwany, 2007).

Slope stability analysis is conducted using method of slices approach with Mohr Coulomb failure envelop, where the sliding surface is divided into several vertical slices. Individual slices are evaluated to analyze the normal and shear stress on the sliding surface and factor of safety is calculated.

Mohr-Coulomb equation evaluates the shear strength of the soil. The factored shear stress can be shown as below.

$$\tau = \frac{c + \sigma \tan \phi}{FOS} \quad (7-2)$$

Where, c is the cohesion.

The process is repeated for other sliding surfaces until the lowest factor of safety is achieved. A reinforced slope is evaluated similarly, with an additional force added as a resisting force.

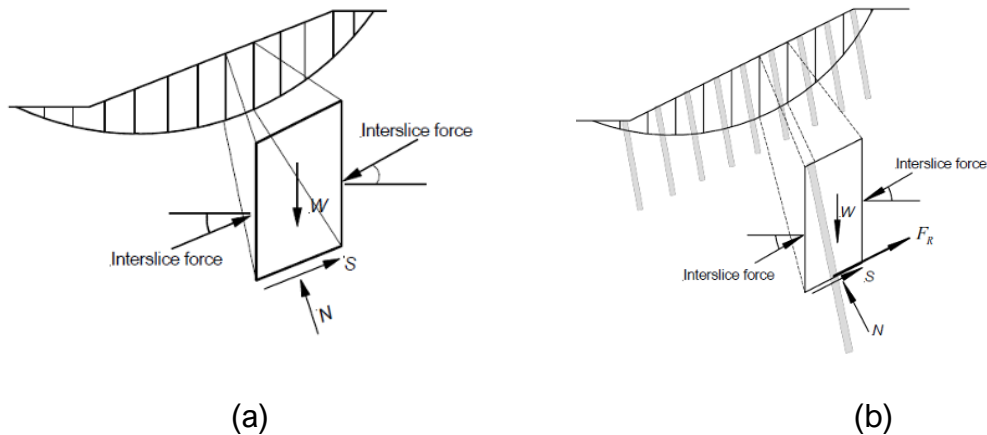


Figure 7.1 Static Equilibrium of Individual Slice in the Method of Slices (a) Unreinforced Slope (b) Reinforced Slope (Loehr and Bowders, 2007)

The resistance (F_R) provided by the reinforcement along the slip surface increases the factor of safety. Loehr and Bowders (2007) mentioned that the reinforcing force provided by the reinforcement is called the limit resistance. A combined limit resistance curve was developed by Loehr and Bowders (2007) by considering two soil failure mechanisms and the structural failure modes as shown in Figure 7.2.

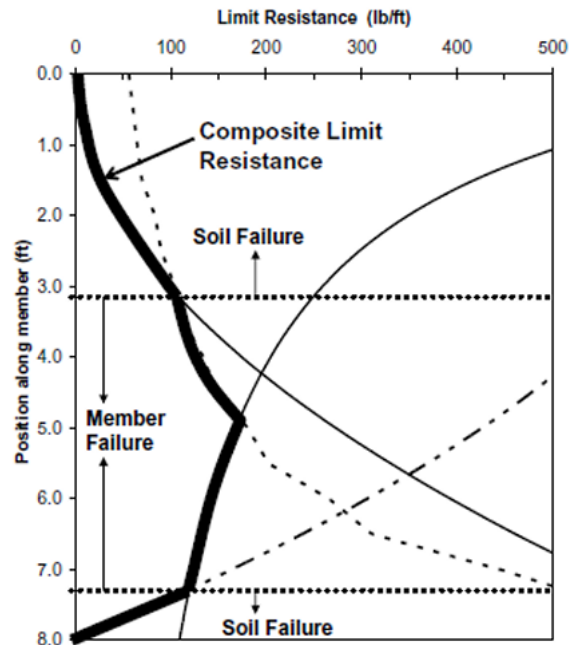


Figure 7.2 Combined Limit Resistance Curve (Loehr and Bowders, 2007)

The resistance of the RPP can be obtained for a specific condition and the factor of safety can be calculated using this simple and straight forward method. But the combined limit resistance curve has to be developed by the user for different conditions. Khan (2013) presented a design approach incorporating the performance of the reinforced slope in addition to the limit failure of the soil considering the limit resistance of RPP, using the maximum lateral displacement and maximum flexure as limiting criteria. The author presented several design charts for limit resistance of RPP, limit horizontal displacement and limit maximum flexure for RPP installed at grade for reinforcement of shallow slope failures. However, failure planes deeper than seven (7) feet were not considered in this study.

Similar approach is followed in the current study with the incorporation of a second overlapping layer of reinforcement and failure planes ranging from 5 ft to 12 ft to consider

deeper failures. The current study evaluates the effect of having two-layer layout on the limit resistance governed by failure modes of soil, limit horizontal displacement and limit maximum flexure of RPP. In addition, this study aims to develop simple model to obtain the resistance provided by the reinforcement depending on the overlap depth of the layers. The details of the design approach are presented below.

7.2 Limit Soil Resistance

Limit soil resistance is the maximum resistance the soil can provide before failure either by flowing of soil above and around the reinforcement or beneath the reinforcement due to loss of anchorage (Loehr et al, 2017). The method commonly followed to determine this resistance is limit state design approach. Therefore, the resistance is called Limit Resistance. Ito and Matsui (1975) and Loehr and Bowders (2007) discussed the general approach to obtain the lateral resistance considering the forces acting on the reinforcing member, by the soil and different failure modes associated with it.

The limit lateral force equation was first presented by Ito and Matsui (1975) considering the interaction region of the reinforcement and the plastic deformation of the soil surrounding the pile. This process is referred as the “theory of plastic deformation”. The following assumptions were made during the study:

1. When soil failure occurs, two sliding surfaces occur creating an angle of $(\pi/4 + \varphi/2)$ with the x-axis
2. The soil layer becomes plastic only in the immediate location around the piles.
3. The soil layer is in plain strain condition in the direction of depth.
4. The stress distribution will be the same with and without frictional forces.

5. Piles are rigid.
6. The ground surrounding the piles is horizontal.

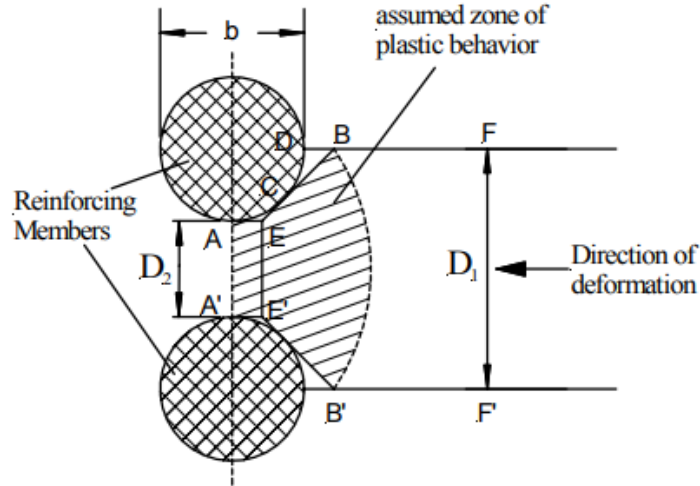


Figure 7.3 Schematic of plastic deformation for theory by Ito and Matsui (1975)

The Limit lateral force equation presented by Ito and Matsui depended on the distance between the piles, cohesion of the soil, friction angle, unit weight and an arbitrary depth from the ground surface. The equation represents the difference between the lateral forces in the BB' and AA' which yield the lateral force on pile per unit thickness of layer in direction of x-axis. The lateral force obtained by the following equation (7-3) per unit length of pile is considered as the difference in soil pressures acting on surfaces BB' and AA' during the plastic state (Loehr & Bowders, 2007).

$$P(z) = cD_1 \left(\frac{D_1}{D_2}\right)^{(N_\phi^{\frac{1}{2}}\tan\phi + N_\phi - 1)} \left[\frac{1}{N_\phi \tan\phi} \left\{ \exp\left(\frac{D_1 - D_2}{D_2} N_\phi \tan\phi \times \tan\left(\frac{\pi}{8} + \frac{\phi}{4}\right)\right) - 2N_\phi^{\frac{1}{2}}\tan\phi - 1 \right\} + \frac{2\tan\phi + 2N_\phi^{\frac{1}{2}} + N_\phi^{-\frac{1}{2}}}{N_\phi^{\frac{1}{2}}\tan\phi + N_\phi - 1} \right] - c \left\{ D_1 \frac{2\tan\phi + 2N_\phi^{\frac{1}{2}} + N_\phi^{-\frac{1}{2}}}{N_\phi^{\frac{1}{2}}\tan\phi + N_\phi - 1} - 2D_2 N_\phi^{-\frac{1}{2}} \right\} + \frac{\gamma z}{N_\phi} \left\{ D_1 \left(\frac{D_1}{D_2}\right)^{(N_\phi^{\frac{1}{2}}\tan\phi + N_\phi - 1)} \times \exp\left(\frac{D_1 - D_2}{D_2} N_\phi \tan\phi \times \tan\left(\frac{\pi}{8} + \frac{\phi}{4}\right)\right) - D_2 \right\} \quad (7-3)$$

Where;

$$N_\phi = \tan^2\left(\frac{\pi}{4} + \frac{\phi}{2}\right)$$

D_1 = Center to center spacing,

D_2 = Inner distance between the piles

c = Cohesion of the soil,

ϕ = Internal friction angle of the soil.

γ = Unit weight of the soil.

z = Depth to Slip Surface.

Although the equation is developed for vertical piles with the assumption of horizontal ground, Loehr et al., (2007) presented that there is no significant change in lateral force exerted on the pins due to inclination of the piles nor the inclination of the surface since the effective overburden stress acting on the reinforcement at any given depth is similar regardless of the inclination of the ground.

Table 7.1 Soil and RPP Parameters for Conventional Layout

Parameters	
Length of Reinforcement (ft)	10
Spacing (ft)	3
Cohesion (psf)	60
Friction Angle (°)	12
Unit Weight (pcf)	120
Size of RPP (inch)	3.5 x 3.5

Using the equation proposed by Ito and Matsui (1975) as limit soil pressure (Figure 7.4), Loehr and Bowders (2007) presented the change in limit soil resistance with respect to failure modes with varying depths. The limit lateral soil pressure is the maximum lateral pressure that the soil adjacent to the reinforcing member can sustain before failure, either by flowing around or between reinforcing members.

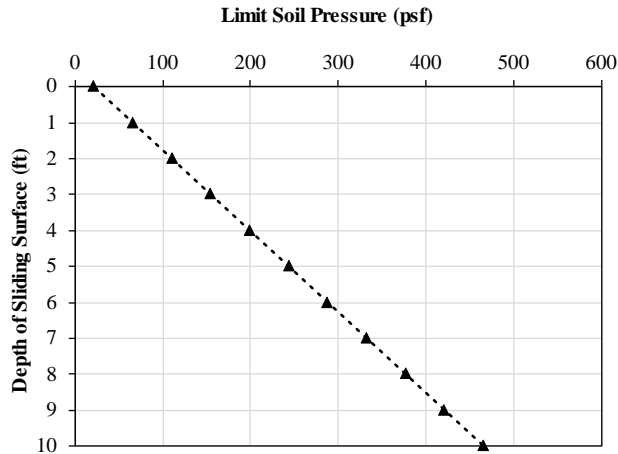


Figure 7.4 Limit Soil Pressure

The Limit soil resistance is defined as the magnitude of the resisting force provided by the reinforcing member as a function of the location where a potential sliding surface crosses the member. Failure mode I considered the failure of the soil between the piles above the failure depth (Figure 7.5 (a)), and Failure II considered the failure of the soil beyond the failure depth (loss of anchorage) (Figure 7.5 (b)).

Table 7.2 Failure Modes

Failure Mode	Description
Failure Mode 1	Failure of soil above the sliding surface
Failure Mode 2	Failure due to lack of anchorage (below sliding surface)

Limit soil resistance for failure mode I is obtained by integrating the limit soil pressure (Ito and Matsui equation) with respect to depth along the pile from the ground surface to the sliding depth (Figure 7.4). It is considered that the limit soil pressure is fully mobilized along the reinforcing member above the sliding surface. The integration is repeated for varying sliding surfaces to obtain the limit resistance curve.

Limit soil resistance for failure mode II is obtained by integrating limit soil pressure along the pile from sliding depth to the end of the pile.

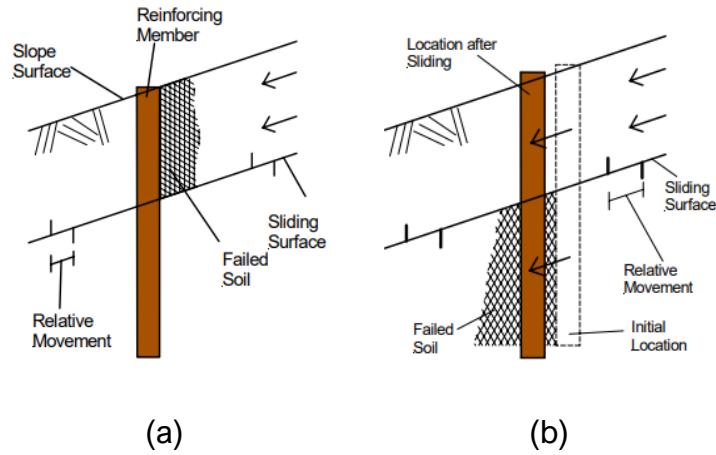


Figure 7.5 Failure Modes (a) Failure Mode I (b) Failure Mode II.

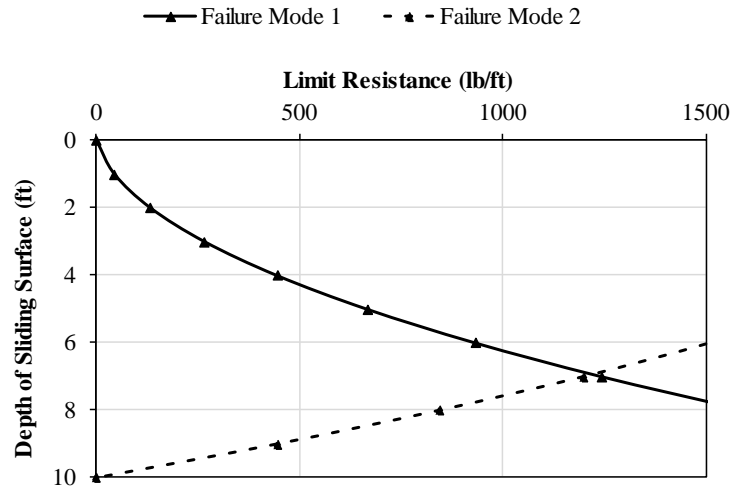


Figure 7.6 Re-plotted to represent the Composite Resistance for Failure modes I and II based on Loehr and Bowders, 2007.

The controlling failure mode depends on the depth of sliding. For the limit resistance plot shown in Figure 7.6, sliding depths of less than 7.5 ft is controlled by failure mode 1, while failure depths while sliding depths greater than 7.5 ft will be typically controlled by failure mode 2 (loss of anchorage).

7.2.1 Limit Soil Resistance for Two Layered Layout

The limit resistance curves depend on the spacing between the piles (inner [D_2] and outer [D_1]) and depth of the pile from the ground surface (y). In the case of having overlap depths/ two layered reinforcement, the spacing and the anchorage depth will differ along the pile length compared to the conventional layout of uniform spacing and length (inner [D_2 and D_2'] and outer [D_1 and D_1']). The limit soil pressure and the limit resistance curves will change accordingly. The schematic of the layout with varying spacing is shown in Figure 7.7.

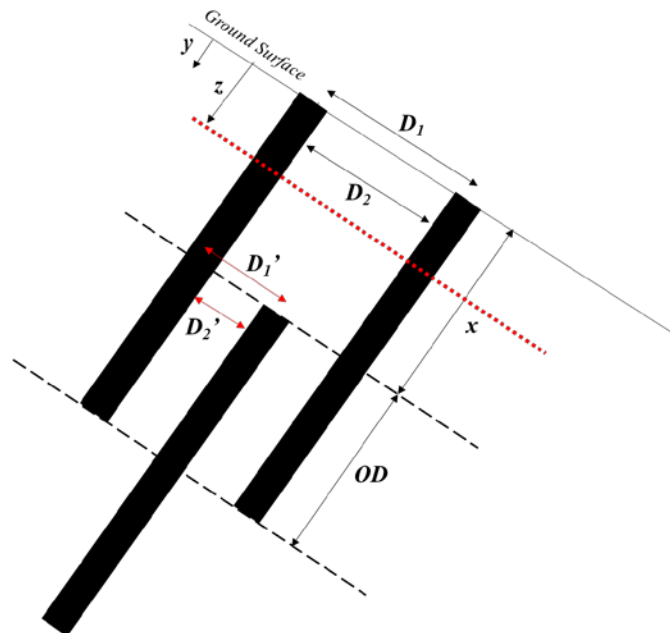


Figure 7.7 Schematic of Two-Layered Layout

x = Distance from ground surface to the second layer of reinforcement

y = Distance from ground surface

z = Distance to Slip surface

OD = Overlap Depth

$$OD = 10 - x$$

D_1 = Center to center spacing of layer 1

D_1' = Center to center spacing between layer 1 and 2

D_2 = Inner spacing between layer 1

D_2' = Inner spacing between layer 1 and layer 2

The limit soil pressure graph is plotted according to the equation of total lateral force equation proposed by Ito and Matsui (1975) considering a change of spacing at the beginning and end of overlap section.

$$P(z) = cD_1 \left(\frac{D_1}{D_2}\right)^{(N_\phi \frac{1}{2} \tan \phi + N_\phi - 1)} \left[\frac{1}{N_\phi \tan \phi} \left\{ \exp \left(\frac{D_1 - D_2}{D_2} N_\phi \tan \phi \times \tan \left(\frac{\pi}{8} + \frac{\phi}{4} \right) \right) - 2N_\phi \frac{1}{2} \tan \phi - 1 \right\} + \frac{2 \tan \phi + 2N_\phi \frac{1}{2} + N_\phi^{-\frac{1}{2}}}{N_\phi \frac{1}{2} \tan \phi + N_\phi - 1} \right] - c \left\{ D_1 \frac{2 \tan \phi + 2N_\phi \frac{1}{2} + N_\phi^{-\frac{1}{2}}}{N_\phi \frac{1}{2} \tan \phi + N_\phi - 1} - 2D_2 N_\phi^{-\frac{1}{2}} \right\} + \frac{\gamma z}{N_\phi} \left\{ D_1 \left(\frac{D_1}{D_2}\right)^{(N_\phi \frac{1}{2} \tan \phi + N_\phi - 1)} \times \exp \left(\frac{D_1 - D_2}{D_2} N_\phi \tan \phi \times \tan \left(\frac{\pi}{8} + \frac{\phi}{4} \right) \right) - D_2 \right\} \quad (7-4)$$

Where;

$$N_\phi = \tan^2 \left(\frac{\pi}{4} + \frac{\phi}{2} \right)$$

D_1 = Center to center spacing,

D_2 = Inner distance between the piles

c = Cohesion of the soil,

ϕ = Internal friction angle of the soil.

γ = Unit weight of the soil.

z = Depth to Slip Surface.

The limit pressure depends on the distance/ spacing between the piles, unit weight of the soil, cohesion, friction angle and an arbitrary depth from the ground surface.

According to Loehr and Bowders (2007), the limit pressure intergrated along the reinforcing member provides the limit resistance of the reinforcing member with respect

to the sliding depth. An arbitrary distance y is incorporated instead of considering ground surface as initial depth for simplification. The above equation (7-4) intergrated is shown below;

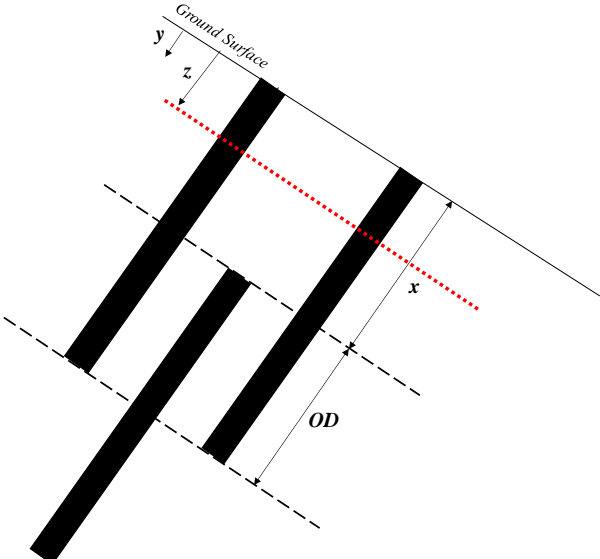
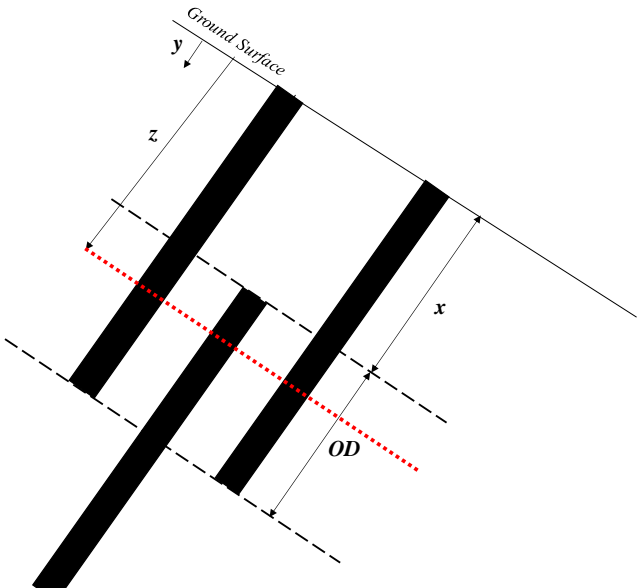
$$\begin{aligned}
\int_y^z P(z) dz = & \left[czD_1 \left(\frac{D_1}{D_2}\right)^{\left(N_\varphi^{\frac{1}{2}}\tan\varphi+N_\varphi-1\right)} \left[\frac{1}{N_\varphi \tan\varphi} \left\{ \exp\left(\frac{D_1-D_2}{D_2} N_\varphi \tan\varphi \times \tan\left(\frac{\pi}{8} + \frac{\varphi}{4}\right)\right) - \right. \right. \\
& \left. \left. 2N_\varphi^{\frac{1}{2}}\tan\varphi - 1 \right\} + \frac{2\tan\varphi+2N_\varphi^{\frac{1}{2}}+N_\varphi^{-\frac{1}{2}}}{N_\varphi^{\frac{1}{2}}\tan\varphi+N_\varphi-1} \right] - cz \left\{ D_1 \frac{2\tan\varphi+2N_\varphi^{\frac{1}{2}}+N_\varphi^{-\frac{1}{2}}}{N_\varphi^{\frac{1}{2}}\tan\varphi+N_\varphi-1} - 2D_2 N_\varphi^{-\frac{1}{2}} \right\} + \\
& \left. \frac{\gamma z^2}{2N_\varphi} \left\{ D_1 \left(\frac{D_1}{D_2}\right)^{\left(N_\varphi^{\frac{1}{2}}\tan\varphi+N_\varphi-1\right)} \times \exp\left(\frac{D_1-D_2}{D_2} N_\varphi \tan\varphi \times \tan\left(\frac{\pi}{8} + \frac{\varphi}{4}\right)\right) - D_2 \right\} \right] - \\
& \left[cyD_1 \left(\frac{D_1}{D_2}\right)^{\left(N_\varphi^{\frac{1}{2}}\tan\varphi+N_\varphi-1\right)} \left[\frac{1}{N_\varphi \tan\varphi} \left\{ \exp\left(\frac{D_1-D_2}{D_2} N_\varphi \tan\varphi \times \tan\left(\frac{\pi}{8} + \frac{\varphi}{4}\right)\right) - 2N_\varphi^{\frac{1}{2}}\tan\varphi - 1 \right\} + \right. \right. \\
& \left. \left. \frac{2\tan\varphi+2N_\varphi^{\frac{1}{2}}+N_\varphi^{-\frac{1}{2}}}{N_\varphi^{\frac{1}{2}}\tan\varphi+N_\varphi-1} \right] - cy \left\{ D_1 \frac{2\tan\varphi+2N_\varphi^{\frac{1}{2}}+N_\varphi^{-\frac{1}{2}}}{N_\varphi^{\frac{1}{2}}\tan\varphi+N_\varphi-1} - 2D_2 N_\varphi^{-\frac{1}{2}} \right\} + \frac{\gamma(y^2)}{2N_\varphi} \left\{ D_1 \left(\frac{D_1}{D_2}\right)^{\left(N_\varphi^{\frac{1}{2}}\tan\varphi+N_\varphi-1\right)} \times \right. \right. \\
& \left. \left. \exp\left(\frac{D_1-D_2}{D_2} N_\varphi \tan\varphi \times \tan\left(\frac{\pi}{8} + \frac{\varphi}{4}\right)\right) - D_2 \right\} \right] \quad (7-5)
\end{aligned}$$

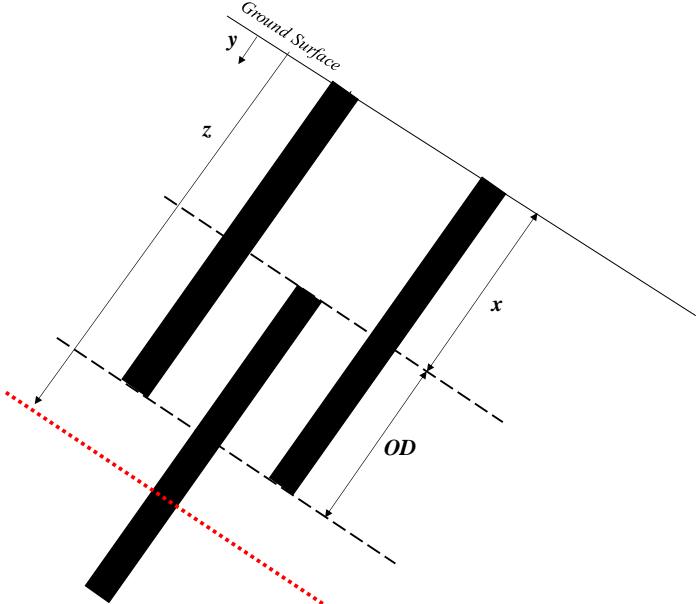
Where:

y = Depth below ground surface

In the current study with staggered deep pin/ two layered reinforcement design, the spacing between the piles and the anchorage depth changes with overlap depth. The spacing of the reinforcement flush to the ground (Layer 1 – D_1) is twice the spacing of the second layer of reinforcement with respect to layer 1 (D_1') (Figure 7.7). Since the spacing changes with the depth (y), the integration is separated according to the position of the slip surface (z). The separated equations with the conditions are shown in Table 7.3. Spacings D_1' and D_2' for $P(z)_2$ are considered when integrating in the overlap depth (OD) section ($x \leq y \leq 10$).

Table 7.3 Limit Soil Resistance Equations and Conditions.

Schematic	Condition	Equation
	$z \leq x$	$\int_0^z P(z)_1 dz$
	$x \leq z \leq 10$	$\int_0^x P(z)_1 dz + \int_x^z P(z)_2 dz$

Schematic	Condition	Equation
	$z \geq 10$	$\int_0^x P(z)_1 dz$ $+ \int_x^{10} P(z)_2 dz$ $+ \int_{10}^z P(z)_1 dz$

The above explained procedure is followed using the parameters shown in Table 7.4. The limit soil pressure of the two layered reinforcement is shown in Figure 7.8. The limit soil pressure is having a similar trend to the conventional layout (Figure 7.4) with pressure increasing with depth but an increase and decrease of lateral pressure is observed due to the decrease of spacing in the overlap depth section.

Table 7.4 RPP and Soil Parameters for Two Layered layout

Parameters	
Length of Reinforcement (ft)	10
Spacing (ft)	6 & 3
Cohesion (psf)	60
Friction Angle ($^{\circ}$)	12
Unit Weight (pcf)	120
Size of RPP (inch)	3.5 x 3.5
Overlap (ft)	4

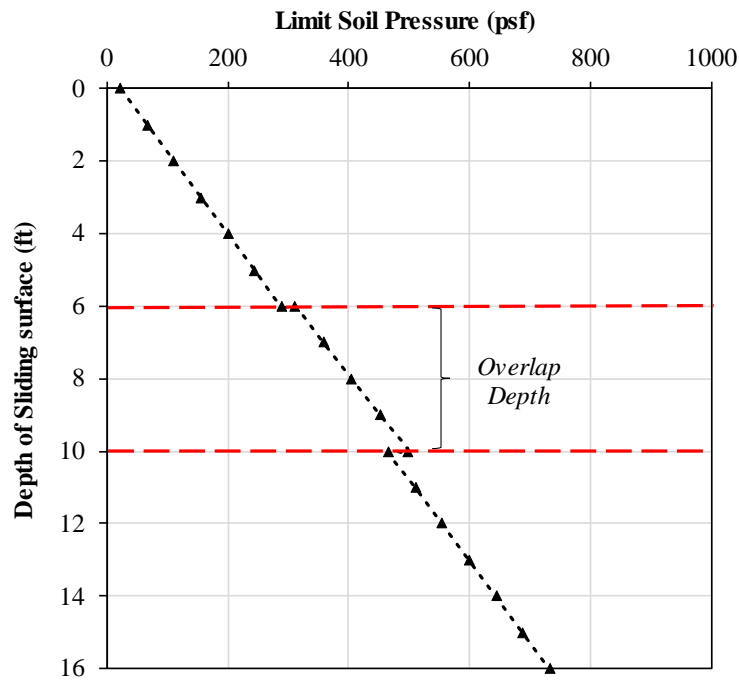


Figure 7.8 Limit Soil Pressure for Two-Layered Layout

The limit resistance was obtained by intergrating the limit soil pressure between the separate sections with respect to slip surface as explained above. The combined limit resistance for the two layered design with 4 feet overlap is shown in Figure 7.9. The combined resistance is obtained by considering the intersection of the two failure modes. The combined limit resistance shows that failure for slip surfaces greater than 11 ft are governed by failure mode 2 and slip surfaces less than 11 ft are governed by failure 1.

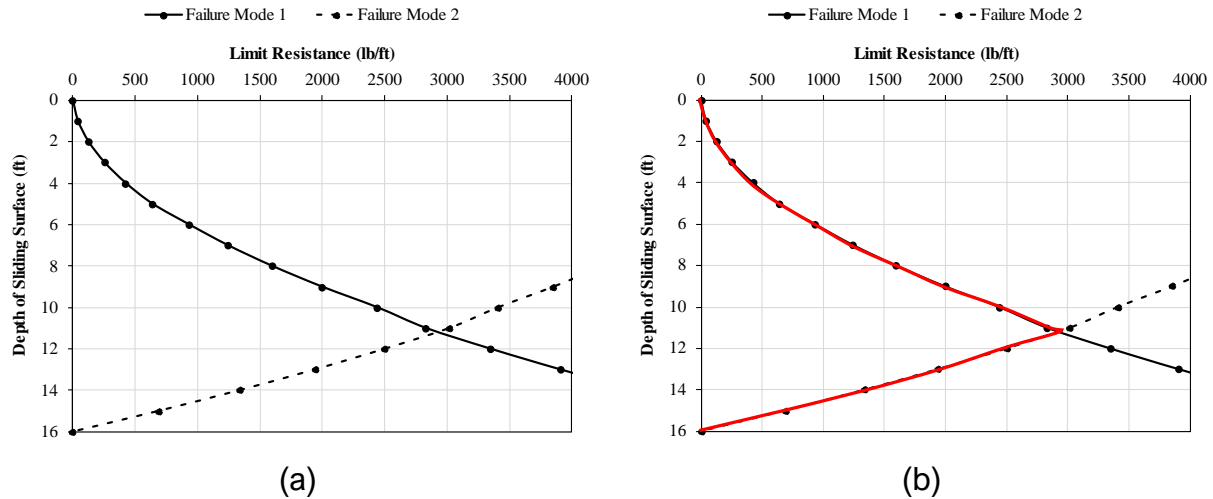


Figure 7.9 (a) Limit Resistance for Two-Layered Layout of Failure modes 1 and 2. (b) Composite Limit Resistance Curve for Overlap Depth of 4 feet.

The comparison of the composite limit soil resistance for the two layouts (conventional layout and 4 ft Overlap) is shown in Figure 7.10. The limit resistance for the two layered layout is observed to be significantly higher due to the anchorage provided by the reinforcement extending into the stiffer strata. In the two layered design, the system will have sufficient resistance against failure due to loss of anchorage up to a depth of 11 feet as opposed to the system being governed by the failure of loss of anchorage at 7 feet in the conventional design. In addition, for a slip surface more than 10 feet in the normal layout, no resistance will be provided since the slip surface is not intersecting the reinforcing member but incorporating the layered design, the slip surface will intersect the second layer providing additional resistance against failure. Therefore, the two layered design is providing higher resisting forces against deeper failure planes.

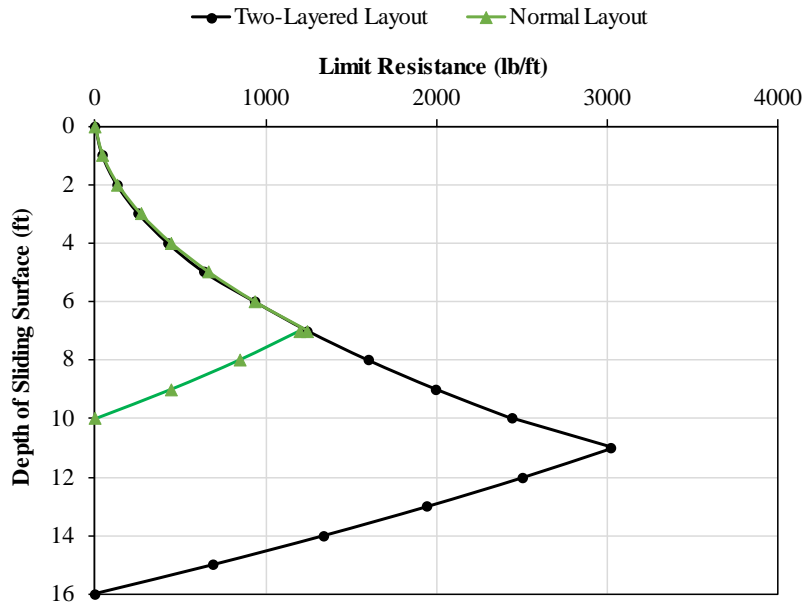


Figure 7.10 Comparison of Limit Soil Resistance for the Two Layouts.

A parametric study was conducted to evaluate effect of each factor on the limit soil resistance according to the failure modes incorporating the two layered design. Spacing between the reinforcement was selected according to the field studies. The larger spacing was the spacing at grade and the lower spacing was between the first and second layer. A wide range of friction angles and cohesion values were considered. The matrix followed is shown in Figure 7.11.

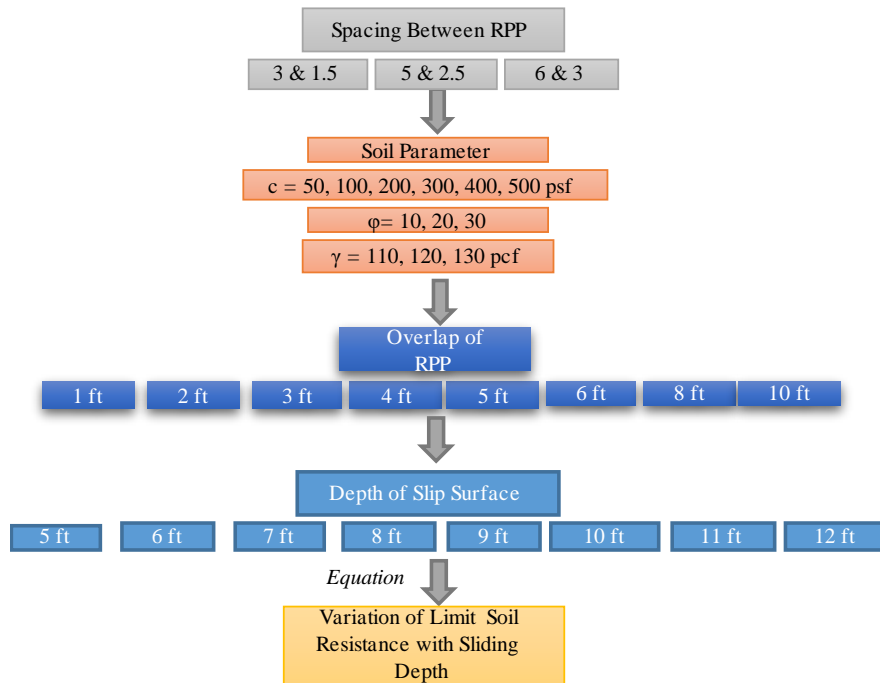


Figure 7.11 Limit Resistance Matrix

The depth of anchorage increases with the decrease of overlap depth. The higher the anchorage provided, the resistance against failure mode 2 increases. This is observed in the variation of limit resistance and overlap depth shown in Figure 7.12. The resistance provided increases with slip surface and the decreases with overlap depth. The depth failure mode 2 governs is observed to extend into deeper slip surfaces. For example, for an overlap depth of 5 ft, the slope is more susceptible to failure due to loss of anchorage after a depth of 10 ft but for an overlap depth of 1 ft, the slope may only be susceptible to failure due to loss of anchorage if the slip surface extends below 13 feet. Therefore, it can be concluded that the lower the overlap, higher resistance is provided against failure due to loss of anchorage.

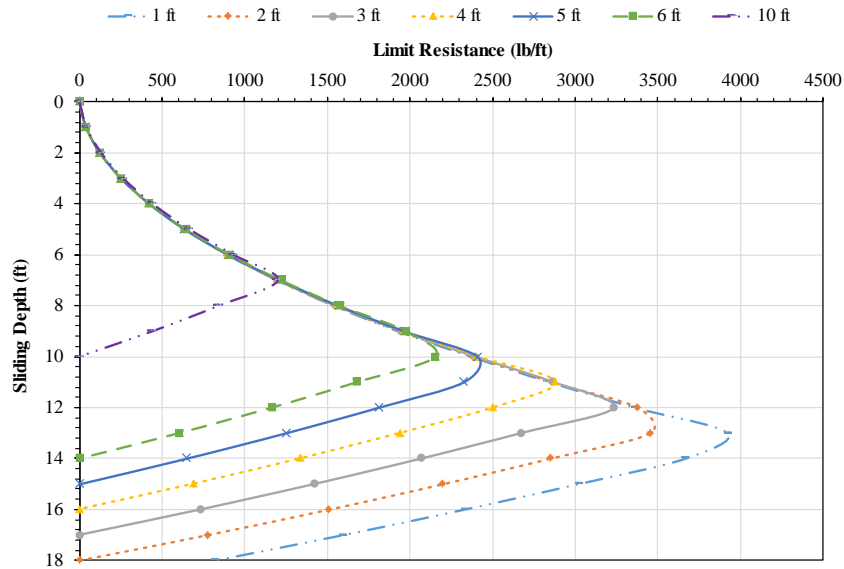
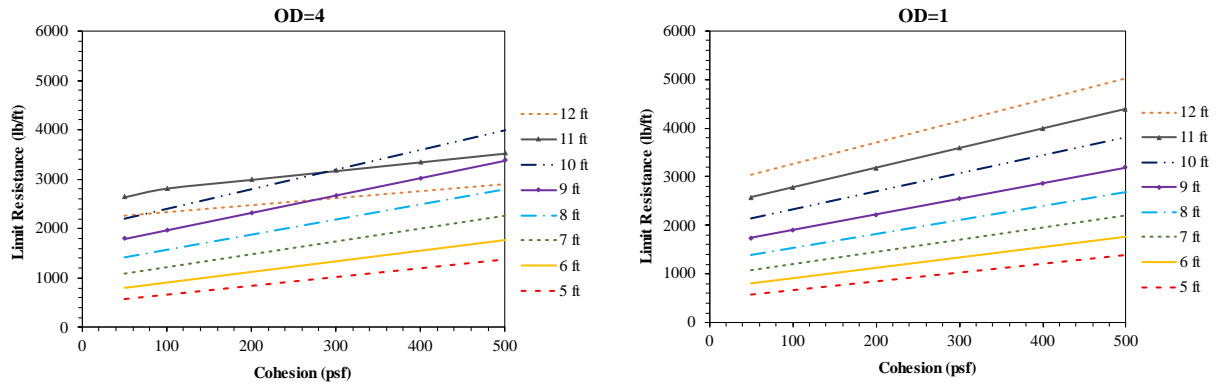


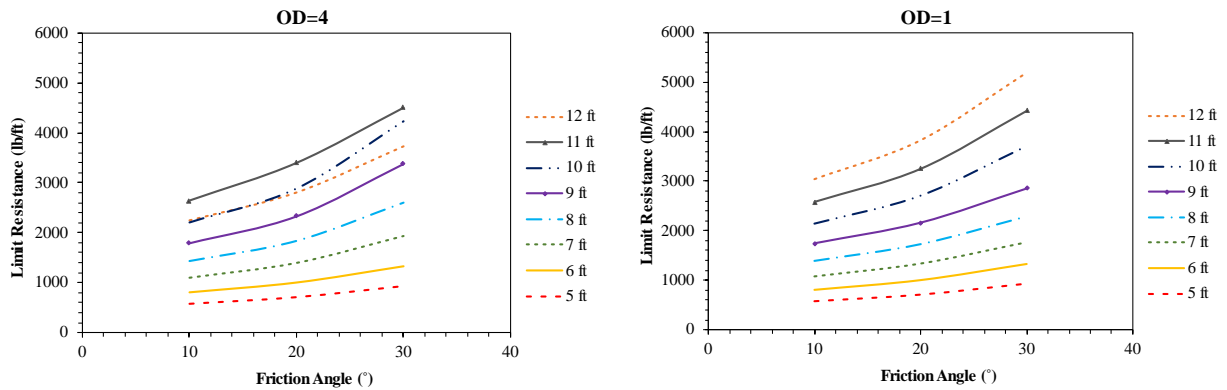
Figure 7.12 Variation of Limit Resistance with Overlap Depth.

The effect of increasing cohesion and friction angle of the soil on the limit resistance with overlap depth of 4 ft and 1 ft was evaluated. It was observed that the increasing of the strength properties increases the limit resistance. This is expected since increasing the strength of the soil provides higher resistance and reduces the chance of failure.

Resistance provided by the reinforcement against failure can also be observed from the following figures. The increasing trend of cohesion with limit resistance was observed to change in gradient for slip surfaces of 11 and 12 in Figure 7.13 (a). A slip surface greater than 11 ft extends under the first layer of reinforcement. Therefore, the resistance decreases but the as shown on Figure 7.13 (b) the resistance increases for the slip surface depth of 11 and 12 with the decrease of overlap. Same trends were observed in the variation of friction angle with limit resistance as shown in Figure 7.14.



(a) (b)
 Figure 7.13 Effect of Cohesion (a) 4 ft OD; (b) 1 ft OD.



(a) (b)
 Figure 7.14 Effect of Friction Angle (a) 4 ft OD; (b) 1 ft OD.

The effect of spacing between the reinforcement was assessed. The variation of limit resistance with spacing for an overlap depth of 1 foot and 4 feet is shown below. Limit resistance is decreasing with the increase of spacing, but the change is negligible. Although spacing is higher at grade, the second layer is improving the resistance provided with the combination spacing. This result is consistent with the factor of safety analysis conducted where the factor of safety had negligible variation with spacing. The negligible change can also be accounted for the use of combination spacing (between the first and the second layer) less than 3 ft c/c. The spacing between the layers is not large enough to show significant change.

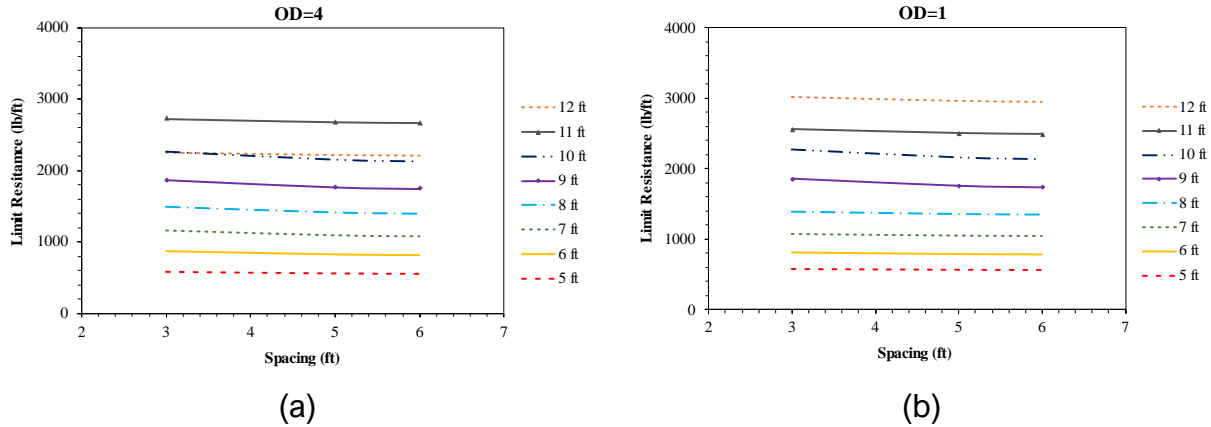


Figure 7.15 Effect of Spacing for Sliding Depths (a) 4 ft OD; (b) 1 ft OD.

7.3 Limit Lateral Displacement and Limit Maximum Flexure

Reinforcing members undergo active pressure and passive resistance of the soil. During failure, an additional soil pressure is exerted on the RPP over the sliding surface. RPP extends into the stiffer strata and obtains extra lateral support from anchorage against failure. But during this process the RPP undergoes a displacement due to the additional pressure during failure. The lateral displacement of RPP depends on the pressure during failure, the anchorage, and active and passive pressures of the soil. The total displacement of the slope will depend on the displacement of the reinforcement. Therefore, it is critical to limit the displacement of RPP.

The modulus of elasticity of RPP is low compared to other structural reinforcing members. Therefore, the slope can be subjected to failure of RPP due to the stress induced by the soil mass above the sliding surface. Failure of the structural member can also occur due to creep. Chen et al., 2007 explored the relationship between the mobilized loads and the design life of RPP. It was concluded that shorter time was required to reach failure when the mobilized loads are close to the ultimate strength of the material. Therefore, it is crucial to limit the maximum flexure experienced by the reinforcing member. According to the

percentage of flexure stress and time to failure presented by the author, the estimated time for creep failure is 100 years if the flexural stress is 35% of the ultimate capacity. Therefore, this criterion is used as the limiting criteria in this study.

Khan (2013) developed design charts to evaluate the load capacity of RPP based on limit resistance of soil, limiting lateral displacement and maximum flexural stress for RPP installed flush to the ground to stabilize shallow slope failures. A series of loads were applied, and the maximum horizontal deformation and maximum bending moment was determined for each case. Slip surface depths ranging from 3 ft to 7 ft was considered in the study with a wide range of soil strength parameters. Similar approach was followed in this study, incorporating the two layered layout and deeper slip surfaces.

The current study explores the effect of the use of two layers to stabilize deeper slope failures. Slip surfaces ranging from 5 ft to 12 ft was considered in this study with overlap depths of 1 ft to 6 ft. Spacing between the reinforcement was not evaluated since negligible change of factor of safety and limit resistance concluded from the previous sections.

Finite element modeling (FEM) was used to evaluate the resistance of RPP. FEM is a simple, accurate and robust method to evaluate the stability and deformation of reinforced slope. Shear strength reduction method have successfully been used to evaluate the stability of slopes reinforced with piles and anchors with the consideration of soil-structure interaction (Khan 2013, Yang et al., 2011, Cai and Ugai, 2003).

The objective of the current study is to develop a design approach to determine the limit resistance of the RPP based on the limiting lateral displacement and the limiting maximum

flexure. Lateral pressures ranging from 100-500 psf was assigned as a uniform load over the depth of slip surface for layer 1 since maximum lateral displacement and maximum bending moment is observed for the layer one during failure (Figure 7.16). One set reinforcement for both layers was utilized to obtain the maximum lateral displacement and the maximum bending moment of RPP. The overlap was varied between the layers to evaluate the effect of the second layer of reinforcement. Shallow slope failures depths typically range from 3-6 feet (Kim et al., 2004). Therefore, slip surfaces ranging from 5 to 12 feet was considered to evaluate the deeper failures. The numerical model matrix utilized is shown in Figure 7.17.

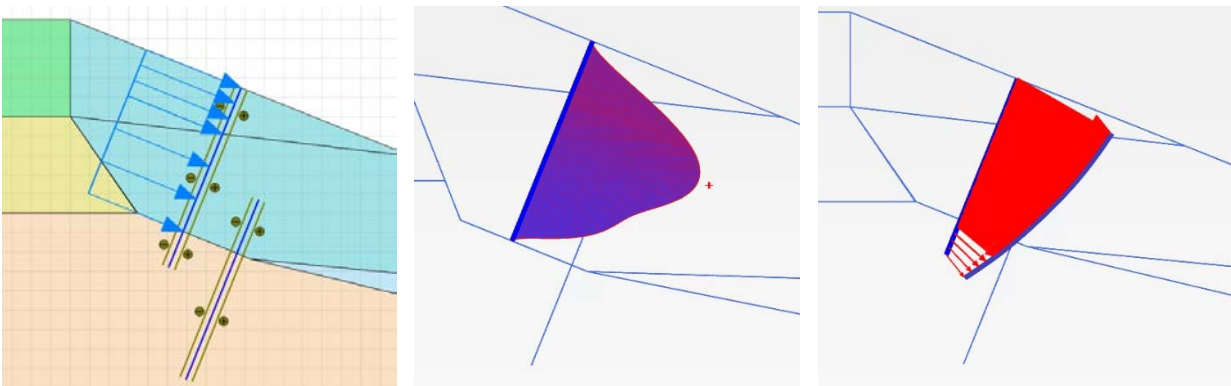


Figure 7.16 Determination of Maximum Bending Moment and Maximum Lateral Displacement

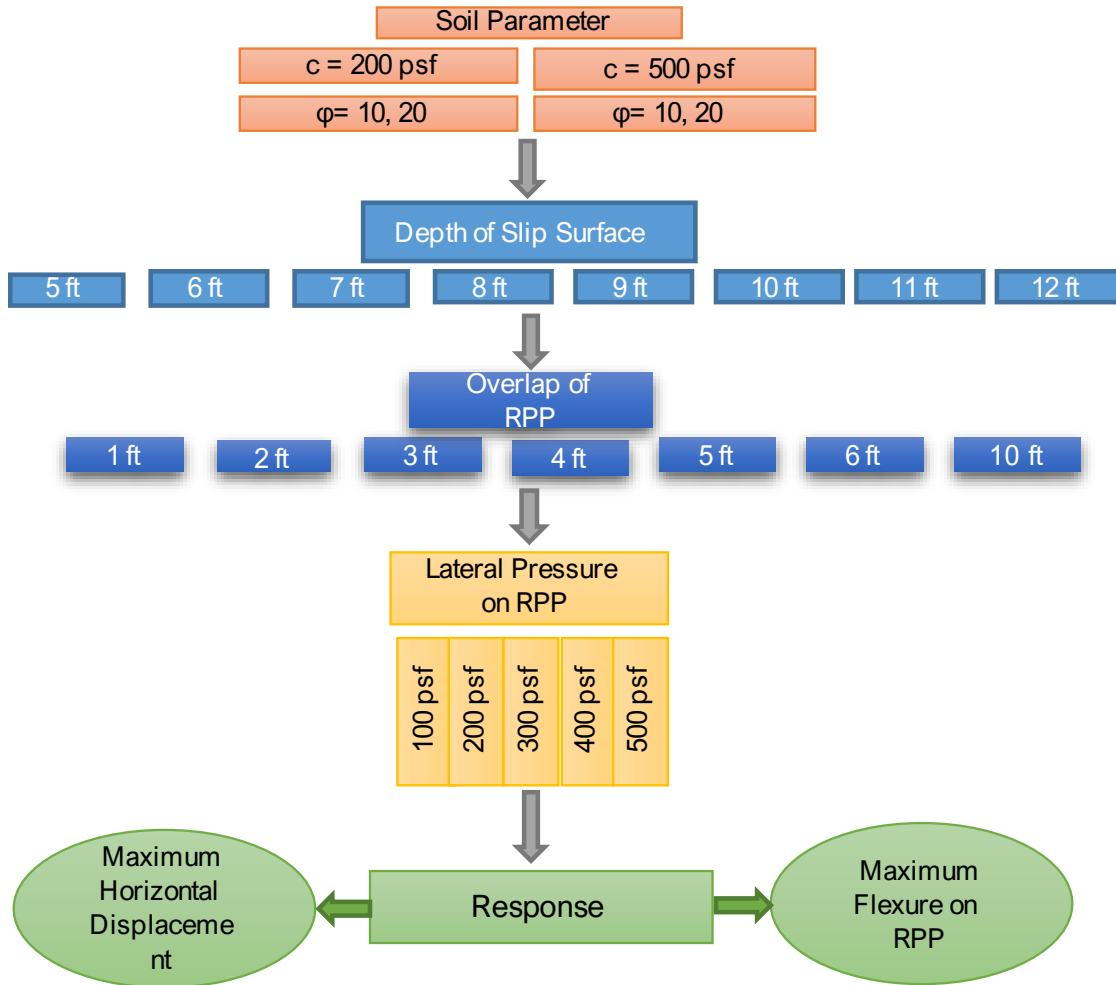


Figure 7.17 Numerical Model Matrix

The variation of maximum lateral displacement with limit resistance for an 8 ft slip surface is shown in Figure 7.18. The lateral displacement was observed to increase with the limit resistance which was determined by increasing increments of lateral load. The increase in displacement is expected as the load increases since additional force is being applied to the model. The effect of the overlap depth was observed. The maximum lateral displacement was observed to increase with the increase of overlap depth. This was also observed in the numerical modeling conducted for the performance of the current study.

The maximum lateral deformation observed at the crest increased with overlap depth but noted to decrease at deeper depths depending on the intersection of the slip surface. The deeper depth effect is not observed in these models since only the maximum lateral displacement was considered. The maximum deformation is considered to obtain the limiting resistance provided by the reinforcement.

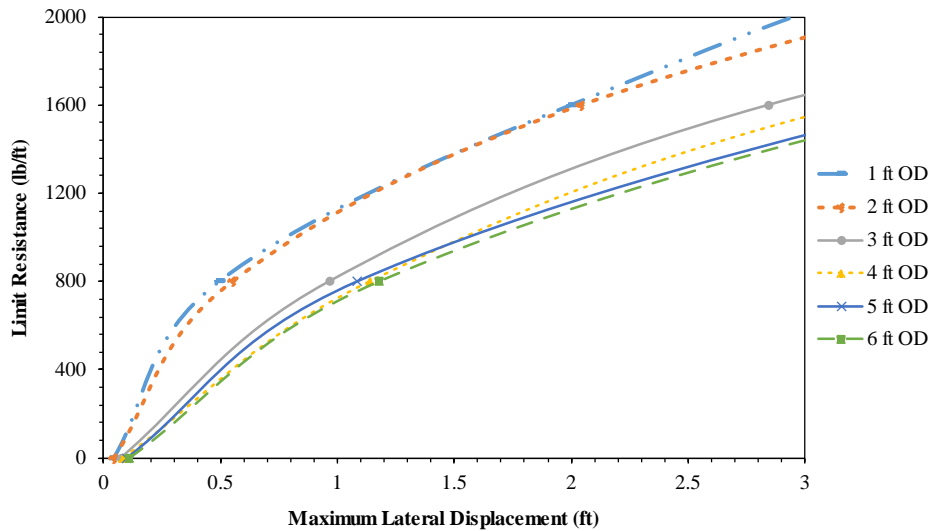


Figure 7.18 Variation of Maximum Lateral Displacement with Limit Resistance for varying Overlap Depths (Slip Surface Depth = 8 ft)

The variation of maximum flexure with limit resistance for an 8 ft slip surface is shown in Figure 7.19. The maximum flexure was also observed to increase with the limit resistance. The anchorage depth decreases with the increase of overlap depth. The bending moment is decreased when the reinforcement has higher anchorage. Therefore, the maximum flexure increasing with overlap depth is expected.

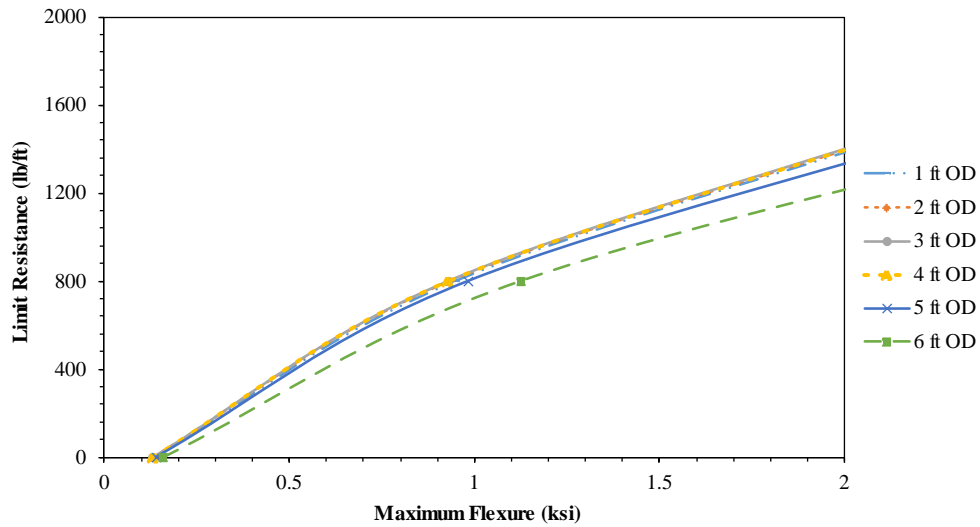


Figure 7.19 Variation of Maximum Flexure with Limit Resistance for varying Overlap Depths (Slip Surface Depth = 8 ft)

Variation of maximum lateral displacement for different overlap depths with cohesion and friction angle was observed. The results for overlap depths of 1 foot and 4 feet are presented below. The maximum lateral displacement decreased with increase of cohesion and friction angle as expected.

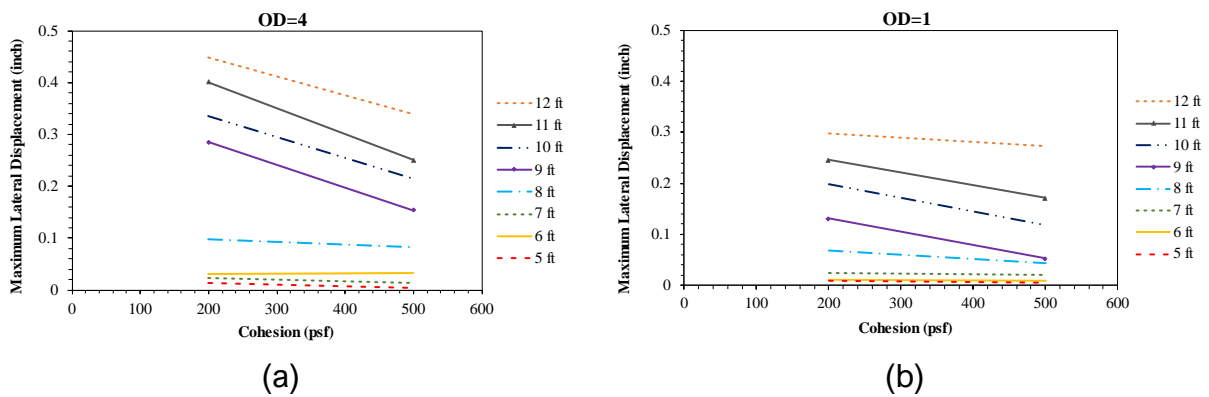
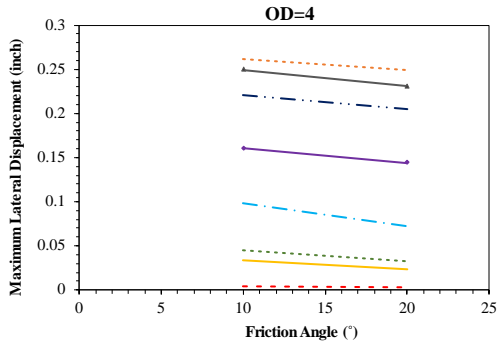
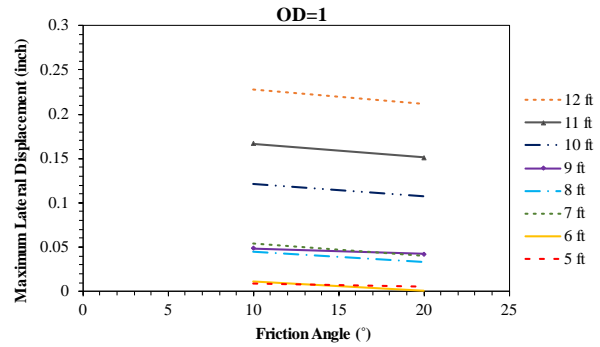


Figure 7.20 Effect of Cohesion on Maximum Lateral Displacement (a) 4 ft OD; (b) 1 ft OD.



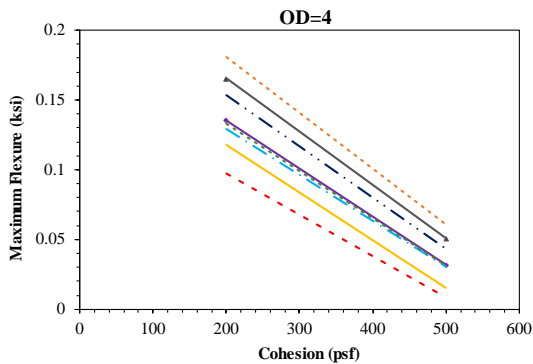
(a)



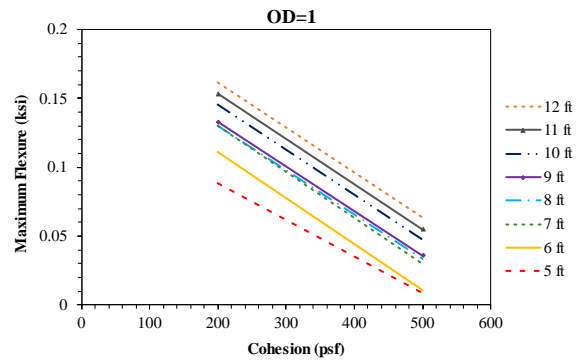
(b)

Figure 7.21 Effect of Friction on Maximum Lateral Displacement (a) 4 ft OD; (b) 1 ft OD.

Variation of maximum flexure for different overlap with cohesion and friction angle was observed. The variation for overlap depths of 1 foot and 4 feet are shown in Figure 7.22 and Figure 7.23 The maximum flexure was observed to decrease with the increase of cohesion and friction angle.

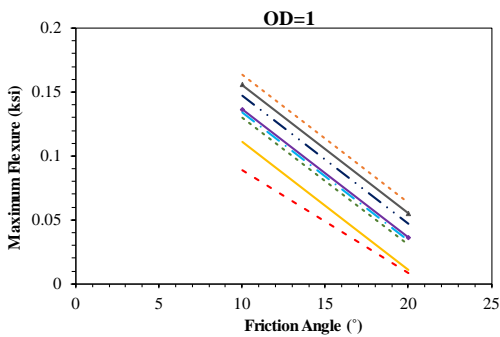


(a)

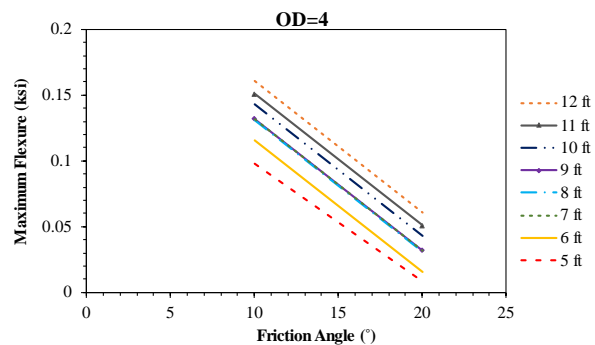


(b)

Figure 7.22 Effect of Cohesion on Maximum Flexure (a) 4 ft OD; (b) 1 ft OD.



(a)



(b)

Figure 7.23 Effect of Friction Angle on Maximum Flexure (a) 4 ft OD; (b) 1 ft OD.

The results obtained from the numerical model was incorporated in statistical modeling to develop design equations to predict limit resistance due to soil failure, maximum lateral displacement, and maximum flexure.

7.4 Statistical Analysis

Analyzing data using a complex equation for different set of variables is time consuming. Finite element modeling is a viable and accurate method to obtain limit resistance values, but it can be time and labor consuming (Ahmed et al., 2020). Statistical modeling of the data acquired can develop a model for prediction of values for a wide range of variables and simplifies the generation of design charts.

In this study, three equations were developed using statistical analysis to obtain the limit resistance of the reinforcement depending on several factors. Comprehensive data set was obtained from numerical modeling and the modified limit resistance equation. Multiple Linear regression (MLR) models were developed from the data and was validated. Statistical models to predict limit resistance based on soil failure, lateral displacement and limit flexure of RPP was developed. Commercially available software RStudio version 4.2.1 was used. The flow of analysis is shown below.

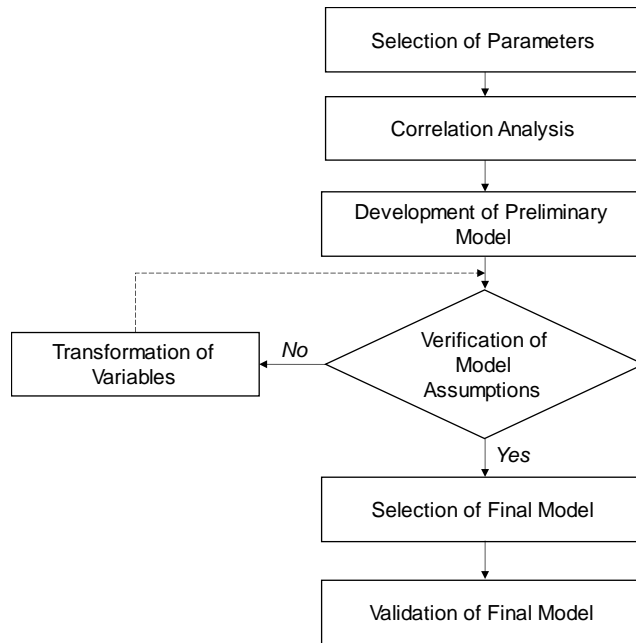


Figure 7.24 Steps of Statistical Model Development

7.4.1 Limit Resistance with Failure modes

7.4.1.1 Selection of Parameters

The predictors were selected based on the input parameters into the equation used for the determination of the limit resistance according to failure modes proposed by Loehr et al., 2007 and Ito and Matsui, 1975. The objective of modifying the existing equation using statistical analysis was to incorporate the overlap depth for the consideration of deeper slip surfaces. The analysis was conducted separately for different overlap depths to adequately evaluate the change of resistance.

In order to develop a reliable statistical model, the predictors should not be highly correlated to each other. If the predictors are highly correlated to each other, it could lead to higher variance, smaller coefficient of regression, and unreliable response outcomes (Stevens, 1996). The limit resistance was modeled as the response outcome for varying

overlap depths with cohesion, friction angle, unit weight, spacing and slip surface depth as predictors. The soil parameters of the layer over the slip surface were considered.

The parameters are denoted as follows:

LR = Limit Resistance

C = Cohesion (psf)

F = Friction angle (degrees)

SS = Slip Surface (ft)

S = Spacing (ft)

UW = Unit Weight (pcf)

OD = Overlap Depth (ft)

7.4.1.2 Correlation Analysis

During a regression analysis, the predictors should have less correlation between themselves and the response variable. Correlation analysis was conducted to determine if the predictors and the response variable is highly correlated. Several problems in statistical models arise due to multicollinearity including large variances, higher R^2 values, and standard errors sensitive to small changes. The Pearson Correlation coefficients was obtained to determine the correlation between variables. According to Kutner et al., (2015), any correlation less than 0.7 is considered weak. And a rule of thumb, correlations between low predictor variables is below -0.9 or above +0.9. The correlation was found to be zero indicating no correlation between independent variables.

Another method to determine collinearity is analyzing the Variance Influence Factor (VIF). According to Shrestha (2020) if the VIF is less than 1, the variables are not related to each

other and if $1 < VIF < 5$, the values are moderately correlated. All the predictor variables had a variance factor of 1 indicating the absence of collinearity.

The signs observed in the correlation indicates the linear strength between the response and the predictor variables. The statistical analysis showed that the cohesion and friction angle showed positive correlation with the limit resistance. This means that an increase of cohesion and friction angle increases the limit resistance. Likewise, spacing has a negative correlation to limit resistance where the closer spacing provides higher resistance against failure. The correlation for slip surface was ignored since it was observed that the slip surface does not have a linear relationship with limit resistance.

Table 7.5 Correlation between Predictors and Outcome Variables.

OD	C	F	SS	UW	S
1	0.19	0.24	0.56	0.07	-0.06
2	0.2	0.24	0.56	0.07	-0.07
4	0.21	0.25	0.54	0.07	-0.07
6	0.24	0.26	0.53	0.07	-0.09
8	0.27	0.28	0.5	0.07	-0.11
10	0.33	0.33	0.49	0.06	-0.16
VIF	1	1	1	1	1

7.4.1.3 Development of Preliminary Model

The preliminary model was developed since no multicollinearity was observed between the predictors and the outcome variable. The preliminary MLR model was formulated as follows for limit resistance due to failure modes as follows:

$$LR = \beta_0 + \beta_1 C + \beta_2 F + \beta_3 SS + \beta_4 UW + \beta_5 S$$

The correlation coefficients β_1 , β_2 , β_3 , β_4 , and β_5 , will be determined through regression analysis by reducing the sum of square errors for the model data. β_0 is an added constant

to account for the error in prediction. The correlation coefficients for the predictors explains the mean response per unit change of variable when all the other variables are kept constant.

Multi linear regression (MLR) analysis was conducted from the data obtained from modified limit resistance equation. The summary of analysis of variance (ANOVA) and parameter estimates are shown in the tables below. The coefficients of the predictors should follow the sign convention are expected to follow the results a discussed above. Th coefficients indicate the unit change of the outcome with the increase or decrease of the predictor. The p- values for the predictors indicate the level of significance of that predictor in the model. All p-values were low indicating high significance of all parameters in the model. The preliminary R^2 value was low with high residual error but expected due to the presence of the variable SS which had a non-linear relationship with LR. Transformation is required.

The coefficients for the preliminary fitted MLR equation are shown below:

Table 7.6 Parameter Estimates of Preliminary Model for Varying Overlap Depths.

OD	β_0	β_1	β_2	β_3	β_4	β_5
1	-2591.43	2.20	54.63	201.86	16.70	-90.98
2	-2360.57	2.12	50.95	194.21	15.16	-89.41
4	-1907.62	1.89	43.58	178.34	12.25	-84.27
6	-1502.75	1.74	36.67	161.03	9.61	-78.75
8	-1141.56	1.58	31.86	145.78	7.37	-80.54
10	-856.54	1.52	29.50	139.63	5.44	-92.49

Table 7.7 ANOVA Summary of Preliminary Model for Varying Overlap Depth.

OD	Residual Standard Error	Multiple R2	Adjusted R2	F statistic	p-value
1	1414	0.4209	0.4199	423	< 2e-16
2	1303	0.4186	0.4176	395.7	< 2.2e-16
4	1085	0.4148	0.4135	3.44E+02	< 2.2e-16
6	879.7	0.4138	0.4124	2.97E+02	< 2.2e-16
8	707.5	0.4172	0.4155	2.54E+02	<2e-16
10	525.5	0.4878	0.486	2.77E+02	<2e-16

The preliminary model is to be verified using several multi-linear regression analysis assumptions. The model has to satisfy the normality of residuals, outliers, constant error variance, and multicollinearity among the predictor variables (Kutner et al., 2005, Faysal, 2017, Bhandari, 2021). The assumptions are as follows.

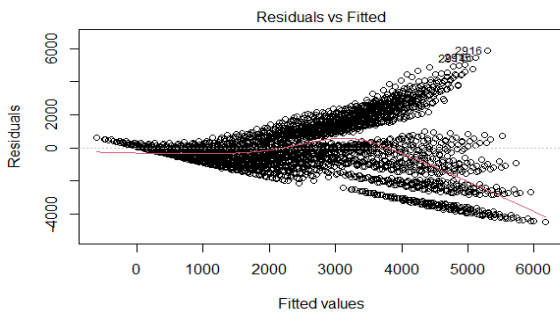
- Linear relationship between response and predictor variables
- Constant variance of residuals
 - Breusch Pagan Test ($p > 0.01$: Homoscedastic Data)
 - Residuals vs. fitted plot
- Normal Distribution of residuals
 - Jarque Bera normality test ($p > 0.01$: Normal Distribution)
 - Density plot of residuals
- Collinearity of residuals
 - Variance Inflation Factor (VIF)

7.4.1.4 Verification of Preliminary Model

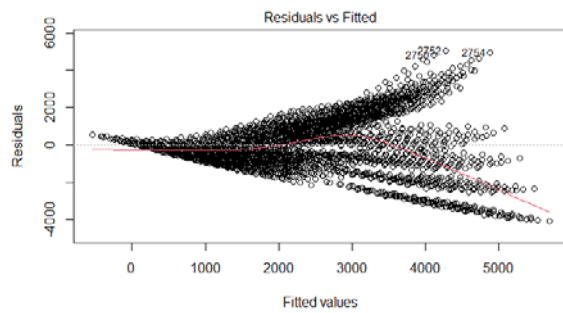
Constant Error Variance

The residuals vs fitted values plot from R-Studio was used to analyze if constant error variance or heteroscedasticity is present in the model. The expected results are that the residuals are randomly scattered without a clear trend. A curvilinear trend or a funnel shape in the residuals indicate that the model is heteroscedastic. Transformation of variables is required in the case of heteroscedastic observation. The residual vs. fitted values plots for Limit resistance of varying overlap depths for the preliminary models are shown in Figure 7.25.

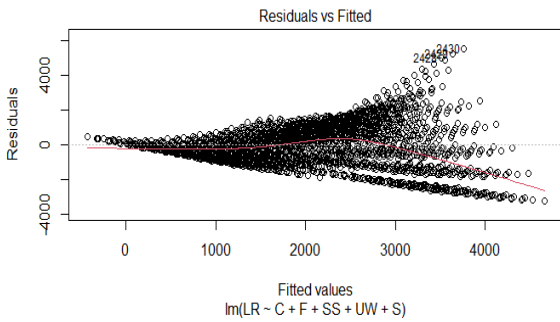
Heteroscedasticity refers to the unequal distribution of error terms or residuals. Furthermore, it refers to the systemic change in the spread of residuals over the range of fitted values as observed in the plot below. Funnel shaped residual plots were observed for all ODs indicating heteroscedastic data.



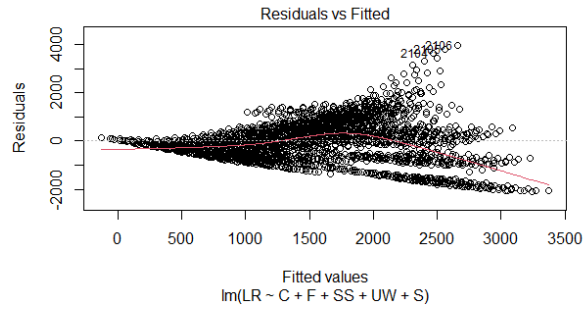
OD=1



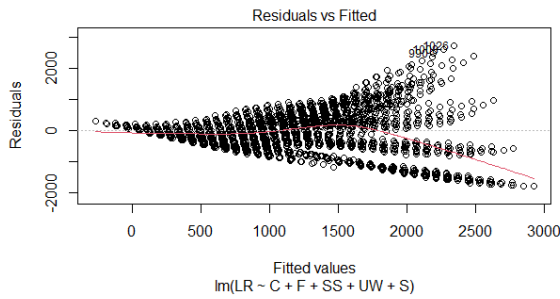
OD=2



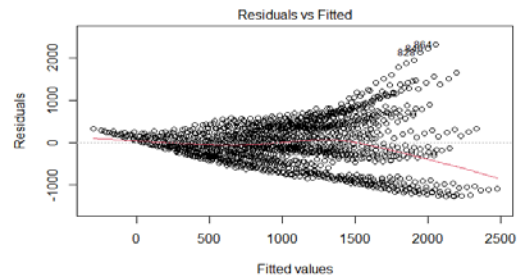
OD=4



OD=6



OD=8



OD=10

Figure 7.25 Residuals vs. Fitted Values for the Preliminary Model.

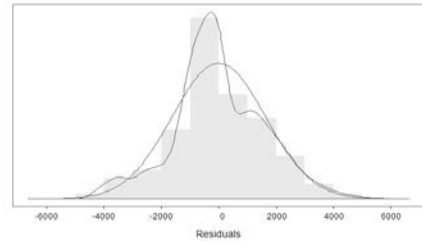
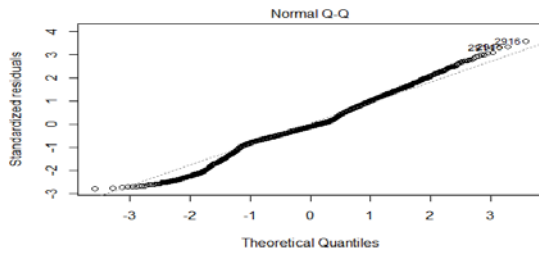
Normality

The residuals in the MLR model should be normally distributed. The Normal Q-Q plot and density plots in R Studio is a method of visual observation to determine if the residuals are normally distributed. Normal data will lie mostly along a straight diagonal line with minor deviations. Figure 7.26 shows the normality plots and the density plots for the preliminary equations. The results show slightly skewed density plots and normal plots with variations from the diagonal including short and long tails.

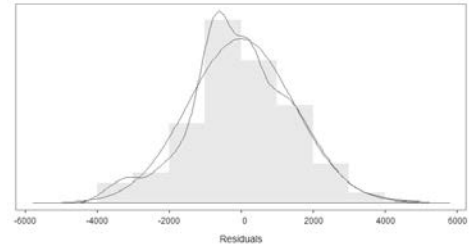
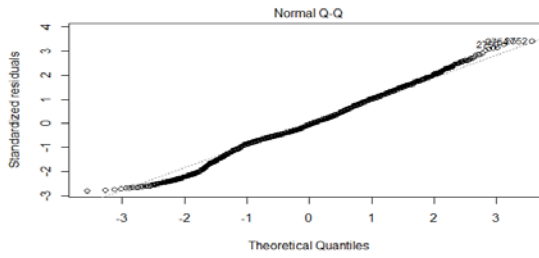
Normality Plot

Density Plot

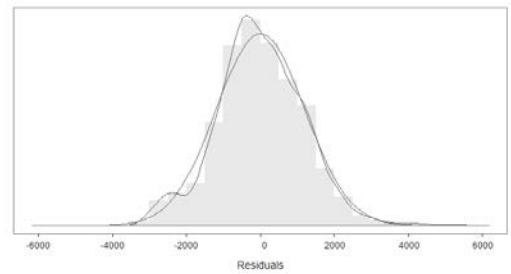
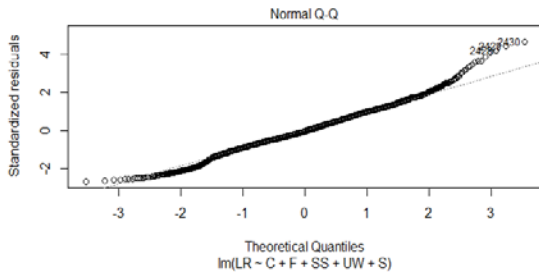
OD=1



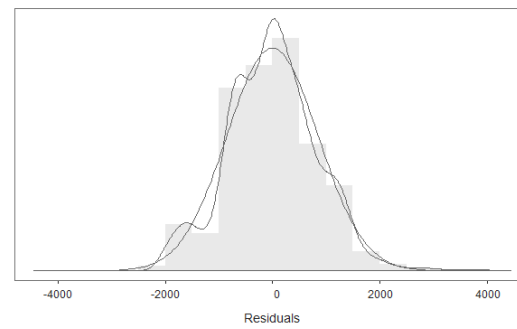
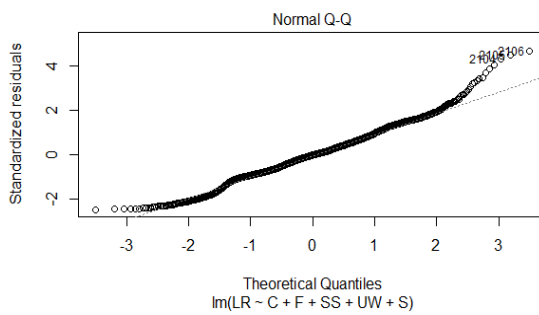
OD=2



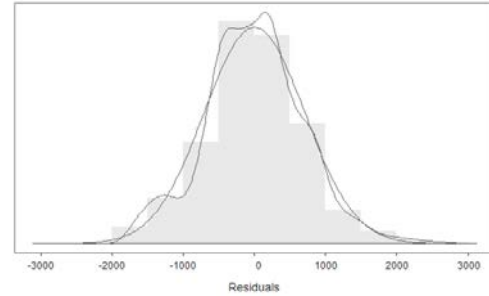
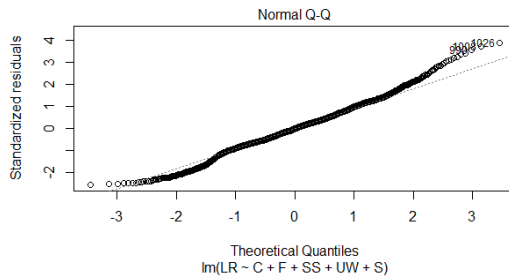
OD=4



OD=6



OD=8



OD=10

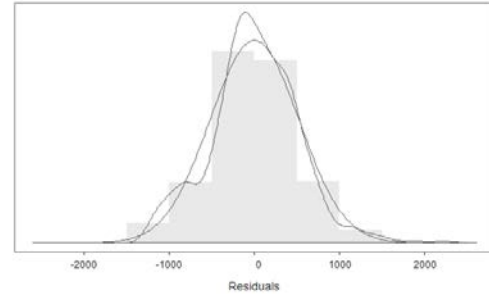
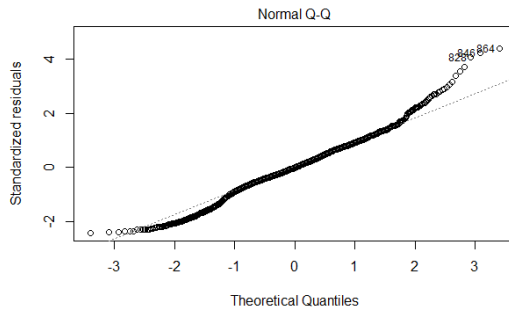


Figure 7.26 Normality Probability Plots and Density Plots for Preliminary Model.

Multicollinearity

Variance Influence Factor (VIF) is used to determine if the predictors are correlated to each other. The method uses ordinary least squares regression analysis method to determine the collinearity between variables. According to Shrestha (2020) if the VIF is less than or equal to 1, the variables are not related to each other and if $1 < \text{VIF} < 5$, the values are moderately correlated. The VIF for all the predictor variables show were found as one which indicated no correlation.

Outlier Test

An outlier is a value or data point that is significantly different from other data points. Outlier data is possible due to variability in observed data points. Outliers can be tested using several methods in R-studio.

Cooks distance was utilized to detect and remove outliers in this study. This method is commonly used to detect outliers that negatively influences the model (Cook, 1977). The

method uses each observations leverage and residuals to calculate the influence on the model. If the observations have higher leverage, the point is likely to be an outlier. The threshold of a cook's distance is greater than $4/n$ was used in this study. Where n is the number of observations.

The outliers detected in the model was removed after examining if the outliers showed any pattern or simply erroneous data. Figure 7.27 shows the plot for the cook's distance. The points above the threshold line were removed. It was observed that 6% of the data was found as outliers.

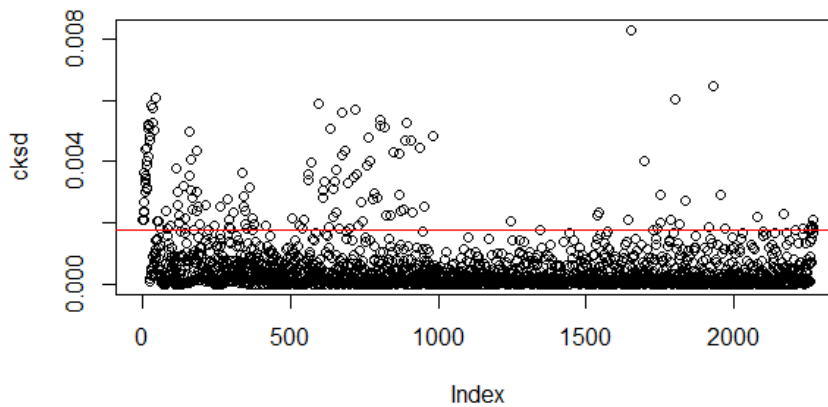


Figure 7.27 Cook's Distance plot for Preliminary Model (5 ft OD).

7.4.1.5 Transformation of Variables

The preliminary model did not satisfy the constant error variance assumption and the normality assumption. Therefore, transformation of response variable was conducted after the removal of the outliers.

The optimum transformation variable was found using the box-cox plot method in R studio. Box cox transformation is generally used to transform a data set that is not normally distributed to a normally distributed dataset. This method finds a value λ that will

transform the data to normally distributed as possible. The optimum value for 5 ft OD preliminary model transformation was obtained as 0.0606 (λ -values) as shown in Figure 7.28. Lambda for all other overlap depth equations were found similarly.

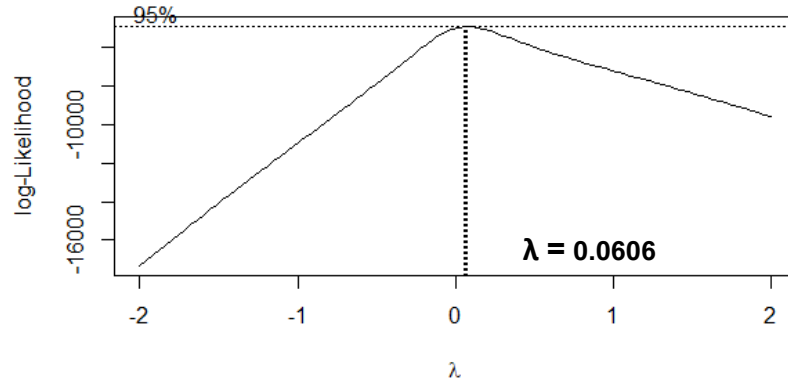


Figure 7.28 Box-Cox Plot for Transformation of Response Variable (5 ft OD) ($\lambda = 0.0606$)

The outcome variable is transformed using the lambda value as follows:

$$(y^\lambda)^{-1/\lambda} = x$$

The preliminary model was transformed using the λ value.

The equations also did not satisfy the constant variance assumption and showed clear funnel shaped normality plots. It was observed from the composite limit resistance for the failure modes that the relationship between the limit resistance and the slip surface shows almost a quadratic relationship. Therefore, it was inferred that the slip surface depth was predictor variable affecting the variability of errors. Square-root transformation was selected to transform the equations to incorporate the curvilinear relationship.

The MLR model analysis and ANOVA results for the transformed model are shown in Table 7.8 and Table 7.9. The adjusted R^2 values were all greater than 0.96 which signifies that more than 96% of the predicted data has been fitted. All predictors were found to be significant with very low p-values. The p-value for the final model was also very low

indicating that the coefficients predicted are the best possible for the inputted data. The residual error was also seen to decrease significantly compared to the preliminary model. The final fitted MLR equation is as follows with the coefficients in Table 7.8;

$$\frac{LR^{\lambda}-1}{\lambda} = \beta_0 + \beta_1C + \beta_2F + \beta_3SS + \beta_4UW + \beta_5S + \beta_6SS^2$$

Table 7.8 Parameter Estimates of the Final Model.

OD	β_0	β_1	β_2	β_3	β_4	β_5	β_6	lambda
1	2.514	0.0020	0.0327	1.0448	0.0098	-0.050	-0.043	0.0606
2	2.379	0.0022	0.0357	1.1471	0.0091	-0.073	-0.051	0.0606
4	2.312	0.0021	0.0333	1.2137	0.0090	-0.061	-0.060	0.0606
6	2.091	0.0023	0.0339	1.3629	0.0089	-0.065	-0.078	0.0606
8	1.936	0.0025	0.0362	1.5679	0.0083	-0.082	-0.105	0.0606
10	1.827	0.0037	0.0541	2.1342	0.0096	-0.161	-0.171	0.101

Table 7.9 ANOVA Summary of the Final Model.

OD	Residual Standard Error	Multiple R2	Adjusted R2	F statistic	p-value
1	0.2644	0.9716	0.9715	1.55E+04	< 2e-16
2	0.2637	0.9709	0.9708	1.43E+04	< 2.2e-16
4	0.2625	0.9694	0.9693	1.20E+04	< 2.2e-16
6	0.2476	0.9704	0.9703	1.07E+04	< 2.2e-16
8	0.2453	0.9684	0.9682	8.49E+03	<2e-16
10	0.3224	0.963	0.9629	5.88E+03	<2e-16

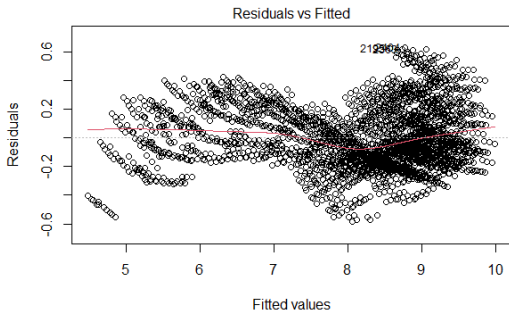
The final model will be checked for the verification of assumptions.

7.4.1.6 Verification of Final Model

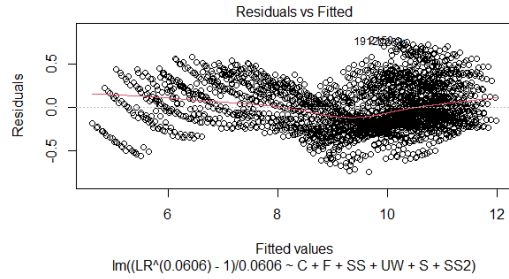
Constant Error Variance

Random scatter of residual values was observed from the transformed plot as shown in Figure 7.29. Breusch-Pagen test was conducted for further analysis. The p-value was

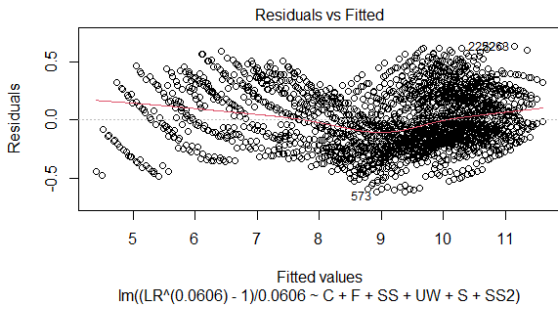
0.01397 which is greater than $\alpha=0.01$, therefore, the null hypothesis was rejected. The residual values are not heteroscedastic.



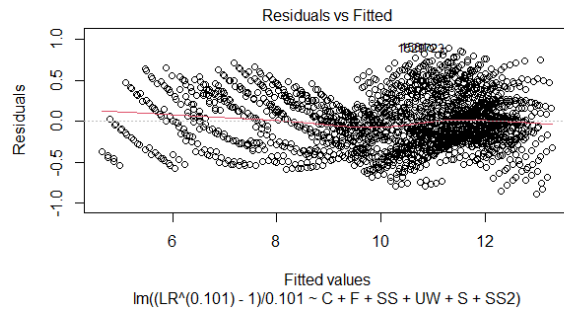
OD=1



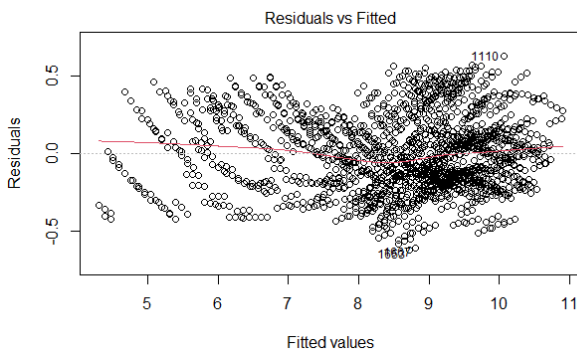
OD=2



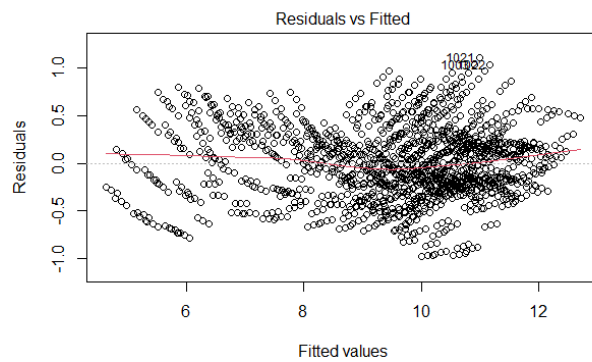
OD=4



OD=6



OD=8



OD=10

Figure 7.29 Residual vs. Fitted Values Plot for Final Model

Normality Test

The transformed model was tested for normality. The normal plot for residuals was inspected. The values follow the straight line, with short tails indicating minimum skewness. The density plot of the residuals shown in Figure 7.30 shows that the residuals are normally distributed.

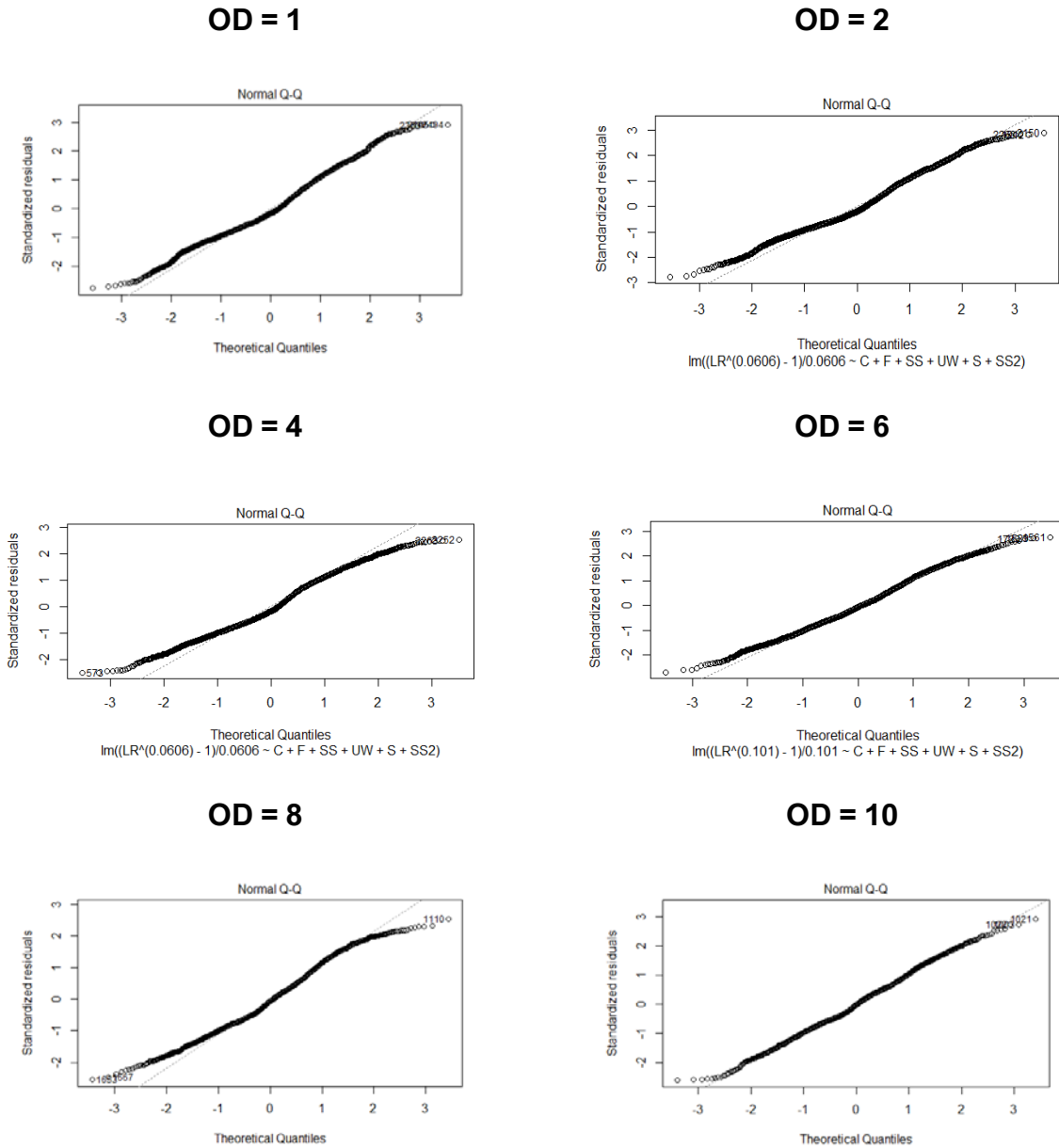


Figure 7.30 The Normal Plot for Final Model.

Multicollinearity

The Variance of Influence values were calculated for the transformed model. The values are shown in Table 7.5. The VIF values indicated that there was no multicollinearity between predictor variables.

Outliers

Bonferroni test was conducted to test for outliers in the transformed model. No variables were flagged as potential outliers.

7.4.1.7 Selection of Final Model

Best Subset Selection

The best subset was selected according to the significance of the independent variable and the value of adjusted R^2 . The significance of the independent variable is shown in Table 7.9 using the p-values. The smaller the p-value, higher the significance for the prediction model. The best subset was found to be the one with all the predictors. All predictors were found to be significant.

7.4.1.8 Validation of Final Prediction Model

The final prediction model was tested using a different set of data obtained from the numerical model. Figure 7.31 shows the variation of values from the numerical model and the prediction model. It was observed that the variation of the limit resistance could be explained more than 95% for all overlap depths.

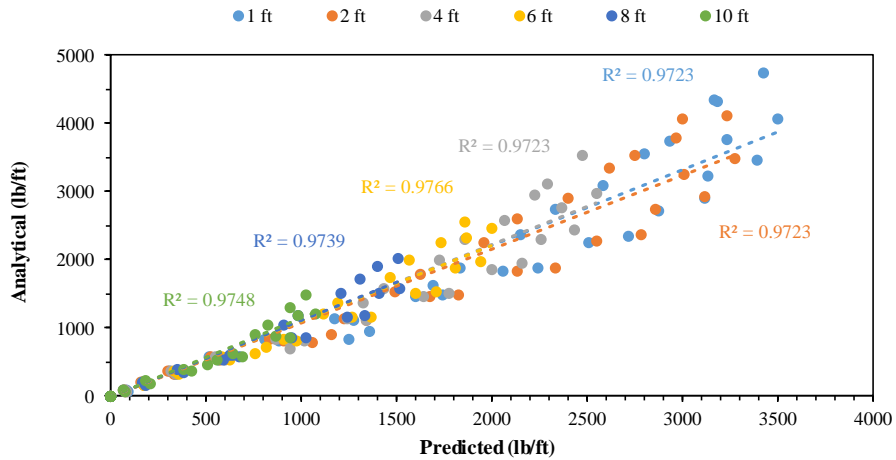


Figure 7.31 Validation of the Final Model.

The plot with the use of the equations for the different overlap is shown below.

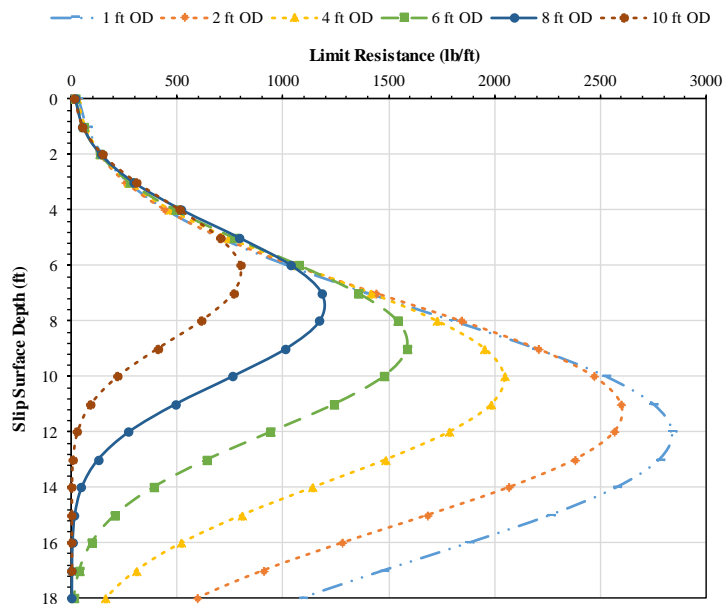


Figure 7.32 Variation of Limit Soil Resistance and Slip Surface Depth ($c=60$ psf, $\phi=12^\circ$)

7.4.2 Maximum Lateral Displacement

7.4.2.1 Selection of Parameters

The predictors were selected based on the input parameters into the finite modeling to obtain the maximum lateral displacement for given loads. In order to develop a reliable statistical model, the predictors should not be highly correlated to each other. If the

predictors are highly correlated to each other, it could lead to higher variance, smaller coefficient of regression, and unreliable response outcomes (Stevens, 1996). The maximum lateral displacement was modeled as the response outcome with cohesion, friction angle, overlap depth, limit resistance and slip surface depth as predictors. The cohesion and friction angle were considered of the soil over the slip surface.

The parameters are denoted as follows:

MD=Maximum Lateral Displacement

LR = Limit Resistance

C = Cohesion (psf)

F = Friction angle (degrees)

OD = Overlap Depth (ft)

SS = Slip Surface (ft)

7.4.2.2 Correlation Analysis

During a regression analysis, the predictors should have less correlation between themselves and the response variable. Correlation analysis was conducted to determine if the predictors and the response variable is highly correlated. Several problems in statistical models arise due to multicollinearity including large variances, higher R^2 values, and standard errors sensitive to small changes. The Pearson Correlation coefficients was obtained to determine the correlation between variables. According to Kutner et al., (2015), any correlation less than 0.7 is considered weak. And a rule of thumb, correlations between low predictor variables is below -0.9 or above +0.9. The correlation between

individual predictors is shown in Table 7.10. There is no significant collinearity observed between predictor variables, all values range between -0.9 and +0.9.

Another method to determine collinearity is analyzing the Variance Influence Factor (VIF). According to Shrestha (2020) if the VIF is less than 1, the variables are not related to each other and if $1 < VIF < 5$, the values are moderately correlated. All the predictor variables show low correlation.

Table 7.10 Correlation between Predictor Variables

Variables	C	F	SS	OD	LR	VIF
C	1.000	-0.500	0.000	0.000	0.000	1.333
F	-0.500	1.000	0.000	0.001	0.000	1.333
SS	0.000	0.000	1.000	0.000	0.340	1.134
OD	0.000	0.000	0.000	1.000	0.000	1.000
LR	0.000	0.000	0.340	0.000	1.000	1.134

The signs observed in the correlation indicates the linear strength between the response and the predictor variables. The statistical analysis showed that the cohesion and friction angle showed negative correlation with the lateral displacement. This means that an increase of cohesion and friction angle decreases the lateral displacement. Likewise, limit resistance, overlap depth and slip surface have a positive correlation to lateral displacement. The maximum lateral displacement was observed to have the highest correlation to limit resistance which means that the limit resistance could affect most of the variability in the prediction model.

Table 7.11 Correlation Limit Resistance and Predictor Variables

	LR	C	F	SS	OD	MD
MD	0.820	-0.130	0.060	0.480	0.110	1.000

7.4.2.3 Development of Preliminary Model

There was no multicollinearity observed between the predictors and the outcome variable. A preliminary MLR model was formulated as follows for the Maximum Lateral Displacement as follows:

$$MD = \beta_0 + \beta_1 C + \beta_2 F + \beta_3 SS + \beta_4 OD + \beta_5 LR$$

The correlation coefficients β_1 , β_2 , β_3 , β_4 , and β_5 , will be determined through regression analysis by reducing the sum of square errors for the model data. β_0 is an added constant to account for the error in prediction. The correlation coefficients for the predictors explains the mean response per unit change of variable when all the other variables are kept constant.

Multi linear regression (MLR) analysis was conducted from the data obtained from the finite element model. The summary of analysis of variance (ANOVA) and parameter estimates are shown in the tables below. The coefficients of the predictors should follow the sign convention are expected to follow the results obtained by parametric study and numerical modeling. The cohesion and friction angle were observed to have negative correlation as expected indicating that the increase of these values decrease the maximum lateral displacement. The limit resistance, overlap depth and slip surface have a positive correlation to lateral displacement showing that the increase of the mentioned parameters will increase the maximum lateral displacement. The correlations obtained were as expected. The p- values were less. The model showed that friction angle was less significant on the outcome. The preliminary R^2 value is acceptable.

The preliminary fitted MLR equation is shown below:

$$MD = -7.4991 - 0.0078C - 0.0155F + 0.8000SS + 0.4917OD + 0.0058LR$$

Table 7.12 Parameter Estimates of Preliminary Model

	Coefficient	Std. Error	t-value	Pr(> t)
Intercept	-7.4991	1.2967	-5.783	1.21E-08
C	-0.0078	0.0014	-5.709	1.83E-08
F	-0.0155	0.0411	-0.377	0.706
SS	0.8000	0.0780	10.252	< 2e-16
OD	0.4917	0.0983	5.001	7.61E-07
LR	0.0058	0.0002	33.15	< 2e-16

Table 7.13 ANOVA Summary of Preliminary Model

Residual Standard Error	R²	Adjusted R²	F-statistic	p-value
4.03	0.7484	0.7462	339.2	<2.2e-16

The preliminary model is to be verified using several multi linear regression analysis assumptions. The model has to satisfy the normality of residuals, outliers, constant error variance, and multicollinearity among the predictor variables (Kutner et al., 2005, Faysal, 2017, Bhandari, 2021). The assumptions are as follows.

- Linear relationship between response and predictor variables
- Constant variance of residuals
 - Breusch Pagan Test ($p > 0.01$: Homoscedastic Data)
 - Residuals vs. fitted plot
- Normal Distribution of residuals
 - Shapiro-wik normality test ($p > 0.01$: Normal Distribution)
 - Density plot of residuals
- Collinearity of residuals
 - Variance Inflation Factor (VIF)

7.4.2.4 Verification of Preliminary Model

Constant Error Variance

The residuals vs fitted values plot from R-Studio was used to analyze if constant error variance or heteroscedasticity is present in the model. The expected results are that the residuals are randomly scattered without a clear trend. A curvilinear trend or a funnel shape in the residuals indicate that the model is heteroscedastic. Transformation of variables is required in the case of heteroscedastic observation. The residual vs. fitted values plot for the lateral displacement model is shown in Figure 7.33.

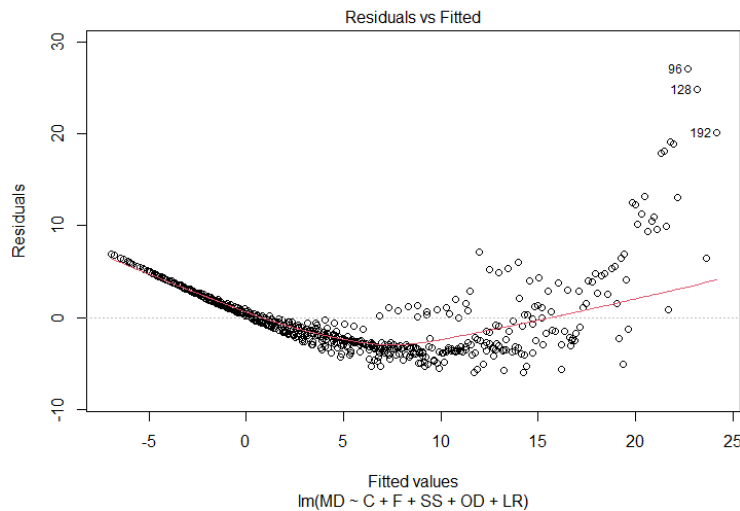


Figure 7.33 Residuals vs. Fitted Values for the Preliminary Model.

The curvilinear trend is seen in the results of the fitted values vs the residuals. Therefore, a transformation is needed since the results show an absence of constant error variance. Studentized Breusch-Pagan test was conducted to further analyze if heteroscedasticity is present in the regression analysis. Heteroscedasticity refers to the unequal distribution of error terms or residuals. Furthermore, it refers to the systemic change in the spread of residuals over the range of fitted values as observed in the plot above.

The p-value for the Breusch-Pagan test (Breusch and Pagan 1979) was less than $5.85e-15$, which is smaller than $\alpha=0.01$. Therefore, the null hypothesis was rejected, suggesting that the residuals are heteroscedastic.

Normality

The residuals in the MLR model should be normally distributed. The Normal Q-Q plot and density plots in R Studio is a method of visual observation to determine if the residuals are normally distributed. Normal data will lie mostly along a straight diagonal line with minor deviations. Figure 7.34 and Figure 7.35 shows the normality plot and the density plot for the preliminary equation. The bow shape observed in the plot indicates excessive skewness. This observation is verified from the density plots where the data is observed to be left skewed.

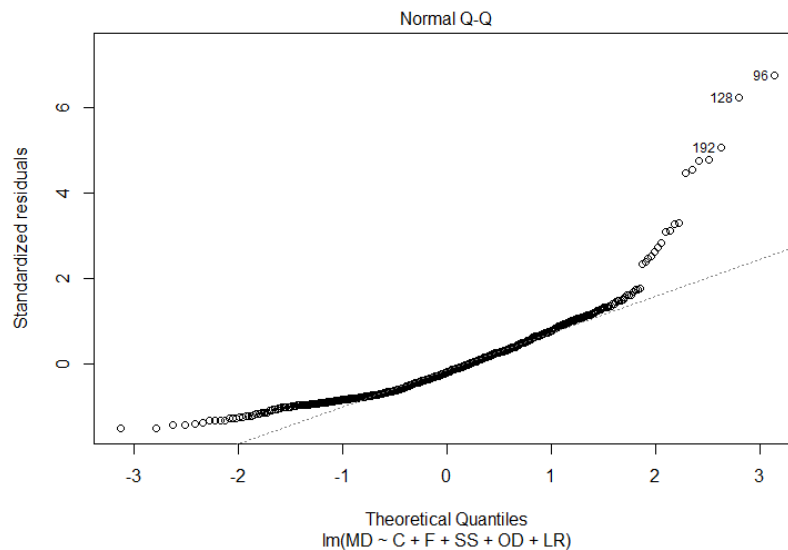


Figure 7.34 Normality Probability Plot for Preliminary Model

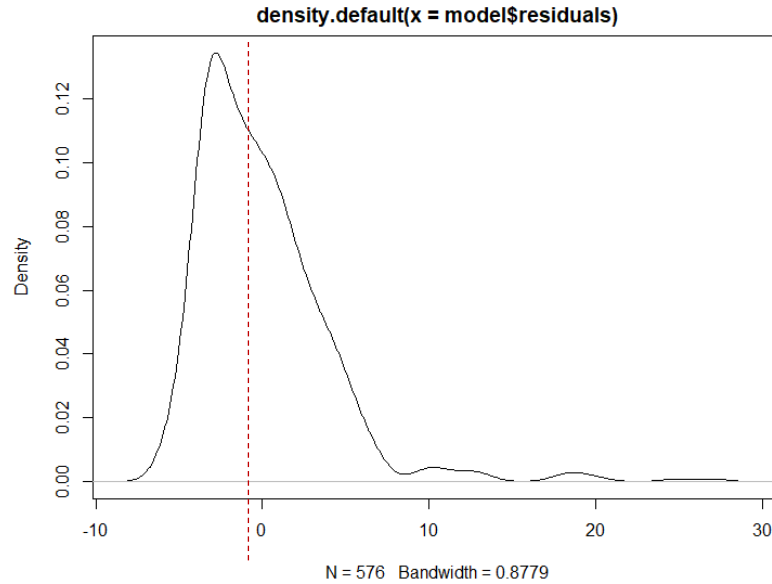


Figure 7.35 Density Plot for Preliminary Model.

Further verification was conducted using the Shapiro-Wik (Shapiro and Wik 1965) normality test in R-studio. The test estimated a p-value of 2.20.e-16 which is less than $\alpha = 0.01$. Therefore, the null hypothesis of this method was rejected indicating that the residuals are not normally distributed.

Multicollinearity

Variance Influence Factor (VIF) is used to determine if the predictors are correlated to each other. The method uses ordinary least squares regression analysis method to determine the collinearity between variables. According to Shrestha (2020) if the VIF is less than 1, the variables are not related to each other and if $1 < \text{VIF} < 5$, the values are moderately correlated. All the predictor variables show low correlation to no correlation.

Outlier Test

An outlier is a value or data point that is significantly different from other data points. Outlier data is possible due to variability in observed data points. Outliers can be tested using several methods in R-studio.

Bonferroni outlier test was conducted to detect outliers. The influence of the outliers must be determined to understand the effect of removing the outliers on the response variable. The influence of outliers in the preliminary model was determined using the DFFITS (Difference in Fits), and Cook's distance.

DFFITS model was proposed by Welsch and Kuh (1977). The model quantifies the change of the fitted values with the number of standard deviations when the outlier is removed. The observed outlier was influential is the cook's distance is greater than $4/n$. Where n is the number of observations.

The outliers detected in the model was removed considering that they have less influence on the prediction model. Figure 7.36 shows the plot for the cook's distance. The points above the threshold line were removed.

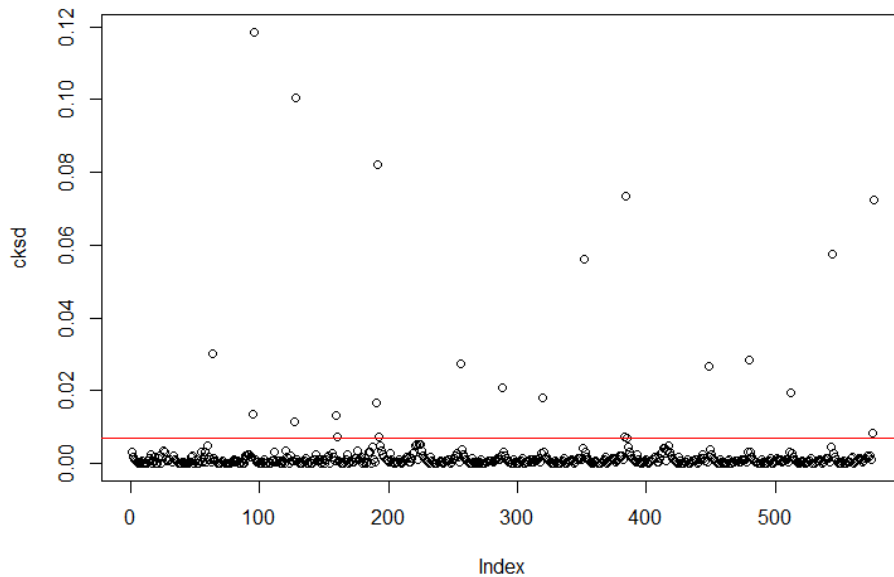


Figure 7.36 Cook's Distance plot for Preliminary Model.

7.4.2.5 Transformation of Variables

The preliminary model did not satisfy the normality test and the constant error variance assumption. Therefore, transformation of response variable was conducted after the removal of the outliers. The optimum transformation variable was found using the box-cox plot method in R studio. Box cox transformation is generally used to transform a data set that is not normally distributed to a normally distributed dataset. This method finds a value λ that will transform the data to normally distributed as possible. The optimum value for the transformation was obtained as 0.2626 (λ -values) as shown in Figure 7.37.

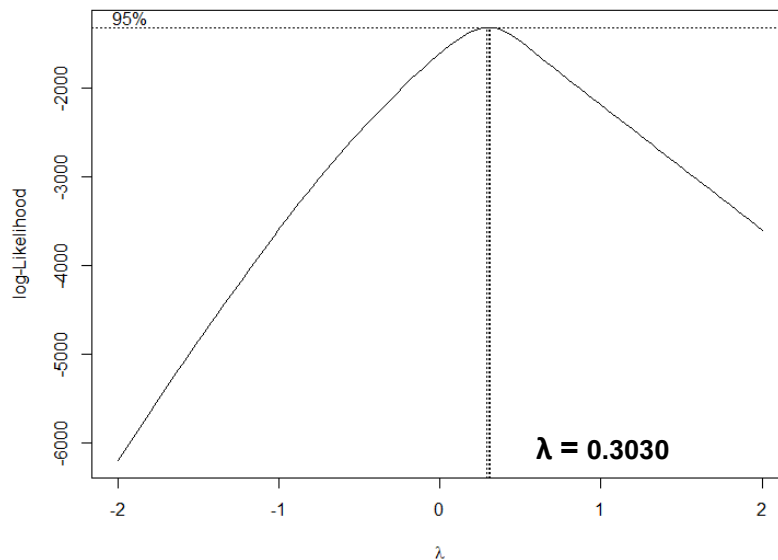


Figure 7.37 Box-Cox Plot for Transformation of Response Variable ($\lambda = 0.3030$)

The outcome variable is transformed using the lambda value as follows:

$$(y^\lambda)^{-1/\lambda} = x$$

The preliminary model was transformed using the λ value. The MLR model analysis and ANOVA results for the transformed model are shown in Table 7.14 and Table 7.15. The coefficients of the predictors are expected to follow trends observed in the numerical

data. The lateral displacement was observed to decrease with the increase of cohesion and friction angle which was observed through the negative coefficients in the final model. The adjust R2 value was 0.9661 which signifies that 96% of the predicted data has been fitted. The p-values for the predictor were also observed to be less except for friction angle.

The final fitted MLR equation is as follows;

$$\frac{MD^{0.3030}-1}{0.3030} = -3.5229-0.0018C-0.0022F+ 0.2395SS+ 0.1748OD+ 0.0019LR$$

Table 7.14 Parameter Estimates of the Final Model

	Coefficient	Std. Error	t-value	Pr(> t)	VIF
Intercept	-3.5229	0.1424	-24.74	< 2e-16	
C	-0.0018	0.0002	-11.59	< 2e-16	1.333
F	-0.0022	0.0044	-0.51	0.612	1.333
SS	0.2395	0.0086	28.01	< 2e-16	1.134
OD	0.1748	0.0109	15.99	< 2e-16	1.000
LR	0.0019	0.000019	101.55	< 2e-16	1.134

Table 7.15 ANOVA Summary of the Final Model.

Residual Standard Error	R²	Adjusted R²	F-statistic	p-value
0.4295	0.9661	0.9658	3047	<2.2e-16

The final model will be checked for the verification of assumptions.

7.4.2.6 Verification of Final Model

Constant Error Variance

Random scatter of residual values was observed from the transformed plot as shown in Figure 7.38. Breusch-Pagan test was conducted for further analysis. The p-value was

0.01397 which is greater than $\alpha=0.01$, therefore, the null hypothesis was rejected. The residual values are not heteroscedastic.

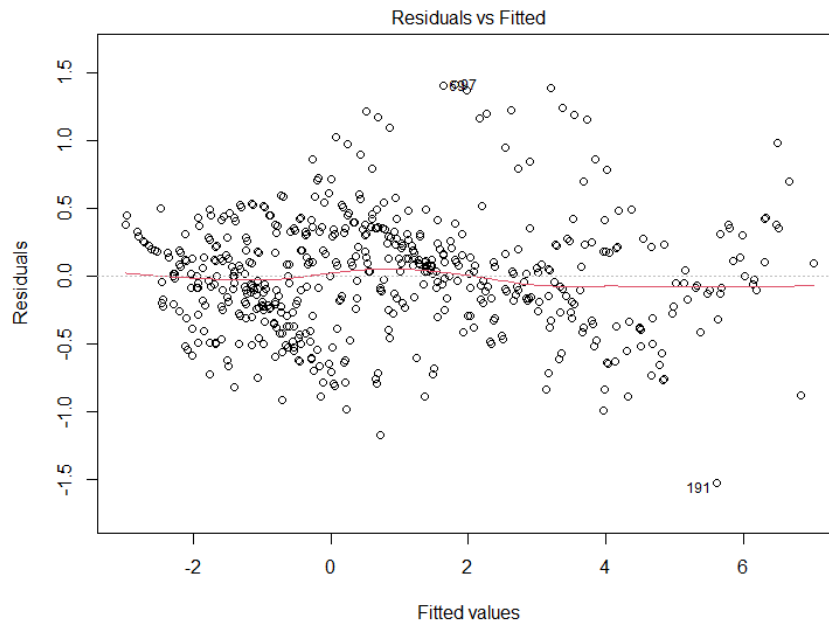


Figure 7.38 Residual vs. Fitted Values Plot for Final Model

Normality Test

The transformed model was tested for normality. The Normal plot for residuals was inspected. The values follow the straight line, but the tail indicates the presence of some outliers. The density plot of the residuals shown in Figure 7.40 shows that the residuals are normally distributed.

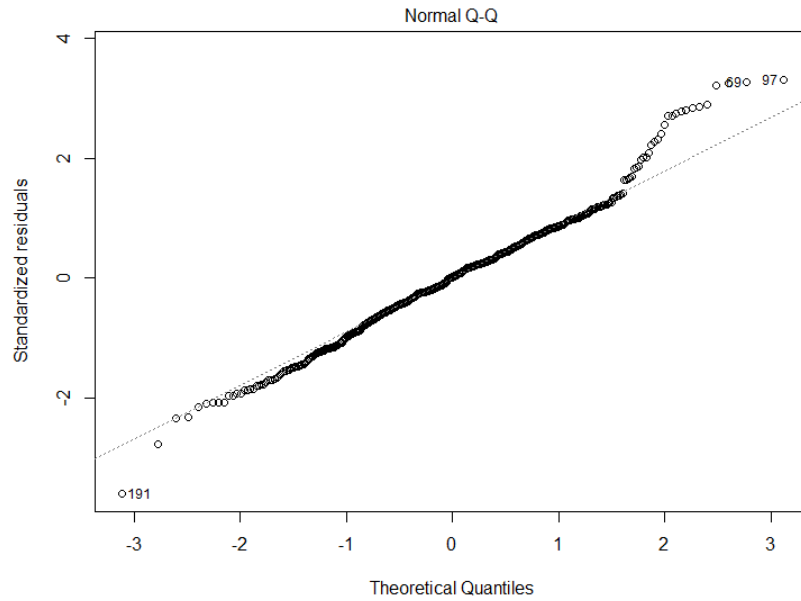


Figure 7.39 The Normal Plot for Final Model

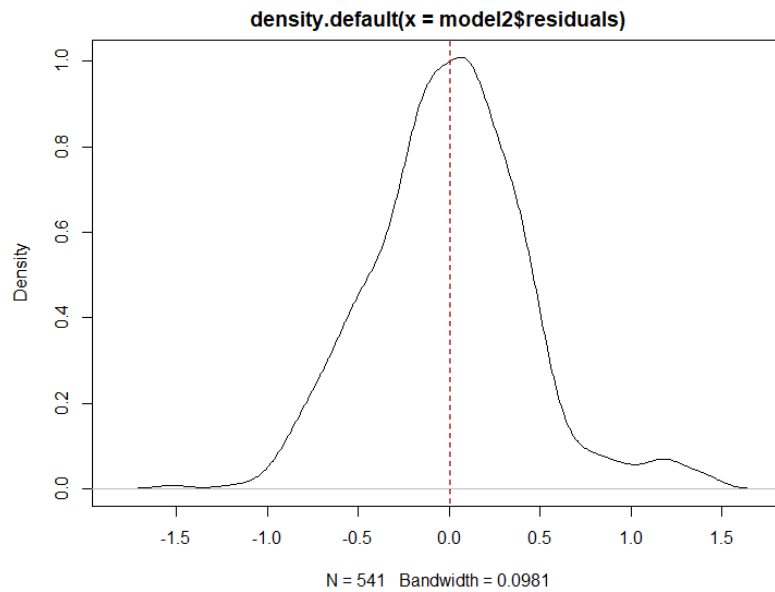


Figure 7.40 Density Plot for Final Model

Further verification was conducted using the Shapiro-wik test in R-studio. The p-value was found to be 0.8498 which is greater than $\alpha=0.01$. Therefore, it can be concluded that the residuals are normally distributed.

Multicollinearity

The Variance of Influence values were calculated for the transformed model. The values are shown in Table 7.14. The VIF values are all less than five (5) indicating that there is very less correlation between predictors.

Outliers

Bonferroni test was conducted to test for outliers in the transformed model. Only one observation was flagged as a potential outlier.

7.4.2.7 Selection of Final Model

Best Subset Selection

The best subset was selected according to the significance of the independent variable and the value of adjusted R². The significance of the independent variable is shown in Table 7.16 using the p-values. The smaller the p-value, higher the significance for the prediction model. Friction angle (F) was observed to have higher p-value, but the best subset selection criteria showed that the inclusion of the F value does not affect the overall relationship.

Table 7.16 Summary of Best Subset Selection Method

C	F	SS	OD	LR	R ² Adjusted	No. of Variables
	-				0.966	4
					0.966	5
-					0.929	4
-	-				0.928	3
	-		-		0.899	3
			-		0.899	4
-			-		0.892	3
-	-		-		0.891	2
	-	-			0.779	3

7.4.2.8 Validation of Final Prediction Model

The final prediction model was tested using a different set of data obtained from the numerical model. Figure 7.41 shows the variation of values from the numerical model and the prediction model. It was observed that the variation of the lateral displacement could be explained up to 93%.

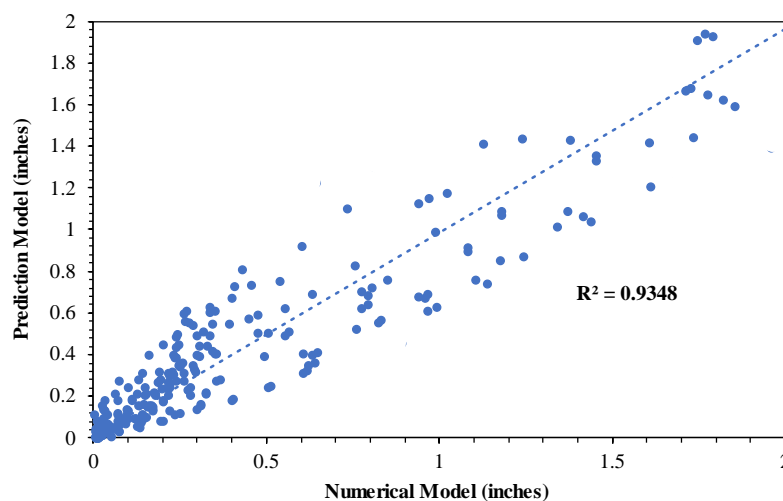


Figure 7.41 Validation of the Final Model

7.4.3 Maximum Flexure

7.4.3.1 Selection of Parameters

The predictors were selected based on the input parameters into the finite modeling to obtain the maximum bending moment for given loads. Maximum flexure was calculated using the maximum bending moment.

In order to develop a reliable statistical model, the predictors should not be highly correlated to each other. If the predictors are highly correlated to each other, it could lead to higher variance, smaller coefficient of regression, and unreliable response outcomes

(Stevens, 1996). The limit flexure was modeled as the response outcome with cohesion, friction angle, overlap depth, and slip surface depth as predictors which were also the parameters varied during the parametric study. The cohesion and friction angle were considered of the soil over the slip surface.

The parameters are denoted as follows:

MF=Maximum Limit Flexure

LR = Limit Resistance

C = Cohesion (psf)

F = Friction angle (degrees)

OD = Overlap Depth (ft)

SS = Slip Surface (ft)

7.4.3.2 Correlation Analysis

During a regression analysis, the predictors should have less correlation between themselves and the response variable. Correlation analysis was conducted to determine if the predictors and the response variable is highly correlated. Several problems in statistical models arise due to multicollinearity including large variances, higher R^2 values, and standard errors sensitive to small changes. The Pearson Correlation coefficients was obtained to determine the correlation between variables. A rule of thumb when considering collinearity is that the correlations are considered significant if below -0.9 or above +0.9. The correlation between individual predictors is shown in Table 7.17. There is no significant collinearity observed between predictor variables.

Another method to determine collinearity is analyzing the Variance Influence Factor (VIF). According to Shrestha (2020) if the VIF is less than 1, the variables are not related to each other and if $1 < VIF < 5$, the values are moderately correlated. All the predictor variables show low correlation.

Table 7.17 Correlation between Predictor Variables

Variable	MF	C	F	SS	OD	VIF
C	-0.020	1.000	-0.500	0.000	0.000	1.333
F	-0.010	-0.500	1.000	0.000	0.000	1.333
SS	0.330	0.000	0.000	1.000	0.000	1.134
OD	0.100	0.000	0.000	0.000	1.000	1.000
LR	0.970	0.000	0.000	0.340	0.000	1.134

The signs observed in the correlation indicates the linear strength between the response and the predictor variables. The statistical analysis showed that the cohesion and friction angle showed negative correlation with the lateral displacement. This means that an increase of cohesion and friction angle decreases the limit flexure. Likewise, limit resistance, overlap depth and slip surface have a positive correlation to maximum flexure. The limit resistance was observed to have the highest correlation to maximum flexure which means that the limit resistance could affect most of the variability in the prediction model.

Table 7.18 Correlation Limit Resistance and Predictor Variables

	MF	C	F	SS	OD	LR
MF	1	-0.02	-0.01	0.33	0.1	0.97

7.4.3.3 Development of Preliminary Model

There was no multicollinearity observed between the predictors and the outcome variable. A preliminary MLR model was formulated as follows for the Maximum Flexure as follows:

$$MF = \beta_0 + \beta_1C + \beta_2F + \beta_3SS + \beta_4OD + \beta_5LR$$

The correlation coefficients β_1 , β_2 , β_3 , β_4 , and β_5 , will be determined through regression analysis by reducing the sum of square errors for the model data. β_0 is an added constant to account for the error in prediction. The correlation coefficients for the predictors explains the mean response per unit change of variable when all the other variables are kept constant.

Multi linear regression (MLR) analysis was conducted from the data obtained from the finite element model. The summary of analysis of variance (ANOVA) and parameter estimates are shown in the tables below. The coefficients of the predictors should follow the sign convention are expected to follow the results obtained by parametric study and numerical modeling. The cohesion and friction angle were observed to have negative correlation as expected indicating that the increase of these values decrease maximum flexure. The limit resistance, overlap depth and slip surface have a positive correlation to lateral displacement showing that the increase of the mentioned parameters will increase the maximum flexure. The correlations obtained were as expected. The p- values were less. The slip surface was seen to show less significance. The preliminary R^2 value is acceptable.

The preliminary fitted MLR equation is shown below:

$$MF = -0.1344 - 0.0004C - 0.00012F + 0.0007SS + 0.0933OD + 0.0015LR$$

Table 7.19 Parameter Estimates of Preliminary Model

	Coefficient	Std. Error	t-value	Pr(> t)
(Intercept)	-0.1344	0.11112	-1.209	2.27E-01
C	-0.0004	0.00012	-3.609	0.0003
F	-0.0106	0.00352	-2.996	0.0029
SS	0.0007	0.00669	0.105	0.9166
OD	0.0933	0.00843	11.075	<2.2e-16
LR	0.0015	0.00002	98.192	<2.2e-16

Table 7.20 ANOVA Summary of Preliminary Model

Residual Standard Error	R²	Adjusted R²	F-statistic	p-value
0.3454	0.951	0.9506	2216	<2.2e-16

The preliminary model is to be verified using several multi linear regression analysis assumptions. The model has to satisfy the normality of residuals, outliers, constant error variance, and multicollinearity among the predictor variables (Kutner et al., 2005, Faysal, 2017, Bhandari, 2021). The assumptions are as follows.

- Linear relationship between response and predictor variables
- Constant variance of residuals
 - Breusch -Pagan Test ($p > 0.01$: Homoscedastic Data)
 - Residuals vs. fitted plot
- Normal Distribution of residuals
 - Shapiro-wik normality test ($p > 0.01$: Normal Distribution)
- Collinearity of residuals
 - Variance Inflation Factor (VIF)

7.4.3.4 Verification of Preliminary Model

Constant Error Variance

The residuals vs fitted values plot from R-Studio was used to analyze if constant error variance or heteroscedasticity is present in the model. The expected results are that the residuals are randomly scattered without a clear trend. A curvilinear trend or a funnel shape in the residuals indicate that that the model is heteroscedastic. Transformation of variables is required in the case of heteroscedastic observation. The residual vs. fitted values plot for the lateral displacement model is shown in Figure 7.42. The plot shows random scatter with an almost straight line. Therefore, the data can be inferred as homoscedastic.

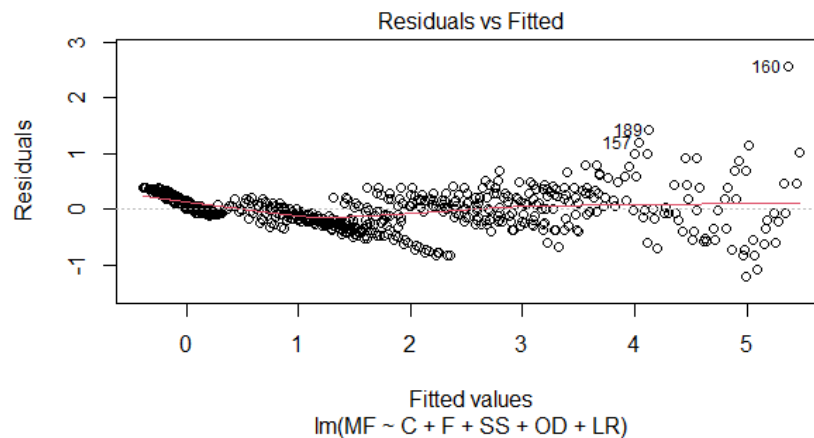


Figure 7.42 Residuals vs. Fitted Values for the Preliminary Model.

Normality

The residuals in the MLR model should be normally distributed. The Normal Q-Q plot and density plots in R Studio is a method of visual observation to determine if the residuals are normally distributed. Normal data will lie mostly along a straight diagonal line with minor deviations. Figure 7.43 and Figure 7.44 shows the normality plot and the density

plot for the preliminary equation. The normal Q-Q plot shows two short tails of the distribution and density plot of residuals show a normal distribution. The lack of clear peak in the bar chart indicates that the model can still be normalized.

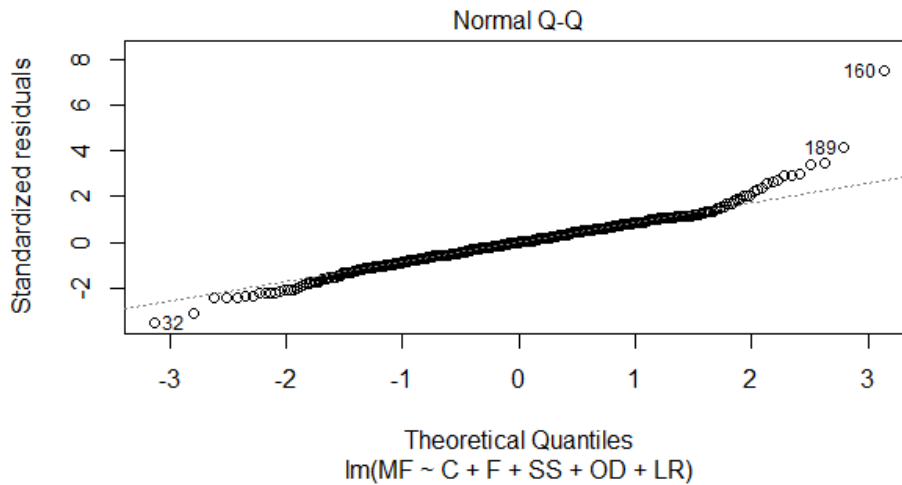


Figure 7.43 Normality Probability Plot for Preliminary Model

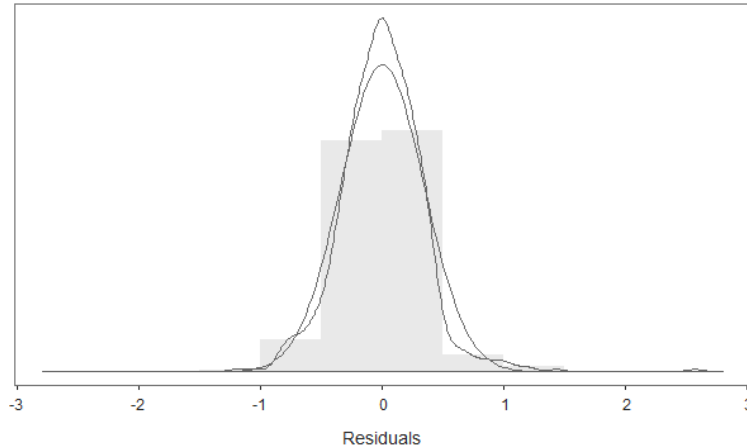


Figure 7.44 Density Plot for Preliminary Model.

Multicollinearity

Variance Influence Factor (VIF) is used to determine if the predictors are corelated to each other. The method uses ordinary least squares regression analysis method to determine the collinearity between variables. According to Shrestha (2020) if the VIF is

less than 1, the variables are not related to each other and if $1 < \text{VIF} < 5$, the values are moderately correlated. All the predictor variables show low correlation to no correlation.

Outlier Test

An outlier is a value or data point that is significantly different from other data points. Outlier data is possible due to variability in observed data points. Outliers can be tested using several methods in R-studio.

Bonferroni test was conducted to detect the outliers. Bonferroni outlier test flags the most extreme observation. Data points 160 and 189 was flagged with p values of 9.1×10^{-12} and 0.0158 respectively.

Cook's distance was utilized to understand the influence of the points flagged as outliers. It was observed that the cook's distance for one was the points flagged by the Bonferroni test was greater than 0.15. Therefore, it was removed since the influence on the model was negligible.

7.4.3.5 Transformation of Variables

The preliminary model showed that the model can be improved to account for normality and significance of slip surface. Therefore, transformation of independent variable was conducted after the removal of the outliers.

Slip surface was selected for square root transformation and the preliminary model was transformed. The MLR model analysis and ANOVA results for the transformed model are shown in Table 7.21 and Table 7.22. The coefficients of the predictors are expected to follow trends observed in the numerical data. The lateral displacement was observed to decrease with the increase of cohesion and friction angle which was observed through

the negative coefficients in the final model. The adjust R² value was 0.9579 which signifies that 96% of the predicted data has been fitted. All variables were found to be significant.

The final fitted MLR equation is as follows;

$$MF = -2.0767 - 0.0004C - 0.0106F + 0.4935SS + 0.0933OD + 0.0015LR - 0.0290SS^2$$

Table 7.21 Parameter Estimates of the Final Model

	Coefficient	Std. Error	t-value	Pr(> t)
Intercept	-2.0767	0.2196	-9.46	<2e-16
C	-0.0004	0.00011	-3.91	0.000103
F	-0.0106	0.0033	-3.25	0.00124
SS	0.4935	0.04966	9.94	<2e-16
OD	0.0933	0.0078	12.0	<2e-16
LR	0.0015	0.0000	106.4	<2e-16
SS2	-0.0290	0.0029	-10.0	<2e-16

Table 7.22 ANOVA Summary of the Final Model.

Residual Standard Error	R²	Adjusted R²	F-statistic	p-value
0.3188	0.9584	0.9579	2184	<2.2e-16

The final model will be checked for the verification of assumptions.

7.4.3.6 Verification of Final Model

Constant Error Variance

Random scatter of residual values was observed from the transformed plot as shown in Figure 7.45. Breusch-Pagan test was conducted for further analysis. The p-value was 0.0145 which is greater than $\alpha=0.01$, therefore, the null hypothesis was rejected. The residual values are not heteroscedastic.

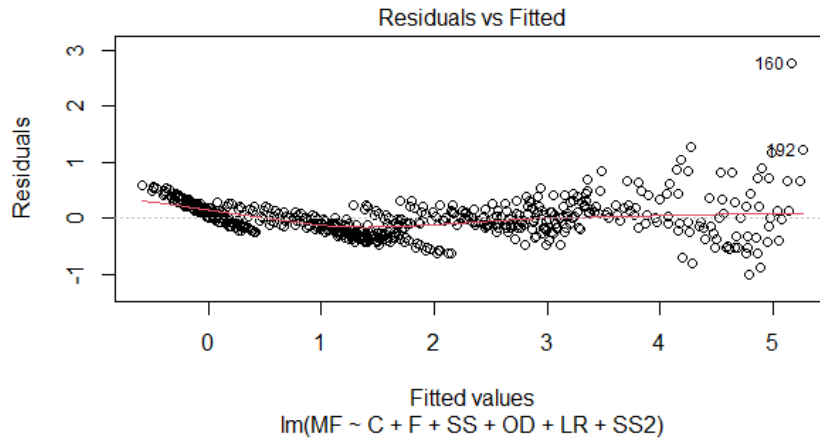


Figure 7.45 Residual vs. Fitted Values Plot for Final Model

Normality Test

The transformed model was tested for normality. The Normal plot for residuals was inspected. The values follow the straight line, but the tail indicates the presence of some outliers. The density plot of the residuals shown in Figure 7.47 shows that the residuals are normally distributed.

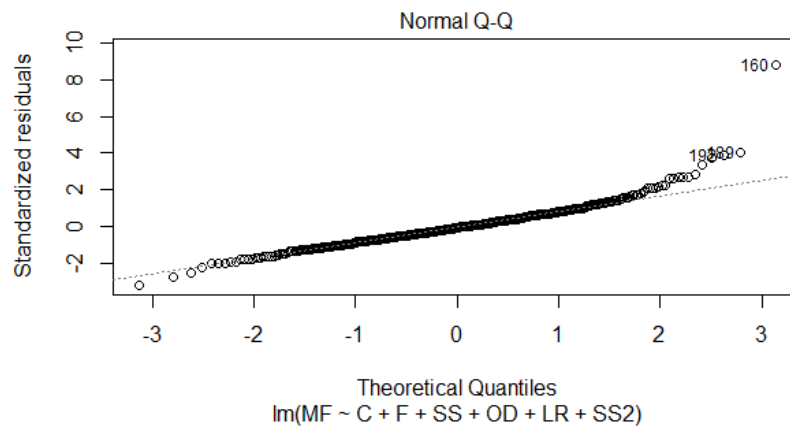


Figure 7.46 The Normal Plot for Final Model

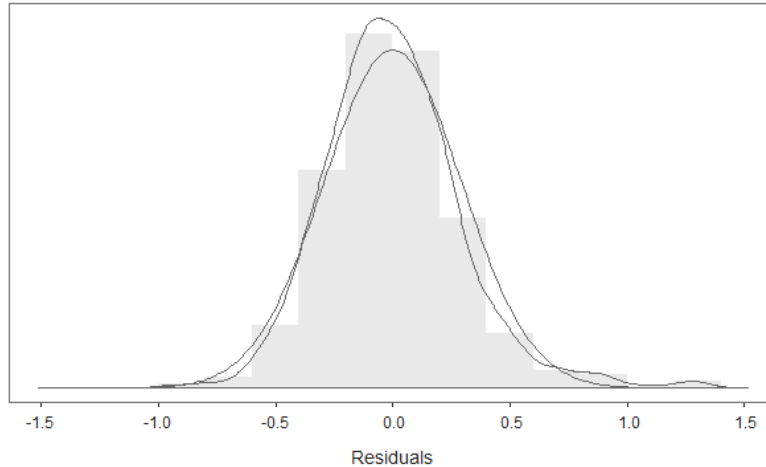


Figure 7.47 Density Plot for Final Model

Further verification was conducted using the Shapiro-wilk test in R-studio. The p-value was found to be 0.0678 which is greater than $\alpha=0.01$. Therefore, it can be concluded that the residuals are normally distributed.

Multicollinearity

The Variance of Influence values were calculated for the transformed model. The values are shown in Table 7.17. The VIF values are all less than five (5) indicating that there is very less correlation between predictors.

Outliers

Bonferroni test was conducted to test for outliers in the transformed model. No potential outliers were flagged.

7.4.3.7 Selection of Final Model

Stepwise Regression Analysis

This analysis consists of iterative addition and elimination of predictors to find the best subset of variables that best fits the data. The three methods of stepwise regression are as follows; (James et al., 2014, Bruce and Bruce 2017).

Forward Selection

This selection method starts the iterations with no predictors. The predictor with the highest significance gets added into the model in turn until there is no change in the significance level.

Backward Selection

This selection method starts with all the predictors and removes each predictor iteratively. The process will stop when all predictors are significant. This method requires a sample size (n) greater than the number of predictors (p).

Stepwise Selection

Stepwise selection is a combination of forward and backward selection methods. The selection method starts with no predictors and then add the most contributive predictors sequentially. The model is inspected and the variables which no longer significant is removed.

All three selection methods indicated that all variables are significant in the model.

Table 7.23 Best Subset Selection

C	F	SS	OD	LR	SS²	R²adj	Number of Variables
						0.958	6
	-					0.957	5
-		-				0.95	4
-	-		-			0.946	3
-	-			-	-	0.119	2
-	-		-	-	-	0.110	1

7.4.3.8 Validation of Final Prediction Model

The final prediction model was tested using a different set of data obtained from the numerical model. Figure 7.48 shows the variation of values from the numerical model and the prediction model. It was observed that the variation of the maximum flexure could be explained up to 97%.

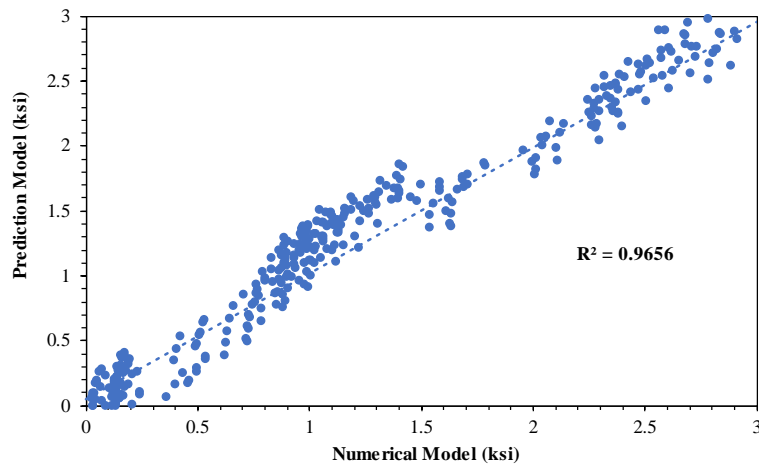


Figure 7.48 Validation of the Final Model.

7.5 Calculation of Factor of Safety

The lateral resistance obtained from the equations can be utilized for calculation of factor of safety of a given slope. During this study, the conventional method of slices is followed to determine the factor of safety.

7.5.1 Conventional Method of Slices

The ordinary method of slices was used to determine the factor of safety of the unreinforced section and reinforced section and the results were compared to the FE modeling. The calculation procedure and the results are discussed below.

The ordinary method of slices assumes that the resultant of all side forces acting on any slice acts parallel to the base of the slice. This method also neglects both shear and normal interslice forces and satisfies moment equilibrium. A trial slip surface is assumed and the soil above the trial surface is divided into several vertical slices.

The soil properties of the topsoil were considered for the calculation since the topsoil up to the slip surface is the most prone to failure. The schematic of the considerations of the ordinary method of slices is shown in Figure 7.49 along with the active forces acting on a single slice. Weight of the slice is represented by W . The normal and tangential components of the reaction are represented by N and T respectively. F_n , F_{n+1} , T_n and T_{n+1} is the interslice forces acting on the n th slice. These forces are assumed to be equal in magnitude and opposite in direction, rendering a resultant of zero. Porewater pressures are also considered to be zero.

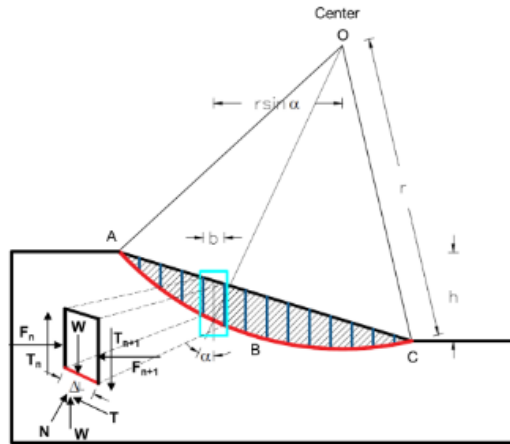


Figure 7.49 Schematic of the Calculation of the Ordinary Method of Slices (Sapkota, 2019).

Critical slip surface for this study was assumed and the slope above the assumed slip surface was divided into vertical slices of approximately equal widths.

$$\text{Normal component of reaction (N)} = W \cdot \cos \alpha \quad (7-6)$$

$$\text{Driving force} = \text{Tangential component of reaction} = W \cdot \sin \alpha \quad (7-7)$$

$$\text{Shear Strength/ Shear Stress} = \tau_f = c' + \sigma' \tan \theta \quad (7-8)$$

$$\text{Allowable Shear Stress } (\tau_d) = \frac{\text{Shear Force } (T_d)}{\Delta L} \quad (7-9)$$

$$\text{Factor of Safety (FS)} = \frac{\text{Shear Stress } (\tau_f)}{\text{Allowable Shear Stress } (\tau_d)} \quad (7-10)$$

Combining equations 7-9 and 7-10;

$$T_d = \tau_d \Delta L = \frac{\tau_f}{FS} \Delta L$$

$$\tau_d \Delta L = \frac{c' + \sigma' \tan \theta}{FS} \Delta L \quad (7-11)$$

$$\text{Normal Stress } (\sigma') = \frac{\text{Normal Force } (N_d)}{\Delta L} = \frac{W \cos \alpha}{\Delta L} \quad (7-12)$$

Where,

W = Weight of slice (lb/ft)

α = Angle between the vertical axis and normal component of reaction ($^{\circ}$)

τ_d = Allowable Stress (lb/ft²)

τ_f = Shear Stress at Failure (lb/ft²)

ΔL = Base Width of Slice (ft)

FS = Factor of Safety

σ' = Effective Stress (lb/ft²)

c' = Effective Cohesion (psf)

θ = Effective angle of Internal Friction (°)

The equilibrium of the trial slip surface is considered. The resisting moment at the center of the slip circle (o) is equal to the driving moment at the center of the slip circle.

Driving moment at the center of the slip circle = (M_d) = Driving Force * Radius (r)

$$M_d = \sum_1^n W * r * \sin \alpha \quad (7-13)$$

Resisting Moment at the center of the slip circle = (M_r) = Resisting Force* Radius (r)

$$M_r = \sum_1^n \frac{1}{FS} * \left(c' + \frac{W \cos \alpha \tan \theta}{\Delta L} \right) * \Delta L * r \quad (7-14)$$

Equating Equations 7-13 and 7-14;

$$\sum_1^n W * r * \sin \alpha = \sum_1^n \frac{1}{FS} * \left(c' + \frac{W \cos \alpha \tan \theta}{\Delta L} \right) * \Delta L * r \quad (7-15)$$

And Factor of Safety can be derived from equation 7-15.

$$FS = \frac{\sum_{n=1}^{n=p} (c' \Delta L + W \cos \alpha \tan \theta)}{\sum_{n=1}^{n=p} W \sin \alpha} \quad (7-16)$$

The details of the calculations to determine the factor of safety for the unreinforced section are shown below.

Table 7.24 Ordinary Method of Slices Calculation.

Slice Information							Driving Force =W sin α	Resisting Force =(c'ΔL+W cos α tan φ) (lbf/ft)
Slice No	Base Width b (ft)	Mid Height d (ft)	Base Length ΔL (ft)	Base angle (α)	Area = bd (ft ²)	Weight = Aγ (lbf/ft)		
1	1.10	5.58	1.95	37	6.16	739.3	444.9	242.7
2	2.31	7.39	4.11	35	17.11	2053.3	1177.7	603.9
3	2.39	8.63	2.58	33	20.64	2477.2	1349.2	596.4
4	2.83	8.65	3.00	31	24.50	2939.4	1513.9	715.6
5	2.91	8.48	3.02	29	24.64	2957.2	1433.7	730.9
6	2.96	8.06	3.03	27	23.84	2860.8	1298.8	723.9
7	3.44	7.54	3.54	25	25.95	3114.0	1316.0	812.3
8	4.93	5.31	5.06	22	26.15	3137.7	1175.4	921.8
8	4.93	1.55	5.06	22	7.65	917.6	343.7	550.5
9	4.92	3.81	5.06	18	18.78	2253.3	696.3	759.0
9	4.92	2.24	5.06	18	11.05	1326.3	409.8	645.2
10	4.93	2.32	5.06	17	11.44	1372.7	401.3	582.5
10	4.93	2.94	5.06	17	14.48	1737.3	507.9	737.6
11	3.93	0.99	4.05	12	3.87	464.9	96.7	339.4
11	3.93	3.54	4.05	12	13.91	1669.5	347.1	660.2
12	3.94	3.90	4.05	9	15.34	1840.3	287.9	702.9
13	3.94	3.25	4.05	5	12.81	1537.5	134.0	636.8
14	3.94	2.61	4.05	2	10.29	1234.8	43.1	568.1
15	3.94	1.97	4.05	-1	7.77	932.0	-16.3	498.4
16	3.94	1.33	4.05	-4	5.24	629.3	-43.9	428.2
17	6.21	0.51	6.39	-4	3.14	377.2	-26.3	534.0
							12891.13	12990.17

$$FS = \frac{\sum_{n=1}^{n=p} (c' \Delta L + W \cos \alpha \tan \theta)}{\sum_{n=1}^{n=p} W \sin \alpha} = \frac{12990.17}{12,891.13} = 1.00$$

When the slope is reinforced with RPP, an additional resisting force is added into the resistance in addition to the resistance provided from the strength of the soil.

$$\text{Shear Force at failure} = T_f = \tau_f \Delta L + P$$

Where P is the minimum limit resistance obtained considering the failure of soil, limit flexure and limit displacement.

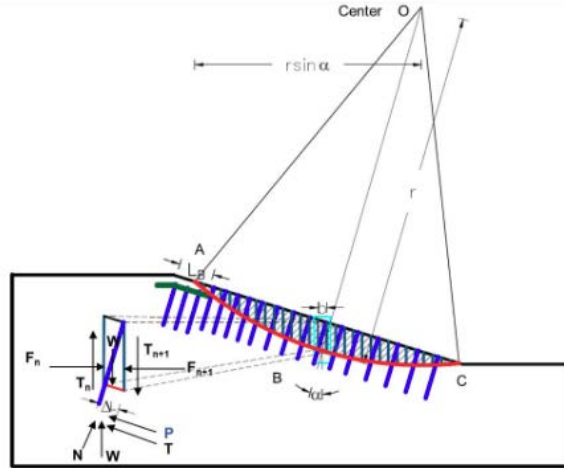


Figure 7.50 Schematic of the Calculation of the Ordinary Method of Slices with Reinforcement (Sapkota, 2019).

Allowable shear force = $T_d = T_f / FS$

$$T_d = \frac{\tau_f \Delta L + P}{FS} \quad (7-17)$$

$$T_d = \frac{c' \Delta L + W \cos \alpha \tan \theta + P}{FS} \quad (7-18)$$

Resisting Moment at the center of the slip circle = $(M_r) = \text{Resisting Force} * \text{Radius } (r)$

$$M_r = \sum_1^n \frac{c' \Delta L + W \cos \alpha \tan \theta + P}{FS} * r \quad (7-19)$$

Driving moment at the center of the slip circle = $(M_d) = \text{Driving Force} * \text{Radius } (r)$

$$M_d = \sum_1^n W * r * \sin \alpha \quad (7-20)$$

Equating Equations 7-19 and 7-20.

$$\sum_1^n W * r * \sin \alpha = \sum_1^n \frac{c' \Delta L + W \cos \alpha \tan \theta + P}{FS} * r \quad (7-21)$$

And Factor of Safety can be derived from equation 7-15.

$$FS = \frac{\sum_{n=1}^{n=p} (c' \Delta L + W \cos \alpha \tan \theta + P)}{\sum_{n=1}^{n=p} W \sin \alpha} \quad (7-22)$$

The resisting force by the reinforcement at different overlap depths and slip surfaces along the slope are calculated either by using the equations or the design charts. A limiting criterion of maximum displacement of 2 inches and a maximum flexure of 1.4 ksi were used in this example.

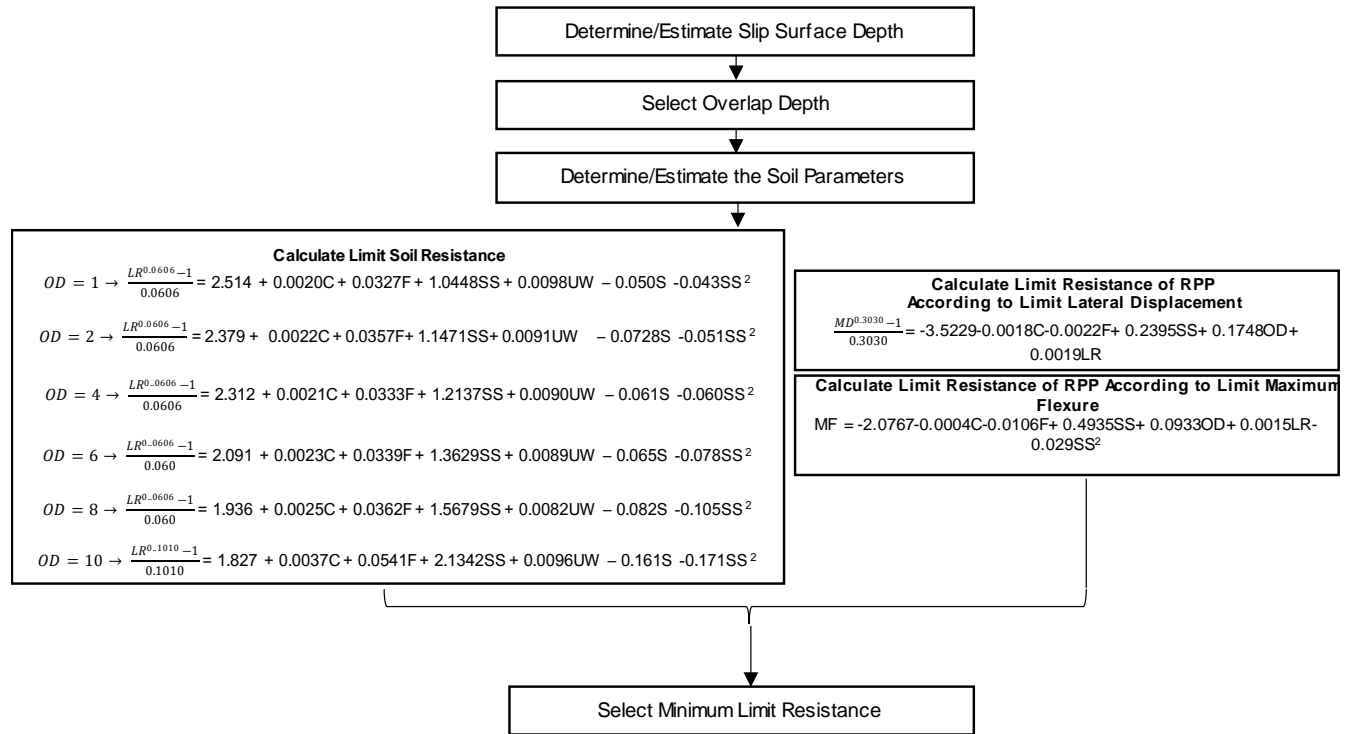


Figure 7.51 Decision Matrix

The determination of Limit soil resistances for few of the critical slip surfaces are shown in Figure 7.52.

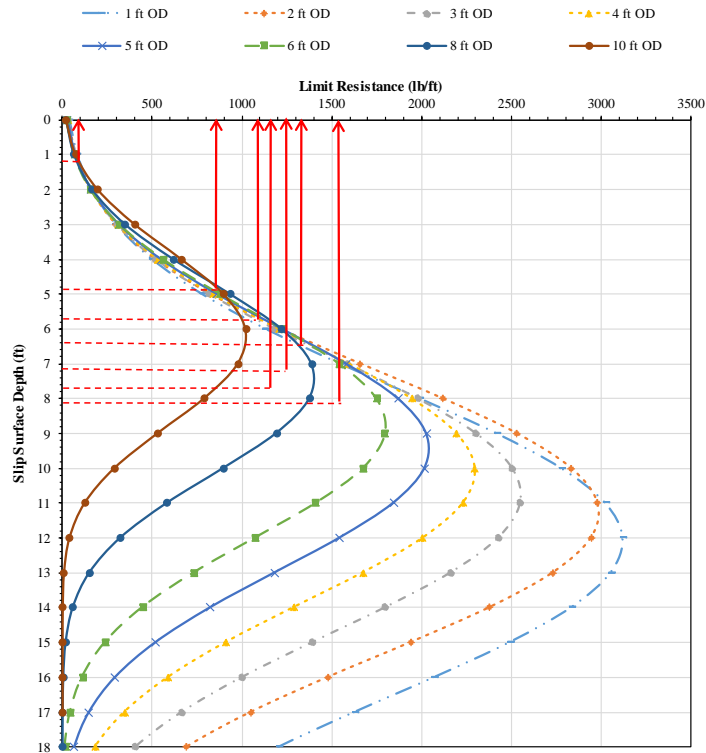


Figure 7.52 Limit Soil Resistance

RPP Row 2

Example calculation for Limit Displacement:

$$\frac{MD^{0.3030-1}}{0.3030} = -3.5229-0.0018C-0.0022F+ 0.2395SS+ 0.1748OD+ 0.0019LR$$

$$\frac{2^{0.3030-1}}{0.3030} = -3.5229-0.0018(60)-0.0022(12)+ 0.2395(5.73)+ 0.1748(5.8)+ 0.0019LR$$

$$LR = 1075.25 \text{ lb/ft}$$

Example calculation for Limit Flexure:

$$MF = -2.0767-0.0004C-0.0106F+ 0.4935SS+ 0.0933OD+ 0.0015LR-0.0290SS^2$$

$$1.4 = -2.0767-0.0004(60)-0.0106(12)+ 0.4935(5.73)+ 0.0933(5.8)+ 0.0015LR-0.0290(5.8)^2$$

$$LR = 807.6 \text{ lb/ft}$$

The use of equations is more accurate than the use of design charts since the exact value for the overlap depth and slip surface can be incorporated.

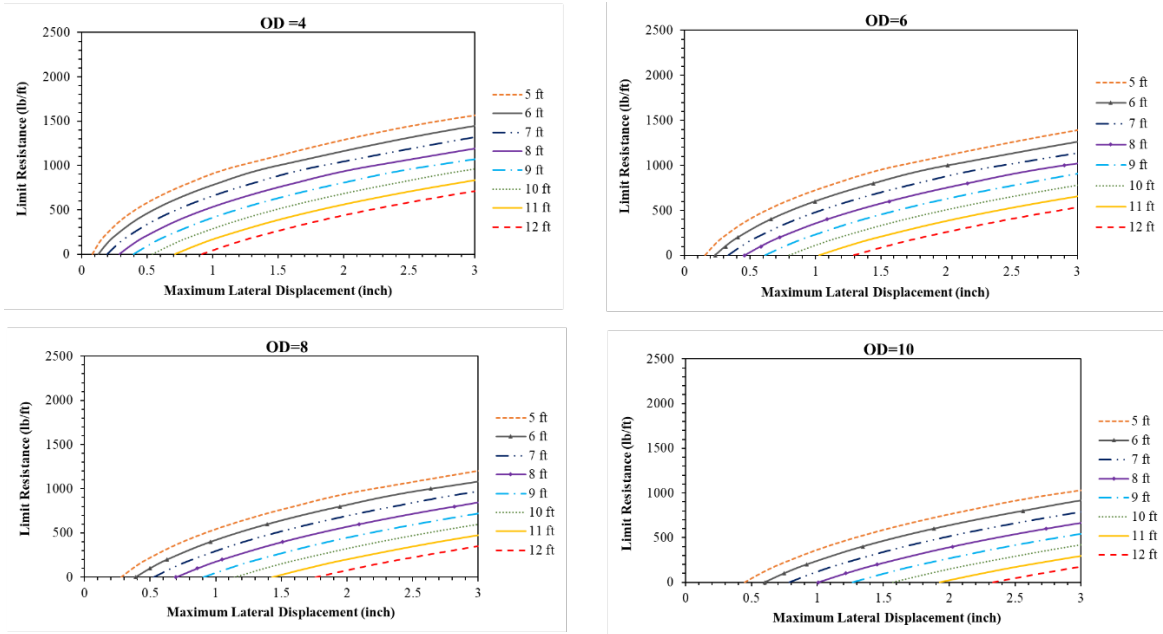


Figure 7.53 Limit Lateral Displacement

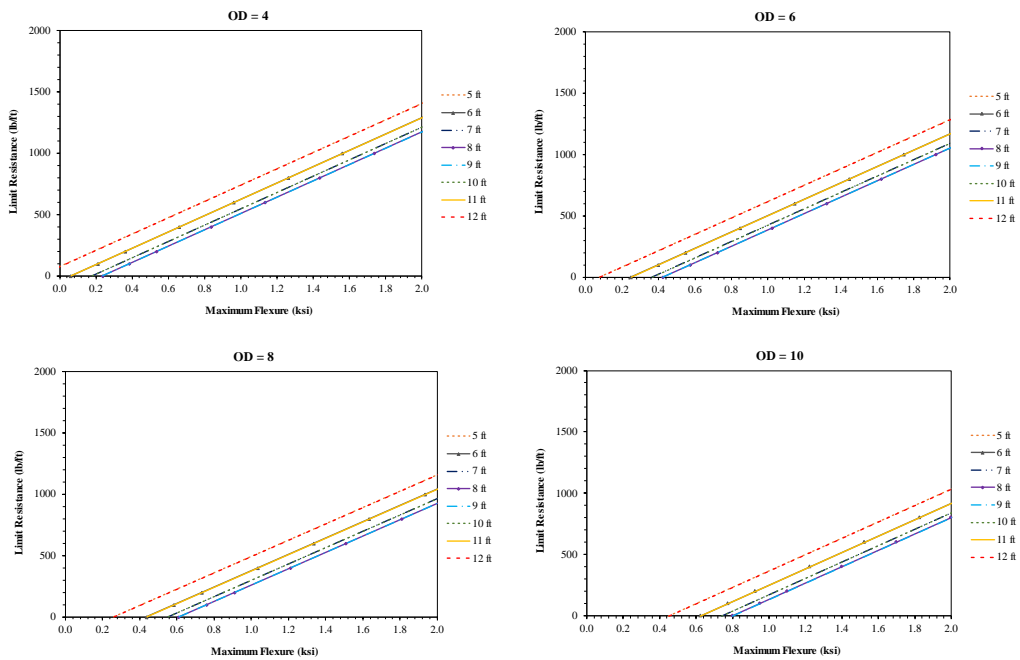


Figure 7.54 Limit Flexure

The limit resistance for the three limiting criteria is selected and the minimum resistance for each row of RPP is used to calculate the total resistance provided by the reinforcement.

Table 7.25 Calculation of Limit Resistance

RPP Row	Depth of RPP at Critical Slip surface	Overlap Depth	Limit Soil Resistance (lb/ft)	Limit Displacement (lb/ft)	Limit Flexure (lb/ft)	Minimum P (lb/ft)
1	1.24	10	80	1254.86	1419.07	80.00
2	5.73	5.80	1090	1075.25	807.69	807.69
3	4.81	7.43	850	1040.98	821.12	821.12
4	8.02	7.43	1550	636.55	561.59	561.59
5	6.42	9.24	1200	670.91	528.15	528.15
6	7.71	9.24	1150	508.99	456.37	456.37
7	7.17	10	1250	507.44	431.74	431.74
8	6.74	10	790	561.38	457.48	457.48
9	6.00	10	800	655.14	519.07	519.07
10	5.25	10	720	748.89	602.05	602.05
11	4.51	10	620	842.64	706.41	620
12	3.91	10	720	917.64	805.30	720
13	3.32	10	510	992.66	917.90	510
14	2.72	10	380	1067.66	1044.17	380
15	2.11	10	320	1144.40	1187.54	320
16	1.50	10	180	1221.15	1345.27	180
17	0.90	10	90	1297.90	1517.34	90
Total Resistance (lb/ft)						8085.25

Factor of safety of the reinforced slope is calculated as follows.

$$FS = \frac{\sum_{n=1}^{n=p} (c' \Delta L + W \cos \alpha \tan \theta + P)}{\sum_{n=1}^{n=p} W \sin \alpha} = \frac{12,990.17 + 8085.25}{12,891.13} = 1.63$$

The factor of safety obtained from Finite element modeling is 1.61 and is comparable to the analytical factor of safety. Therefore, the equation can be hence validated.

7.6 Limitations of the Design Model

The current study is modeled according to the dimensions and properties of the field study and considers only the soil above the sliding surface. Therefore, the limit resistance values may be underestimated resulting in lower factor of safety. These values will represent a conservative design.

CHAPTER 8

CONCLUSIONS AND RECOMMENDATIONS

8.1 Summary and Conclusion

The current study explores the stabilization of deep slope failures using Recycled Plastic Pins (RPP). Two highway slopes located in Interstate highway 820 and U.S Highway 67 in Texas were selected due to the nature of failure. The failures observed at these sites included a crest drop averaging between 5 to 5.5 feet indicating the presence of deeper slip surfaces.

Site investigation of the sites indicated the presence of high plastic clays, which are susceptible to expansion and shrinkage during wet and dry periods. This soil behavior leads to the development of micro and macro fractures that extend into the slope increasing the infiltration of rainwater. These cracks extend deeper into the slope overtime improving the permeability of the soil at deeper depths. This in turn increases the depth of the active zone and allows deeper slip surfaces. Deeper slope failures can occur progressively after shallow slope failures. Cracking influences the rate at which the water enters and leaves the slope. The cracks provide sites for stress concentration that can lead to local movement and progressive failures as the soil moves towards residual strength (Stirling et al., 2021). The shallow slope failures prevalent in Texas highway embankments could extend to deeper failure planes over time if left unreinforced.

Recycled Plastic Pins (RPP) have been successfully utilized for over a decade to reinforce against shallow slope failures. But if the failure planes extend beyond the length of the RPP (10 feet), the reinforcement does not provide sufficient resistance against failure.

Therefore, a two layered reinforcement method was developed for this study to reinforce against deeper slip surfaces. The results of this study are summarized below.

Design of Slope Stabilization and Installation

- The installation scheme was designed and implemented in the two selected sites.
- The crest fall observed at field was utilized to install the first layer of RPP that will extend deeper into the slope. The slope was then backfilled and installed with another layer of reinforcement. This method ensures that deeper failure planes will intersect at least one layer of reinforcement and provide sufficient resistance against failure.

Performance Monitoring

- Performance monitoring was conducted monthly.
- The lateral displacement was limited to the top six feet (6 ft) of the slope. In comparison lateral movement up to depths of ten feet (10 ft) was observed in the unreinforced section adjacent to the reinforced section.
- Incremental lateral deformation results showed that the variation of displacements over time and rainfall are minimized for the reinforced section. In contrast, the unreinforced section showed increase and decrease of deformation resulting from swell and shrinkage behavior.
- Vertical deformation was observed to be higher due to excessive erosion caused by lack of vegetation on the slope after installation in IH-820 and Rosedale Street site.

- Vertical deformation and surface erosion were observed to be lowered due to the use of closer spacing in U.S 67 Alvarado site compared to Rosedale St.
- The performance monitoring indicated that the deformations are being reduced from incorporating a two layered design with reinforcement extending deeper into the slope.

Numerical Study

- The IH-820 and Rosedale Street slope was modeled using PLAXIS 2D to conduct deformation analysis and parametric study.
- The model was calibrated with residual soil parameters to initiate failure and represent the failure nature observed at site.
- The lateral deformation was found to be greater than the lateral deformation in the field due the use of residual parameters.
- The calibrated model was used to analyze a model with RPP installed in one layer for comparison. The results showed that the maximum deformation at the crest was reduced by 15% while the deformation was reduced by 45% at slip surface depth by having two layers of reinforcement.
- The bending moment of RPP showed that the load transfer is less than 30% indicating that the RPP will not fail under creep for over 100 years.
- The numerical study showed that the two layered design reduces lateral deformation at deeper depths.

Parametric Study

- The calibrated model was used to conduct a parametric study that analyzed the effect of construction sequence, spacing, number of layers of deep pins, and the overlap depth on factor of safety and lateral deformation.
- An adequate factor of safety ($F.S > 1.3$) was achieved after the reinforcement of 2/5th to 2/3rd of the slope. The optimum number of lines for this study was found to be the use of three lines as in the field demonstration.
- Factor of safety and deformation analysis for the effect of overlap showed that having a second layer reduces the deformation at the slip surface. The optimum results were observed when the slip surface intersected both layers of reinforcement for slip surfaces less than 8 feet. It was concluded that the anchorage takes precedence over overlap depth at slip surfaces greater than 8 feet.

Design Methodology

- The models were further utilized to develop performance-based design charts incorporating three limiting criteria (Limit soil resistance, limit lateral displacement, and limit flexure) to obtain the resistance provided by the reinforcement.
- The limit soil resistance equations proposed by Loehr and Bowders (2007) were modified to include overlap depth.
- The limit resistance was observed to inversely related to overlap depth for deeper slip surfaces due to higher resistance provided by anchorage.

- The numerical models were used to obtain the maximum lateral displacement and maximum bending moment with the two layered design for varying soil properties.
- The results were statistically analyzed to develop equations for the limiting criteria incorporating overlap depth.
- The limit resistance values obtained were used to calculate the factor of safety using the conventional method of slices. The factor of safety value obtained was comparable and the model was validated.
- The equations/design charts can be utilized to find the factor of safety.

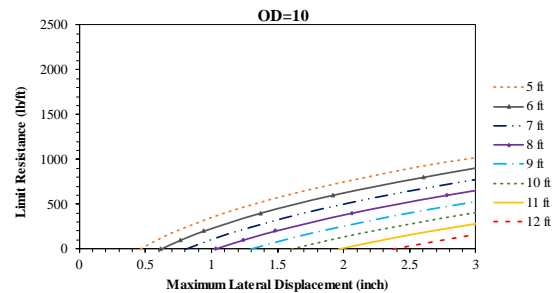
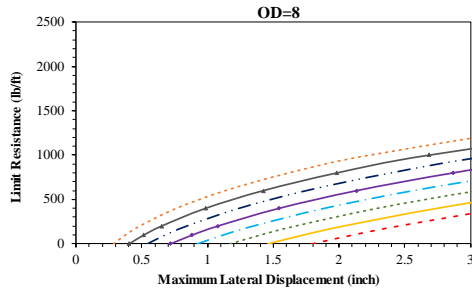
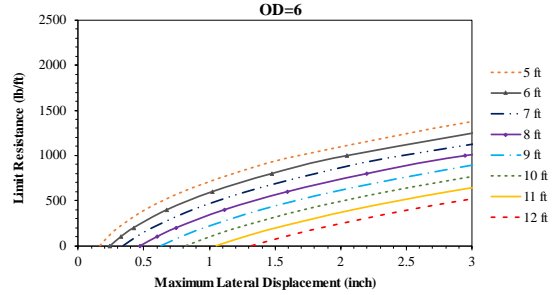
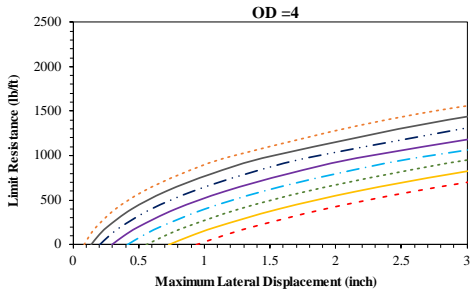
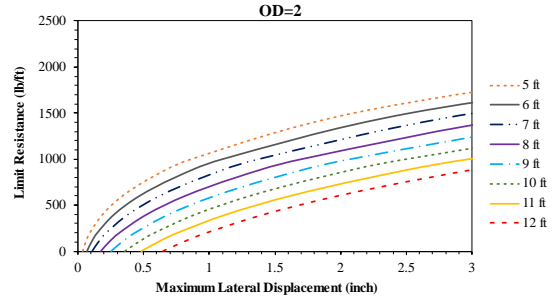
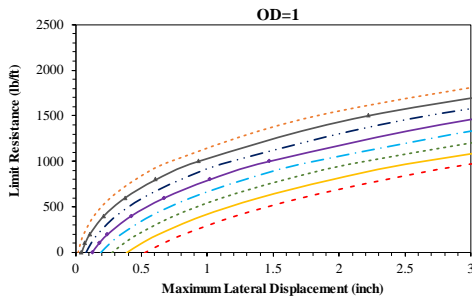
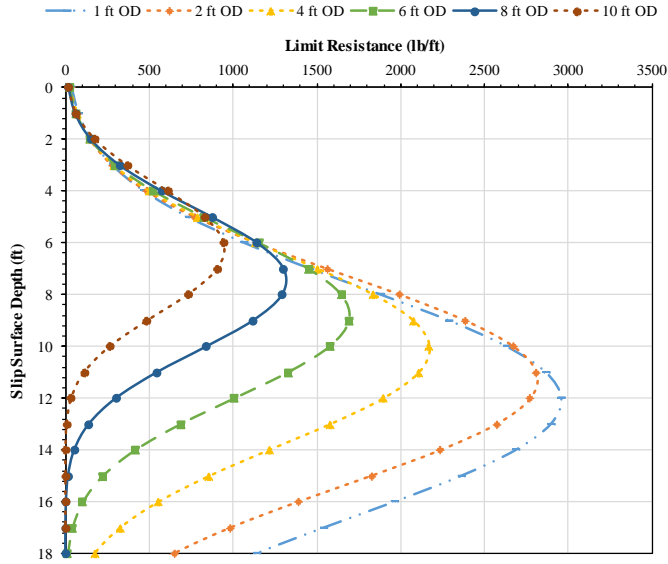
8.2 Recommendations for Future Studies

Based on the current study, the following recommendations are proposed for future studies.

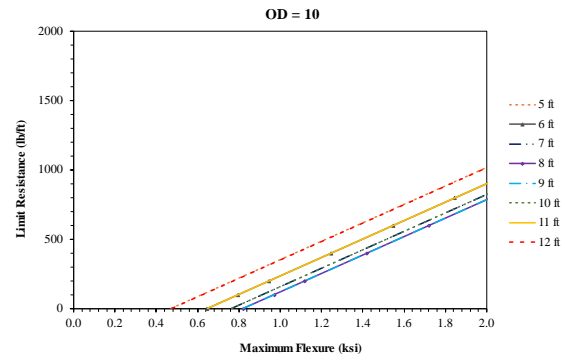
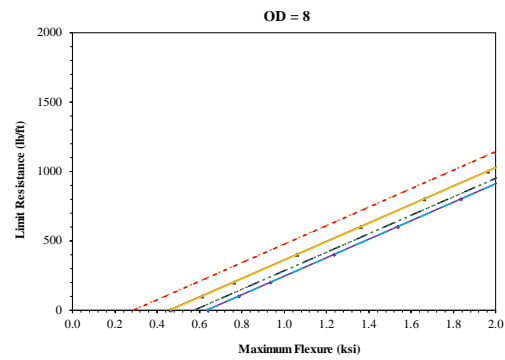
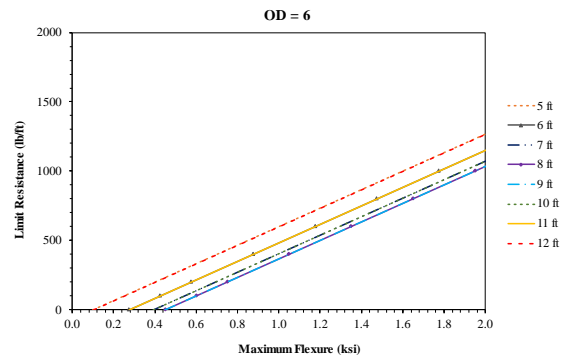
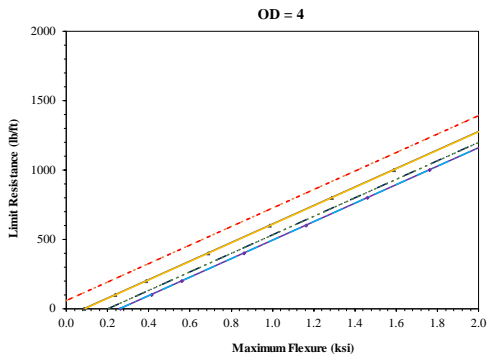
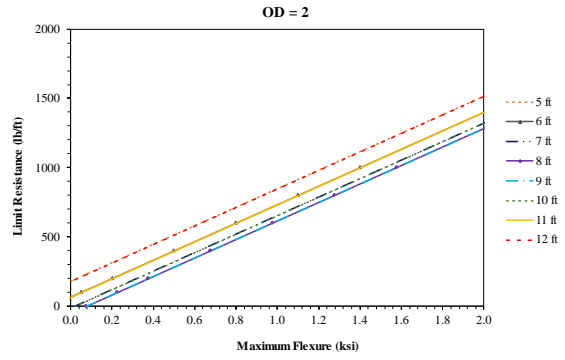
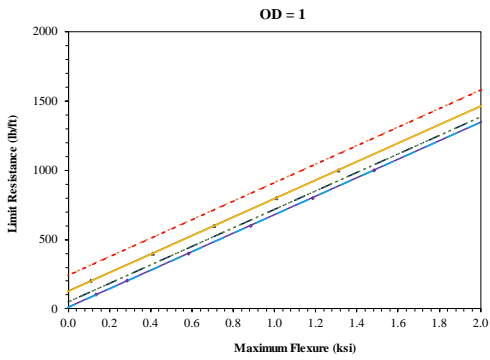
- It was concluded from the current study that the lateral deformation is decreased, and the factor of safety is increased, as the slip surface intersects both layers of reinforcement. Staggered overlap corresponding to slip surface depth using cuts along the slope so that all RPP are installed in optimum position can be considered for future studies.
- The analysis was conducted by considering only two layers of reinforcement. The group effect of reinforcement on limit resistance can be considered.
- The effect of groundwater or fluctuating pore water pressures were not considered in this study. The effect can be considered for future studies.

- During the current study, numerical analysis of one site was considered for the development of design charts. It is recommended to use varying geometry to get a more generalized design chart.
- Long term effects of using the two layered design for slope stabilization can be considered.

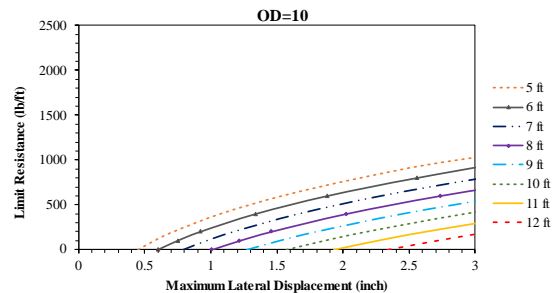
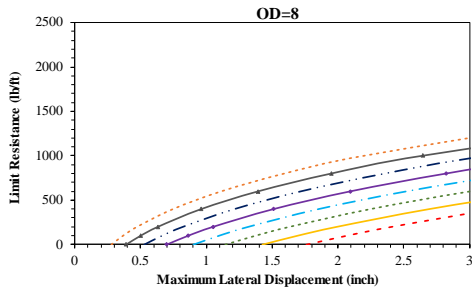
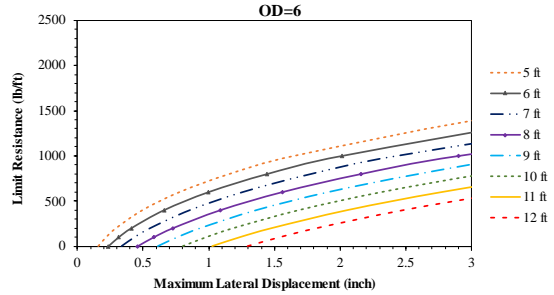
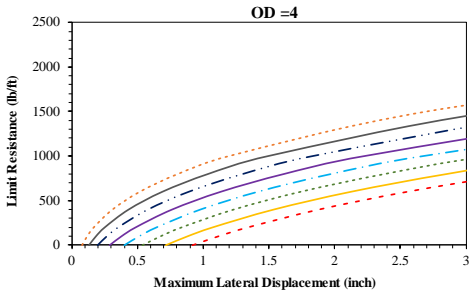
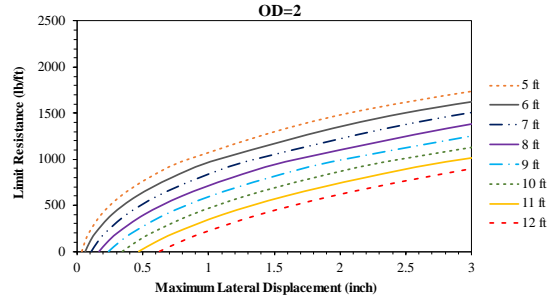
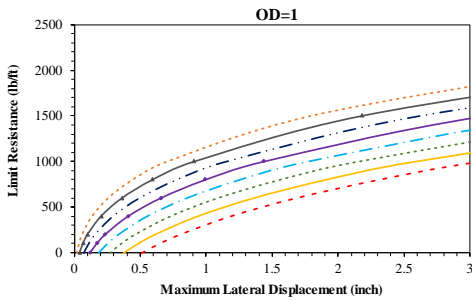
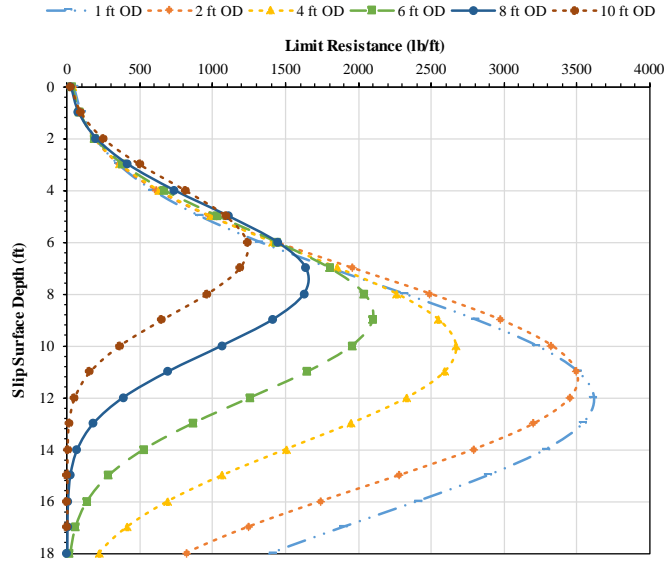
APPENDIX A
DESIGN CHARTS



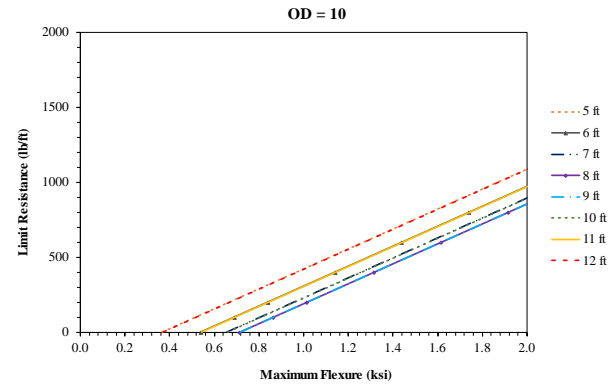
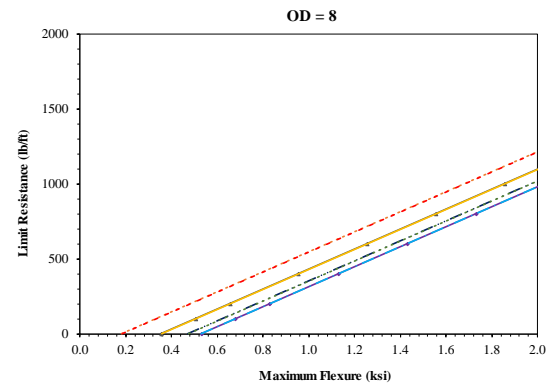
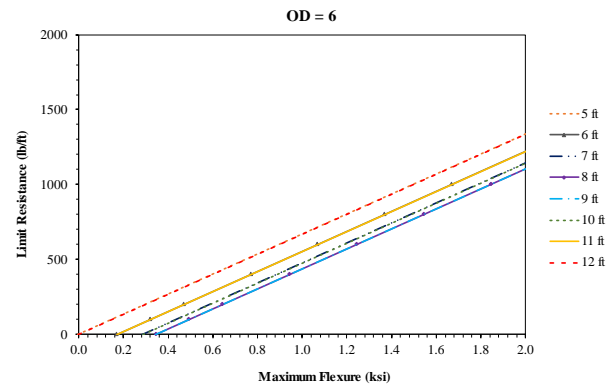
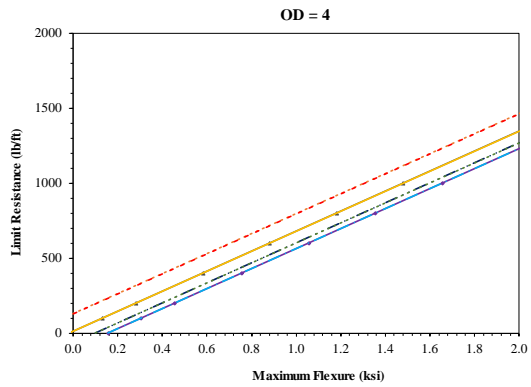
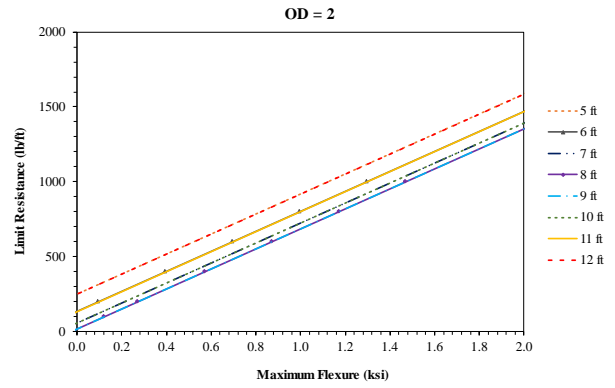
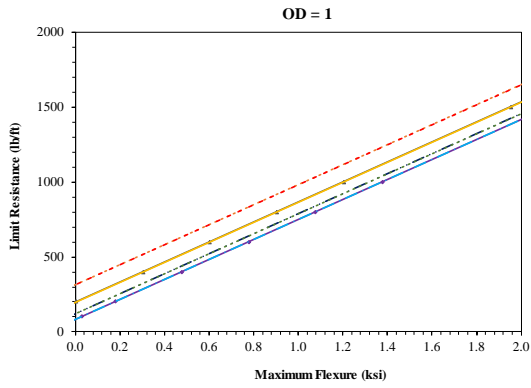
Limit Soil Resistance and Maximum Lateral Displacement for $c=50$ psf, $\phi=10^\circ$



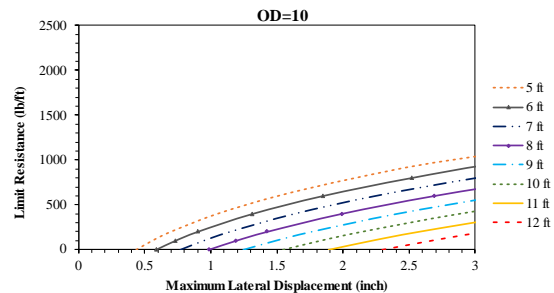
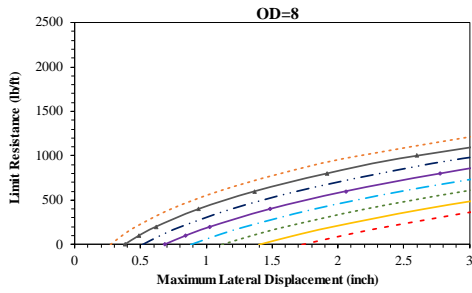
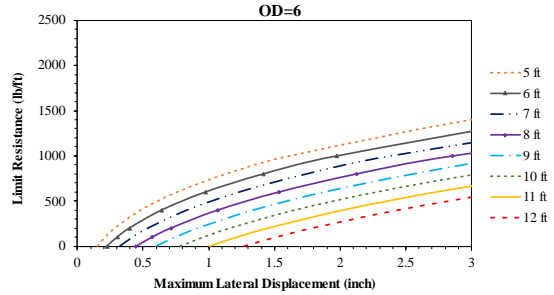
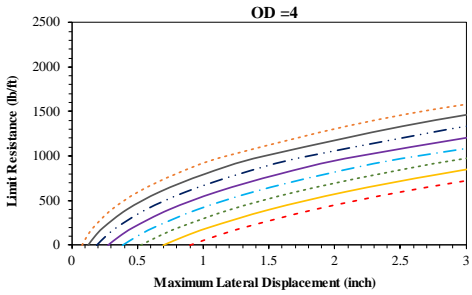
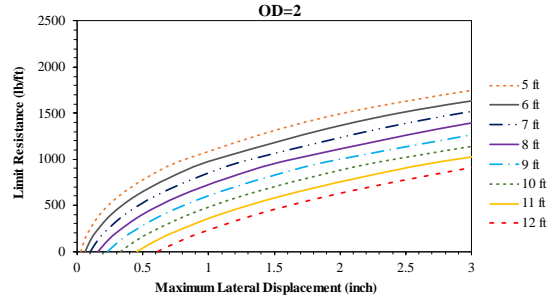
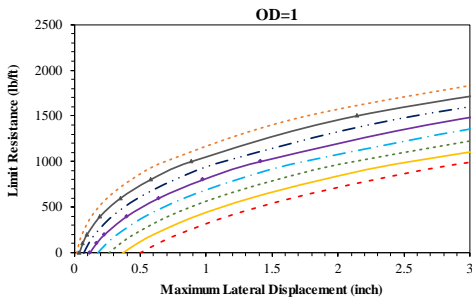
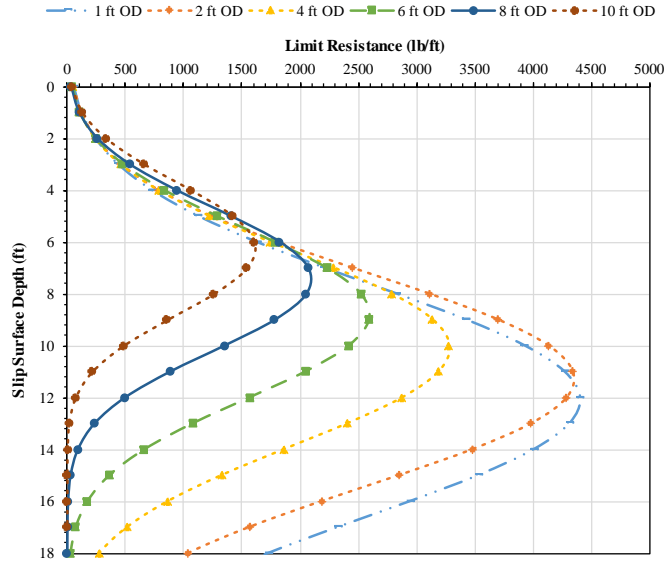
Limit Flexure for $c=50$ psf, $\phi=10^\circ$



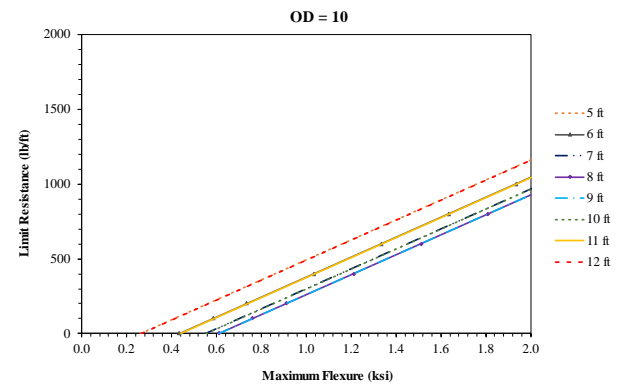
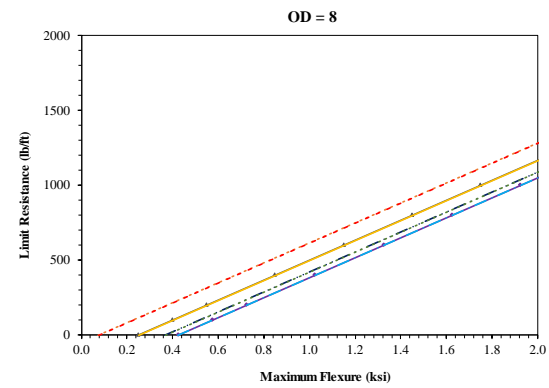
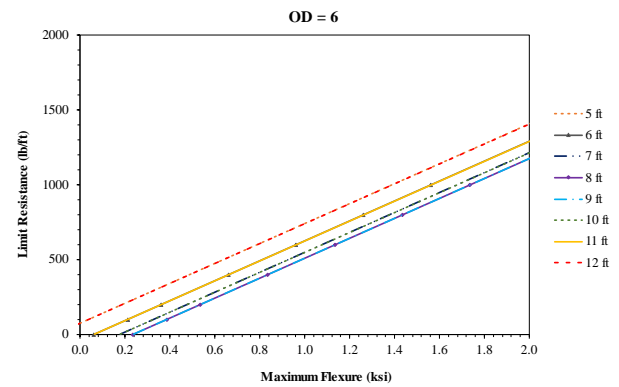
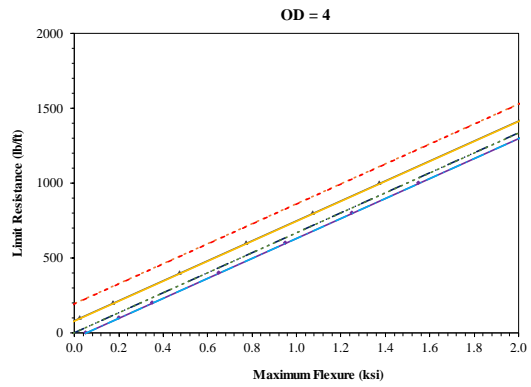
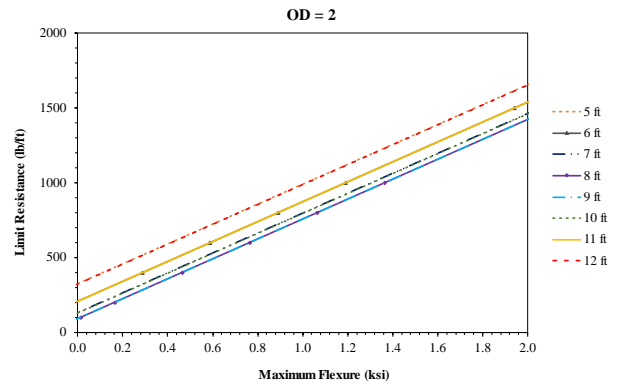
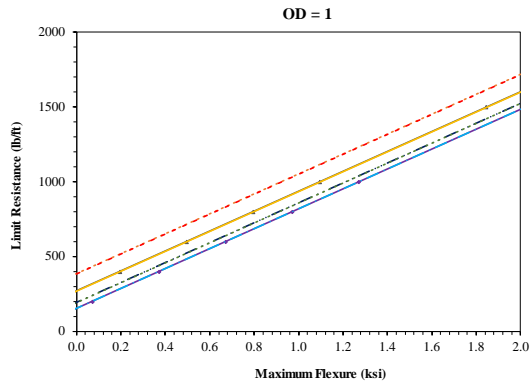
Limit Soil Resistance and Maximum Lateral Displacement for $c=50$ psf, $\phi=20^\circ$



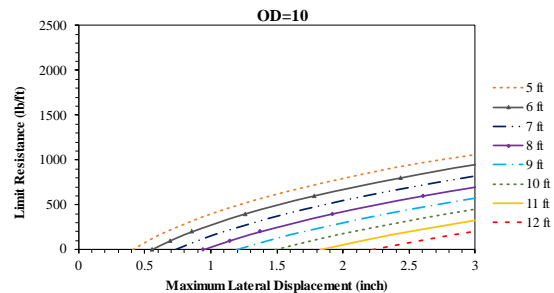
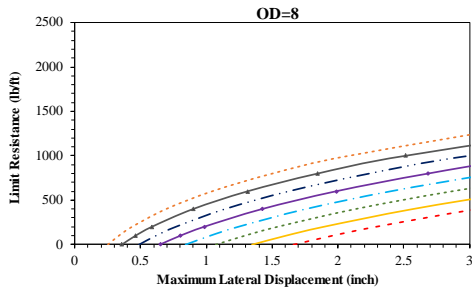
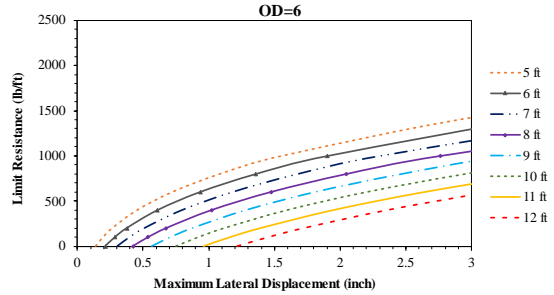
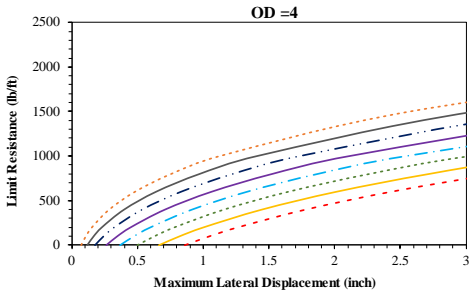
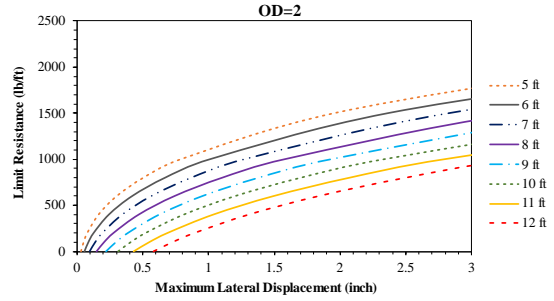
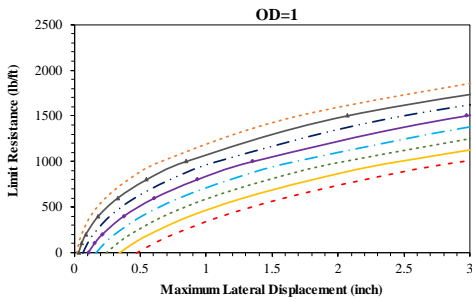
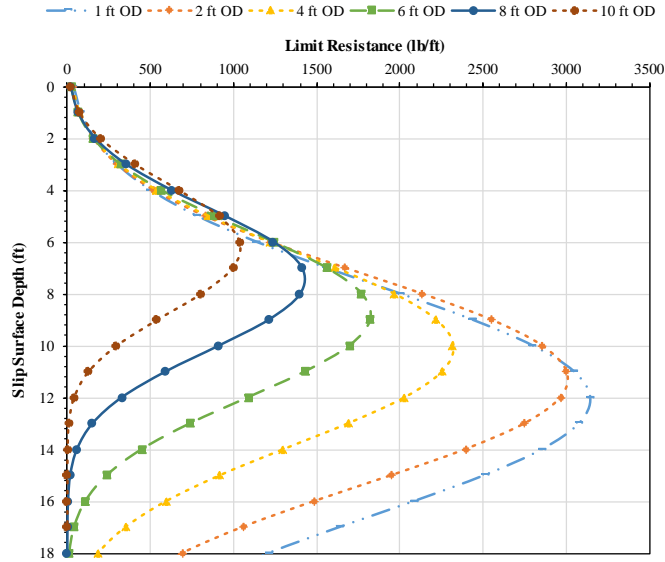
Limit Flexure for $c=50$ psf, $\phi=20^\circ$



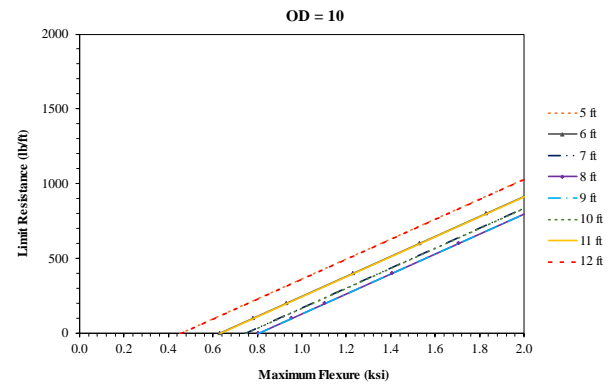
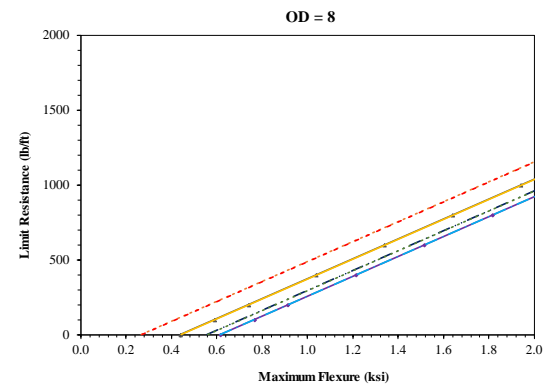
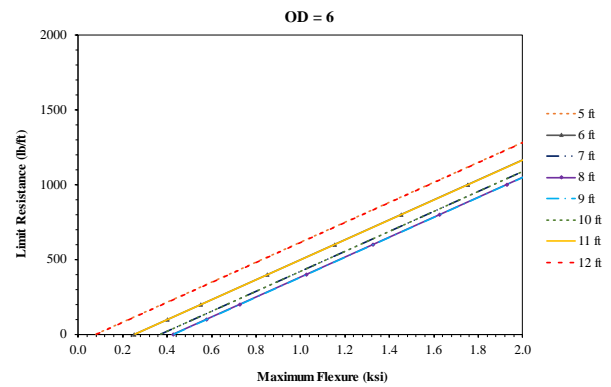
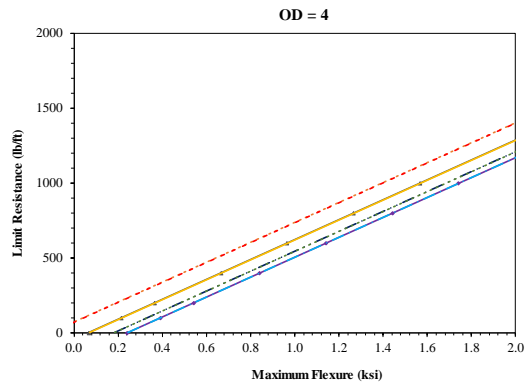
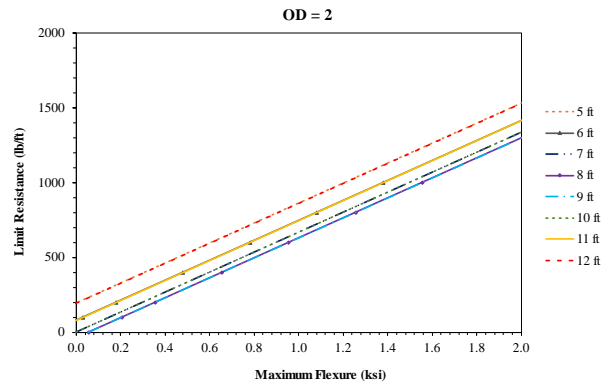
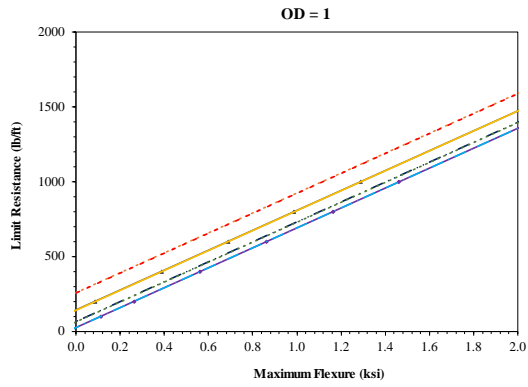
Limit Soil Resistance and Maximum Lateral Displacement for $c=50\text{psf}$, $\phi=30^\circ$



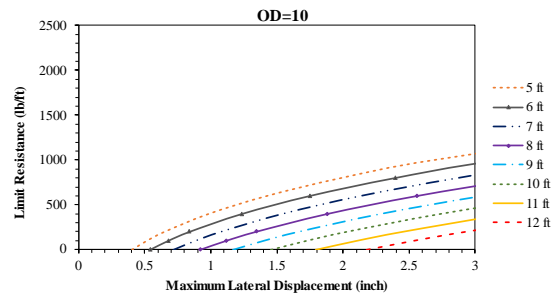
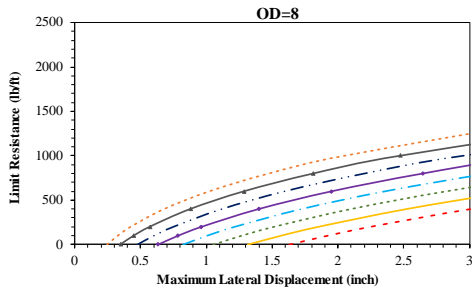
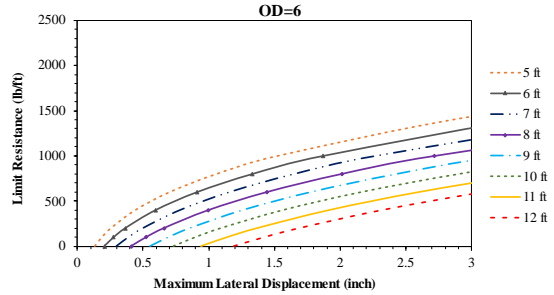
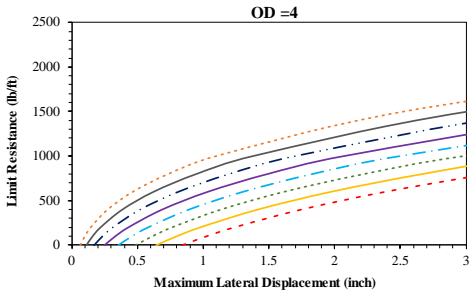
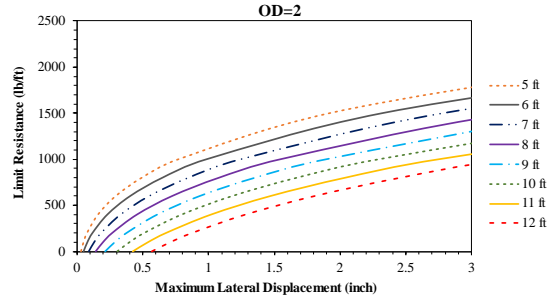
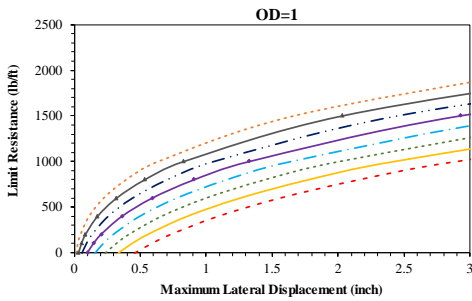
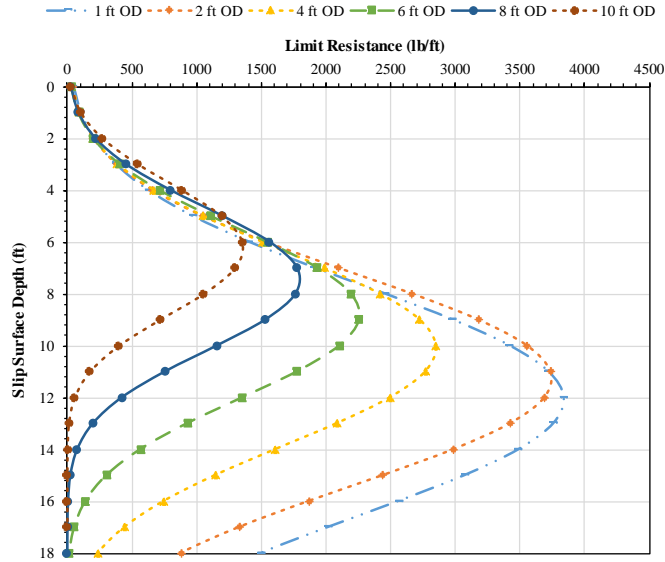
Limit Flexure for $c=50$ psf, $\phi=30^\circ$



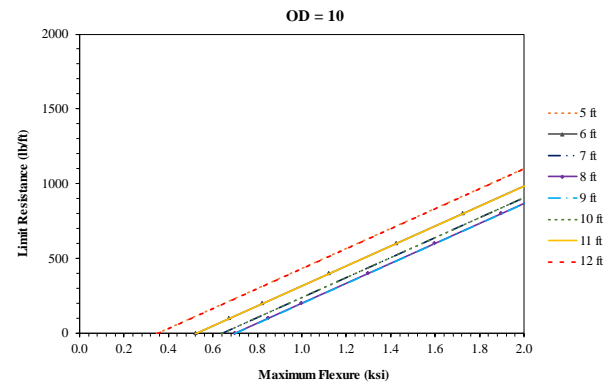
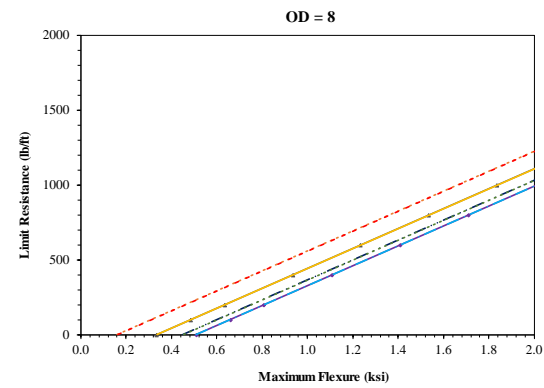
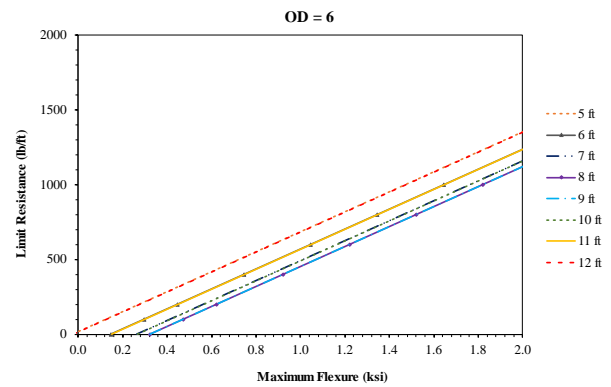
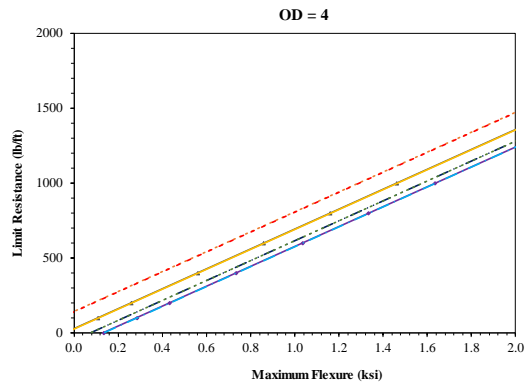
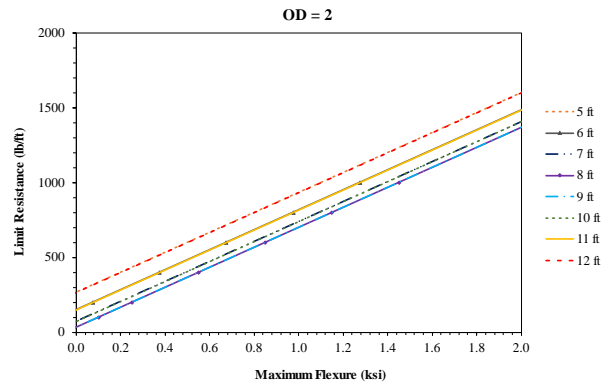
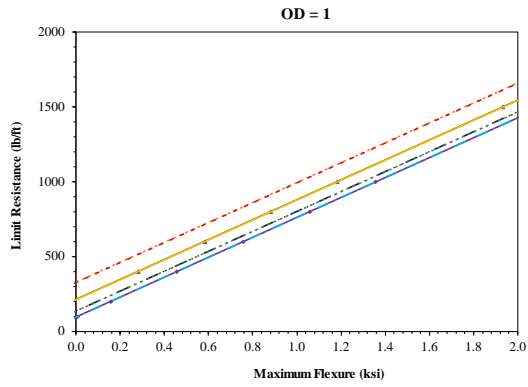
Limit Soil Resistance and Maximum Lateral Displacement for $c=100\text{psf}$, $\phi=10^\circ$



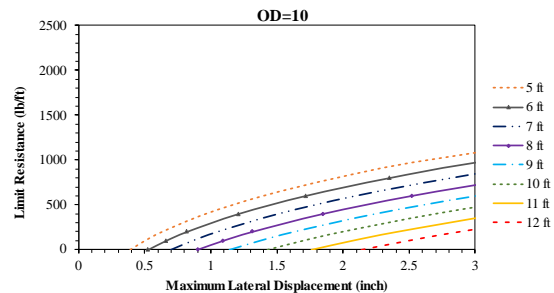
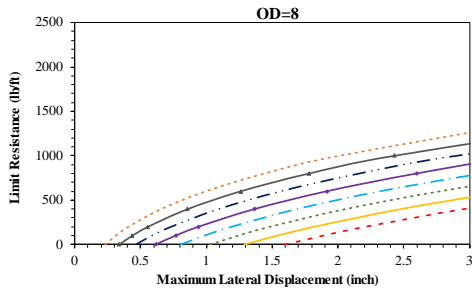
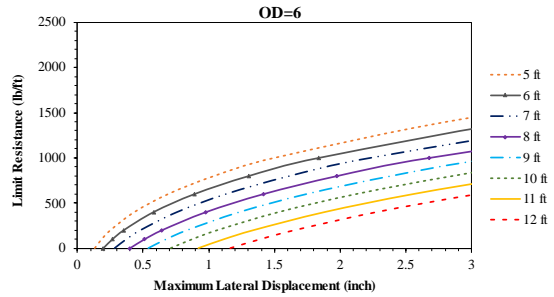
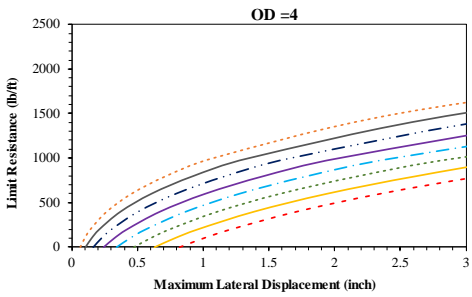
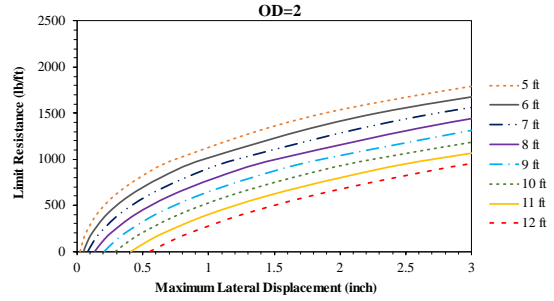
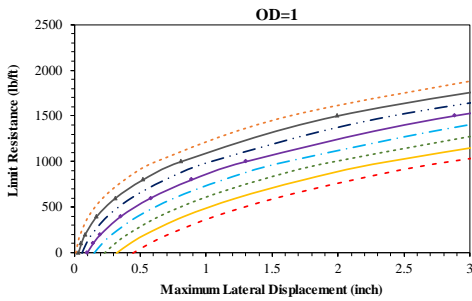
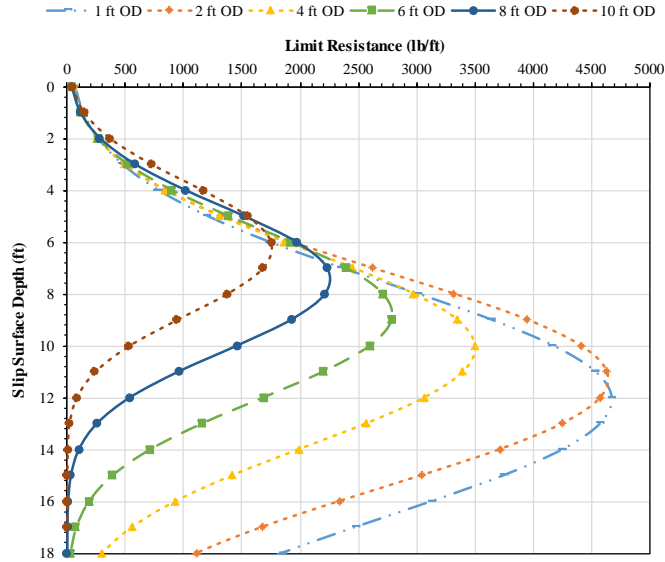
Limit Flexure for $c=100$ psf, $\phi=10^\circ$



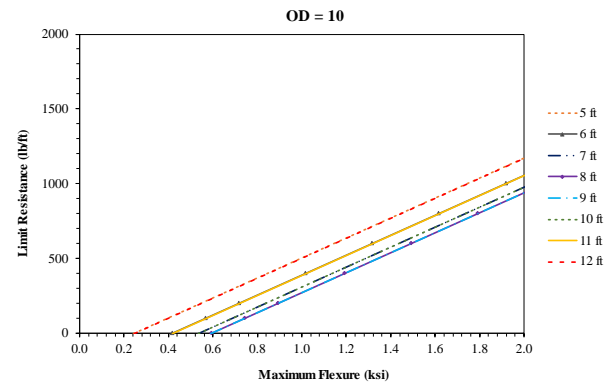
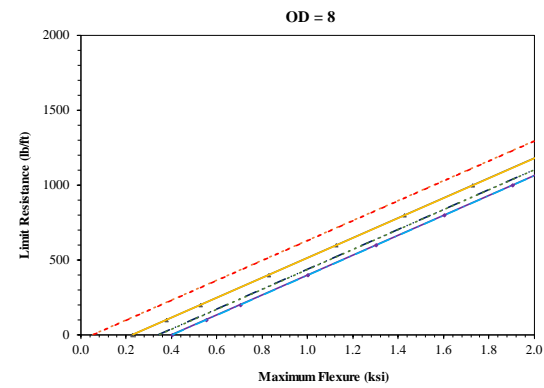
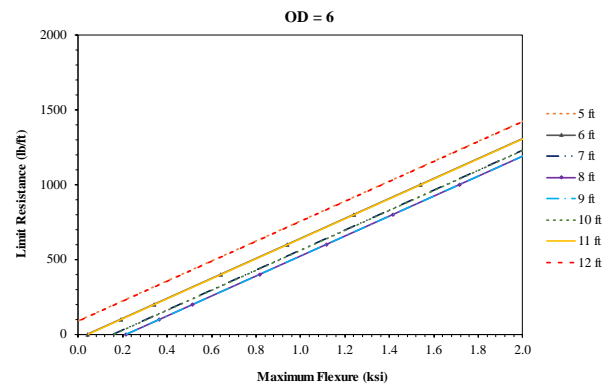
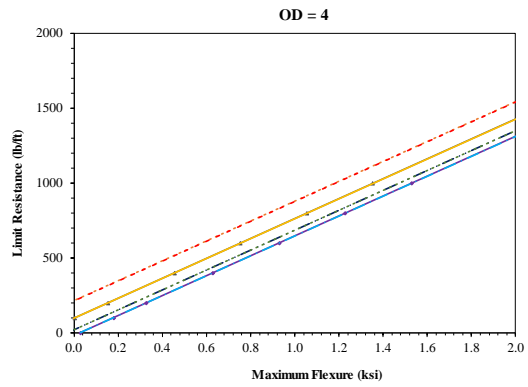
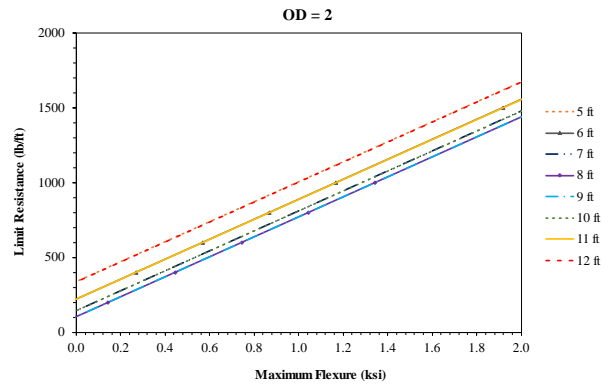
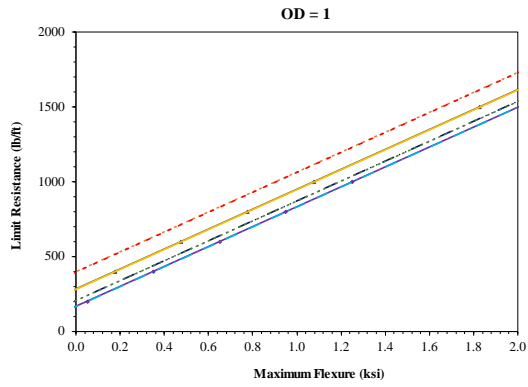
Limit Soil Resistance and Maximum Lateral Displacement for $c=100\text{psf}$, $\phi=20^\circ$



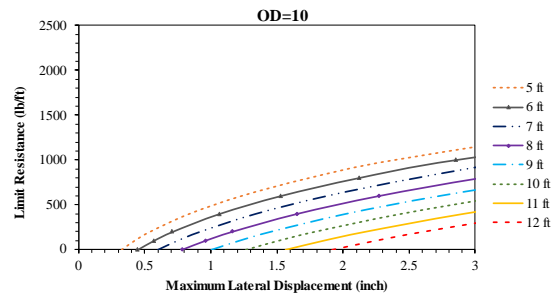
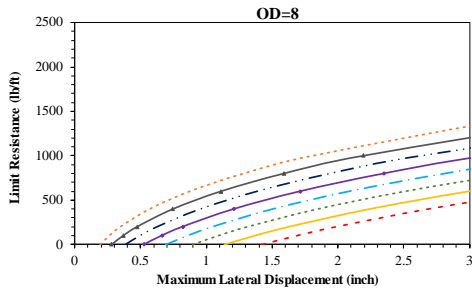
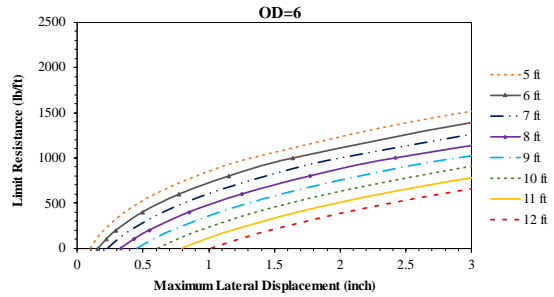
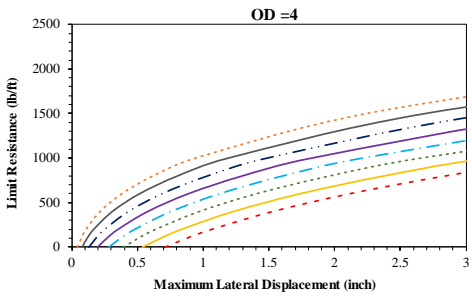
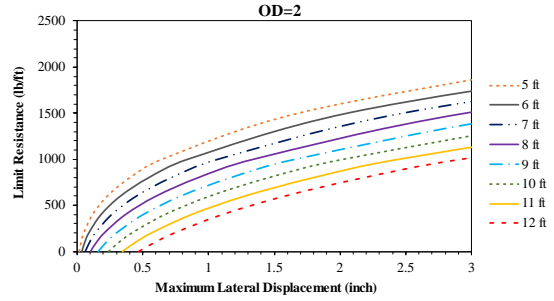
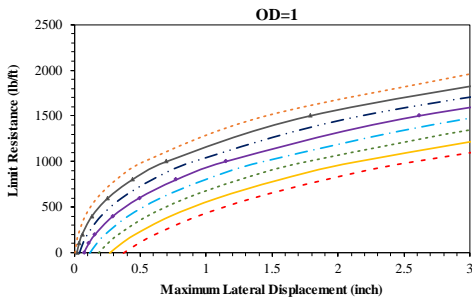
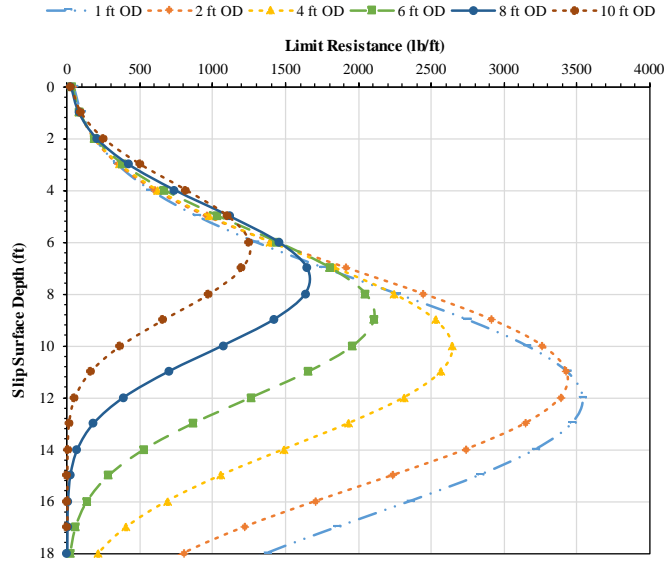
Limit Flexure for $c=100$ psf, $\phi=20^\circ$



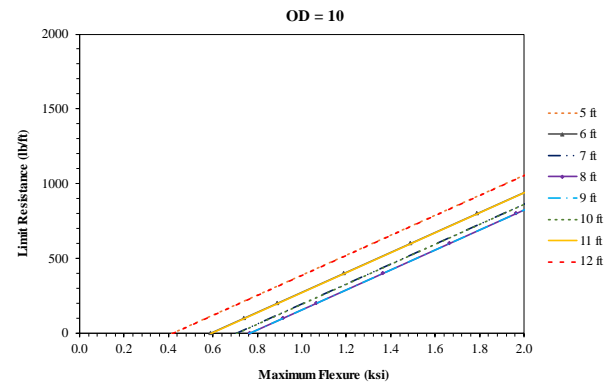
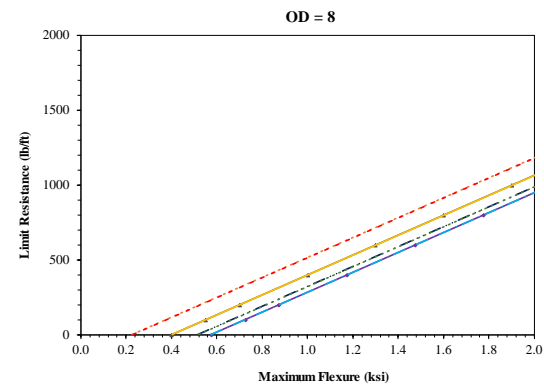
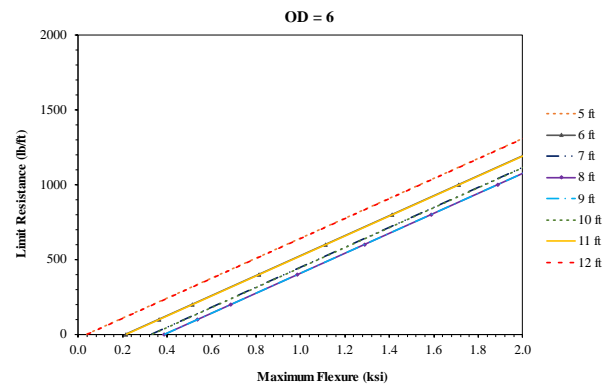
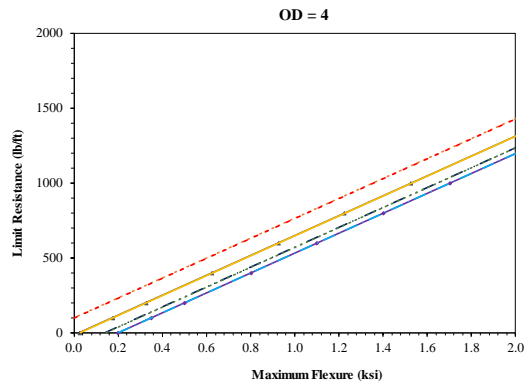
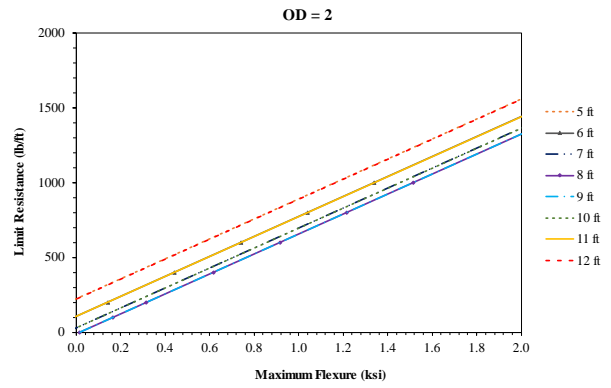
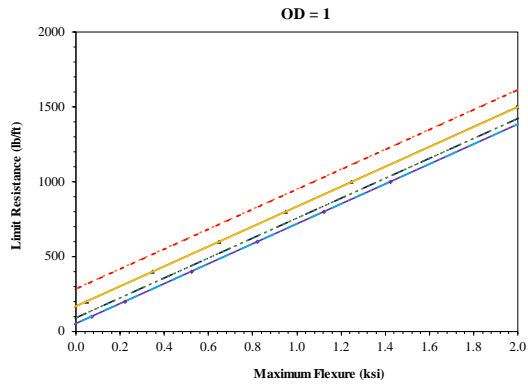
Limit Soil Resistance and Maximum Lateral Displacement for $c=100\text{psf}$, $\phi=30^\circ$



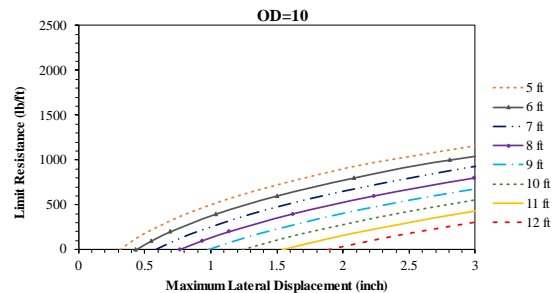
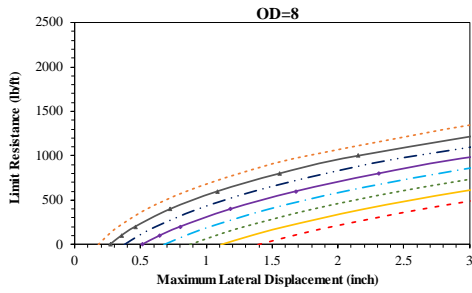
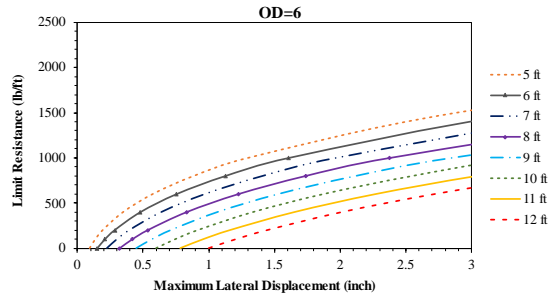
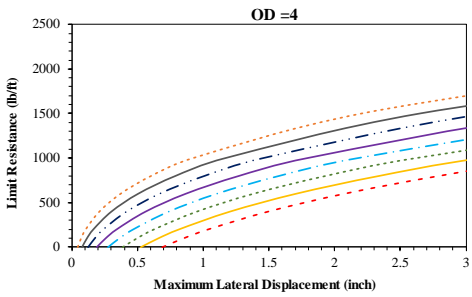
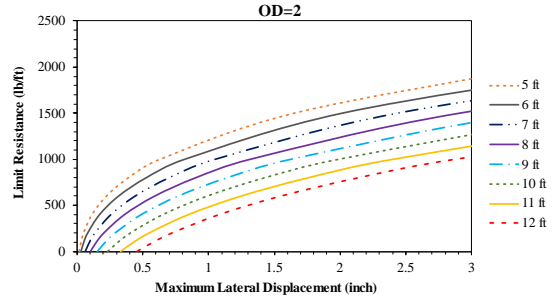
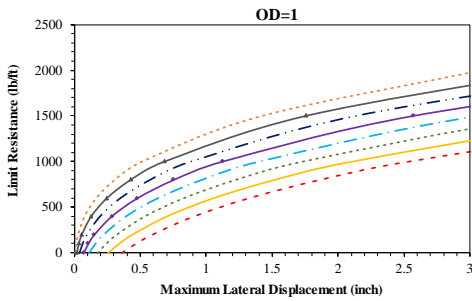
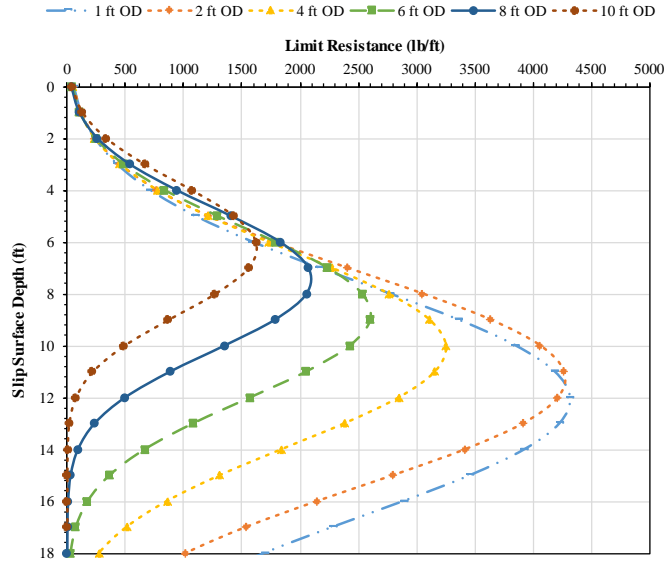
Limit Flexure for $c=100$ psf, $\phi=30^\circ$



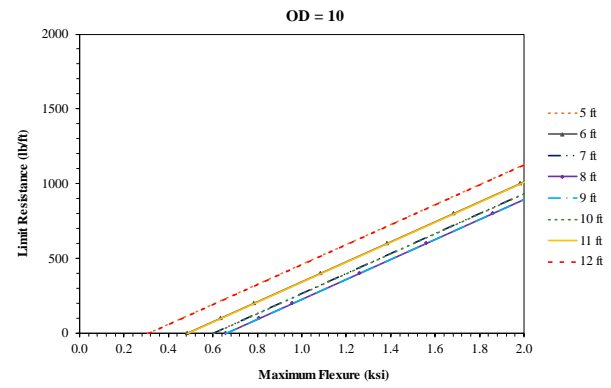
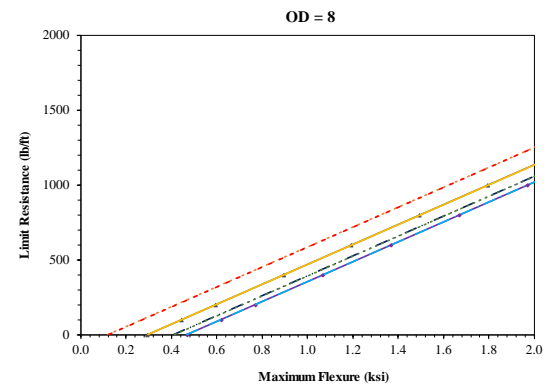
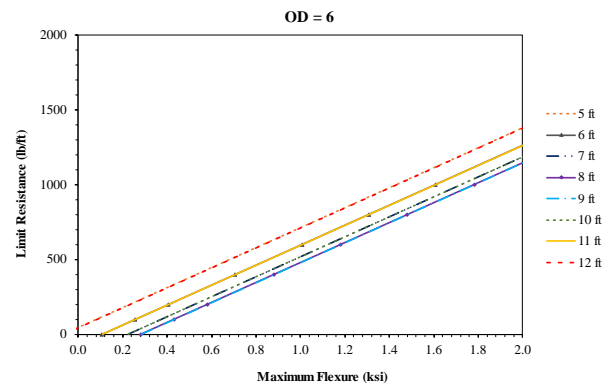
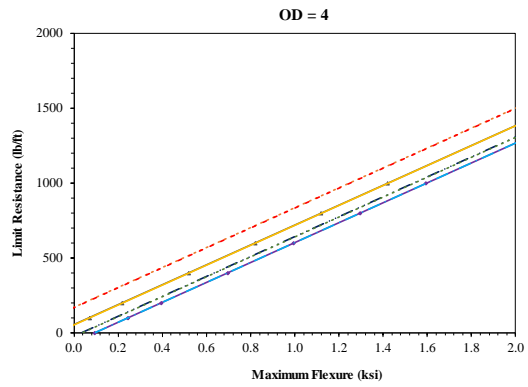
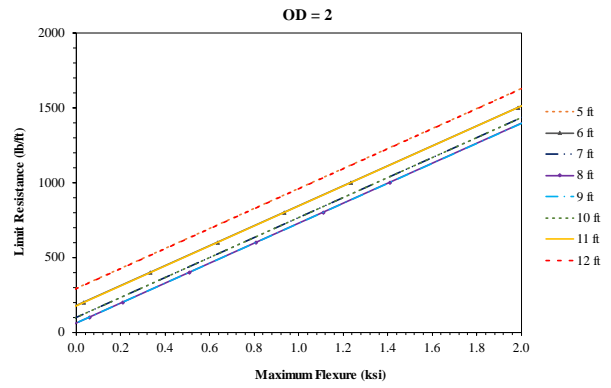
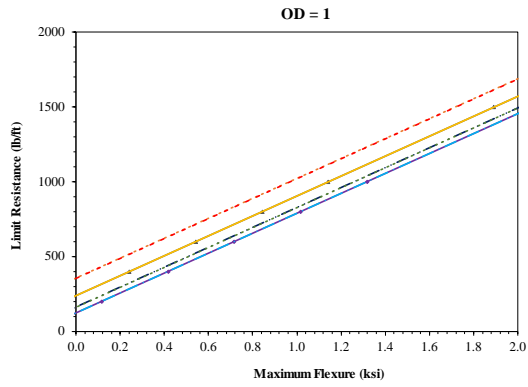
Limit Soil Resistance and Maximum Lateral Displacement for $c=200\text{psf}$, $\phi=10^\circ$



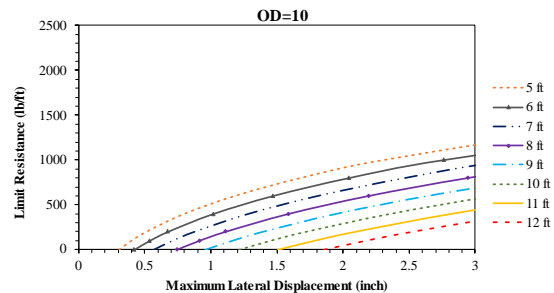
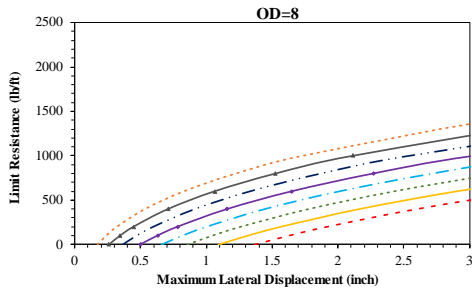
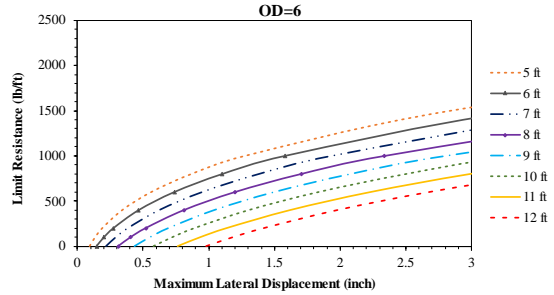
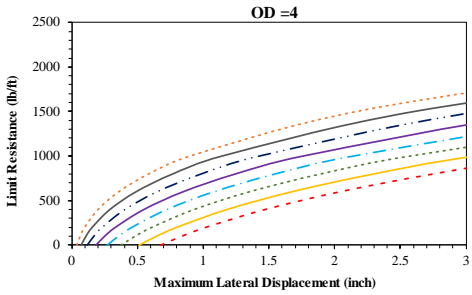
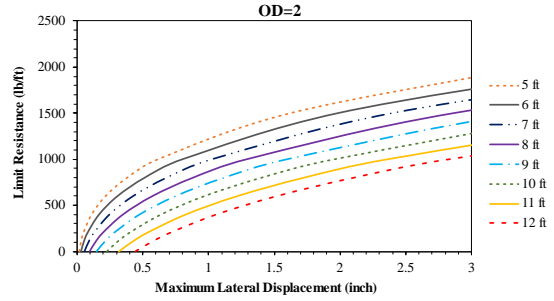
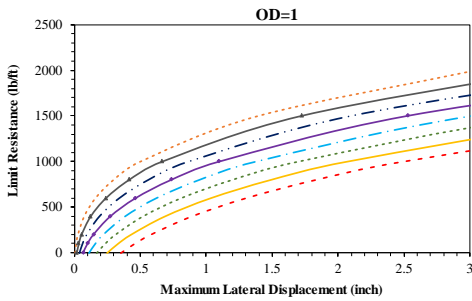
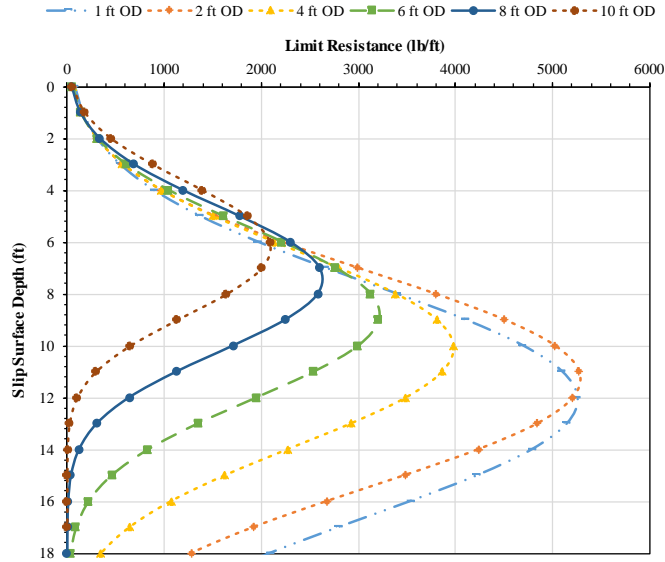
Limit Flexure for $c=200$ psf, $\phi=10^\circ$



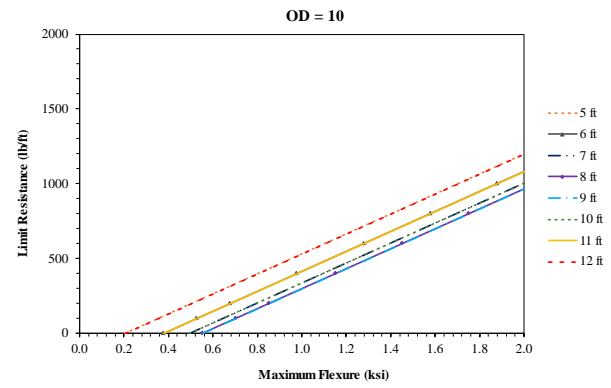
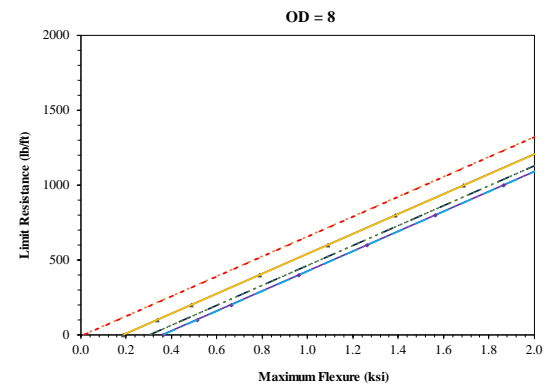
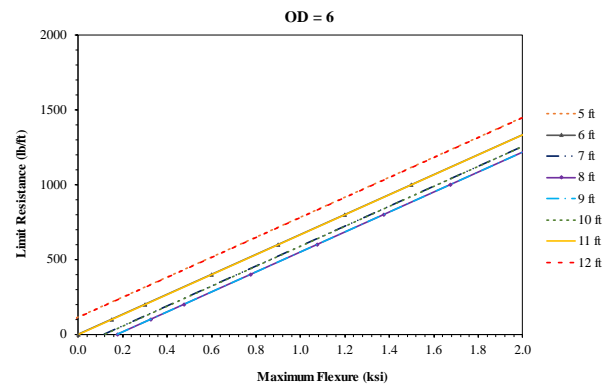
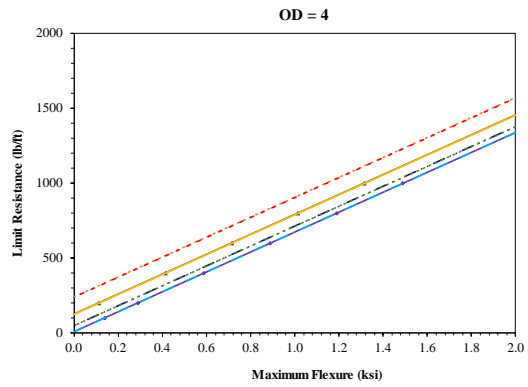
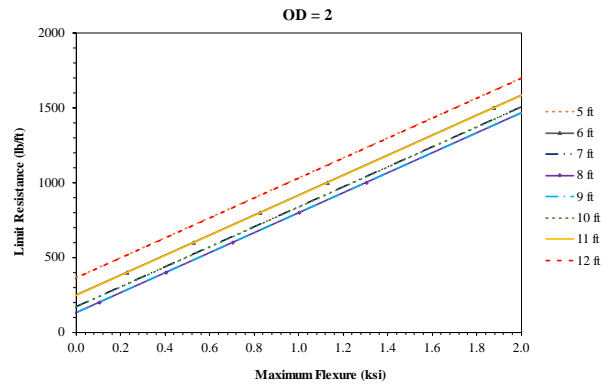
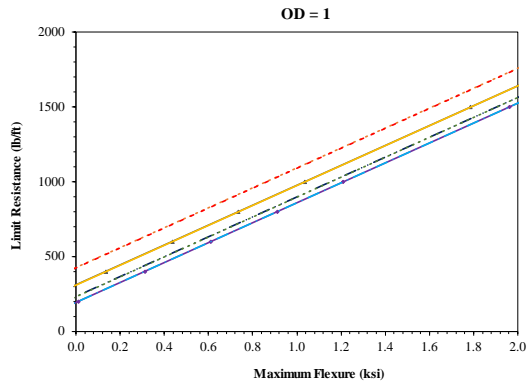
Limit Soil Resistance and Maximum Lateral Displacement for $c=200\text{psf}$, $\phi=20^\circ$



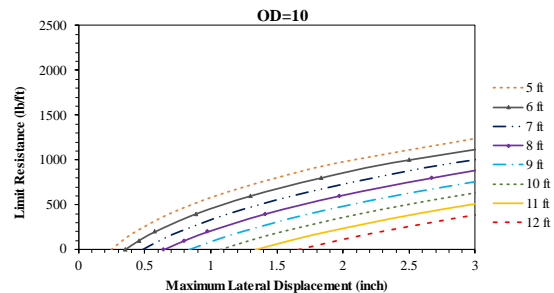
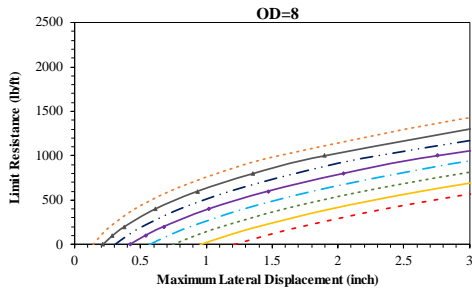
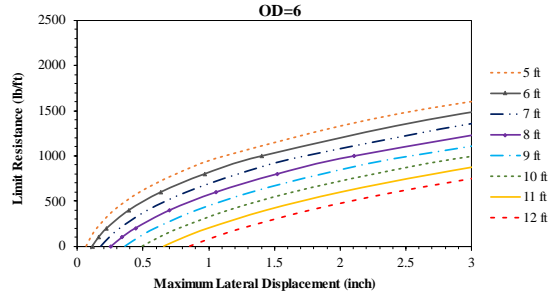
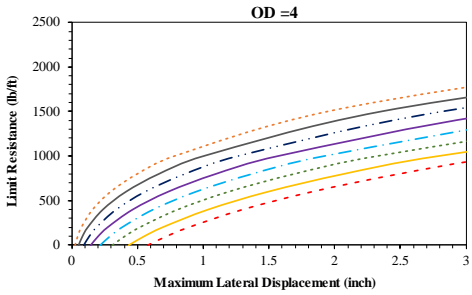
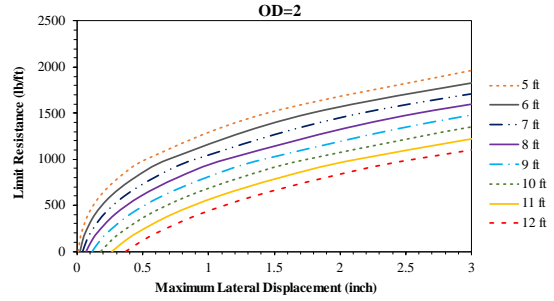
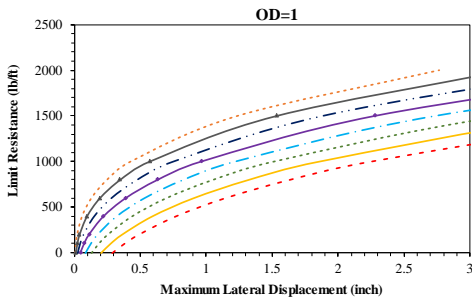
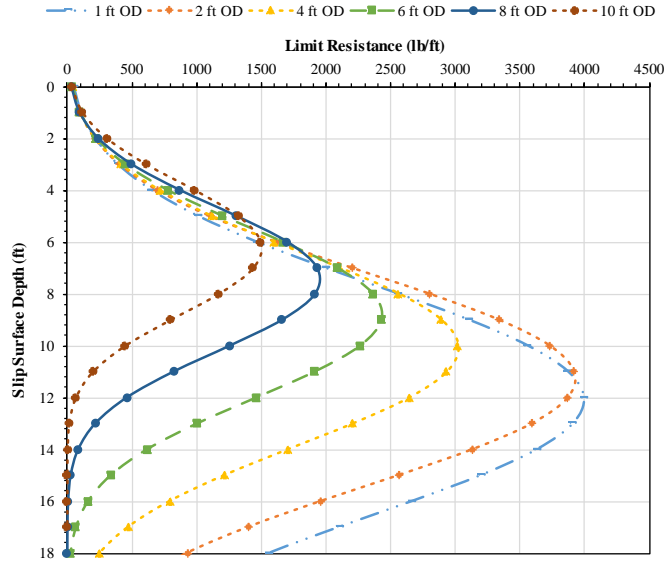
Limit Flexure for $c=200$ psf, $\phi=20^\circ$



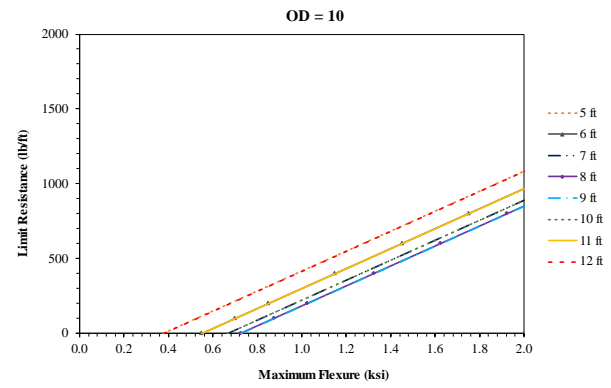
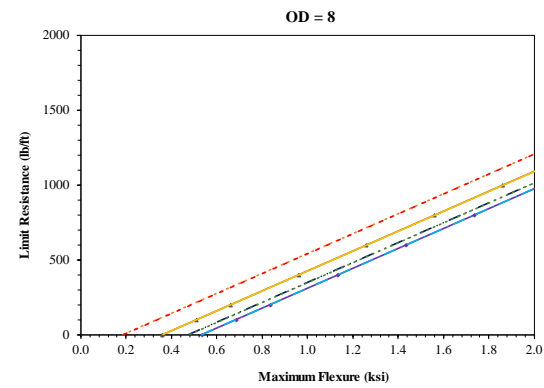
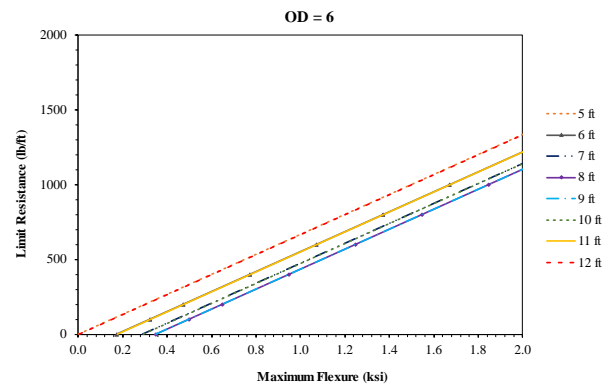
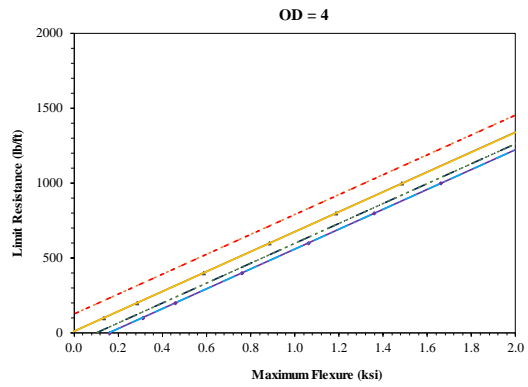
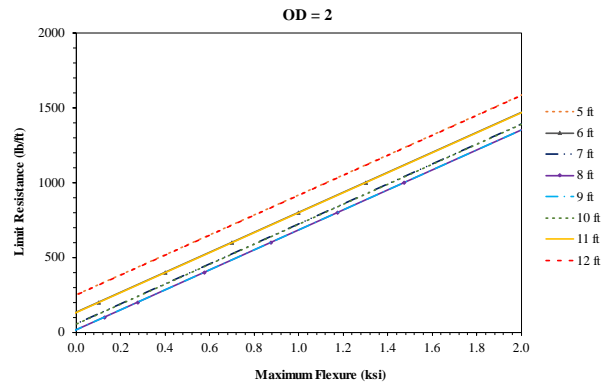
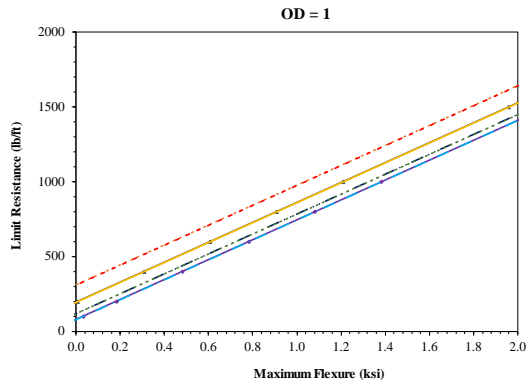
Limit Soil Resistance and Maximum Lateral Displacement for $c=200\text{psf}$, $\phi=30^\circ$



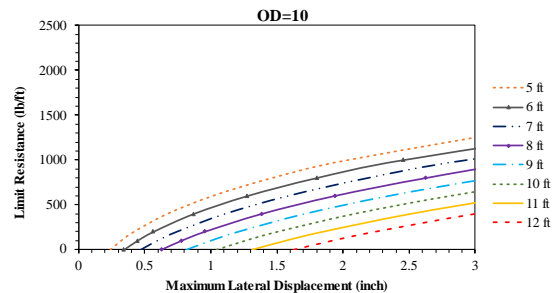
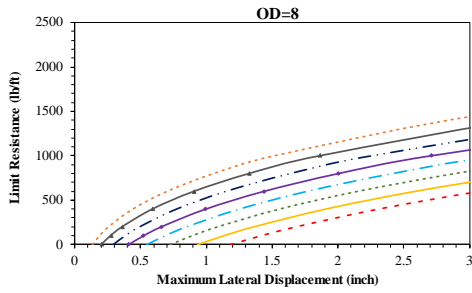
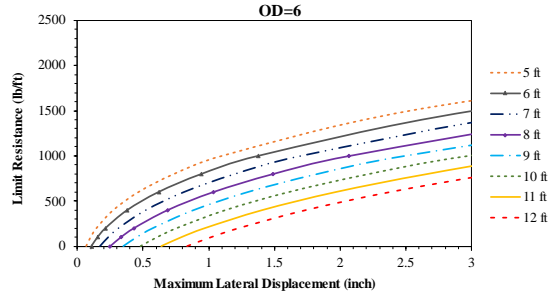
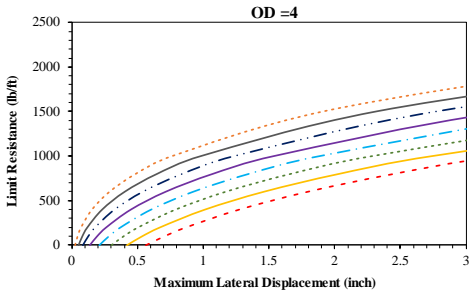
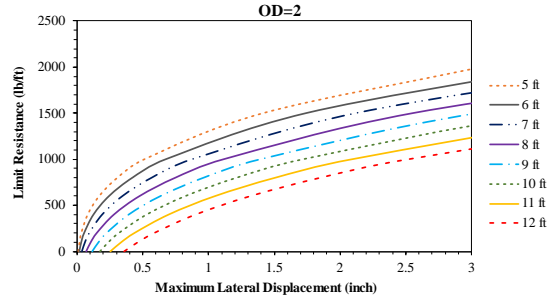
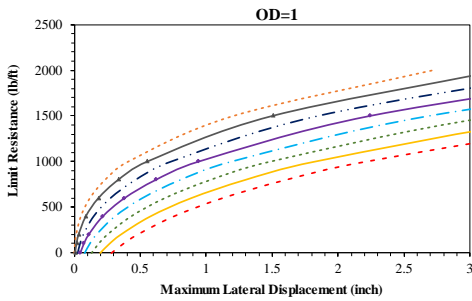
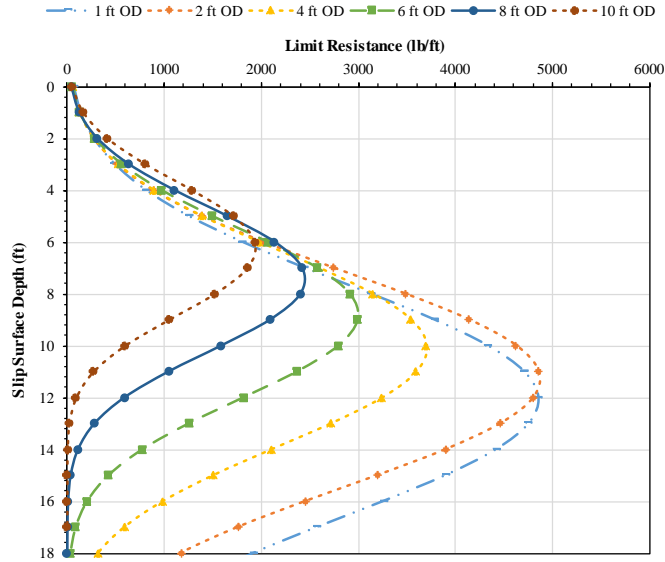
Limit Flexure for $c=200$ psf, $\phi=30^\circ$



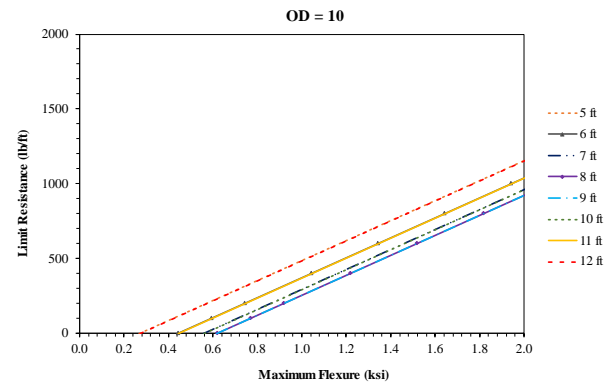
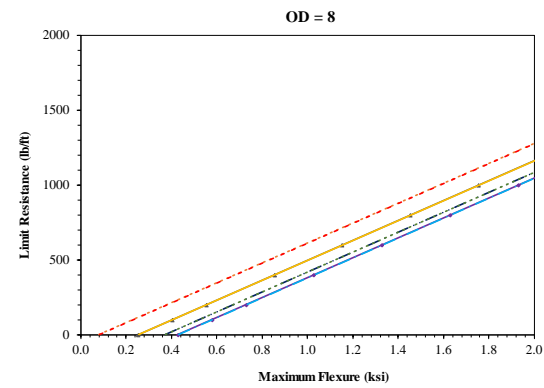
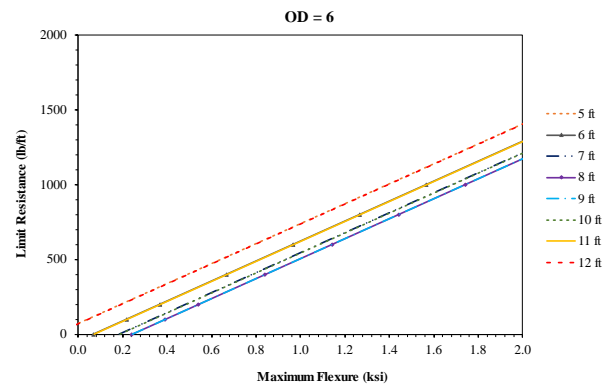
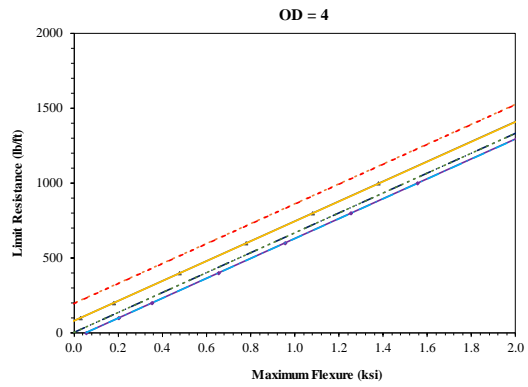
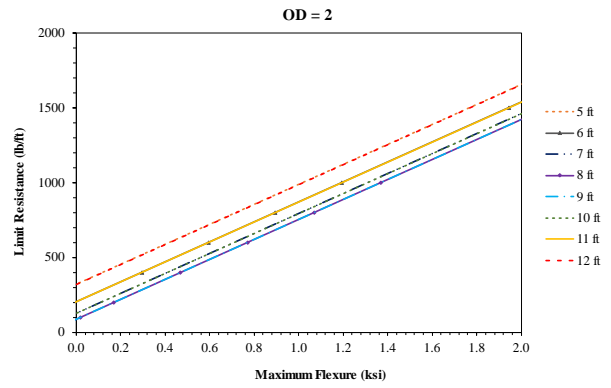
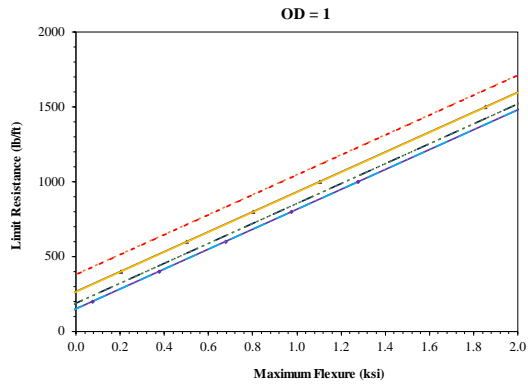
Limit Soil Resistance and Maximum Lateral Displacement for $c=300\text{psf}$, $\phi=10^\circ$



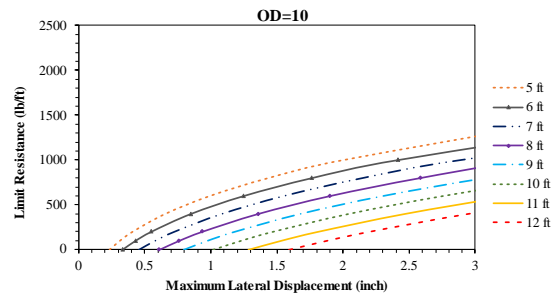
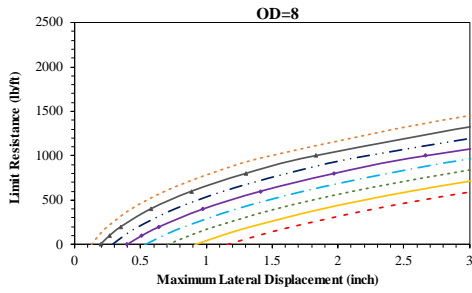
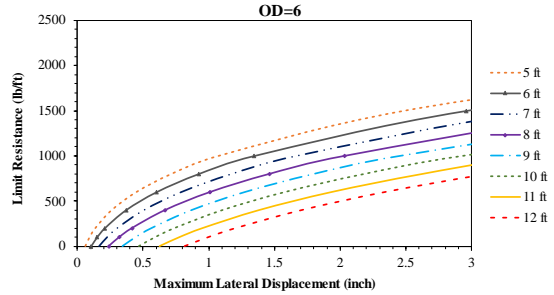
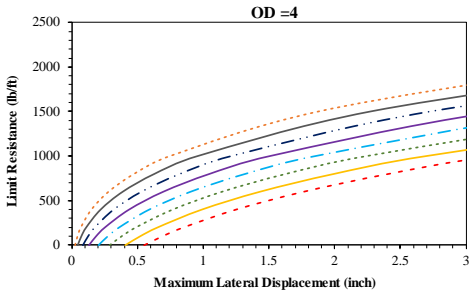
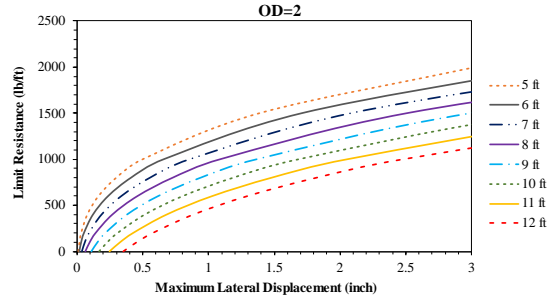
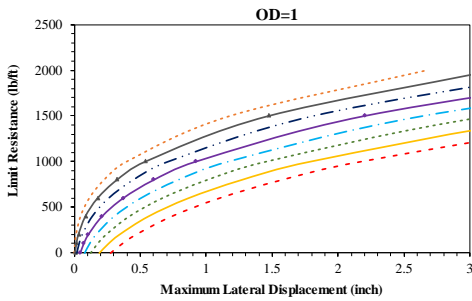
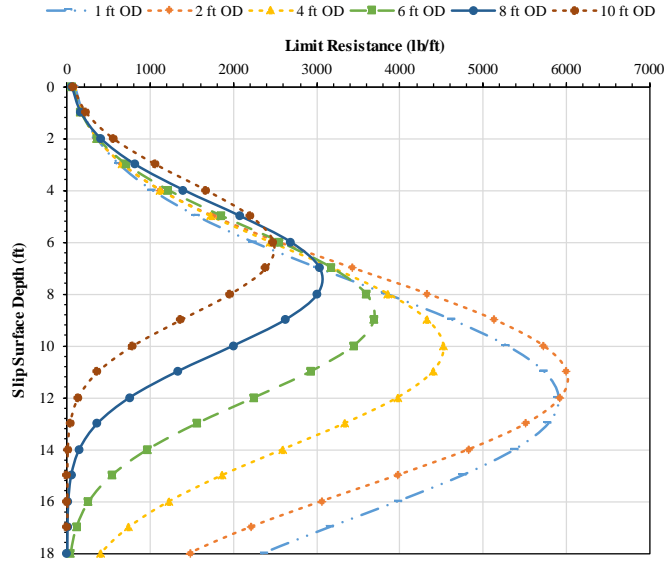
Limit Flexure for $c=300$ psf, $\phi=10^\circ$



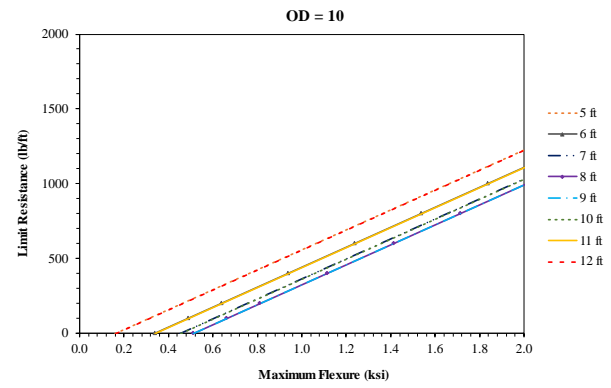
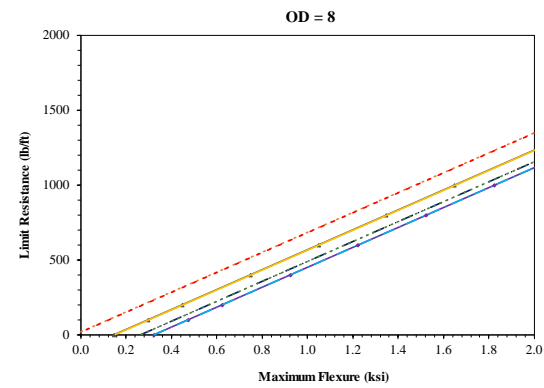
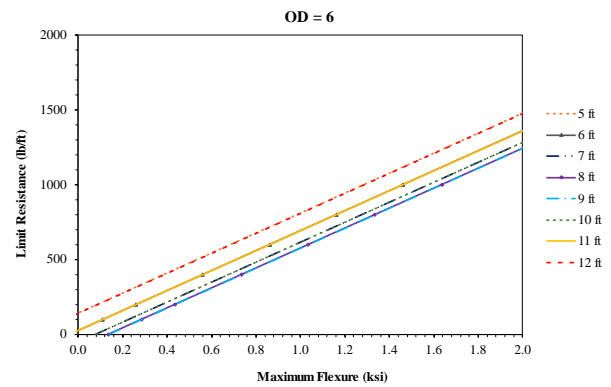
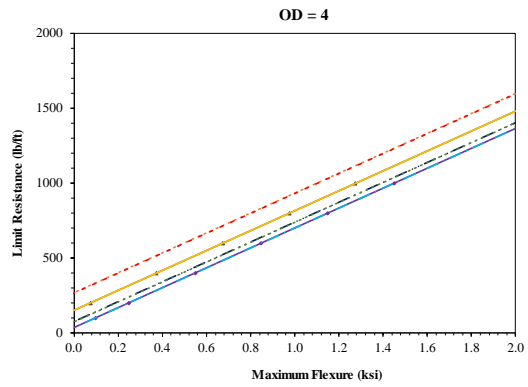
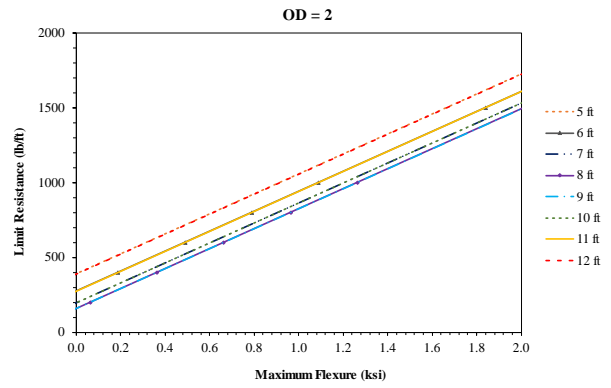
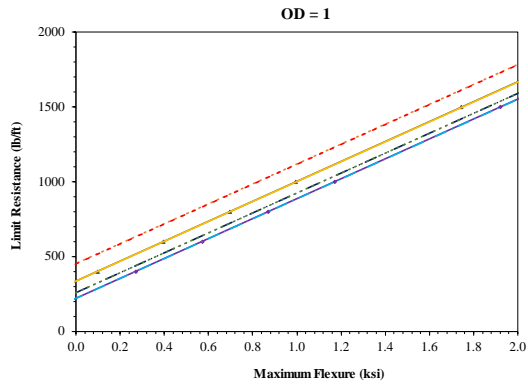
Limit Soil Resistance and Maximum Lateral Displacement for $c=300\text{psf}$, $\phi=20^\circ$



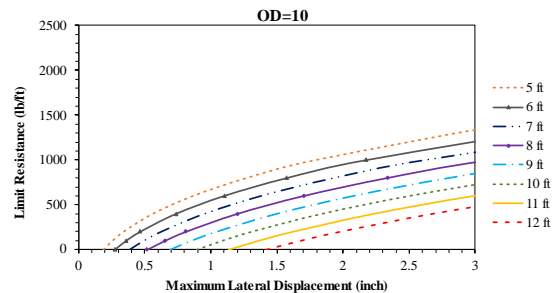
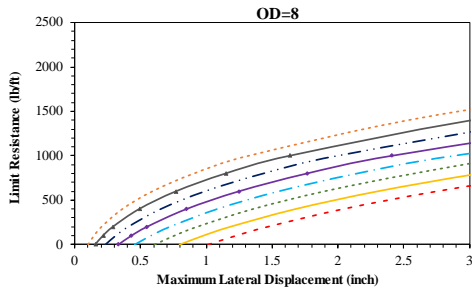
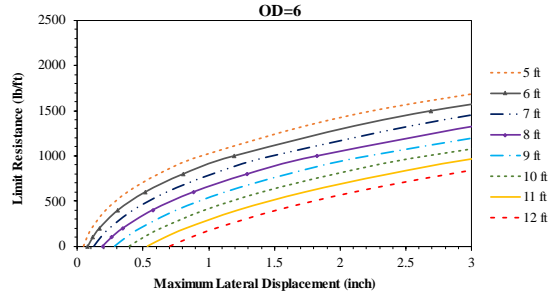
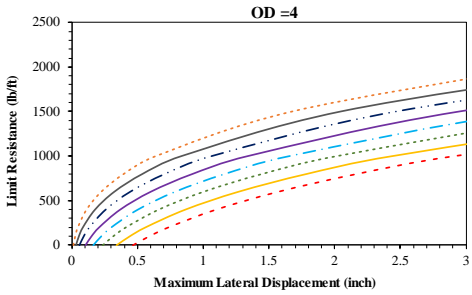
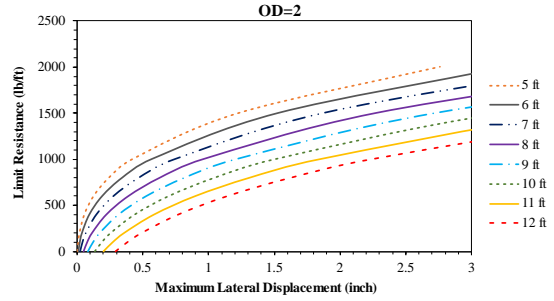
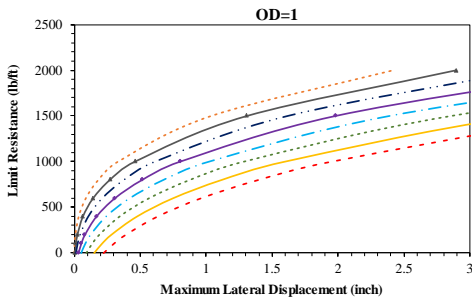
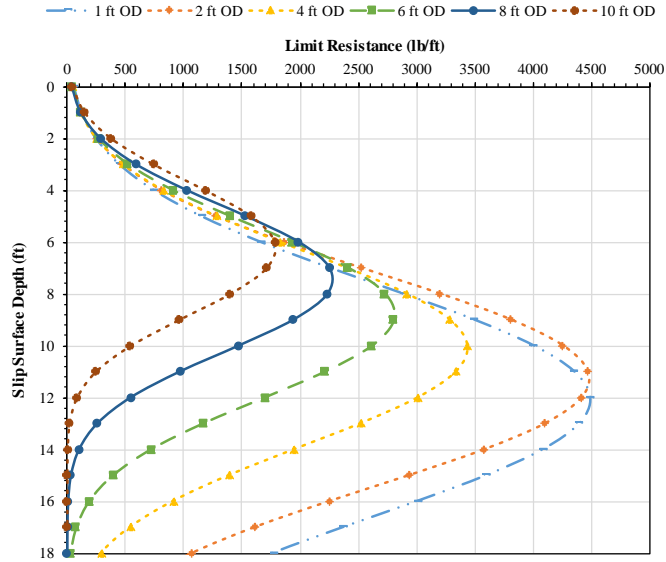
Limit Flexure for $c=300$ psf, $\phi=20^\circ$



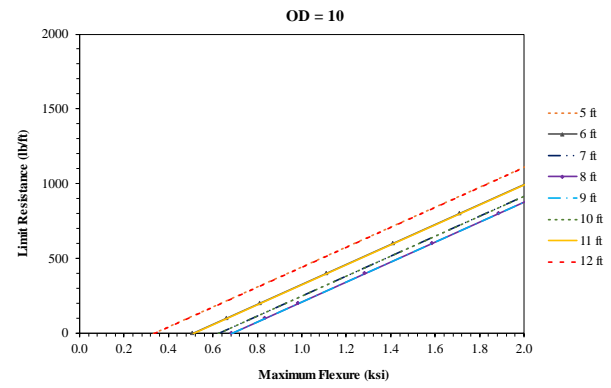
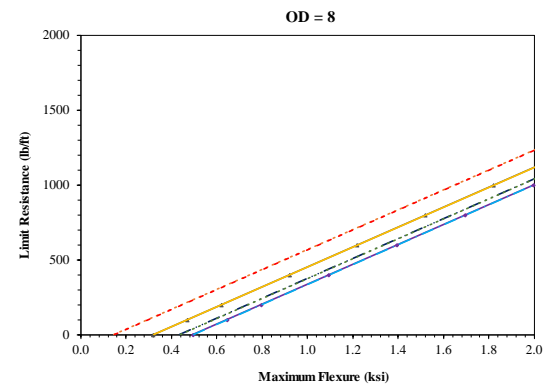
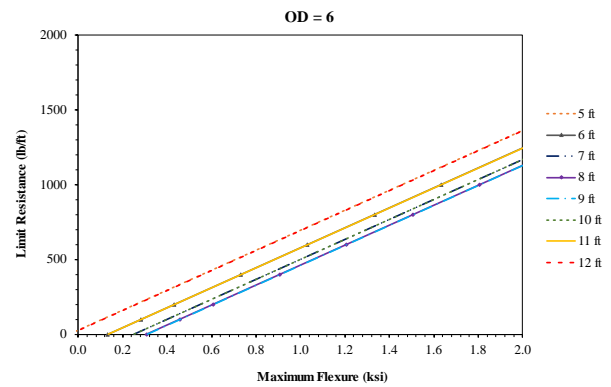
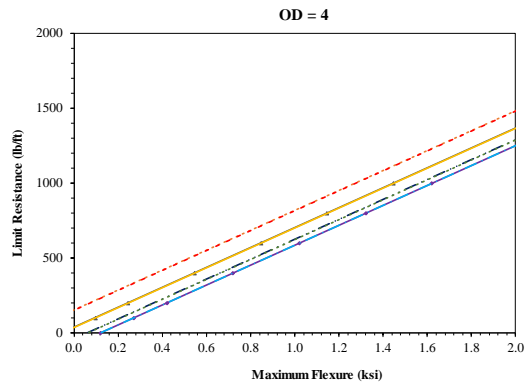
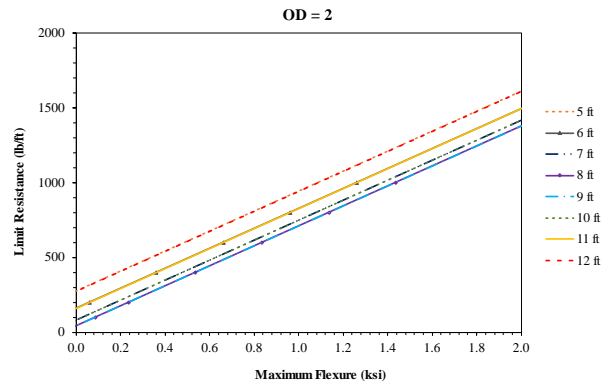
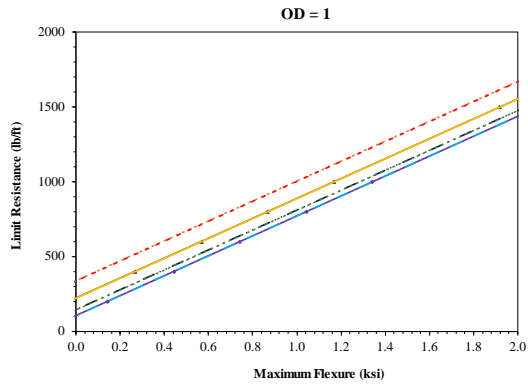
Limit Soil Resistance and Maximum Lateral Displacement for $c=300\text{psf}$, $\phi=30^\circ$



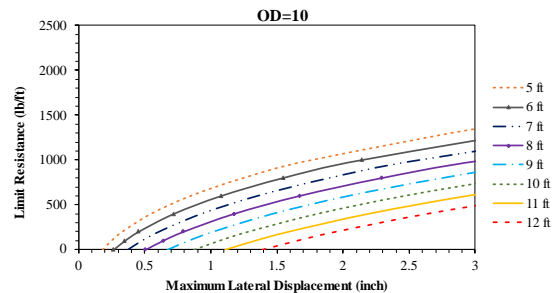
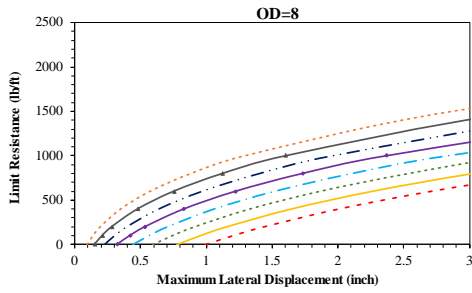
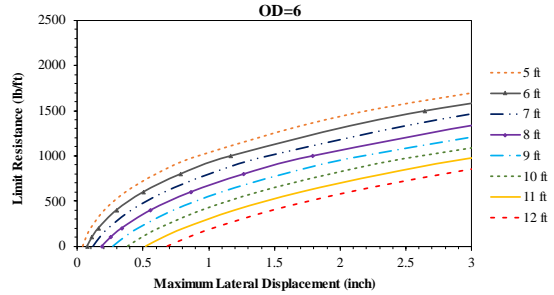
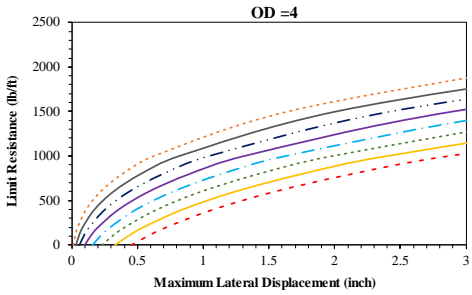
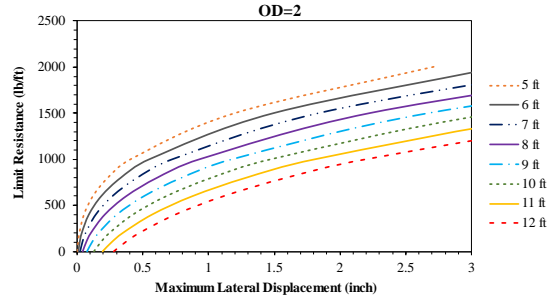
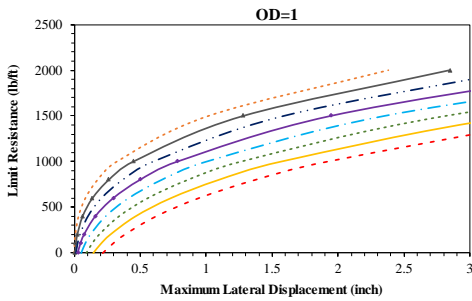
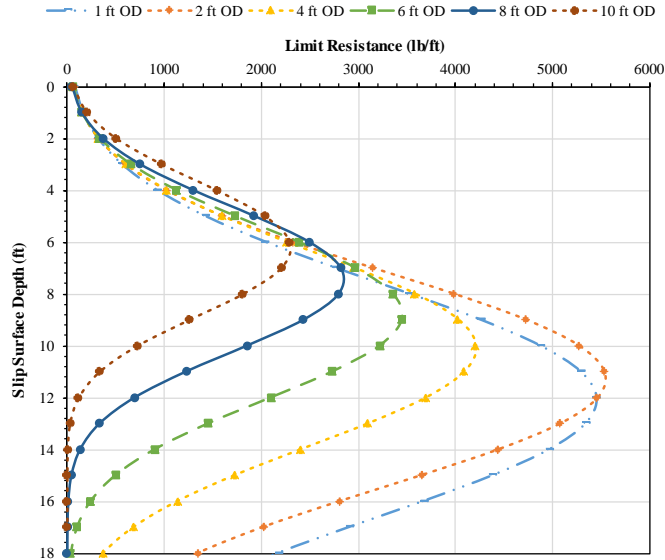
Limit Flexure for $c=300$ psf, $\phi=30^\circ$



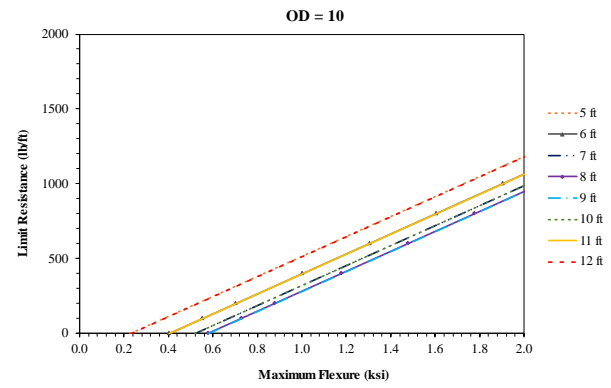
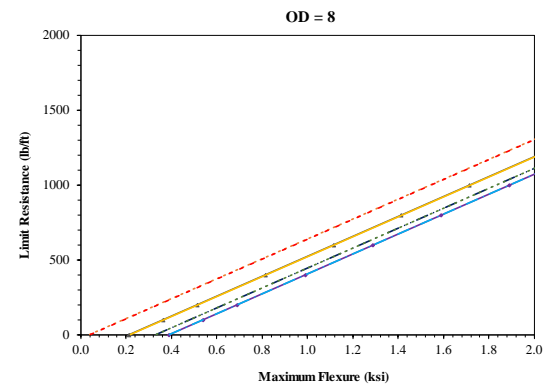
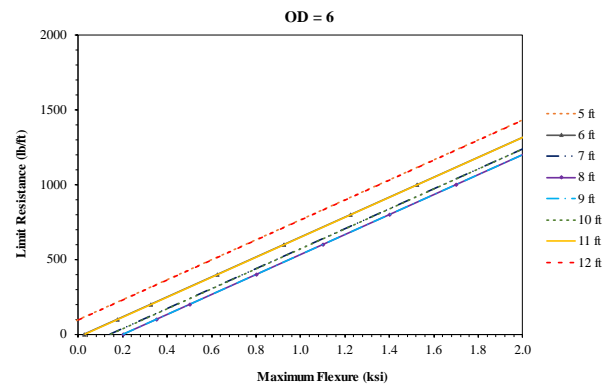
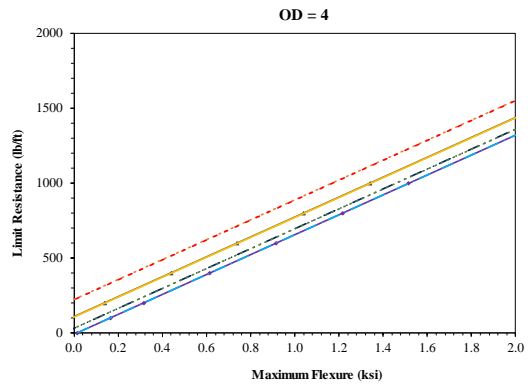
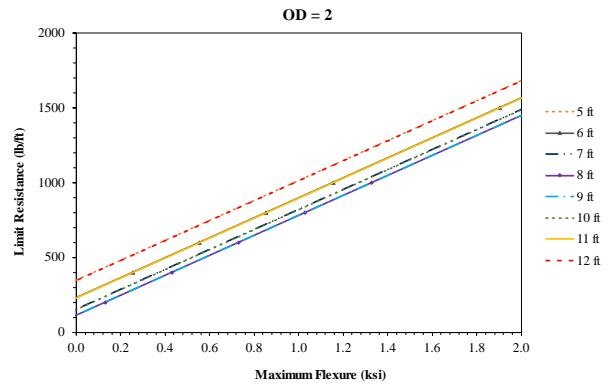
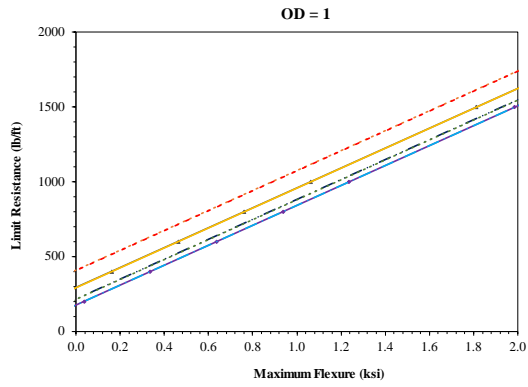
Limit Soil Resistance and Maximum Lateral Displacement for $c=400\text{psf}$, $\phi=10^\circ$



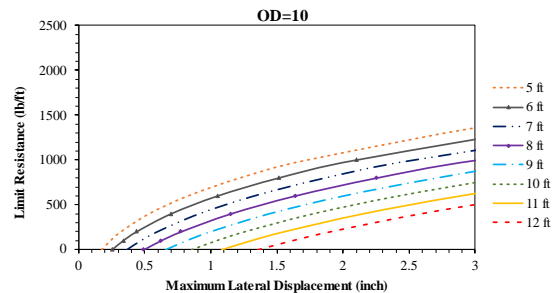
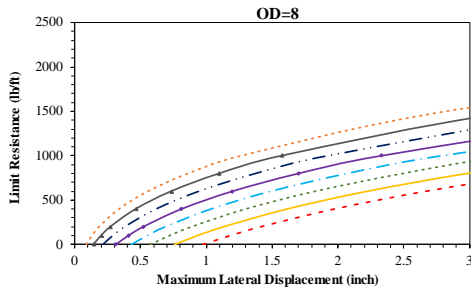
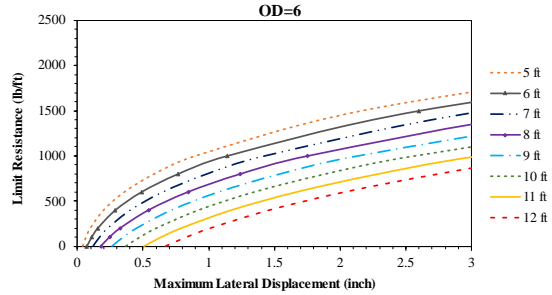
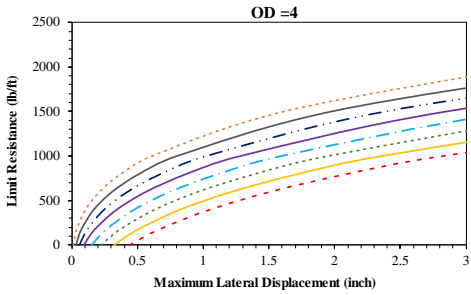
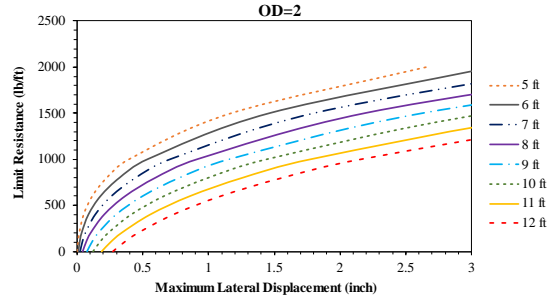
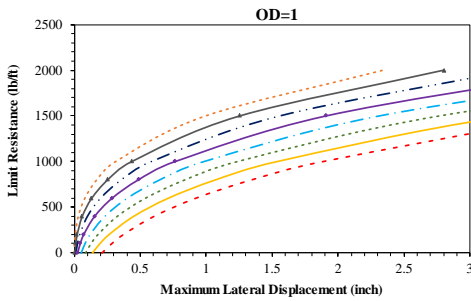
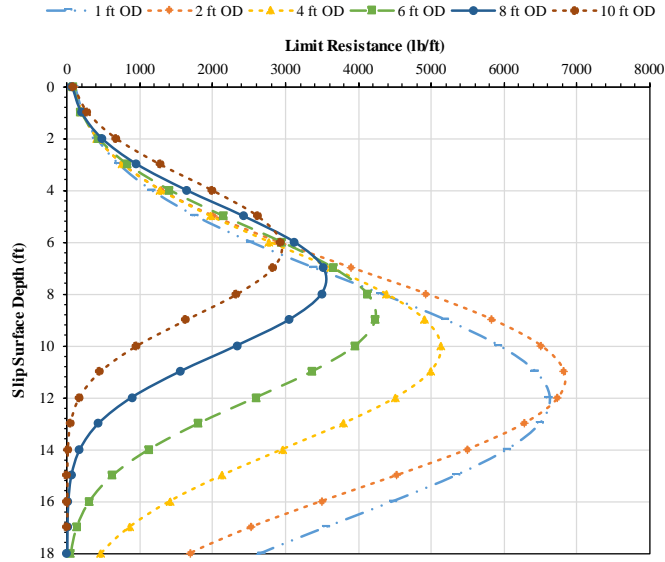
Limit Flexure for $c=400\text{psf}$, $\phi=10^\circ$



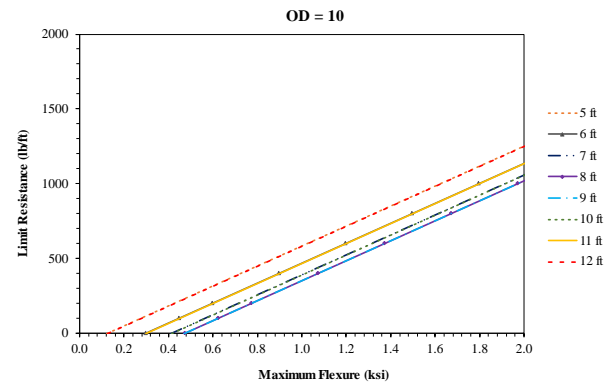
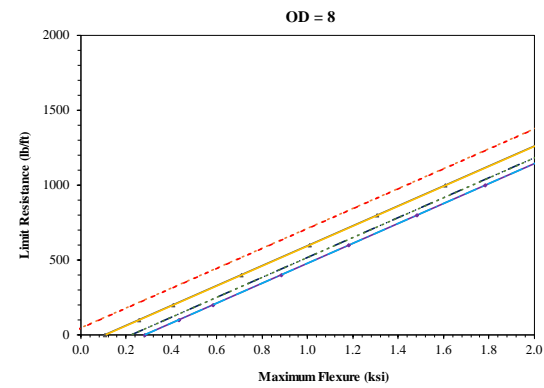
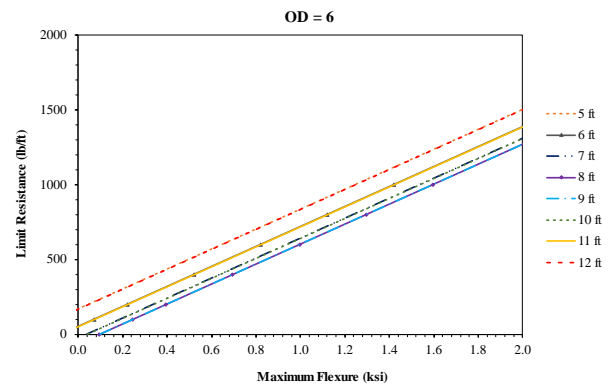
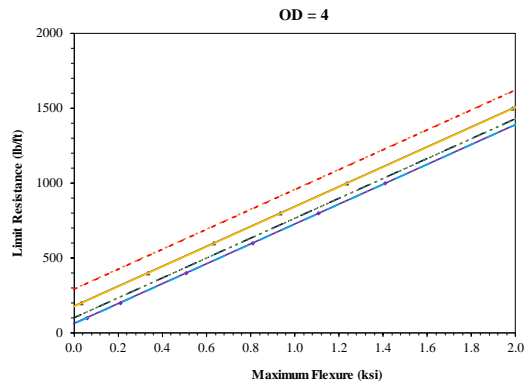
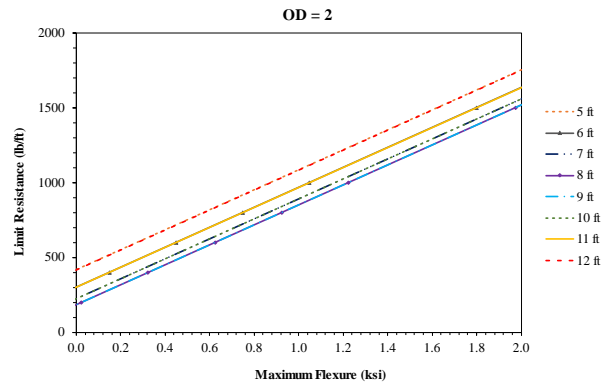
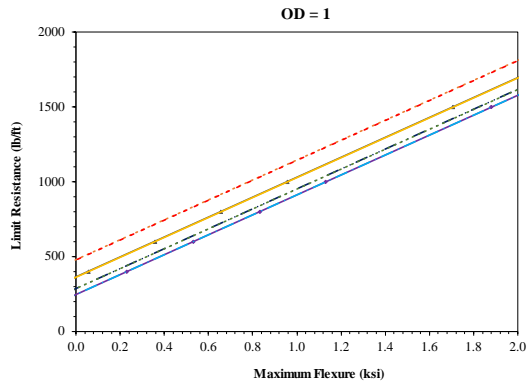
Limit Soil Resistance and Maximum Lateral Displacement for $c=400\text{psf}$, $\phi=20^\circ$



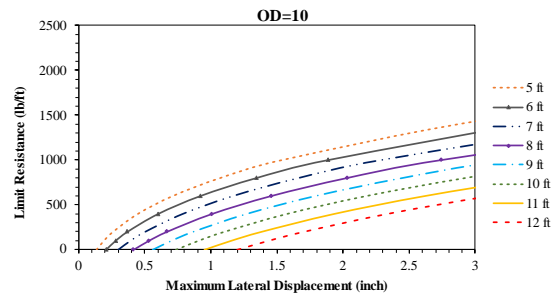
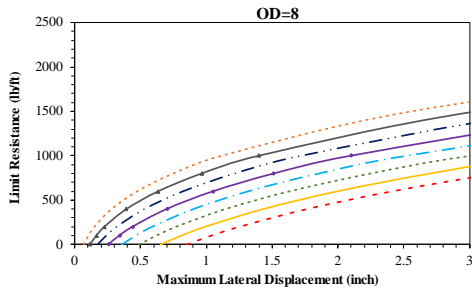
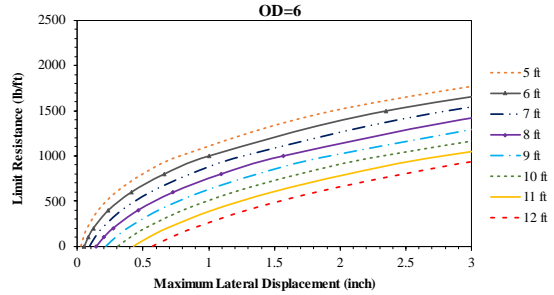
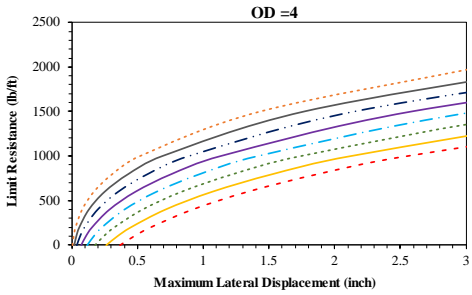
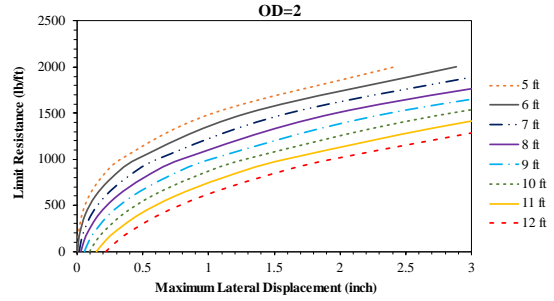
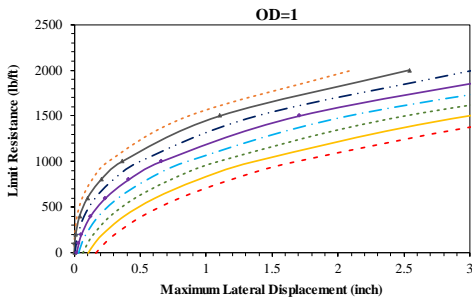
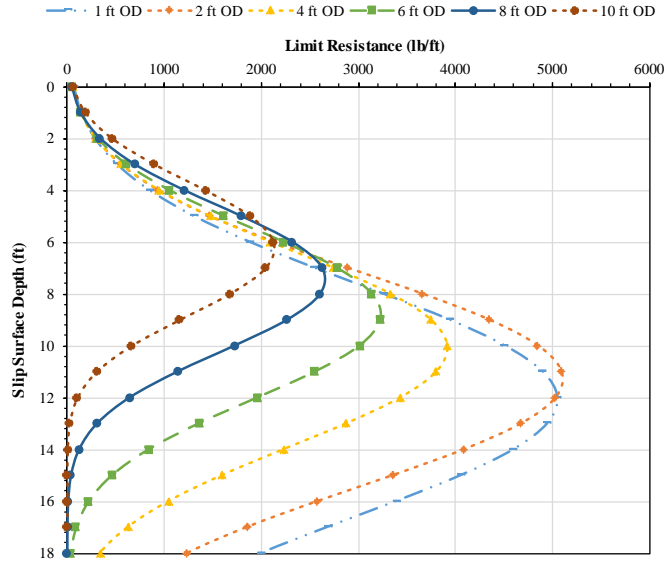
Limit Flexure for $c=400\text{psf}$, $\phi=20^\circ$



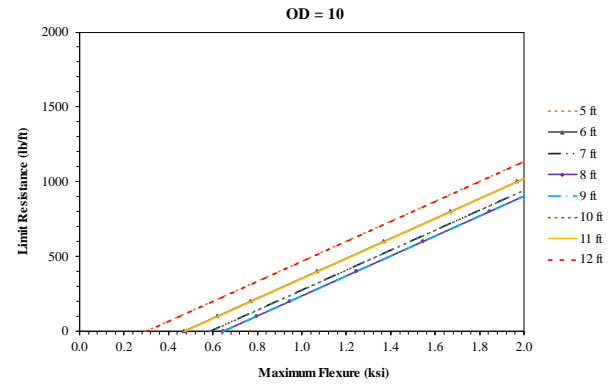
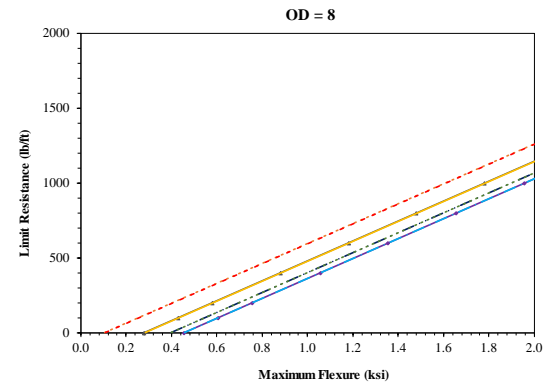
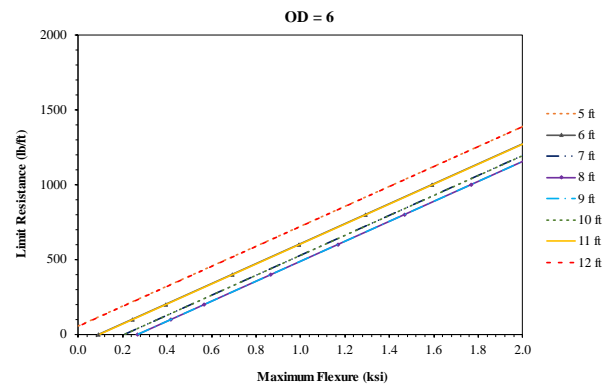
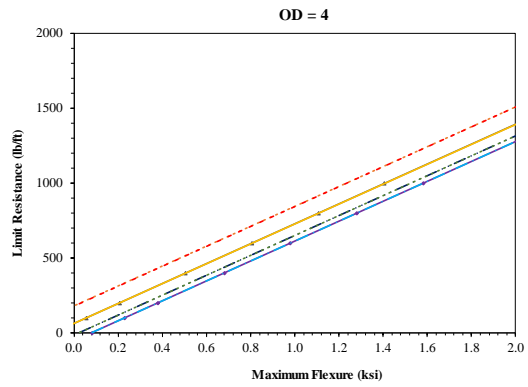
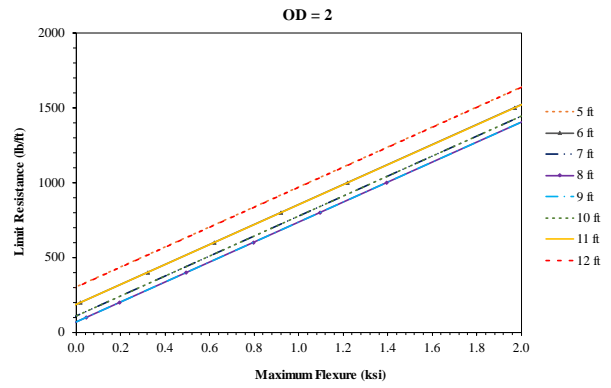
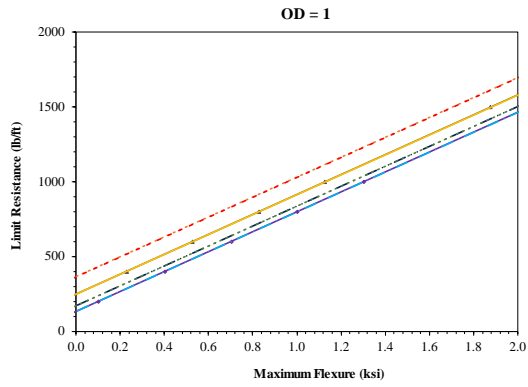
Limit Soil Resistance and Maximum Lateral Displacement for $c=400\text{psf}$, $\phi=30^\circ$



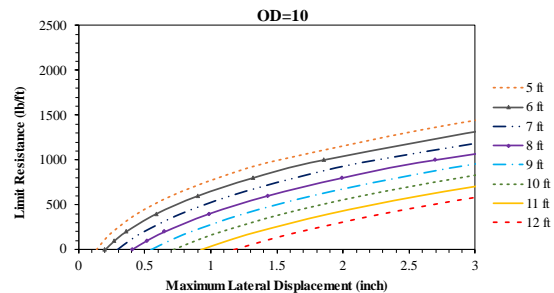
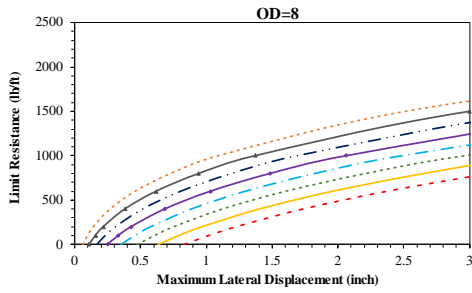
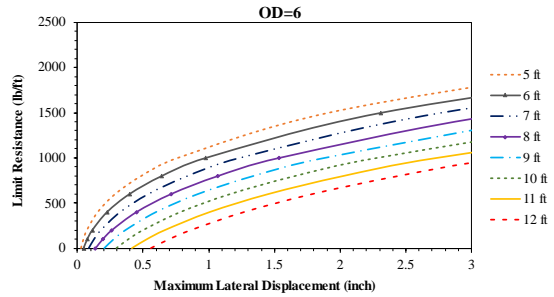
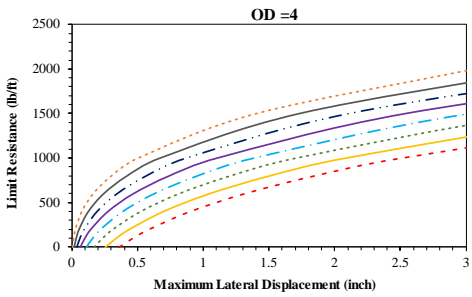
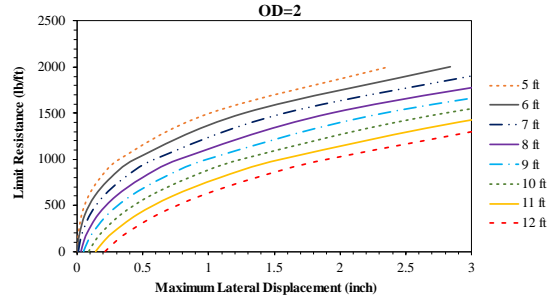
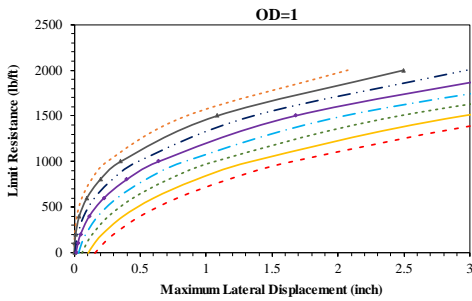
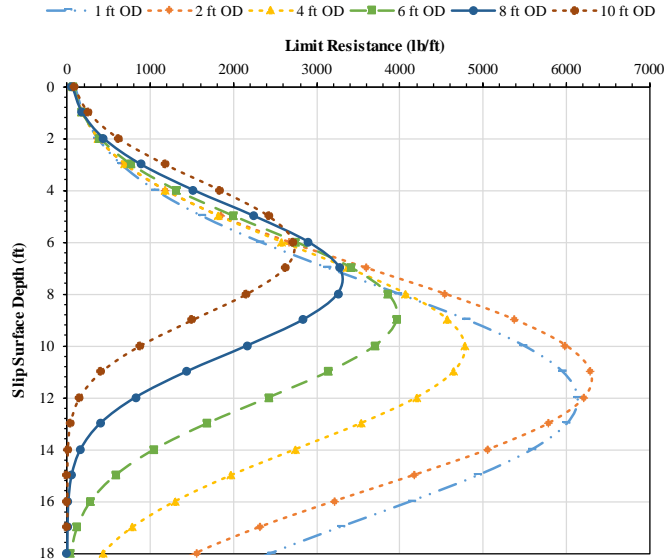
Limit Flexure for $c=400\text{psf}$, $\phi=30^\circ$



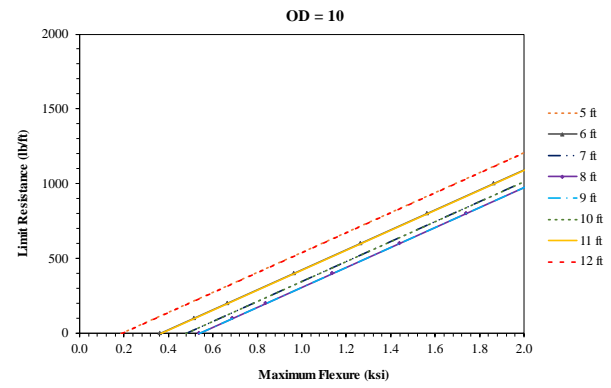
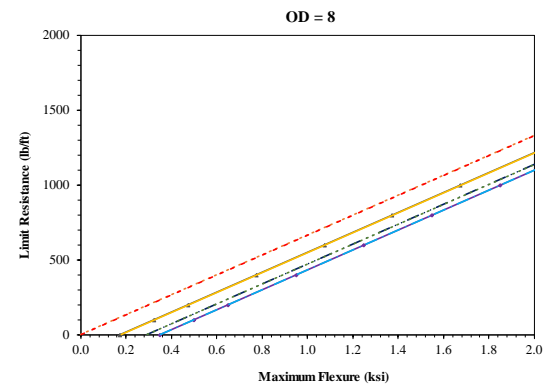
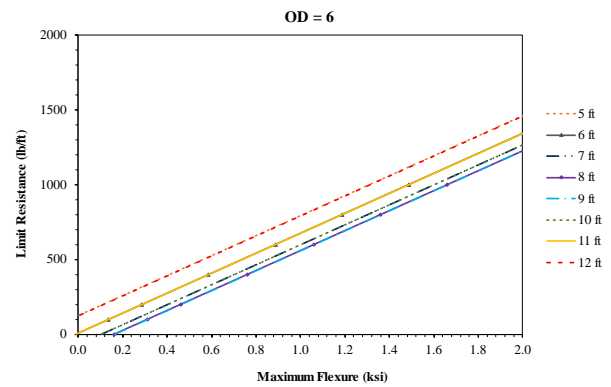
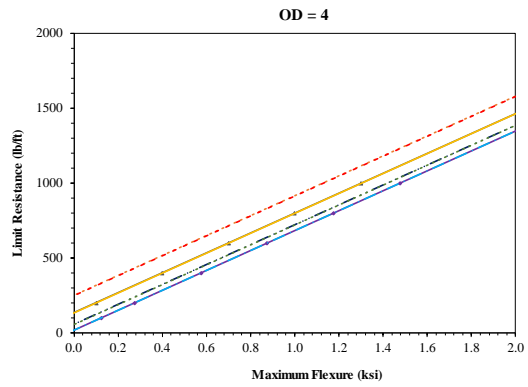
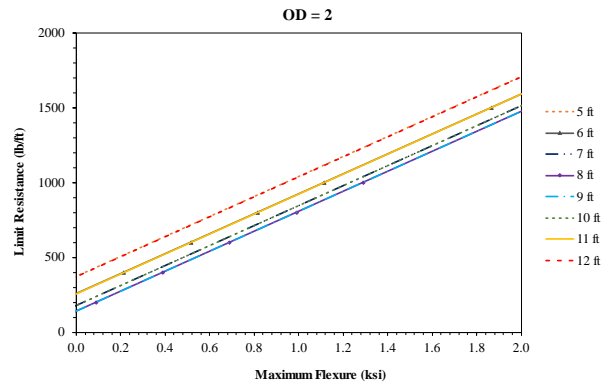
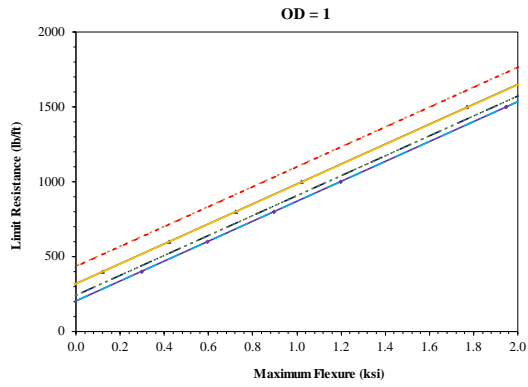
Limit Soil Resistance and Maximum Lateral Displacement for $c=500\text{psf}$, $\phi=10^\circ$



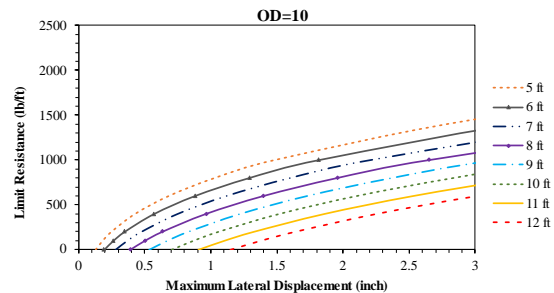
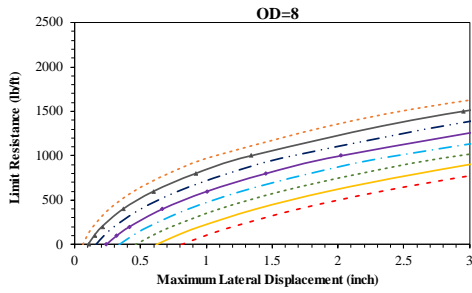
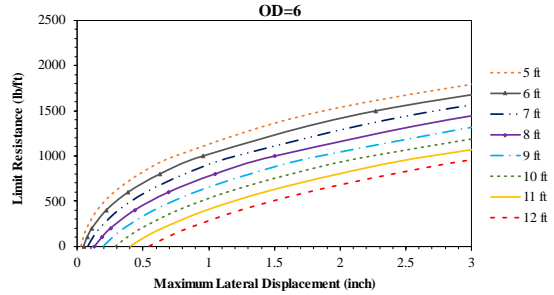
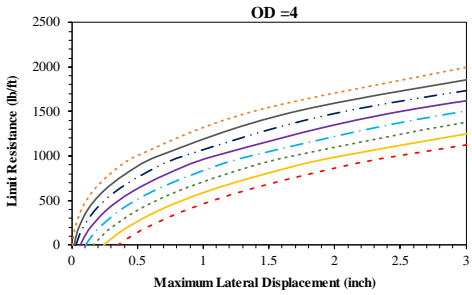
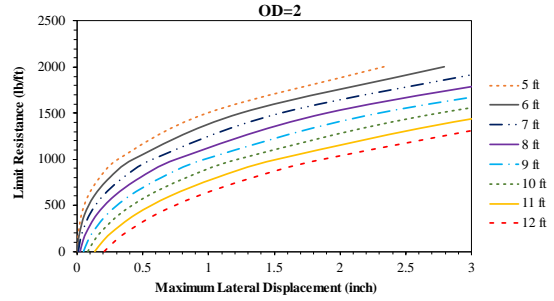
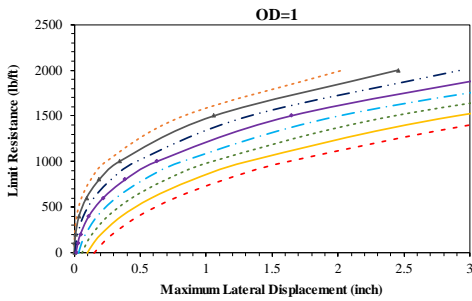
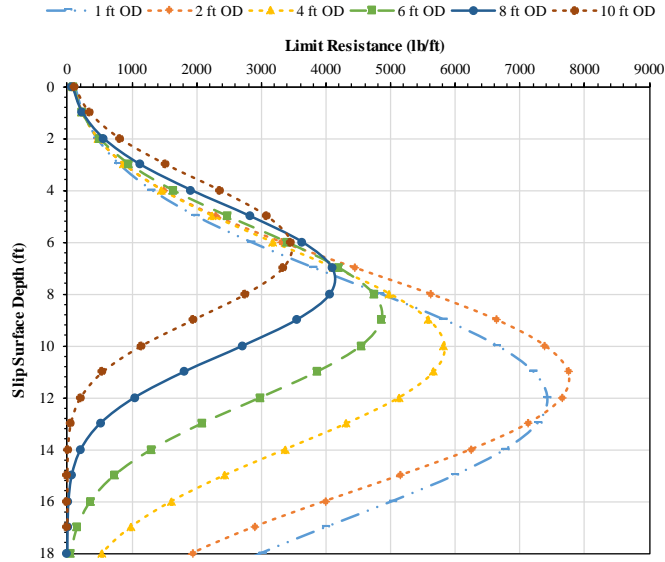
Limit Flexure for $c=500\text{psf}$, $\phi=10^\circ$



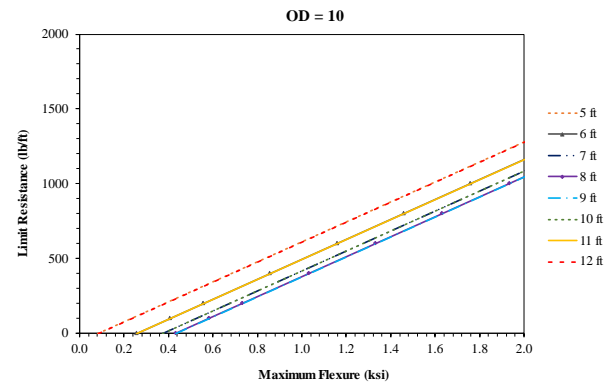
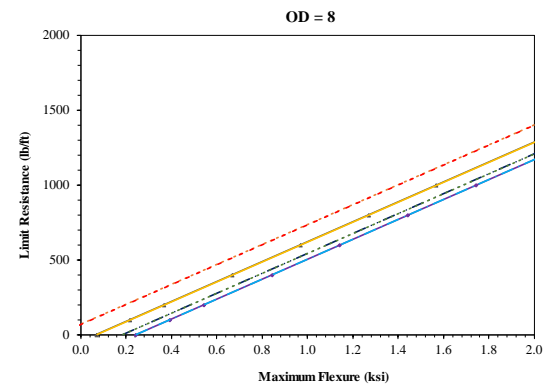
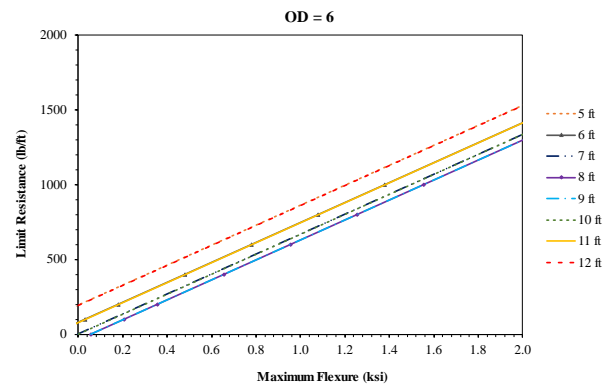
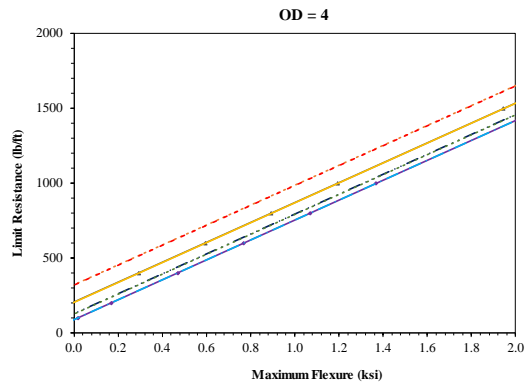
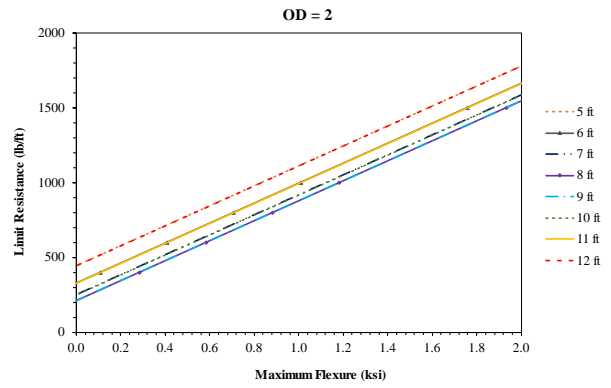
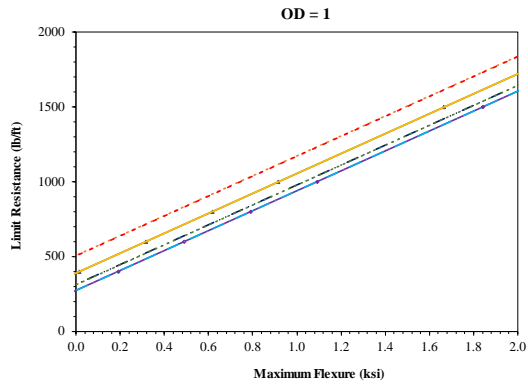
Limit Soil Resistance and Maximum Lateral Displacement for $c=500\text{psf}$, $\phi=20^\circ$



Limit Flexure for $c=500\text{psf}$, $\phi=20^\circ$



Limit Soil Resistance and Maximum Lateral Displacement for $c=500\text{psf}$, $\phi=30^\circ$



Limit Flexure for $c=500\text{psf}$, $\phi=30^\circ$

APPENDIX B
SOIL BORING LOGS

G:\GEOCH\BH\COLUMNS - GINT STD US LAB.GDT - 12/5/19 15:36 - C:\USERS\JP\3319\ONE\DRIVE - UNIVERSITY OF TEXAS AT ARLINGTON\2 FORTWORTH INSTALLATION\DRILLING\BORELOGS_1820 AND ROSEDALE ST\1820 AND ROSEDALE ST\B1.GPJ



UTA

BORING NUMBER BH-1

PAGE 1 OF 2

CLIENT <u>TxDOT - Fort Worth</u>	PROJECT NAME <u>Fort Worth Slope Stabilization</u>
PROJECT NUMBER <u>5</u>	PROJECT LOCATION <u>1820 and Rosedale St</u>
DATE STARTED <u>10/1/19</u> COMPLETED <u>10/1/19</u>	GROUND ELEVATION _____ HOLE SIZE <u>inches</u>
DRILLING CONTRACTOR _____	GROUND WATER LEVELS:
DRILLING METHOD <u>Hollow Stem Auger</u>	AT TIME OF DRILLING <u>--</u>
LOGGED BY <u>UTA</u> CHECKED BY <u>UTA</u>	AT END OF DRILLING <u>--</u>
NOTES _____	AFTER DRILLING <u>--</u>

DEPTH (ft)	GRAPHIC LOG	MATERIAL DESCRIPTION	SAMPLE TYPE NUMBER	BLOW COUNTS (N VALUE)	MOISTURE CONTENT (%)
0					
5		Gray Silty clay	ST TCP	6-6 (12)	
		Brown Clay with traces of small stones	AU		
10		Brown Clay	ST TCP	9-8 (17)	
			AU		
15		Light brown Clay	ST TCP	3-4 (7)	
			AU		
20			ST TCP	8-9 (17)	
			AU		
25		Dark brown Clay	ST TCP	7-10 (17)	
			AU		
30			ST TCP	7-11 (18)	

Bottom of borehole at 30.0 feet.

GEO TECH B41 COLUMNS - GINT STD US L48 GDT - 12/15/19 15:36 - C:\USERS\JP\B3319\ONE DRIVE - UNIVERSITY OF TEXAS AT ARLINGTON\2. FORT WORTH INSTALLATION\DRILLING\BORELOGS_1820 AND ROSEDALE ST\1820 AND ROSEDALE ST\1820 AND ROSEDALE ST\B01.GPJ

LOGO	UTA	BORING NUMBER BH-2	
		PAGE 1 OF 2	
CLIENT <u>TxDOT - Fort Worth</u>		PROJECT NAME <u>Fort Worth Slope Stabilization</u>	
PROJECT NUMBER <u>5</u>		PROJECT LOCATION <u>1820 and Rosedale St</u>	
DATE STARTED <u>10/1/19</u> COMPLETED <u>10/1/19</u>		GROUND ELEVATION _____ HOLE SIZE <u>inches</u>	
DRILLING CONTRACTOR _____		GROUND WATER LEVELS:	
DRILLING METHOD <u>Hollow Stem Auger</u>		AT TIME OF DRILLING <u>---</u>	
LOGGED BY <u>UTA</u> CHECKED BY <u>UTA</u>		AT END OF DRILLING <u>---</u>	
NOTES _____		AFTER DRILLING <u>---</u>	

DEPTH (ft)	GRAPHIC LOG	MATERIAL DESCRIPTION	SAMPLE TYPE NUMBER	BLOW COUNTS (N VALUE)	MOISTURE CONTENT (%)	
0						
5		Gray Silty clay	ST TCP	2-2 (4)		
10		Brown Clay	AU ST TCP	5-7 (12)		
15		Brown Clay	AU ST TCP	4-5 (9)		
20		Light brown Clay	AU ST TCP	6-8 (14)		
25		Dark brown Clay	AU ST TCP	7-9 (16)		
30				ST TCP	7-10	

Bottom of borehole at 30.0 feet. (17)



University of Texas at Arlington

BORING NUMBER BH-2

PAGE 1 OF 1

CLIENT TxDOT Ft Worth PROJECT NAME Emergency Site
 PROJECT NUMBER _____ PROJECT LOCATION US 67-Alvarado
 DATE STARTED 3/12/21 COMPLETED 3/12/21 GROUND ELEVATION _____ HOLE SIZE 6 inches
 DRILLING CONTRACTOR _____ GROUND WATER LEVELS:
 DRILLING METHOD _____ AT TIME OF DRILLING ---
 LOGGED BY UTA CHECKED BY UTA AT END OF DRILLING ---
 NOTES _____ AFTER DRILLING ---

GEO TECH BH COLUMNS . GINT STD US LAB GDT . 5/18/21 18:51 . C:\USERS\SX\4431\ONE DRIVE - UNIVERSITY OF TEXAS AT ARLINGTON\1319W & HENDERSON STREET\BORE LOG.GPJ

DEPTH (ft)	GRAPHIC LOG	MATERIAL DESCRIPTION	SAMPLE TYPE NUMBER	BLOW COUNTS (AL VALUE)	POCKET PEN. (tsf)
0		Dark to medium brown topsoil	ST		
0		Brown Clay			
5		Brown Clay	ST		
5		Brown Clay	TCP	6-7-7 (13)	
5			AU		
10		Yellowish brown Clay	ST		
10		Yellowish brown Clay	TCP	4-5-4 (9)	
10			AU		
15		Grey brown Clay	TCP	5-5-8 (10)	
15			AU		
20		Dark Brown Clay	ST		
20		Dark Brown Clay	TCP	5-7-10 (12)	
20			AU		
25		Light brown Clay	TCP	8-12-12 (20)	
25			AU		
30			TCP	15-16-15 (31)	

Bottom of borehole at 30.0 feet.



University of Texas at Arlington

BORING NUMBER BH-1

PAGE 1 OF 1

CLIENT TxDOT Ft Worth PROJECT NAME Emergency Site
 PROJECT NUMBER _____ PROJECT LOCATION US 67-Alvarado
 DATE STARTED 3/12/21 COMPLETED 3/12/21 GROUND ELEVATION _____ HOLE SIZE 6 inches
 DRILLING CONTRACTOR _____ GROUND WATER LEVELS:
 DRILLING METHOD _____ AT TIME OF DRILLING ---
 LOGGED BY UTA CHECKED BY UTA AT END OF DRILLING ---
 NOTES _____ AFTER DRILLING ---

GEO TECH BH COLUMNS - GINT STD US LAB GDT - 5/18/21 16:45 - C:\USERS\XIM443\ONE DRIVE - UNIVERSITY OF TEXAS AT ARLINGTON\315W & HENDERSON STREET\BORE LOG.GPJ

DEPTH (ft)	GRAPHIC LOG	MATERIAL DESCRIPTION	SAMPLE TYPE NUMBER	BLOW COUNTS (N VALUE)	POCKET PEN. (tsf)
0		Dark to light brown topsoil	ST		
0		Brown Clay			
5		Reddish brown Clay	ST TCP	5-6-7 (11)	
5			AU		
10		Yellowish brown Clay	ST TCP	4-4-4 (8)	
15		Grey brown Clay	AU TCP	4-5-6 (9)	
20		Light brown Clay	AU ST TCP	4-7-9 (11)	
25		Light brown Clay	AU TCP	7-10-12 (17)	
30			TCP	13-16-15 (29)	

Bottom of borehole at 30.0 feet.

REFERENCES

- Abusharar, S. W., & Han, J. (2011). Two-dimensional deep-seated slope stability analysis of embankments over stone. *Engineering Geology*, 103-110.
- Ahmed, A., Khan, S., Hossain, S., Sadigov, T., & Bhandari, P. (2020). Safety prediction model for reinforced highway slope using a machine learning method. *Transportation research record*, 2674(8), 761-773.
- Ahmed, Faisal Shakib. "Engineering Characteristics Of Recycled Plastic Pin, Lumber And Bamboo For Soil Slope Stabilization." (2013).
- Al-Homoud, Azm S., Ahmad B. Tal, and Salah A. Taqieddin. "A comparative study of slope stability methods and mitigative design of a highway embankment landslide with a potential for deep seated sliding." *Engineering geology* 47.1-2 (1997): 157-173.
- Alkasawneh, Wael, et al. "A comparative study of various commercially available programs in slope stability analysis." *Computers and Geotechnics* 35.3 (2008): 428-435.
- Altalhe, E. B., & Abdalftah, H. (2019, March). Study using nails in sand soil: stability, anchored length. In *International Conference on Technical Sciences (ICST2019)* (Vol. 60, p. 40).
- American Geological Institute. *Glossary of Geology and Related Sciences*. Washington, DC., 1957m 325 pp; supplement, 1960, 72 pp.
- Asuri, S., & Keshavamurthy, P. (2016). Expansive soil characterization: an appraisal. *INAE Letters*, 1(1), 29-33.
- Aurpa, Sehneela Sara. *Characterization of MSW and Plastic Waste Volume Estimation During Covid-19 Pandemic*. Diss. The University of Texas at Arlington, 2021.

Bowders, J. J., Loehr, E. J., & Chen, C.-W. (2003). *Evaluation of Recycled Plastic Products in Terms of Suitability for Stabilization of Earth Slopes*. Missouri Department of Transportation.

Bowders, J. J., Loehr, J. E., & Chen, C.-W. (2002). Engineering Properties of Recycled Plastic Pins for Slope Stabilization. *Transportation Research Record*, 39-46.

Bruce, Peter, and Andrew Bruce. 2017. *Practical Statistics for Data Scientists*. O'Reilly Media.

Castellanos, Bernardo A., Thomas L. Brandon, and Daniel R. VandenBerge. "Use of fully softened shear strength in slope stability analysis." *Landslides* 13.4 (2016): 697-709.

Chen, C. W., Salim, H., Bowders, J., Loehr, E., & Owen, J. (2007). Creep behavior of recycled plastic lumber in slope stabilization applications. *Materials of Civil Engineering*, 130-138.

Cook, R. Dennis (February 1977). "Detection of Influential Observations in Linear Regression". *Technometrics* (American Statistical Association)).

Day, R. W. (1996, August). Design and Repair for Surficial Slope Failures. *Practice periodical on structural design and construction*, pp. 83-87.

Duncan, J. M. (James Michael) et al. *Soil Strength and Slope Stability*. Second edition. Hoboken, New Jersey: Wiley, 2014. Print.

Environmental analysis. Environmental Analysis | KYTC. (n.d.). Retrieved October 4,

2022, from

<https://transportation.ky.gov/EnvironmentalAnalysis/Pages/default.aspx>

- Fox, N. S., & Cowell, M. J. (1998). *Geopier Foundation and Soil Reinforcement Manual*. Blacksburg, VA: Geopier Foundation Company.
- G. E. P. Box and D. R. Cox. An analysis of transformations. *Journal of the Royal Statistical Society B*, 26 (2):211–252, 1964. URL <http://citeseerx.ist.psu.edu/viewdoc/summary?doi=10.1.1.321.3819>. [p99, 100, 101, 102]
- Gregory, Garry H. 2011. "Stabilization of Deep Slope Failure with Drilled Shafts." *Geo-Frontiers*.
- Griffiths, D. V., and P. A. Lane. "Slope stability analysis by finite elements." *Geotechnique* 49.3 (1999): 387-403.
- Han, J., Chai, J.-C., Leshchinsky, D., & Shen, S.-L. (2004). Evaluation of Deep-Seated Slope Stability of Embankments. *GeoSupport 2004: Drilled Shafts, Micropiling, Deep Mixing, Remedial Methods, and Specialty Foundation Systems*, 945-954.
- Hassiotis, J., Chameau, J. L., & Gunaratne, M. (1997). Design Method for Stabilization of Slopes with Piles. *Journal of Geotechnical and Geoenvironmental Engineering*, 314-323.
- Hughes PN, Glendinning S, Mendes J et al (2009) Full-scale testing to assess climate effects on embankments. *Proc Inst Civ Eng Sustain* 162:67–79. doi:10.1680/ensu.2009.162
- Idiculla, G. T., & Dasaka, S. M. (n.d.). Discrete Piles as a Measure to Control the Slope Instability Issues in Urban Areas- A case study from Mumbai, India. *International Society for Soil Mechanics and Geotechnical Engineering*.

- Ito, T., & Matsui, T. (1975). Methods to estimate lateral force acting on stabilizing piles. *Soils and foundations*, 15(4), 43-59.
- James, Gareth, Daniela Witten, Trevor Hastie, and Robert Tibshirani. 2014. *An Introduction to Statistical Learning: With Applications in R*. Springer Publishing Company, Incorporated.
- Jeng, Ching-Jiang & Yo, Yo & Zhong, Kai-Lan. (2017). Interpretation of slope displacement obtained from inclinometers and simulation of calibration tests. *Natural Hazards*. 87. 10.1007/s11069-017-2786-6.
- Jutkofsky, W. S., Sung, J. T., & Negussey, D. (1999). Stabilization of Embankment Slope with Geofam. *Transportation Research Board*, 94-102.
- Khan, M. S. (2014). Sustainable slope stabilization using recycled plastic pins in Texas. PhD dissertation.
- Khan, M. S., Hossain, M. S., & Lozano, N. (2014). A Numerical Study on Slope Stabilization using Recycled Plastic Pin. *Geo-Congress 2014*, (pp. 3092-3101).
- Khan, M. S., Hossain, S., & Kibria, G. (2015). Slope Stabilization Using Recycled Plastic Pins. *Journal of Performance of Constructed Facilities*.
- Khan, M. S., Hossain, S., Ahmed, A., & Faysal, M. (2017). Investigation of a shallow slope failure on expansive clay in Texas. *Engineering Geology*, 118-129.
- Khan, Muhammad Israr, and Shuhong Wang. "Slope Stability Analysis to Develop Correlations between Different Soil Parameters and Factor of Safety Using Regression Analysis." *Polish Journal of Environmental Studies* 30.5 (2021).

- Kim, Jaehong, et al. "Influence of rainfall-induced wetting on the stability of slopes in weathered soils." *Engineering Geology* 75.3-4 (2004): 251-262.
- Kiousis , P. D., Griffiths, D. V., & Stewart, J. A. (2010, December). *Optimization of stabilization of highway embankment ... - inside mines*. Retrieved from https://inside.mines.edu/~vgriffit/pubs/Some_C_Pubs/dot_18454_DS1.pdf
- Lazarte, C. A., Elias, V., Espinoza, R. D., & Sabatini, P. J. (2003). *Geotechnical Engineering Circular No. 7: Soil Nail Walls*. Federal Highway Administration, Washington, DC.
- Loehr, J. E., Bowders, J. J., Owen, J. W., Sommers, L., & Liew, W. (2000). Stabilization of Slopes Using Recycled Plastic Pins. *Journal of the Transportation Research Board*.
- Loehr, J. E., Fennessey, T. W., & Bowders, J. J. (2002). Mechanical Stabilization of Earth Slopes Using Recycled Materials. *Proceedings of Beneficial Use of Recycled Materials in Transportation Applications*. Washington D.C.
- Loehr, J. Erik, and John J. Bowders. "Slope Stabilization Using Recycled Plastic Pins, Phase III." (2007).
- Loehr, J.E., Parra, J.R., E-C Ang, and J.J. Bowders (2004). "Design Method for Slope Stabilization Using Recycled Plastic Pins," *Proceedings of Geo-Trans 2004: Geotechnical Engineering for Transportation Projects*, M.K. Yegian and E. Kavazanjian, Editors, ASCE, GSP 126, Vol. 1, pp. 723-731
- Madanayake, Sachini, Muhasina Manjur Dola, and Md Sahadat Hossain. "Recycled Plastic Pins for General Slope Failures—A Case Study." *Geo-Congress 2022*.
- McLaren, M. G. (1995). Recycled plastic lumber and shapes design and specification. *Proceedings of 13th Structures Congress* (pp. 819-833). Reston, VA: ASCE.

- Mokhtari, M., & Masoud, D. (2012). Swell-shrink behavior of expansive soils, damage and control. *Electronic Journal of Geotechnical Engineering*, 2673-2682.
- Nelson, John D., Daniel D. Overton, and Dean B. Durkee. "Depth of wetting and the active zone." *Expansive clay soils and vegetative influence on shallow foundations*. 2001. 95-109.
- Parra, J. R., Caskey, J. M., Marx, E., & Dennis, N. (2007). Stabilization of Failing Slopes Using Rammed Aggregate Pier Reinforcing Elements. *Geo-Denver 2007: New Peaks in Geotechnics*. Denver: ASCE.
- Parra, J. R., Loehr, J. E., Hagemeyer, D. J., & Bowders, J. J. (2003). Field Performance of Embankments stabilized with Recycled Plastic Reinforcement. *Transportation Research Board*, 31-38.
- Phanikanth, V. S., Deepankar Choudhury, and G. Rami Reddy. "Response of single pile under lateral loads in cohesionless soils." *Electronic Journal of Geotechnical Engineering* 15.10 (2010): 813-830.
- Poulos, H. G. (2011). Design of Reinforcing piles to increase slope stability. *Canadian Geotechnical Journal*.
- Rauss, C. A. (2019). *Long Term Performance Monitoring of Shallow Slope Stabilization Utilizing Recycled Plastic Pins*.
- Rawat, S., & Gupta, A. K. (2016). Analysis of a nailed soil slope using limit equilibrium and finite element methods. *International Journal of Geosynthetics and Ground Engineering*, 2(4), 1-23.

- Reddy, BV Venkatarama. "Stabilised soil blocks for structural masonry in earth construction." *Modern earth buildings*. Woodhead Publishing, 2012. 324-363.
- Rowe, R. K., & Soderman, K. L. (1985). An approximate method for estimating the stability of. *Canadian Geotechnical Journal*, 392-398.
- S. S. Shapiro and M. B. Wilk. An analysis of variance test for normality. *Biometrika*, 52(3/4):591–611, 1965. URL <https://www.jstor.org/stable/2333709>. [p102]
- Sabatini, P.J., Elias, V., Schmertmann, G.R., Bonaparte, R. (1997). 'Geotechnical Engineering Circular No. 2, Earth Retaining Systems.' Publication FHWA-SA-96-038, Federal Highway Administration, Washington, D.C.
- Sapkota, A. (2019). Effect of Modified Moisture Barriers on Slopes with Recycled Pins. PhD Dissertation. Sapkota, A. (2019). *Effect of Modified Moisture Barriers on Slopes with Recycled Pins*. PhD Dissertation.
- Shrestha, N. (2020). Detecting multicollinearity in regression analysis. *American Journal of Applied Mathematics and Statistics*, 8(2), 39-42.
- Siddiqui, F. I., and S. B. A. B. S. Osman. 2013. "Simple and multiple regression models for relationship between electrical resistivity and various soil properties for soil characterization". *Environmental earth sciences*, 70 (1), 259-267.
- Sindlinger, A. (2009, March). Asset management highlights slope maintenance. *Asset Management Highlights Slope Maintenance | FHWA*. Retrieved May 30, 2022, from <https://highways.dot.gov/public-roads/marapr-2009/asset-management-highlights-slope-maintenance>

- Skempton, A.W. (1977) "Slope Stability of Cuttings in Brown London Clay." Proc., Ninth Int. Conf. on Soil Mechanics and Foundation Engineering, Tokyo, Vol. 3, 261-270
- Stirling, R. A., Toll, D. G., Glendinning, S., Helm, P. R., Yildiz, A., Hughes, P. N., & Asquith, J. D. (2021). Weather-driven deterioration processes affecting the performance of embankment slopes. *Géotechnique*, 71(11), 957-969.
- Strata Systems. (n.d.). Reinforced soil slopes and embankments. Retrieved May 31, 2022, from https://cdn.glenraven.net/geogrid/pdf/en_us/StrataSlope_Reinforced-soil-slopes-embankments.pdf
- Sudha, K., M. Israil, S. Mittal, and J. Rai. 2009. "Soil characterization using electrical resistivity tomography and geotechnical investigations". *Journal of Applied Geophysics*, 67(1), 74-79.
- Sun, J., Liu, Q., Li, J., & An, Y. (2009). Effects of rainfall infiltration on deep slope failure. *Science in China Series G: Physics, Mechanics and Astronomy*, 52(1), 108-114.
- Sun, Shu-Wei, Jia-Chen Wang and Xiao-Lin Bian. "Design of micropiles to increase earth slopes stability." *Journal of Central South University* (2013): 1361-1367.
- T. S. Breusch and A. R. Pagan. A simple test for heteroscedasticity and random coefficient variation. *Econometrica*, 47(5):1287-1294, 1979. URL <https://www.jstor.org/stable/1911963>. [p102]
- Titi, H. H., & Helwany, S. (2007). *Investigation of Vertical Members to Resist Surficial Slope Instabilities*. The Wisconsin Department of Transportation.

- Trinidad González, Yuderka, Vernon R. Schaefer, and Derrick K. Rollins. "Statistical assessment of factor of safety for pile-reinforced slopes." *Journal of Geotechnical and Geoenvironmental Engineering* 146.9 (2020): 04020083.
- Turner, A. K., & Schuster, R. L. (1996). *Landslides: Investigation and Mitigation. Transportation Research Board Special Report 247*. Washington, D.C: National Research Council.
- TxDOT. (2000). Geotechnical Manual. Austin, Texas.
- TxDOT. Global Stability Analysis. Geotechnical Manual: Analysis and Design. (2020). Retrieved April 7, 2022, from http://onlinemanuals.txdot.gov/txdotmanuals/geo/analysis_and_design.htm
- Wang, Yuke, and Musen Han. "Optimal design of slope reinforcement by a new developed polymer micro anti-slide pile in case of emergency and disaster relief." *Natural Hazards* (2022): 1-19.
- Wright, S. G., (2005). "Evaluation of Soil Shear Strengths for Slope and Retaining Wall Stability Analyses with Emphasis on High plasticity Clays." Federal Highway Administration, Washington, D.C, FHWA/TX-06/5-1874-01-1.
- Wu, J. T., & Helwany, S. M. (2001). Examining the Effects of Reinforcement in U.S. Forest Service Deep-Patch Landslide Repair Technique. *Transportation Research Board*, 203-210.
- Xu, L., Dai, F., Chen, J., Iqbal, J., & Qu, Y. (2014). Analysis of a progressive slope failure in the Xiangjiaba reservoir area, Southwest China. *Landslides*, 11(1), 55-66.

Yang, G., Zhong, Z., Zhang, Y., & Fu, X. (2015). Optimal design of anchor cables for slope reinforcement based on stress and displacement fields. *Journal of Rock Mechanics and Geotechnical Engineering*, 7(4), 411-420.

Zhdanov, M. S., and G. V. Keller. 1994. "The geoelectrical methods in geophysical exploration". *Methods in geochemistry and geophysics*, 31, I-IX.

BIOGRAPHY

Sachini Madanayake earned her bachelor's degree in Civil Engineering from the University of Texas at Arlington in May 2019 and graduated with Summa Cum Laude honors. She continued her graduate studies at University of Texas at Arlington in the field of Geotechnical Engineering. She worked as a graduate research assistant from June 2019 to June 2022 under Dr. MD Sahadat Hossain. She was awarded the Dwight E. Eisenhower Transportation fellowship for two consecutive years during her doctorate program. In July 2019, she joined Converse Consultants as a Senior Staff Professional. The author's research experience and interests include slope stability, expansive soil, numerical modeling, statistical analysis, recycled materials, field instrumentation, foundation analysis, geotechnical laboratory testing, geophysical investigation, and sustainable waste management.